Modeling Nanoparticle Formation in Reactive Flows with Quadrature-based Moment Methods

Modellierung der Nanopartikelbildung in reaktiven Strömungen mit quadraturbasierten Momentenmethoden

Zur Erlangung des akademischen Grades Doktor-Ingenieur (Dr.-Ing.)
Genehmigte Dissertation von Robert Martin Schmitz aus Worms
Tag der Einreichung: 05.12.2023, Tag der Prüfung: 20.02.2024

1. Gutachten: Prof. Dr.-Ing. Christian Hasse
2. Gutachten: Jun.-Prof. Dr.-Ing. Federica Ferraro
Darmstadt, Technische Universität Darmstadt

TECHNISCHE UNIVERSITÄT DARMSTADT

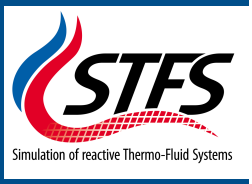

Modeling Nanoparticle Formation in Reactive Flows with Quadrature-based Moment Methods
Modellierung der Nanopartikelbildung in reaktiven Strömungen mit quadraturbasierten Momentenmethoden

Accepted doctoral thesis by Robert Martin Schmitz

Date of submission: 05.12.2023
Date of thesis defense: 20.02.2024

Darmstadt, Technische Universität Darmstadt

Abstract

The alternative fuel oxymethylene ether (OME) combines CO_2-neutral and simultaneously almost sootless combustion under the condition of a sustainable synthesis. A precise understanding of its mechanisms that lead to reduced soot emissions is necessary for the efficient utilization of this valuable and limited alternative to fossil fuels. This study examines the impact of mixing processes between fuel and oxidator, as well as the influence of OME fuel on soot formation. The investigation is structured into six scientific objectives, isolating influencing factors systematically. Laminar premixed and counterflow diffusion flame configurations are numerically considered. For the soot modeling, the simulations use direct chemistry coupled with two distinct quadrature-based moment methods. The modeling of the physical and chemical processes enables the examination and explanation of the impact of individual factors throughout the entire chain of events on a mechanistic level. The validation of the soot modeling shows that numerical results are congruent with the experimental results.

Strain has minimal quantitative influence on the soot processes, whereas fuel dilution significantly reduces all soot sub-processes. Adding OME_3 into sooting ethylene flames causes a substantial reduction in soot aggregates and shows only a slight influence on nanoparticles. The decrease is related to the OME_3 decomposition in the gas phase towards mainly formaldehyde (CH_2O) without a direct reaction pathway to species crucial to soot formation. Therefore, soot precursor species such as acetylene (C_2H_2) are reduced leading to weakened soot growth processes. An increase in the OME_3 content within the fuel mixture results in a linear decrease in soot volume fraction. The three OME_n variants, OME_2, OME_3, and OME_4, show similar qualitative and quantitative effects on the soot precursors and formation. Closer investigations of the particle size distribution provide further insights into the underlying processes.

Kurzfassung

Der alternative Kraftstoff Oxymethylenether (OME) kombiniert CO_2-neutrale und gleichzeitig beinahe rußfreie Verbrennung unter der Voraussetzung einer nachhaltigen Synthese. Für eine effiziente Nutzung dieser teuren und nur begrenzt verfügbaren Alternative zu fossilen Kraftstoffen, sind genaue Kenntnisse über die Wirkmechanismen, die zu einer Reduktion der Rußemissionen führen, notwendig. In dieser Ausarbeitung wird der Effekt von der Vermischung zwischen Oxidator und Brennstoff sowie der Einfluss des Brennstoffs OME auf die Rußbildung analysiert. Die Untersuchung ist in sechs wissenschaftliche Ziele unterteilt, in der Einflussfaktoren systematisch voneinander isoliert untersucht werden. Laminar vorgemischte Flammen und Gegegenstromdiffusionsflammen werden numerisch betrachtet. Für die Simulation wird direkte Chemie genutzt, die mit zwei verschiedenen quadraturbasierten Momentenmethoden zur Rußmodellierung gekoppelt ist. Die Modellierung der physikalischen und chemischen Prozesse ermöglicht es, den Einfluss einzelner Faktoren auf die gesamte Wirkkette auf einer mechanistischen Ebene zu untersuchen und zu erklären. Die Validierung der Rußmodellierung zeigt, dass die Simulationsergebnisse mit den experimentellen Ergebnissen übereinstimmen.

Streckung bewirkt einen geringen Einfluss auf die Rußprozesse, wohingegen Brennstoffverdünnung alle Rußraten stark reduziert. Die Hinzugabe von OME_3 in eine rußende Ethenflamme führt zu einer starken Reduktion von Rußaggregaten und zeigt nur einen geringen Einfluss auf Nanopartikel. Diese Abnahme ist durch die Aufspaltung von OME_3 in der Gasphase zu hauptsächlich Formaldehyd (CH_2O) ohne direkte Reaktionspfade zu rußrelevanten Spezies zu begründen. Die hierdurch verringerte Acetylenbildung (C_2H_2) wird zusätzlich mit zunehmendem OME_3-Anteil im Brennstoffgemisch verstärkt, wodurch das Rußwachstum abgeschwächt wird und der Rußvolumenbruch linear abnimmt. Die drei OME_n Varianten OME_2, OME_3 und OME_4 zeigen ähnliche qualitative und quantitative Effekte auf die Rußvorläufer und die Rußbildung. Die nähere Betrachtung der Partikelgrößenverteilung gibt weiteren Aufschluss über die zugrunde liegenden Vorgänge.

Table of contents

Acronyms

AALH	Aromatic aliphatic linked hydrocarbons
CQMOM	Conditional quadrature method of moments
DLR	Deutsches Zentrum für Luft- und Raumfahrt
DQMOM	Direct quadrature method of moments
DSM	Discrete sectional method
EQMOM	Extended quadrature method of moments
GQMOM	Generalized quadrature method of moments
HAB	Height above the burner
HACA	Hydrogen abstraction carbon addition
HMOM	Hybrid method of moments
KDF	Kernel density function
LIF	Laser-induced fluorescence
LII	Laser-induced incandescence
MC	Monte Carlo
MD	Molecular dynamics
MOM	Method of moments
MOMIC	Method of moments with interpolative closure
NDF	Number density function
PAH	Polycyclic aromatic hydrocarbon
PBE	Population balance equation
PCAH	Pericondensed aromatic hydrocarbon
PSD	Particle size distribution

QbMM	Quadrature-based moment method
QMOM	Quadrature-based method of moments
RSM	Reactive Flows and Diagnostics
S-EQMOM	Split-based extended quadrature method of moments
SM	Sectional method
STFS	Simulation of reactive Thermo-Fluid Systems
TUDa	Technical University of Darmstadt

List of Figures

List of Tables

1 Introduction

This cumulative dissertation is based on five journal publications, as listed in the appended Chap. *Publications*. While the primary outcomes of the underlying publications are combined and discussed in this manuscript, the reader is referred to the publications themselves for more comprehensive details.

1.1 Motivation for chemical energy carriers and soot modeling research

Driven by the continuously progressing climate change, the world is rapidly transitioning towards electrification of industrial production, private households, and the overall transport sector. Increasing adoption of renewable energy sources turns the energy sector upside down and will potentially replace fossil fuel-based power plants in the long term. Electric vehicles already provide efficient and sustainable transportation without carbon dioxide emission, assuming that they are charged with electricity from renewable sources. Still, numerous obstacles exist, especially in the near future and medium term. Renewable energies such as wind or solar-based energy sources typically encounter fluctuations due to outside influences, namely weather conditions. Energy storage systems could bridge these periods of low or no renewable energy output, which often coincide with periods of high energy demand. Batteries based on electrochemical principles do not qualify for energy storage on large scales due to their low capacity [1].

Therefore, chemical energy carriers are assumed to remain playing a vital role [2] also in the future. One primary benefit of chemical energy carriers is their higher energy density compared to electrical energy storage systems [1], making them an attractive option for storing energy on large scales or for energy-intensive transport applications. Given the availability of the required fuels, this benefit is accompanied by their controllable supply, e.g., independence of wind or solar conditions.

Alternative fuels could combine both benefits when synthesized using renewable energy and on the basis of carbon sources such as carbon waste streams or atmospheric carbon capture. No additional CO_2 is released into the atmosphere compared to the carbon that is bound during their production, creating a closed carbon loop. The synthesis or utilization of many e-fuels such as hydrogen, ammonia, sustainable aviation fuels, methanol, and alternatives to fossil gasoline or diesel fuel [3] are topics for various current and past research programs. They combine a low impact on the global carbon balance with the possibility of being used as alternatives to fossil fuels in current combustion devices. This retrofitting allows for extending the life span of already

existing systems with more or less adaptations. Hence, their usage exhibits great potential in short-term or medium-term time frames. For areas of application that are hard to electrify, such as aero-engines, they also present a valid solution for the long term. Overall, synthesized alternative e-fuels could complement the transition toward climate neutrality.

Besides these huge potentials, major disadvantages still remain. Carbon-based e-fuels negatively impact the environment due to the emission of unwanted combustion byproducts such as soot particles. Soot particles are respirable and harm human health due to an increased risk of cancer and respiratory, or cardiovascular diseases [4]. Human exposure to such combustion emissions is assumed to result in increased mortality [5]. Hence, predicting, controlling, and reducing such soot particulate matter emissions is of utmost importance and, at the same time, challenging [6].

The application of oxygenated, synthetic fuels is one solution to reduce soot particle emissions due to the oxygen enclosed in this fuel. Promising candidates are oxymethylene ethers (OMEs), which exhibit similar properties compared to commercial diesel fuel, favoring their utilization in compression-ignition engines.

Several experimental studies demonstrated the performance of OME fuels as a blending component or as a neat fuel. Significant reductions of soot particle emissions were observed for a wide range of operating conditions, effectively overcoming the soot-NO_x trade-off encountered for fossil diesel fuel. Despite these studies, more profound knowledge of the underlying principal mechanisms of the chemical and physical effects of OME_n fuel on the soot formation processes is still missing.

By modeling the individual physical and chemical phenomena of the soot formation processes, a detailed understanding can be achieved. The need for closer insights in order to control soot particle emissions in future engines is the motivation for the underlying publications of this dissertation. Here, the main parameters, including chemical fuel structure and mixing, which control soot formation and evolution processes, are analyzed using two numerical quadrature-based moment method approaches. These parameters involve the mixing of fuel and oxidizer through variations of strain and fuel dilution. Additionally, the effect of the chemical fuel structure for OME on the gas-phase soot precursors and the subsequent effect on soot particle development is systematically investigated. Hence, this dissertation and underlying publications aim to understand the cause-and-effect chain of the soot formation processes in OME_n flames and their comprehensive, numerical modeling. The latter is crucial to optimize combustion systems further, ensure efficient usage of cost-intensive synthetic fuels with limited availability, and simultaneously reduce unwanted emissions.

After highlighting the relevance of alternative fuels as sustainable energy carriers and soot formation research in order to reduce soot particulate emissions, the remainder of this manuscript is structured as follows: In the beginning, in Sec. 1.2 a brief overview of the chemical and physical soot formation mechanisms is given, as these processes are essential for this study. Then, in Sec. 1.3, general soot modeling approaches are presented before details of the two applied modeling strategies are described in Sec. 1.3.1 and Sec. 1.3.2. The current state of research and understanding of the OME fuel and its effect on soot formation is summarized in Sec. 1.4. Chapter 2 defines the scientific research objectives, that guide the following chapters. The main outcomes and findings for the individual objectives are reassembled based on the underlying publications and discussed

in Chap. 3. Additionally, the manuscript ends with a conclusion and outlook about possible future research topics in Chap. 4.

1.2 Basics of soot formation processes

Soot particulate matter represents a liquid-like or solid phase dispersed within the gas phase. Soot particles mainly consist of carbon atoms and, depending on their age, of varying amounts of hydrogen. Additional elements, such as oxygen, were also found to be embedded in soot particles. The soot particles originate from the fuel decomposition and soot precursor formation in the gas phase. Gas-phase precursors lead to the formation of initial, young particles. Subsequently, particles grow in size and evolve due to interactions with the gas phase or collisions among themselves.

The following sections briefly describe these processes of soot formation and their further evolution. Fig. 1.1 visually represents the gas-phase and solid-phase steps of the soot formation processes and aids their corresponding description below.

1.2.1 Fuel decomposition and soot precursor formation

Requirements for forming carbonaceous soot particles are a surplus of hydrocarbon fuels with direct carbon-to-carbon bonds combined with sufficient temperatures for thermal cracking of the fuel [7]. These conditions can occur during premixed combustion processes with mixtures richer than stoichiometric fuel-to-oxidizer ratios, locally under non-premixed or partially premixed combustion, or in pyrolytic conditions entirely without or with little presence of oxygen. In practical applications, such as aero-engines, gas turbines, or piston-driven combustion engines, conditions prone to soot formation can be present despite overall stoichiometric combustion events. Here, primarily insufficient mixing of the fuel and oxidizer leads locally to fuel-rich conditions, causing one of the major sources of soot emissions [8].

Fuel-rich or pyrolytic conditions lead to incomplete combustion without complete oxidation of hydrocarbon fuels due to the lack of oxygen in the mixture composition. Unwanted byproducts such as soot precursor species are formed, which lead in subsequent steps to soot particle formation [8] instead of fuel oxidization toward the combustion products CO_2 and H_2O.

The fuel molecules are decomposed by thermal cracking, H-abstraction, or β-scission reactions if the required activation energy is available, such as in close proximity to the flame front [9]. Depending on the initial fuel mixture, the products of these decomposition processes are smaller alkenes, alkynes, aromatic structures, or radicals. Acetylene (C_2H_2) can be found as a decomposition product in sooting conditions [10], which promotes the formation of soot precursor species and also interacts directly with the soot particles, leading to soot growth. These fuel fragments are not oxidized but participate in forming polycyclic aromatic hydrocarbons (PAHs).

The formation of PAHs is initiated with the emergence of small, aromatic ring structures such as benzene (C_6H_6) or naphthalene ($C_{10}H_8$). In premixed acetylene and ethylene flames, benzene is mainly formed by the combination of C_2H_2 to several C_4 species (n-C_4H_x) [11, 12] or through

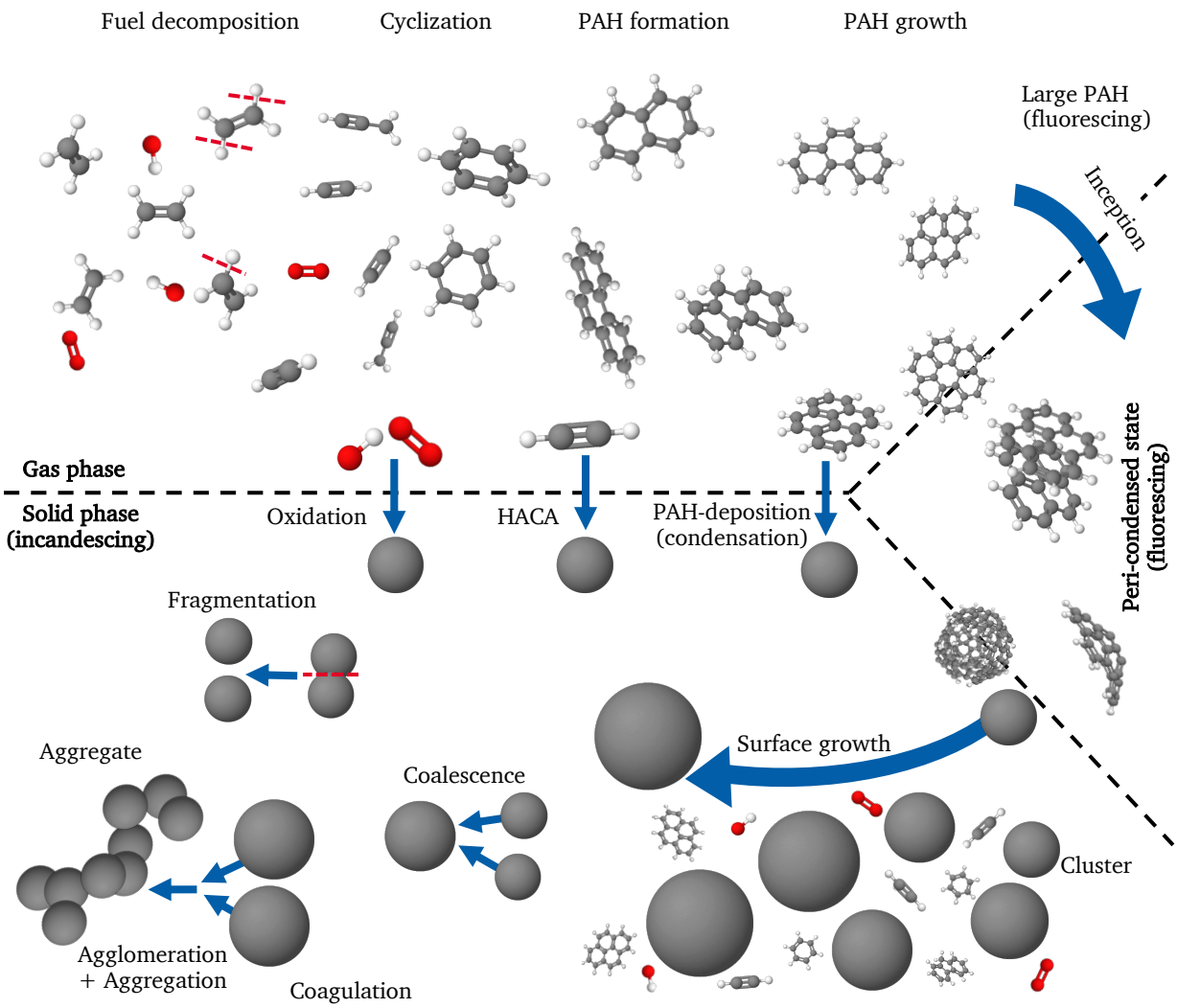

Fig. 1.1: Schematic overview of fuel decomposition, soot precursor formation, and further soot evolution.

propargyl radicals (C_3H_3) and successive cyclization reactions [13, 14, 15, 16]. On the other hand, the two-ring aromatic compound naphthalene can directly emerge through the combination of cyclopentadienyl (C_5H_5) [9].

The initial aromatic ring structures grow in size and weight by multiple reaction pathways, accumulating to PAHs with several aromatic ring structures. For instance, two acetylene molecules can connect to adjacent edges of the PAH with subsequent closure of a new ring structure while hydrogen gets abstracted following the hydrogen abstraction carbon addition mechanism (HACA) [17, 12, 18]. This chain of reactions leads to pericondensed aromatic hydrocarbons (PCAHs) featuring mainly six-membered rings and a high carbon-to-hydrogen ratio. On the other hand, benzyl, propargyl, or cyclopentadienyl radicals or other aromatic and aliphatic compounds add further

weight to the PAHs by the resonance stabilized free radical reaction and, therefore, lead to the growth of the molecule [19, 20, 21, 22, 23]. Reaction products of the latter pathways are aromatic aliphatic linked hydrocarbons (AALH) featuring lower carbon-to-hydrogen ratios than PCAH. Their structure consists of pentagonal, aromatic, or heptagonal groups of planar or curved shape [7]. Further PAH growth mechanisms can be found in the literature [24, 25].

1.2.2 Soot particle inception

Inception describes the transition from PAHs of the gas phase to young nanoparticles. The large number of available inception models illustrates that this process is not fully understood up to today and is still a topic of current research [7, 26, 27]. Physical, chemical or a combination of both phenomena are current explanations for the inception process in the literature. A concurrent combination of several pathways is most likely, and some pathways may be favored depending on the flame conditions and existing species pool. A widely assumed process is the stacking of multiple large PAHs with a planar shape connected through van der Waals forces [28, 29, 30, 24, 31]. Others explain the process by chemical interlinking of multiple PAHs through, e.g., acetylene, by continuous chemical growth through adsorption of acetylene, aromatic, or aliphatic hydrocarbons [32]. Another theory is the transition from planar PAHs toward three-dimensional, curved shells. The subsequent layering of several of these shells forms fullerene-like spheres [24].

Incipient soot particles are in a condensed state with liquid-like properties and turn to solid soot nuclei after further particle growth processes. These young soot particles consist of a three-dimensional structure in the range of one to six nanometers in size [33, 34, 35] and work as growth centers for subsequent particle evolution. Due to their origin from gas-phase hydrocarbons, they contain a low molar carbon-to-hydrogen ratio of approximately 1.4-2.5 [26, 33, 36, 37] combined with a low density, which changes with further growth.

1.2.3 Soot particle evolution and growth

After their initial formation, particle structures interact with the gas-phase species leading to surface growth, oxidation, or dehydrogenation processes. Gas-phase species are adsorbed by the particles and form layers around the surface of the initial growth centers either by chemical bonds or physical adsorption processes. Similar to the PAH formation in the gas-phase due to the HACA mechanism, acetylene can deposit onto the particle by chemisorption [38, 39]. PAHs condense onto the particle surface [12], and depending on the flame conditions and species pool of the gas phase, additional deposition or physisorption processes are possible [26].

These processes lead to a continuous evolution of the young particles toward matured soot particles with a spheroidal shape. Their chemical and physical properties are altered, and they grow in mass and size while their molar carbon-to-hydrogen ratio increases, which leads to a carbonization of their chemical composition. Simultaneously, oxygen-containing species, such as OH, O, O_2, and O_3, oxidize or desorb parts of the outer particle surface and inner structure, forming CO, CO_2, and H_2O [40, 41, 42, 43]. These oxidating processes lead to particle shrinking or their complete oxidation.

Besides the interaction of particles with gas-phase species, collisions of several primary particles among one another can occur. This coagulation process forms joined particles with a larger size. Depending on the size of the involved primary particles and underlying flame conditions, coagulation can lead to coalescence or agglomeration of these particles. Younger soot particles with a smaller size tend to fully merge upon collision [18], creating a new particle of spheroidal shape such that the initial entities smelt to one structure without any distinguishable boundaries. Agglomeration, on the other hand, loosely connects several primary particles at confined areas of their surface such that the individual primary particles are still identifiable [44]. Aggregation describes further surface growth, which strengthens the bond between these sub-units of the agglomerate to form a chain- or fractal-like structure [45]. These aggregates grow up to several micrometers, while larger aggregates are also referred to as super-aggregates. The later process may be reversed by oxygen, which diffuses into the particle structure and weakens their bonds through oxidizing their connecting links, increasing the possibility for an O_2-induced fragmentation of the aggregates into its primary particles again [46, 42, 47].

1.3 Soot modeling approaches

Additionally to the description of the gas-phase chemistry and thermodynamic evolution, the formation of the dispersed particles and further interaction with the gas phase and among the particles themselves must be modeled appropriately. A short overview of different soot particle modeling classifications is described in the following before models based on particle property distributions are explained.

An exhaustive reproduction of all the described chemical and physical processes for the soot precursor species and soot particle formation in a model requires considerable computational power. Therefore, the applied modeling strategy is adjusted to the scientific objective of the research, the desired level of accuracy, and the scale of the numerical domain but is limited by the compromise between modeling accuracy and calculation costs.

Different types of modeling strategies can be grouped on the basis of the length scales they are reflecting for the gas-phase phenomena and soot formation processes of the dispersed phase into molecular dynamics (MD) models, models considering one or several property distributions of the particles, and empirical modeling approaches [48]. Figure 1.2 visualizes these modeling approaches, and a brief overview of current soot modeling strategies is described in the following before explaining the applied models of the current work. Li et al. [48] wrote a review article that provides a detailed overview of the different soot formation modeling types.

MD models consider processes on the intermolecular scale to describe the evolution of molecules, such as the formation of larger PAHs. Interatomic forces [49] and the motion of the individual atoms within the molecules are directly taken into account to describe the microscale processes of molecules quantitatively [50]. Newton's second law of motion and interatomic potentials, such as the force field of the atoms, govern the atoms' motion [50]. The motion path of the molecules and constituent atoms is numerically evaluated by integrating these equations over time for a significantly large set of particles [50]. While this approach provides detailed insights into molecule

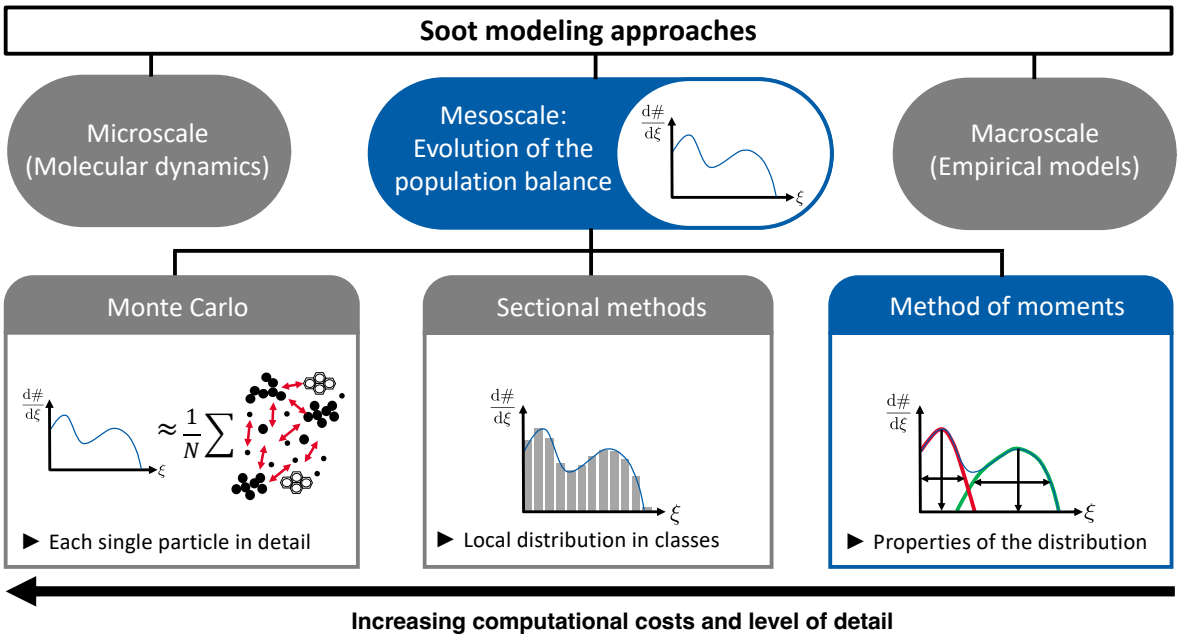

Fig. 1.2: Overview of soot modeling approaches.

interactions and subsequent reaction paths, numerical costs and small time scales of atomic motions prevent soot simulations of application scale. In the context of soot formation, MD are used to investigate the stability and internal properties of PAH dimers [51, 52], the interaction forces between nanoparticles [49], or the PAH growth to incipient particles [53].

Models on the macroscale are able to describe integral properties of the soot formation process, such as the soot mass or soot number density. These models are based on one or two transport equations, and the soot formation processes are empirically or semi-empirically fitted approximations [48]. A widely used model is the model that is developed by Khan et al. [54], which only contains a soot creation and soot destruction step. A prominent two-equation model with slightly larger complexity [55, 56] includes additional surface growth and coagulation phenomena. Due to their simple formulation and minimal number of transport equations, these models involve low numerical expenses. Although quantitative predictions of soot formation can be accurately predicted within specific scenarios for which they are designed and empirically optimized, their lack of generality can restrict their predictability in other cases. Macroscale models mainly assume monodispersed particle distributions [48] and only reflect a small number of particle properties. In contrast, particles generated from combustion processes exhibit polydisperse characteristics, leading to distribution functions of their physical features, chemical compositions, and molecular structures.

A compromise between the simulation of the individual atoms composing the soot particles with MD and the confinement to integral values with the macroscale models is to resolve such distribution functions of the particles as described above for the modeling of the particle processes. This dissertation applies a distribution-based approach for the soot particle properties. The distribution

function or number density functions (NDFs) $n(t, \underline{x}; \underline{\xi})$ of the particles describing the distribution of the entire particle population within a volume of interest is modeled at the spatial coordinates $\underline{x}$ in time t [57]. Each soot particle can be described by its properties or coordinates, accumulated in the internal coordinate vector $\underline{\xi}$ [57].

The general population balance equation (PBE) describes the evolution of the NDF and is defined as [58]:

$$\underbrace{\frac{\partial n(t,\underline{x};\underline{\xi})}{\partial t}}_{\text{rate of change}} + \underbrace{\frac{\partial \underline{u} n(t,\underline{x};\underline{\xi})}{\partial \underline{x}}}_{\text{convection}} - \underbrace{\frac{\partial}{\partial \underline{x}}\left(0.55\frac{\nu}{T}\frac{\partial T}{\partial \underline{x}} n(\underline{x},t;\underline{\xi})\right)}_{\text{thermophoresis}} - \underbrace{\frac{\partial}{\partial \underline{x}}\left(\Gamma_m \frac{\partial n(t,\underline{x};\underline{\xi})}{\partial \underline{x}}\right)}_{\text{molecular diffusion}} \tag{1.1}$$
$$= R_{inc} + R_{sg} + R_{depo} + R_{ox} + R_{coag}.$$

The balance equation includes the temporal rate of change, spatial convection considering the velocity vector $\underline{u}$ of the gas phase, the molecular diffusion term considering the Brownian diffusion Γ_m, and thermophoresis with the kinematic viscosity ν and temperature T of the gas phase [59]. The source terms $R_{sootprocess}$ with $R_{sootprocess} \in \{inc, depo, sg, coag, ox\}$ represent the source terms of the NDF due to the interaction of the particles with the gas-phase species (inception, surface growth, deposition, oxidation) and collisions among themselves (coagulation). Due to their small size, soot particles follow the streamlines of the gas-phase flow, resulting in low Stoke's number flow, which justifies applying the velocity vector of the gas phase [60, 61, 62]. Molecular diffusion is neglected in this work, considering the particles' high Schmidt numbers according to the approach of Bisetti et al. [63].

It is difficult to solve the PBE directly with analytical or numerical approaches, considering its high complexity [64]. Several models have been developed to simplify the representation of the NDF and to solve approximations of the PBE in soot simulations. Figure 1.2 shows three commonly applied methods in the context of soot simulations for the calculation of the PBE: Monte Carlo methods (MC), sectional methods (SM), and method of moments (MOM). These methods utilize different approaches to approximate the NDF and, therefore, reduce the complexity of the PBE. The basic concepts of these strategies are presented in this overview, while combinations of these modeling strategies have been proposed in the past to overcome some of their limitations.

MC methods approximate the evolution of a particle ensemble by individually tracking the maturation process of particles [65, 66]. Each individual particle undergoes a series of soot maturation steps, which are selected by a stochastic algorithm. These steps follow a probability distribution based on the individual rates of the soot processes, which are calculated from the respective particle properties and the thermo-chemical state of the gas phase [65, 66]. Considering a statistically sufficient number of particles leads to an exact representation of the soot particle processes for the considered particle distribution [67] and thus results in a detailed evolution of the NDF. The requirement of tracking a large number of particles is accompanied by high computational demands, limiting this method to relatively simple configurations [48]. This approach is mainly used to generate reference solutions for evaluating and validating SM and closure assumptions in MOM models [57, 68, 67, 69, 70, 71].

SMs, or class methods, divide the NDF into discrete sections or bins, and transport equations are formulated and evaluated for each individual section [72, 73]. The NDF within each section can be approximated by a low-order polynomial [74] or assumed to be constant [57]. Depending on the number of considered soot particle properties, hence the NDF's dimensionality, and the resolution choice for the NDF discretization, this can lead to many equations accompanied by high computational costs [48]. Without prior knowledge of the property space and especially of its upper boundaries, it can be challenging to define a suitable discretization for the coordinates of the property vector that cover the complete NDF due to contrary aspects of computational efficiency and sufficient resolution [48].

Both the MC and the SM approximate and solve for the shape of the NDF. On the other hand, MOMs solve for the statistical moments of the NDF and approximate the NDF by their mean quantities [69]. Following Marchisio and Fox [57], a moment $m_{\underline{k}}$ with the moment order $k_1, ..., k_{N_\xi}$ of a NDF consisting of N_ξ internal coordinates $\underline{\xi} = \left[\xi_1, ..., \xi_{N_\xi}\right]^T$ is defined as

$$m_{\underline{k}} = m_{k_1,...,k_{N_\xi}} = \int_{\Omega_{\underline{\xi}}} n(t, \underline{x}; \underline{\xi}) \xi_1^{k_1}, ..., \xi_{N_\xi}^{k_{N_\xi}} \mathrm{d}\underline{\xi}. \tag{1.2}$$

Herein, $\Omega_{\underline{\xi}}$ delimits the definition interval of the internal coordinates [57]. The PBE describes the particle distribution's evolution and can be reformulated by approximating the NDF by its moments. This results in the following moment transport equations

$$\frac{\partial m_{\underline{k}}(\underline{x}, t)}{\partial t} + \frac{\partial \underline{u} m_{\underline{k}}(\underline{x}, t)}{\partial \underline{x}} - \frac{\partial}{\partial \underline{x}} \left(0.55 \frac{\nu}{T} \frac{\partial T}{\partial \underline{x}} m_{\underline{k}(\underline{x},t)} \right) = \dot{m}_{\underline{k}}(\underline{x}, t). \tag{1.3}$$

Like equation 1.1, equation 1.3 includes the temporal evolution, advection, thermophoresis, and source terms (l.t.r), while the diffusion term is neglected in this study. Knowing and solving for all moments of the NDF would be equivalent to calculating the PBE.

For the practical simulations of combustion-generated soot, only a small set of moments and, hence, equations are of interest to limit numerical costs. Therefore, a small set of the low-order moments of the NDF is used to approximate the statistical evolution of the soot particle distribution. Considering only a finite number of equations for the low-order moments leads to unclosed terms since the source terms of the moments additionally include moments that are not directly solved for [69]. In order to retrieve a closed set of equations, all terms must be formulated based on a finite number of low-order moments, which are then transported in the simulations. Multiple approaches have been developed to overcome this closure problem by modeling these unclosed terms.

The most prominent variants of the MOM are based on interpolation and Gaussian quadrature. The method of moments with interpolative closure (MOMIC) interpolates the higher-order moments based on the transported, lower-order moments [18].

The quadrature-based moment methods (QbMMs) use the Gaussian quadrature rule to approximate the integral within the moment definition of Eq. 1.2.

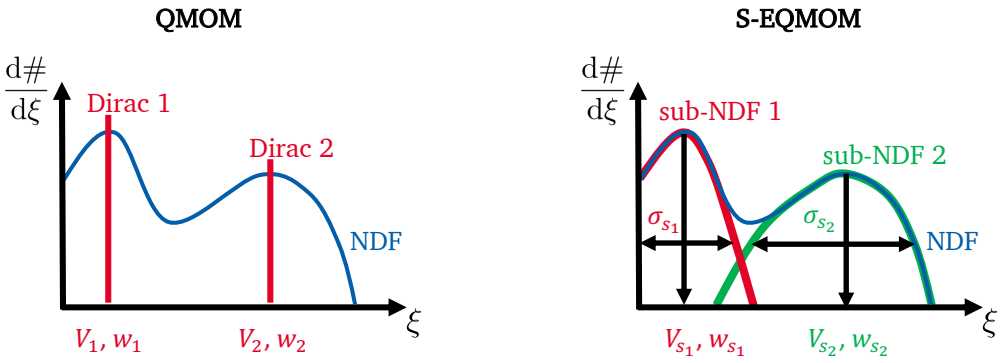

Fig. 1.3: Approximation of the NDF by QMOM (left) and S-EQMOM (right).

A sum of weighted functions estimates the integral term, and based on this simplification, the moment definition of order $\underline{k}$ can be reformulated as

$$m_{\underline{k}} = \int_{\Omega_{\underline{\xi}}} n(t, \underline{x}; \underline{\xi}) \xi_1^{k_1}, ..., \xi_{N_\xi}^{k_{N_\xi}} \mathrm{d}\underline{\xi} = \sum_{i=1}^{M} w_i \prod_{j=1}^{N_\xi} \underline{\xi}_{j,i}^{k_i}. \tag{1.4}$$

Herein, w_i are the weights, and ξ are the abscissas or nodes used for the calculation of the unclosed terms for the M-point quadrature, while the temporal and spatial dependencies are dropped for brevity.

McGraw et al. [75] suggested utilizing a set of simple Dirac delta functions for $f(\xi_i)$, leading to the qudrature method of moments (QMOM). The resulting approximation is schematically illustrated in the left part of Fig. 1.3.

Yuan et al. [76] and Chalons et al. [77] applied, on the other hand, several kernel density functions of a known shape, such as gamma or lognormal distributions, for the NDF approximation, leading to the extended quadrature method of moments (EQMOM). This approach allows for a continuous reconstruction of the NDF in contrast to standard QMOM.

For bivariate and multivariate systems, the conditional quadrature method of moments (CQMOM) has been introduced by Cheng et al. [78] and further developed by Yuan and Fox [79]. In a bivariate case, this model considers an independent first distribution and second distribution, which is conditioned on the first one. For a first, fixed distribution and each of its sets of weights and abscissas, conditioned weights and abscissas reflecting the second internal variable are searched [78].

Additional variations or combinations of the methods above have been proposed in the past years. In the direct quadrature method of moments (DQMOM), the weights and abscissas are directly tracked and transported in the simulations instead of moment transport equations [80, 44]. The hybrid method of moments (HMOM) combines benefits from DQMOM and MOMIC.

Two soot modeling approaches are applied in the simulations of this dissertation to analyze the soot formation and growth processes. These two modeling approaches are described in the following

section, together with the considered processes of particle evolution and their implementation. The reader is referred to the cited literature for additional details. The first model is a univariate, split-based extended quadrature method of moments (S-EQMOM) [81, 58], and the second one is a quadvariate CQMOM [58, 82].

1.3.1 Univariate split-based extended quadrature method of moments

The S-EQMOM is an advancement to the EQMOM and has been introduced by Salenbauch et al. [81, 58]. It solely characterizes soot particles by their volume V. It is, therefore, a univariate model with the internal coordinate $\xi_{S-EQMOM} = V$. All particles are assumed to have a spherical shape with constant density. The moment definition introduced in equation 1.2 reduces to:

$$m_k = \int_{V=V_{init}}^{\infty} V^k n(t, \underline{x}; V) \mathrm{d}V. \tag{1.5}$$

Herein, V_{init} represents the smallest possible volume of the particles after their initial inception. Similar to the EQMOM approach of Yuan et al. [76], the complete NDF is reformulated in dependence on N_{s_i} sub-NDFs as illustrated in the right part of Fig. 1.3. The sum of these sub-NDFs $n_{s_i}(V)$ is approximated by the sum of kernel density function (KDF) δ_{σ_i} of a defined shape. Each KDF is weighted by the weighting factor w_{s_i}, leading to the following approximation of the NDF for this model:

$$n(V) = \sum_{i=1}^{N_{s_i}} n_{s_i}(V) \approx \sum_{i=1}^{N_{s_i}} w_{s_i} \delta_{\sigma_{s_i}}(V, V_{s_i}). \tag{1.6}$$

The kernel density functions are characterized by the shape parameter σ_{s_i} and by the node positions V_{s_i}. s_i represents the individual sub-NDFs. The main difference between the standard EQMOM and S-EQMOM lies in the inversion process of the moments. In standard EQMOM, moments of the entire NDF are considered, and the moment inversion step is applied for the moments of the entire NDF. In contrast, moments of each sub-NDF are inverted individually in the S-EQMOM approach, but adding the requirement to transport these moments for each sub-NDF during the simulations. The sum of the strongly coupled sub-NDFs composes the complete NDF by superposition after the individual inversion steps. Inverting the moments of each sub-NDF leads to a unique solution and, therefore, to a more stable inversion process and more robustness of the soot model. The individual shape parameters are independent in the S-EQMOM. Three sub-NDFs are utilized in this dissertation, each approximated by a KDF of a gamma-function shape [81]. These kernel density functions are approximated by their three lower-order moments, resulting in nine moment transport equations for describing the soot particles. Due to its limited numerical costs based on this small number of transport equations, this soot modeling approach is also suitable for application in simulations of turbulent jet flames or aero-engine combustors, such as in [83, 84]. This efficiency

goes along with a relatively simple description of the soot evolution. Not all soot processes, as described in Sec. 1.2, are implemented due to the limitation of a univariate particle distribution considering one soot particle property.

Therefore, the source term $\dot{m}_k$ of the moments in equation 1.3 is limited to inception, surface growth through the HACA-mechanism as well as PAH-deposition, particle oxidation, and particle collisions. Due to the limitation of purely spherical particles, coagulation is assumed to only lead to the coalescence of the colliding particles. Inception is realized through a dimer reaction involving two $C_{16}H_{10}$ molecules, which are also involved in the PAH-deposition process.

The soot particulate model in this dissertation is combined with detailed chemistry of the gas phase. A bidirectional coupling between the soot model and the description of the gas phase is achieved through the species H_2, H, CO, H_2O, O_2, OH, C_2H_2, and $C_{16}H_{10}$. Additional source terms are added to the balance equations of these species, which represent the sink and source terms arising from interaction with the soot particles. The gas-phase kinetics itself is based on the Deutsches Zentrum für Luft- und Raumfahrt (DLR) Concise mechanism [85] with minor adaptations. This mechanism considers the breakdown and oxidation of ethylene fuel. Additional kinetics were added for the description of kerosene surrogate species such as toluene, n-propylbenzene, m-xylene, and 1,3,5-trimethylbenzene, whereas other fuels were removed, leading to 214 species and 1539 reactions. Pyrene is the species with the highest carbon number and simultaneously the largest PAH species in the gas phase.

1.3.2 Quadvariate conditional quadrature method of moments

The quadvariate CQMOM soot model achieves a more detailed description of the soot particles by considering multiple physical and chemical soot particle properties. The quadvariate particle distribution is based on the internal coordinate vector $\underline{\xi} = [\xi_{type}, \xi_{stat}, \xi_{\#C}, \xi_{H/C}]^T$. The internal coordinate $\xi_{type} \in A, A = \{$*large PAH, cluster, aggregate*$\}$ captures the type or level of maturity of a particle. Three stages during the evolution process of particles are, therefore, differentiated. The first step involves *large PAHs* of a liquid-like state during their transition towards soot particles. *Clusters* represent young soot particles with a spherical shape after their inception step. The last stage contains *aggregates*, which are matured soot particles of fractal-like shape. The second tracked property of the particle $\xi_{stat} \in B, B = \{$*radical, stable*$\}$ covers the reactivity of the particles and divides them into the two groups of *radical* or *stable* molecules and particles. The coordinates $\xi_{\#C} \in [0, \infty)$ and $\xi_{H/C} \in [0, 1]$ represent the number of carbon atoms in a particle and the ratio of hydrogen to carbon atoms, respectively. The internal coordinates ξ_{type} and ξ_{stat} contain discrete values, which allows to simplify the quadvariate NDF. For all six discrete combinations of the internal coordinates ξ_{type} and ξ_{stat}, one bivariate distribution containing the internal coordinates $\xi_{\#C}$ and $\xi_{H/C}$ can be formulated. The single quadvariate NDF is reformulated into a system of six bivariate NDFs, which are strongly coupled. CQMOM is utilized to solve this system.

All entities (*large PAHs*, *clusters*, and *aggregates*) are able to gain mass through the HACA-mechanism and the addition of aromatic structures, whereas oxidation and dehydrogenation lessen their total carbon number and hydrogen-to-carbon ratio. *Large PAHs* additionally deposit onto *clusters* and *aggregates*. The inception can occur through PAHs of the gas-phase mechanism, *large PAHs* tracked

by the soot model or a mix of both. Collisions of several *clusters* can lead to both coalescence or aggregation towards the entity of *aggregates*. Collisions of two *aggregates* result in aggregation, whereas mixed collisions can also lead to coalescence of *clusters* with *aggregates*.

The soot model is coupled to the gas-phase kinetics in a two-way manner similar to the approach of the S-EQMOM model described in Sec. 1.3.1. The species H, OH, H_2, H_2O, C_2H_2, HCO, CO, O_2, and aromatic compounds starting from C_6H_6 to $C_{16}H_{10}$ are directly involved in soot processes and therefore considered for coupling. The applied kinetic mechanism is composed of a base mechanism by D'Anna et al. [86] featuring ethylene decomposition/oxidation reactions and the formation of aromatic species up to pyrene. Kinetic rates of the CH_2O decomposition are updated according to literature values [87, 88, 89, 90, 91, 92] as further discussed in [93]. Reactions for the oxymethylene ethers OME_2 and OME_3 are taken from Sun et al. [94]. OME_4 kinetics are introduced with reaction pathways corresponding to the smaller OMEs. The final mechanism consists of 154 species with 758 elementary reactions.

1.4 Oxymethylene ether as sustainable future fuel

Polyoxymethylene dimethyl ethers or oxymethylene ethers are a group of alternative fuels mainly investigated due to their applicability in compression ignition engines.

Their molecular structure is illustrated in Fig. 1.4 for OME_2, OME_3, and OME_4 in comparison to n-dodecane ($C_{12}H_{26}$), representing one component for diesel or kerosene surrogates and ethylene (C_2H_4), which is widely employed for studies analyzing soot formation phenomena. In contrast to the shown alkane and alkene, OME_n does not contain any direct carbon-to-carbon bonds.

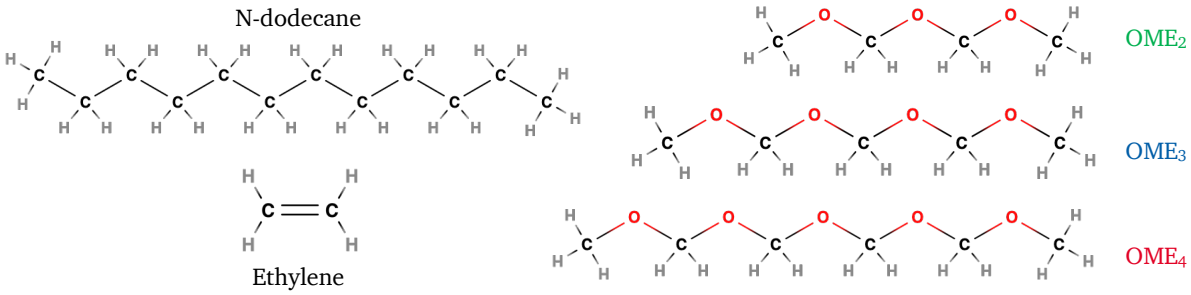

Fig. 1.4: Molecular structure of C_2H_4, $C_{12}H_{26}$, OME_2, OME_3, and OME_4.

The properties of OME_n fuels can be summarized as follows: The cetane number for OME_2, OME_3, and OME_4 increases with the chain length starting from 68, over 72 to 84. In contrast to alcohols or biodiesel fuels, OMEs combine sizable cetane numbers with high oxygenation levels of $45.2\,\%_{\mathrm{wt}}$, $47\,\%_{\mathrm{wt}}$, and $48.1\,\%_{\mathrm{wt}}$ for OME_2, OME_3, and OME_4, respectively. Melting points of temperatures below $0\,^{\circ}\mathrm{C}$ [95] and boiling points starting above $100\,^{\circ}\mathrm{C}$ [95] for OME_n for $n = 2, 3, 4$ are comparable to values of diesel fuel. Viscosity and density do not comply with the regulations for conventional diesel fuel according to the standard DIN EN 590:2022 [96], as density [95] exceeds and viscosity [97] is below the required values for diesel fuel. Since OMEs have heating values

of $20.2\,\mathrm{MJ\,kg^{-1}}$ for OME_2 and smaller values for longer OME_n variants [98], fuel consumption is approximately doubled when compared to conventional diesel fuel [99]. Even slight efficiency increases through engine optimizations [100] cannot compensate for this deficiency, leading to limitations by the injection system and the fuel pump for retrofitting current generations of diesel engines. Smaller OMEs exhibit better miscibility with diesel fuel than long-chain OME_n variants, while the overall miscibility can be altered by additives [101].

Due to these promising properties of OME fuels, multiple experimental studies have been performed on various types of compression ignition engines, such as single-cylinder research engines, commercial engines already in series production, and light-duty or heavy-duty versions. Different load cases and also legislation-relevant test cycles within transient operations were tested.

For earlier studies, Liu et al. [99] provide an overview of OME fuel investigations in compression ignition engines and their emission measurement results. Slightly higher NO_x emissions are observed for OME fuels in some of the studies, which was compensated for in other studies with optimizations of the combustion strategy and engine adaptations according to the fuel specifics. On the other hand, almost complete suppression of soot particulate matter is found for wide ranges of load cases for neat OME fuel and also significant soot emission reduction for diesel/OME blends. This benefit breaks the soot-NO_x trade-off and allows focusing on reducing NO_x through optimizations such as increased exhaust gas recirculation ratios. Additionally, CO and total hydrocarbons are reduced in most cases, indicating a change in the combustion efficiency [102].

More recent studies analyze the influence of the exhaust gas system components on the particle emissions and found that for neat OME blends, the number of particles, which are larger than $23\,\mathrm{nm}$, is one order lower than the legal requirements [103]. Later, sub-$10\,\mathrm{nm}$ particles were identified to be primarily volatile, whereas solid particle numbers between $10\,\mathrm{nm}$ and $23\,\mathrm{nm}$ were also decreased, even without a diesel particle filter [104]. Zacherl et al. [105] provide particle size distributions for diesel fuel and OME blends measured in a non-road single-cylinder engine. Here, OME leads to a shift of the particles into the sub-$23\,\mathrm{nm}$ range. On the other hand, some conditions lead to the significant formation of nanoparticles, which was assumed to originate from the combustion of engine oil. Barro et al. [106, 107] also observed higher numbers of particles in the range below $20\,\mathrm{nm}$ for OME/diesel blends despite a reduction of total particle mass.

Engine investigations, including simulations with soot modeling, are sparse. Ren et al. [108] performed such simulations and compared OME_3 against diesel and other fuels. The soot reduction was attributed to a larger proportion of premixed combustion with OME_3 fuel. In [109], the reduced soot formation is explained by the combustion of OME fuel in areas of lower equivalence ratios. Wei et al. [110] found that soot highly decreased for high-load cases, whereas no significant changes were found for low loads compared to diesel fuel.

All in all, numerous analyses have already been performed, which mostly observed a significant reduction of the soot particles. Primarily, studies focused on engine-out or tail-pipe emissions since these values are most relevant for the cost-reduction of exhaust treatment systems and fulfilling legal requirements. Because the application of neat OME or OME-blends comes with changes to additional aspects, no apparent connection between reduced soot emissions and chemical fuel structure can be established based on the studies above. These changes are to the exhaust temperatures, the center of combustion, mixture formation, possibly different engine strategies,

and further variations of the combustion conditions. Analyzing the universally valid fundamental processes has not been prioritized so far, leading to limited deeper insights, which comprehensively explain the reduced soot formation for OME-doped flames. Unlike these studies, this current work emphasizes the fundamental soot formation processes for OME_n combustion in particular.

2 Research objectives

Research studies involving laboratory-scale or even full-scale engines similar to production versions are of high practical significance. They are essential for evaluating complete combustion systems for, e.g., exhaust gas emission legislation of combustion engines. On the other hand, the presence of multiple simultaneous phenomena such as transient flow, turbulence, chemical reactions, and their interactions in such complex systems prevents a detailed analysis of fundamental soot formation processes and their chain of events. Here, only the result of many superposed mechanisms can be observed. In studies observing complete engine systems, these simultaneous processes may provoke similar or competing effects, complicating the cause-and-effect chain analyses of the underlying chemistry and physics. As a consequence, the reduction of soot particle emissions with OME addition can not solely be attributed to chemical fuel effects for investigations of full engine scale. OME addition also changes the injection and evaporation processes of the fuel, mixture formation, possible development of a wall film, and all subsequent processes in a combustion engine. Thus, the quantitative contribution of the chemical fuel effect can not precisely be quantified in engine investigations and may be exceeded by other indirect effects.

2.1 Definition of the research objectives

This work pursues a different approach following the example of the International Sooting Flame workshop [111]. In the soot research community, soot particle formation is frequently investigated based on canonical flame configurations that feature a reduced complexity but are well characterized. Here, the studies focus on one specific effect, and investigations are performed on a suitable flame configuration. This way, the effect of interest is isolated from other phenomena to the greatest possible extent, enabling a detailed cause-and-effect chain analysis. More profound knowledge of the underlying basic principles, e.g., the initial steps leading to soot particle formation, can be obtained this way. The findings observed based on the underlying fundamental chemical and physical processes exhibit general universality, and the conclusions can be transferred from these more straightforward canonical flame configurations to other combustion systems, such as real passenger engines or aero-engines with multiple combined aspects and thus higher complexity.

This dissertation and the underlying publications investigate the main parameters controlling the soot emissions in flames. These soot formation processes are highly dependent on the chemical structure of the burnt fuel and the gas-phase composition. The latter is controlled by the mixing between fuel and oxidizer, limiting the presence of fuel-rich zones in proximity to the flame for cases of non-premixed combustion. This mixing process can be quantified by the strain rate of

the flow field. It is highly relevant, especially in turbulent flames that are present in most of the practical combustion chambers. In a counterflow diffusion flame, this quantity determines the mixing of the two opposing fuel/oxidizer streams and affects flame stretch and the residence time of soot particles in areas prone to soot formation. The fuel dilution controls the excess fuel and, consequently, the concentration of soot precursors in the fuel/oxidizer mixture. Exhaust gas recirculation is one practical application causing fuel dilution in combustion devices. Exhaust gas recirculation dilutes the fuel/oxidizer mixtures with mainly nitrogen and combustion products, both acting approximately as inert gases.

The fuel-specific influence on the soot formation is studied based on the alternative fuel OME. OME fuels exhibit a molecular structure without direct carbon-to-carbon bonds. In contrast, fossil fuels with aliphatic or aromatic structures feature single, double, or triple carbon-to-carbon bonds. This molecular structure determines the initial dissociation reactions and decomposition pathways of the fuel. The subsequent influence on the species pool, the formation of aromatic structures, hence soot-relevant species, and finally, on soot formation itself is determined.

OME_n molecules of different chain lengths decompose into similar molecule fragments but in varying numbers. This dissertation examines the consequences of soot precursor species formation for different OMEs. Effects of three OME_n variants and their differences or similarities are determined. The goal is to evaluate whether their soot reduction characteristics are comparable.

As OME fuel is currently only available in limited quantities, and due to its high production costs, a fuel blend of OME together with fossil fuel is the most viable option for its usage.

Different blending ratios of OME in combination with conventional fuels and the resulting soot emissions are additional practical aspects of interest in order to optimize this fuel type's usage. Hence, the effects of different amounts of OME fuel on the soot precursors and soot formation are evaluated.

Mixing between the fuel and oxidizer, fuel dilution, and fuel-specific effects are investigated independently in this dissertation to isolate their effects. With that, the overarching goal is subdivided into six parts, each focusing on one specific scientific objective (O). All of these scientific objectives aim to increase the mechanistic understanding of the physical and chemical principles of the soot formation processes and are defined as follows:

- **(O0): Validation of the soot modeling approach**
  The requirement for subsequent studies is a validation of the applied modeling approaches of the gas-phase kinetics combined with the soot models against experimental data. These modeling approaches should capture fundamental trends and sensitivities observed in experimental data.
- **(O1): Influence of the strain and fuel dilution on soot formation**
  The processes controlling the mixing of fuel and oxidizer are investigated separately from the fuel-specific effects. The well-understood fuel ethylene is diluted with nitrogen. Strained flow conditions are realized through a counterflow diffusion flame configuration. The influence of different strain rates and fuel dilutions is evaluated based on integral soot quantities, soot production rates of the individual soot processes, and the PSD.

- **(O2): Influence of OME_3 fuel chemistry on gas-phase species and soot precursor pool**
  The fuel-specific influence of OME_3 fuel on soot-relevant species is investigated. This study includes the initial decomposition pathways of the OME_3 molecule, resulting species fragments, and subsequent formation of PAH species as well as acetylene. The sensitivity of selected initial decomposition reactions on the formation of PAH species is additionally quantified to evaluate the importance of these reactions for the predictivity of their soot reduction potential.
- **(O3): Influence of OME_3 on soot formation and growth**
  The fuel-specific influence of OME_3 fuel on the soot formation process is evaluated based on integral quantities of the nanoparticles, soot particles, and the PSD.
- **(O4): Influence of OME_3 blending ratios on soot formation and growth**
  Blends of increasing amounts of OME_3 combined with ethylene and their effect on the soot formation and growth processes are analyzed. Changes in different blending ratios and their quantitative influence on the species pool, on young, and on matured soot particles are investigated.
- **(O5): Influence of OMEn variants - from fuel chemistry to soot evolution**
  OMEs with an engine-relevant molecule length of OME_n with $n = 2, 3, 4$ are compared for their influence on soot formation. It is tested whether this results in significant differences or similarities regarding the soot formation processes. This includes the fuel decomposition pathways, resulting species pool, species relevant for soot formation, the soot formation itself, and its further evolution. It is validated if the findings of O2 and O3 regarding the influence of OME_3 can also be generalized for smaller or larger OME_n variants.

The combination of these six scientific objectives enables a deeper understanding of the effects of OME_n fuel, fuel dilution, and strain rate on the relevant phenomena during the soot formation processes. A brief overview of the main outcomes and accomplishments is presented in Chap. 3, while details about the individual investigations are part of the corresponding publications.

2.2 Contribution to the research objectives by each publication

Below is a brief description of the individual flame configurations and applied conditions used in the investigations of the underlying publications. The purpose is to provide a brief overview and understanding of the boundary conditions necessary to relate critical assumptions of the flame sets to the defined objectives. Further details are described in the individual publications. Each objective is covered in one or multiple publications (P) as reported in Tab. 2.1.

Laminar flames of premixed and non-premixed conditions are chosen to investigate the influence of the described parameters on the gas-phase chemistry and soot formation processes. The mixture composition and the flame type are adjusted to match the intended research objective.

A non-premixed counterflow diffusion flame is selected for studying objective O1, which features strained flow in a simple flame configuration of two opposing streams with a nozzle distance of $L = 12.5\,\mathrm{mm}$. Artificial air with a molar composition of $21\,\%$ oxygen combined with $79\,\%$

Tab. 2.1: Scientific objectives (O) of this dissertation, contribution by each publication (P), and applied soot modeling strategy.

Scientific objectives	Publications	Soot model
O0: Validation of the soot modeling approaches	P2, P3, P4, P5	both
O1: Influence of the strain and fuel dilution on soot formation	P4	S-EQMOM
O2: Influence of OME_3 fuel chemistry on species and soot precursors	P1, P2, P3	CQMOM
O3: Influence of OME_3 on soot formation and growth	P1, P2, P3, P5	CQMOM
O4: Influence of OME_3 blending ratios on soot formation and growth	P1	CQMOM
O5: Influence of OME_n variants - from fuel chemistry to soot evolution	P2, P3	CQMOM

nitrogen at a temperature of $300\,\mathrm{K}$ is supplied as the oxidizer stream. The fuel stream of an identical temperature can be independently adjusted from the oxidizer to consider fuel dilution. The ethylene mass fraction Y_f in the fuel/nitrogen mixture is listed in Tab. 2.2 additionally to the applied strain rate K, which is based on the oxidizer stream.

The numerical modeling for O1 is performed on the basis of a one-dimensional domain representing the center line between the two nozzles. The univariate soot modeling approach, as described in Sec. 1.3.1 is chosen. The studies of the influence of both, strain and fuel dilution, effects are performed with the well-understood fuel ethylene.

Objectives 02-05, on the other hand, are investigated in premixed flames of a flat-flame burner. Most parts of the fuel breakdown, precursor formation, initial soot particle inception, and particle growth are spatially separated in this configuration, making it possible to distinguish the influences of the applied fuel on each individual step of the complete sequence of events.

Inlet streams for the objectives O2, O3, and O5 consist of C_2H_4/OME_n/N_2/O_2-mixtures according to the mole fraction values stated in Tab. 2.3. Neat C_2H_4/N_2/O_2-flames without any OME_n are considered as reference flames, whereas OME_n replaces $20\,\%$ of the carbon atoms ($20\,\%_{\mathrm{carbon}}$) in the C_2H_4/OME_n/N_2/O_2-flames. The four different equivalence ratios of $\phi = 2.01$, $\phi = 2.16$, $\phi = 2.31$, and $\phi = 2.46$ are investigated. Hence, all flames with identical equivalence ratios also feature identical carbon streams, allowing for a fair comparison of the soot evolution. Nitrogen

Tab. 2.2: Investigated flame conditions in O1. Ethylene mass fraction Y_f of the ethylene/nitrogen fuel stream and strain rate K.

Strain rate K in s^{-1}	C_2H_4 mass fraction Y_f in fuel mixture
50	0.30
60	0.30
70	0.30
60	0.20
60	0.25
60	0.35

and oxygen streams are adapted accordingly to ensure identical inlet velocities of $0.1\,\mathrm{m\,s^{-1}}$ (at standard conditions) and simultaneously fixed equivalence ratios.

Investigations of O4 follow the same methodology of constant carbon streams and fixed inlet velocities by adapting N_2 and O_2 streams but instead are limited to the two equivalence ratios of $\phi = 2.16$ and $\phi = 2.46$. Additionally, different blending ratios are investigated in O4, resulting in OME_3 not replacing $20\,\%_{\mathrm{carbon}}$ of the carbon streams but varying amounts between $0\,\%_{\mathrm{carbon}}$ and $100\,\%_{\mathrm{carbon}}$ in increments of $5\,\%_{\mathrm{carbon}}$.

Tab. 2.3: Mixture compositions for O2, O3, and O5 of the C_2H_4-flame and OME_n-doped flames in mole fractions. OME_n indicates OME_2, OME_3, and OME_4 in their corresponding flames, respectively.

ϕ		C_2H_4-flame	OME_2-doped flame	OME_3-doped flame	OME_4-doped flame
2.01	OME_n	-	0.0123	0.0099	0.0082
	C_2H_4	0.1234	0.0987	0.0987	0.0987
	N_2	0.6925	0.7110	0.7147	0.7172
	O_2	0.1841	0.1780	0.1767	0.1759
2.16	OME_n	-	0.0131	0.0105	0.0088
	C_2H_4	0.1313	0.1051	0.1051	0.1051
	N_2	0.6862	0.7055	0.7093	0.7119
	O_2	0.1824	0.1763	0.1751	0.1743
2.31	OME_n	-	0.0139	0.0111	0.0093
	C_2H_4	0.1392	0.1114	0.1114	0.1114
	N_2	0.6800	0.7000	0.7040	0.7066
	O_2	0.1808	0.1747	0.1735	0.1727
2.46	OME_n	-	0.0147	0.0118	0.0098
	C_2H_4	0.1469	0.1175	0.1175	0.1175
	N_2	0.6739	0.6946	0.6987	0.7015
	O_2	0.1792	0.1732	0.1720	0.1712

For O2-O5, soot particles are modeled with the quadvariate CQMOM approach, which is described in Sec. 1.3.2. This detailed soot model covers the chemical features of soot particles and their differences due to the OME fuels and their influences on the species pool and soot precursors. Ethylene fuel is used as a reference fuel modeling a generic fossil combustible with a high sooting propensity. OME-blended flames and pure ethylene flames are compared on the basis of constant carbon streams and identical equivalence ratios. Several sooting intensities due to multiple investigated equivalence ratios are covered. Experimentally obtained temperature profiles for neat ethylene flames are adopted for the soot simulations. These temperature profiles, which depend on the equivalence ratio, are prescribed in the numerics. Hence, chemical effects of the fuel on precursor formation are isolated from thermal effects.

Precisely defined boundary conditions in the applied laminar flames and consistency between simulation and experiment simplify the validation of numerical results against the measurement

data. Experimental measurements conducted at Karlsruhe Institute of Technology (Karlsruhe, Germany) comprise laser-induced incandescence (LII) measurements to quantify soot volume fraction in the counterflow diffusion flames. Intrusive particle sampling feeds particles through a probing tube to a scanning mobility particle sizer to obtain information about the PSD. These data sets establish the basis for validating the S-EQMOM model applied in O1. Measurements of the premixed OME_n/C_2H_4-flames performed at the Università degli Studi di Napoli Federico II and Consiglio Nazionale delle Ricerche STEMS (both Neaples, Italy) feature laser-induced fluorescence (LIF) and (LII) data to evaluate the volume fraction of nanoparticles and soot particles, respectively. Additional data include PSD measured by a nano-differential mobility analyzer and physiochemical particle characterization after intrusive particle sampling onto a glass plate. PSD, LIF, and LII data of the latter flames are used for comparison of the CQMOM modeling results for validation. In P2-P5, further details of the comparisons for the soot modeling results against the corresponding experiments are described, which are part of this dissertation.

Additionally, in P4, the S-EQMOM soot modeling approach is benchmarked based on a set of established literature flames covering numerical and experimental data [112]. Validation of the findings is additionally obtained by comparison against another soot modeling approach, the discrete sectional method (DSM) [113], which implements a chemical and physical description of the soot formation processes similar to the S-EQMOM. Similar trends can be observed for the applied soot models and experimental or numerical reference results for all cases. Therefore, both soot modeling approaches, the univariate S-EQMOM and quadvariate CQMOM, are able to model the principal soot formation processes. Validation is hence obtained, and the usage of these models within the studies of this dissertation is justified, accomplishing objective O0. Since the validation against measurements is a part of most of the publications, there is no separate section in this dissertation, and it is not explicitly mentioned throughout the remainder of this manuscript, whereas experimental reference data is shown in some of the figures.

3 Results

This chapter summarizes the underlying publications and describes their main outcomes concerning the topic of this dissertation. Their contribution in investigating the individual aspects of the complete soot formation process is explained. This is done following the scientific research objectives as defined in Chap. 2. In their entirety, these research objectives lead to the overarching goal of investigating the main controlling parameters of the soot formation processes, emphasizing the soot reduction effects of OME$_n$ fuels.

3.1 Influence of the strain and fuel dilution on soot formation

The influence of strain and fuel dilution on soot formation and evolution is analyzed based on a set of counterflow diffusion flames fueled with ethylene according to the mixture and flow conditions stated in Tab. 2.2. In the left part of Fig. 3.1, the soot volume fraction profile over the height above the burner (HAB) is shown for a fixed fuel dilution with an ethylene mass fraction of $Y_F = 0.30$. By varying strain rates between $K = 50\,\mathrm{s}^{-1}$, $K = 60\,\mathrm{s}^{-1}$, and $K = 70\,\mathrm{s}^{-1}$ their influence is discussed. The S-EQMOM model reproduces the experimentally observed reduction of the soot volume fraction with increasing strain rates. In contrast, the numerical sensitivity to strain variations is quantitatively smaller compared to the measured soot volume fraction reduction. The right part of Fig. 3.1 displays the soot volume fraction profiles for varying ethylene mass fractions between $Y_F = 0.20$, $Y_F = 0.25$, $Y_F = 0.30$, and $Y_F = 0.35$ at a constant strain rate of $K = 60\,\mathrm{s}^{-1}$. Again, the soot model covers the main trend of increasing soot volume fraction for higher fuel mass fraction, while the numerical results are less sensitive to changing fuel dilution compared to the experimental data. For both data sets, the S-EQMOM slightly overpredicts the overall amount of soot, while the soot volume fraction of the richer flames is within the same order of magnitude.

Figure 3.2 shows the modeled contribution to soot particulate matter itemized by the individual rates of the soot sub-processes inception, PAH-deposition also referred to as PAH-condensation, and surface growth by the HACA mechanism for the same sets of flames as above. Increasing strain rates slightly reduce all three soot sub-processes, as shown in the left part of Fig. 3.2. At the same time, this change is negligible compared to the soot volume fraction reduction, as seen in Fig. 3.1. Consequently, a reduction of soot for increased strain rates can not entirely be attributed to the quantitative changes of the underlying soot sub-processes. Similar acetylene and pyrene volume fractions in the gas phase for different strain rates support this finding, as shown in P4. However, strain rates mainly affect the underlying flow field. Increased strain rates lead to higher velocities in the gas phase and, subsequently, to smaller residence times of soot particles in areas prone to

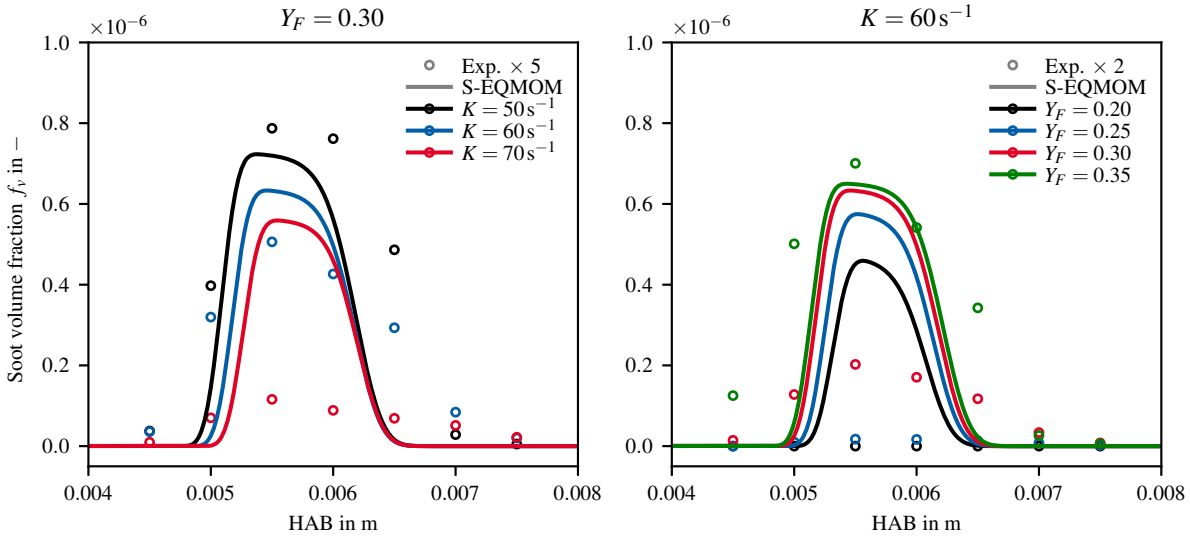

Fig. 3.1: Soot volume fraction profiles for varying strain rates at a fixed fuel mass fraction of $Y_F = 0.3$ (left), and for varying fuel mass fraction at a fixed strain rate of $K = 60\,\mathrm{s}^{-1}$ (right) over HAB. Modeled results are shown as lines and experimental data as dots.

soot formation. The contribution to soot formation and soot growth by the soot sub-processes for different ethylene fuel mass fractions is shown on the right part of Fig. 3.2. Here, higher fuel mass fractions notably increase all three soot processes. As a consequence, higher amounts of soot are mainly the result of increased rates of the underlying soot sub-processes. In addition to a quantitative increase of the peak values, the area of surface growth by the HACA mechanism is widened for higher fuel mass fractions. Since surface growth is the dominant contributor to soot mass [98, 114], this also affects the overall amount of soot.

The influence of strain and fuel dilution on the modeled and measured particle size distribution is displayed in Fig. 3.3. It has to be noted that the measurement results are limited by the measurement range of the SMPS system to mobility diameters approximately between $d_m = 2\,\mathrm{nm}$ and $d_m = 79\,\mathrm{nm}$. On the left side, flames at a fixed fuel mass fraction of $Y_F = 0.30$ are presented with varying strain rates. On the right side, flames at a fixed strain rate of $K = 60\,\mathrm{s}^{-1}$ are plotted with varying ethylene fuel mass fractions. Measurement results suggest a shift of the second mode towards larger particle diameters for decreasing strain rates or for increasing fuel mass fractions. Identical trends are found in the results of the S-EQMOM model, though modeled differences are less obvious, corresponding to lower sensitivities for these parameters. The measured peak particle density is less affected by the strain rate variation visible by the minor decrease as the strain rate decreases and a slight increase for higher fuel mass fractions. S-EQMOM reproduces this trend for the strain rate variation, whereas the modeled peak particle density is more or less unchanged for a fuel mass fraction variation.

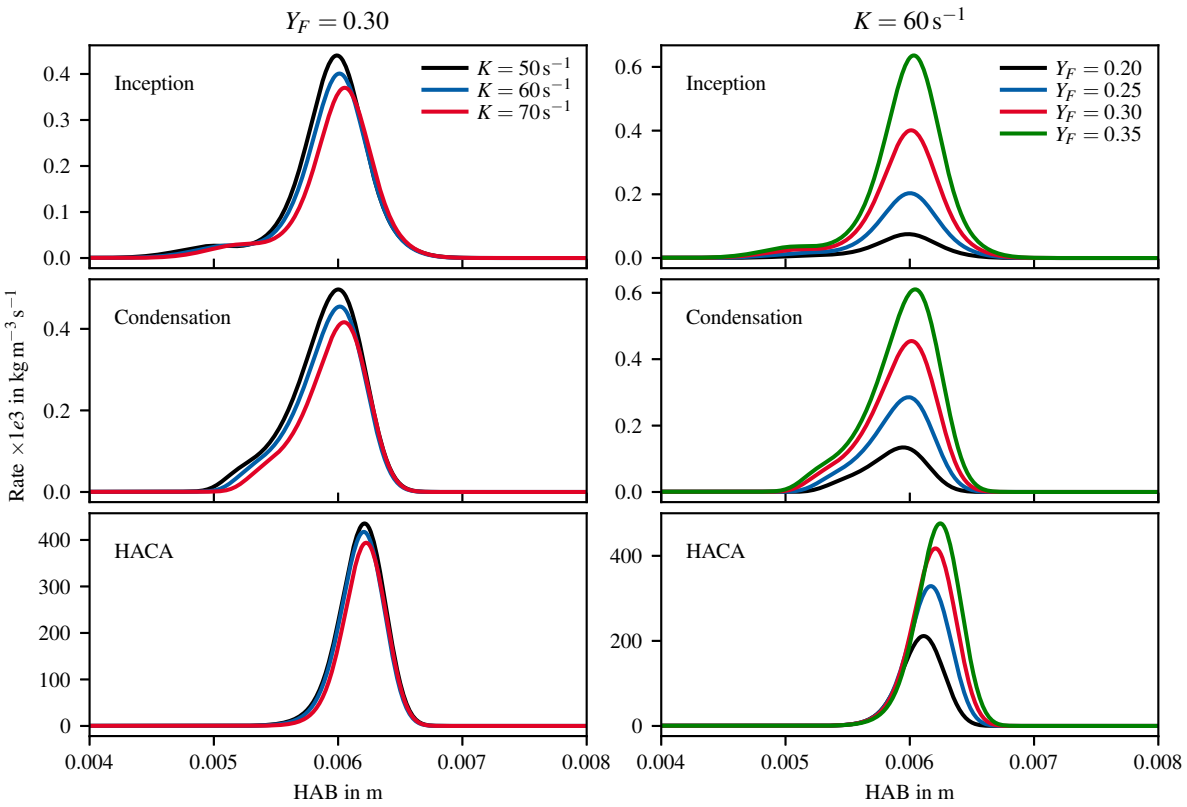

Fig. 3.2: Modeled profiles of the soot sub-processes inception (top), Polycyclic aromatic hydrocarbon (PAH) condensation (center), and surface growth by the HACA mechanism (bottom) over HAB. Varying strain rates at a fixed fuel mass fraction of $Y_F = 0.3$ (left), and varying fuel mass fractions at a fixed strain rate of $K = 60\,\mathrm{s}^{-1}$ (right).

In contrast to the other flames, the experimental data of the flame with a fuel mass fraction of $Y_F = 0.20$ solely contains particles of smaller diameters forming the first mode of the PSD while the second mode starts to form. A pronounced first mode is also visible in the S-EQMOM results, a unique feature among the modeled flames. In the S-EQMOM results, the second mode is established to a larger extent. At the same time, its peak position and overall shape of the PSD still deviate from the other flames, suggesting a transition from an unimodal to a bimodal shape for similar fuel dilutions. For both variations, the S-EQMOM reproduces the principal shape characteristics and trends, whereas the overall particle density and particle diameters are overpredicted, consistent with the integral values of the soot volume fraction. A more detailed discussion of the results, also concerning a comparison of the experimental and modeling results for different HABs, is covered in P4 to a larger extent.

Overall, the applied univariate S-EQMOM soot formation model is able to replicate the critical trends of the soot volume fraction profiles and characteristic features of the particle size distribution with respect to changes in the strain rate and fuel dilution in the investigated set of flames. The

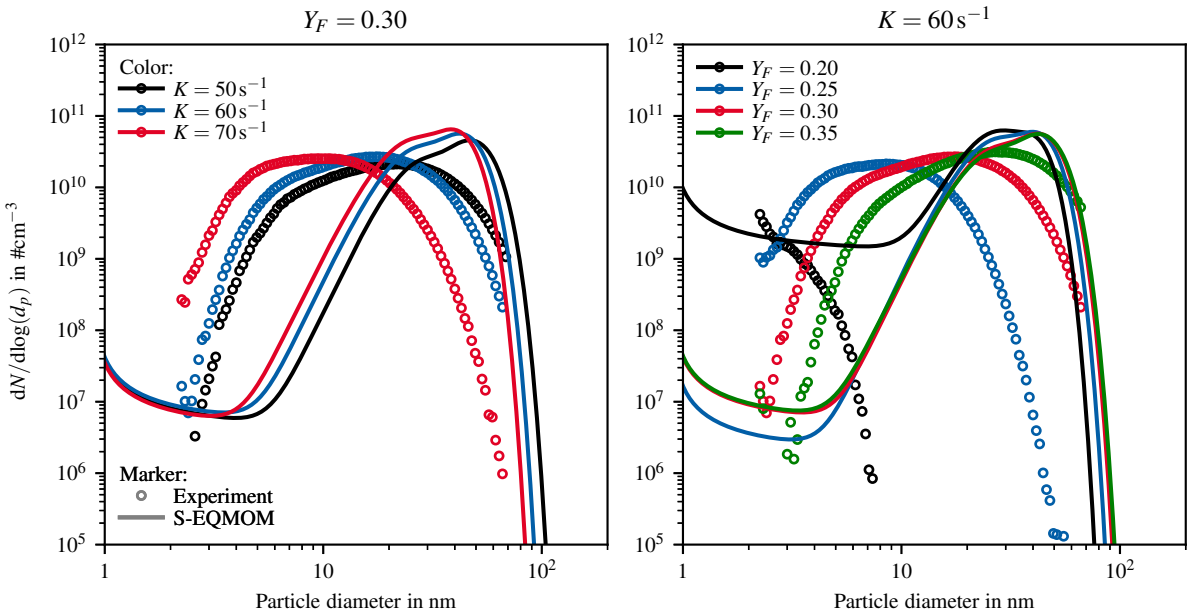

Fig. 3.3: Modeled (lines) and measured (dots) particle size distribution at the peak position of their corresponding soot volume fraction profiles. Varying strain rates at a fixed fuel mass fraction of $Y_F = 0.3$ (left), and varying fuel mass fractions at a fixed strain rate of $K = 60\,\mathrm{s}^{-1}$ (right).

decreasing amounts of soot with increasing strain rates are found to be mainly caused by changes in the flow field and, subsequently, of the residence times of the particles rather than changes in the soot formation sub-processes themselves. On the other hand, lowering the fuel dilution significantly intensifies all underlying soot sub-processes and broadens the main contributor to soot particulate matter, the HACA mechanism. An increase of the soot volume fractions occurs as a result. Numerical data sets of a DSM modeling approach result in similar conclusions. The S-EQMOM modeling results and experimental data exhibit consistent trends, resulting in a high qualitative agreement. No exact quantitative agreement is observed while modeling results of the integral values are still within the same order of magnitude as their corresponding measurement data for the richer flames. The applied modeling approach quantitatively overpredicts the soot formation processes, and a lower sensitivity of the investigated parameters onto the soot formation processes is obtained. Both the soot volume fraction and sensitivity to strain are discussed in Wang et al. [115] for different kinetic mechanisms of the gas-phase chemistry. Large variations in the computed soot volume fraction and the sensitivity to strain were found with the applied base mechanism of this dissertation, showing good quantitative agreement but lacking in their sensitivity to strain [115]. Within this context, the current results are considered to reasonably agree with the measurements.

Several studies include variations of strain rate [112, 116, 117] or fuel dilution [116, 117] and discuss the corresponding effects on particle formation. The overall findings of the current work agree well with the previous studies. In Wang et al. [112], strain rate variations and their influence

on soot formation are investigated, and the importance of the residence time changes is highlighted for the contribution of the HACA process. Kruse et al. [116] study a set of flames, including fuel dilution and strain rate variations and their effects on soot formation, but without further analyzing the underlying processes. Hagen et al. [117] feature a similarly comprehensive set of flames and also analyze the fuel dilution effects but lacked a detailed analysis of the strain effects. To the best of my knowledge, this combined study and the underlying publication P4 represent the first comprehensive examination based on a systematic analysis of the soot sub-processes as well as the modeled soot particle size distributions for both parameters, strain and fuel dilution. The other studies focus on one of the two parameters and gain only partial insights into the underlying principal processes. Moreover, the contrasting juxtaposition of both phenomena within this study clearly emphasizes the similarities and differences between both parameters on the soot formation processes. The combined consideration of both parameters highlights the relevant aspects and decisive underlying chemical and physical phenomena.

3.2 Influence of OME_3 fuel chemistry on gas-phase species and soot precursor pool

The investigation to achieve O2 is performed with laminar premixed flames at four different equivalence ratios corresponding from lightly to highly sooting flames. $20\,\%$ OME_3 is added to ethylene-fuel flames according to the mixture compositions in Tab. 2.3. Neat ethylene flames serve as the reference. The influence of the OME_3 fuel chemistry on the gas-phase species and soot precursor pool is analyzed by following the sequence of events leading to the soot formation described in Sec. 1.2. Firstly, the initial decomposition pathways of the OME_3 molecule are analyzed to identify the main fuel fragments under rich conditions relevant to the formation of soot. Secondly, the resulting species pool is contrasted against pure ethylene flames. The species are evaluated based on their relevance during the soot precursor and soot formation processes before the aromatic species are quantitatively compared against ethylene decomposition products.

Figure 3.4 displays the decomposition pathways of an $OME_3/C_2H_4/N_2/O_2$ flame with an equivalence ratio of $\phi = 2.46$ at a position close to the flame front with a temperature of $T = 1500\,\mathrm{K}$. The shown numbers next to the arrows indicate the carbon fluxes starting from the source species toward the decomposition products. Therefore, they quantify the contribution to soot-relevant or to species that are oxidized in subsequent reaction steps. Formaldehyde (CH_2O) is the main decomposition product, whereas hydrogen radicals (H), methyl radicals (CH_3), and aldehydic compounds are formed in smaller amounts through the dissociation of the fuel molecule. While the aldehydic compounds mainly lead to subsequent oxidation of the carbon matter, CH_3 additionally can form unsaturated hydrocarbons and subsequently aromatic structures after multiple following reactions. However, this decomposition pathway is fundamentally different from the one of an ethylene flame, as reported in Wang et al. [115]. Starting from C_2H_4, two subsequent H-abstraction reactions form C_2H_2, which rapidly leads to the formation of aromatic structures. Due to the molecular structure of the OME_3 fuel, no direct dissociation pathways towards C_2H_2 or alkenes are present, hence slowing down the formation of soot precursors. In contrast to earlier studies

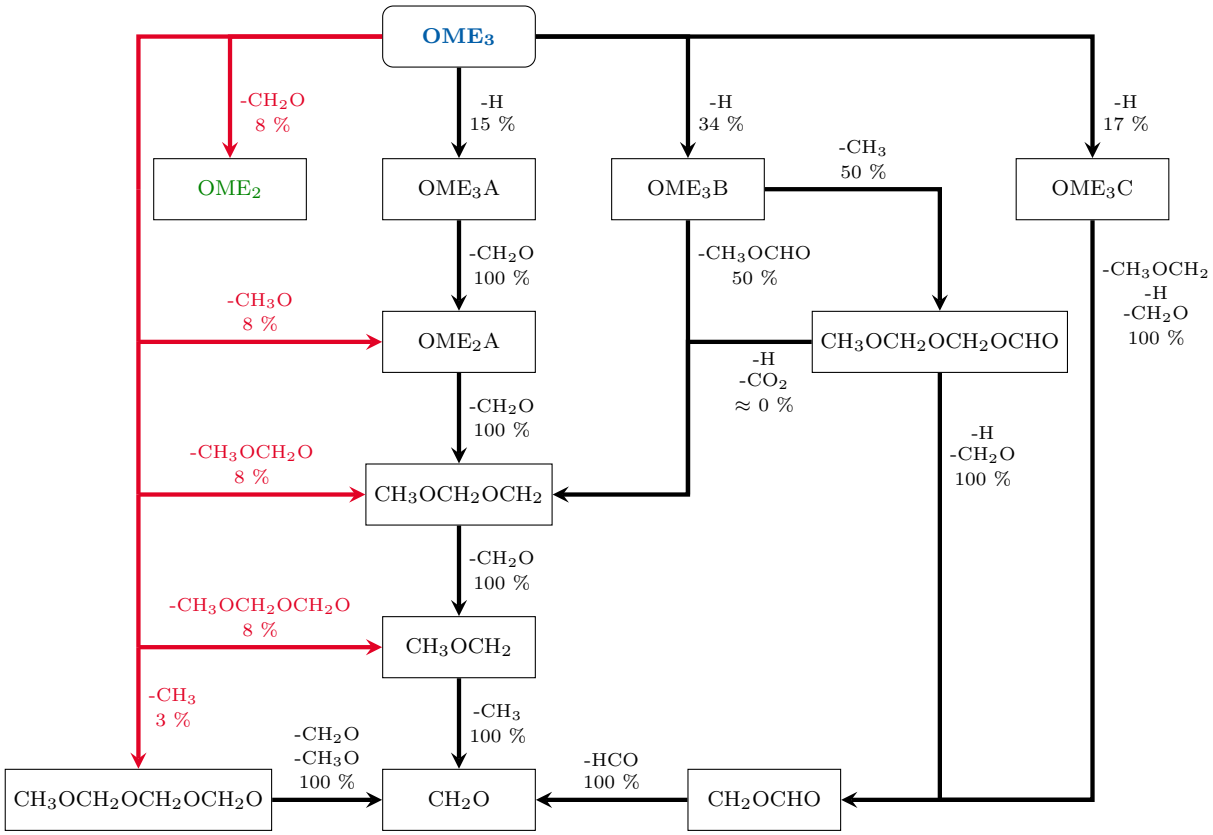

Fig. 3.4: Decomposition pathways of an $OME_3/C_2H_4/N_2/O_2$ flame of an equivalence ratio of $\phi = 2.46$ for a temperature of $T = 1500\,\mathrm{K}$. Unimolecular decomposition reactions in red, reactions initiated by H-abstraction reactions in black, numbers represent the carbon flux percentages with respect to the source species.

with emphasis on leaner combustion conditions [94], unimolecular pathways play an essential role in OME_3 decomposition in soot-relevant conditions.

In Fig. 3.5, selected mole fraction profiles of the resulting species pool are shown for the $OME_3/C_2H_4/N_2/O_2$ flames at lower heights above the burner, corresponding to the initial fuel decomposition and further species formation. The species profiles confirm that OME_3 decomposition pathways for the OME_3-doped flames lead to significant differences in the species pool compared to neat ethylene flames. For the OME_3-blended flame, higher peaks of the CH_2O and CH_4 mole fraction profiles are visible since CH_2O is directly dissociated from the OME_3 molecule, and CH_4 gets formed subsequently to CH_3 cleavage. Analyzing the profile of CH_4 instead of CH_3 radicals is advantageous since CH_4 is more stable and, therefore, less affected by subsequent reactions. CH_2O leads to a higher level of fuel oxidation, proven by the slightly increased CO_2 profiles in the OME_3-doped flame. The carbon following this reaction pathway does not participate in the soot precursor formation. As a consequence, C_2H_2 and C_6H_6 profiles are reduced in the OME_3-doped flames. Substantial amounts of C_2H_2 and C_6H_6 still remain present in the presented flames since only $20\,\%$ of the fuel is replaced by the OME_3 regarding its carbon content. Adding OME_3 subtracts

carbon from forming soot-relevant species, leading toward a more complete oxidation process of the OME_3 fuel.

Overall, the influence of OME_3 on the fuel decomposition pathways, species pool, and the formation of soot-relevant species can be summarized as follows based on the conducted investigations. Further information is detailed in P1, P2, P3, and P5: The decomposition process of the OME_3 molecule deviates fundamentally from ethylene, the reference fuel in this dissertation representing a sooting fossil fuel. During the breakdown of OME_3, mainly CH_2O, other aldehydic species, and CH_3 are formed. These fuel fragments lead to a species pool mainly consisting of oxygenated species with no direct formation pathway to unsaturated hydrocarbons. The composition of the species pool prevents a fast formation of C_2H_2 or other species that would lead to the formation of aromatic structures. Instead, OME_3 fuel fragments favor the complete oxidation of the carbonaceous fuel. The formation of soot-relevant species is reduced in quantity and additionally slowed down.

With that, the fuel-specific influences of OME_3 on the initial steps toward soot precursor formation are explained. The chemical mechanisms subtracting carbon from the formation of soot-relevant species and aromatic growth pathways are analyzed starting from its origin, the molecular fuel structure.

No direct validation against measured species data is performed for these findings since experimental species quantification does not exist for these conditions. However, experimental studies with stoichiometric to slightly rich conditions observe similar trends with oxygenated species and aldehydes in the species pool of OME_3-fueled flames [118, 118, 94, 119].

In general, the development of kinetic gas-phase mechanisms for OME_3 decomposition, oxidation, and also for OME_n fuels started in more recent years [120]. Relatively limited knowledge about exact reaction rates and the importance of different reaction pathways has been obtained up to this point. The kinetic focus has been on conditions close to stoichiometry or slightly rich conditions. Rich conditions are less known, primarily due to a lack of comprehensive experimental data for sooting conditions regarding species concentration and basic combustion properties, such as flame speed and ignition delay times [120]. Therefore, quantitative optimization of reaction kinetics can be expected in the future as the number of experimental examinations increases and kinetic uncertainties are reduced.

As part of this study, the preferential class of decomposition pathways has been observed for the investigated, rich conditions. Unimolecular pathways are relevant for the topic of soot formation in OME_3-flames. Additional sensitivity studies on the initial decomposition reactions of OME_3 and their influence on the formation of aromatics have been conducted, as described in P3. These studies demonstrate the potential for a quantitative improvement of the kinetic rates under these conditions.

Further numerical and experimental research is needed for rich OME flames, particularly emphasizing the soot precursors and soot formation pathways.

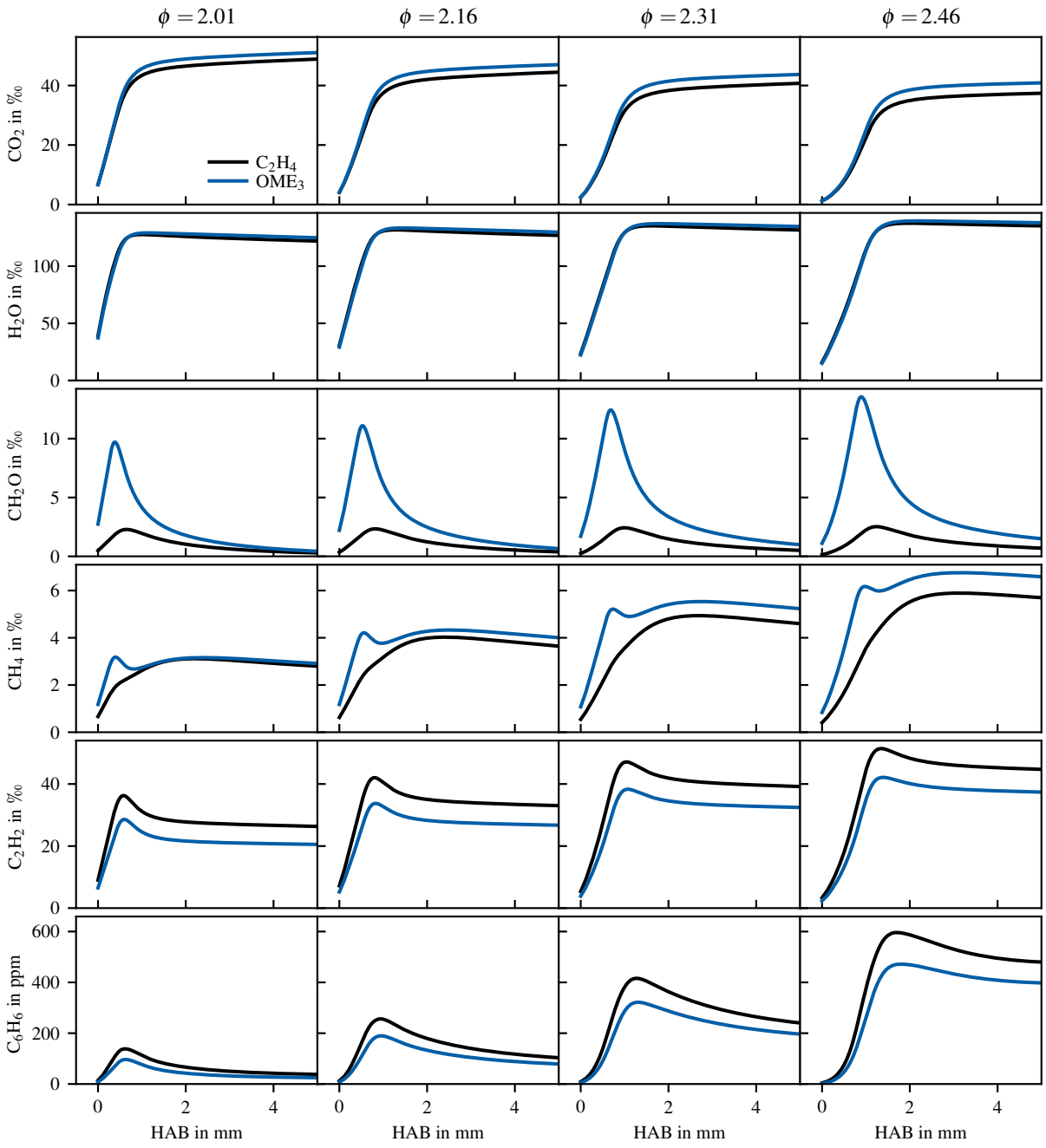

Fig. 3.5: Mole fraction profiles of the species CO_2, H_2O, CH_2O, CH_4, C_2H_2, and C_6H_6 along the height above the burner of the $OME_3/C_2H_4/N_2/O_2$ flames for the investigated equivalence ratios.

3.3 Influence of OME_3 on soot formation and growth

After the effect of OME_3 on the gas phase has been unraveled, the influence of OME_3 on the soot formation itself and further soot evolution and growth processes is analyzed. Soot simulations using the quadvariate CQMOM soot model are conducted on the laminar flames reported in Tab. 2.3. In Fig. 3.6, the comparison of experimental and corresponding numerical results for LIF and LII is shown over the height above the burner.

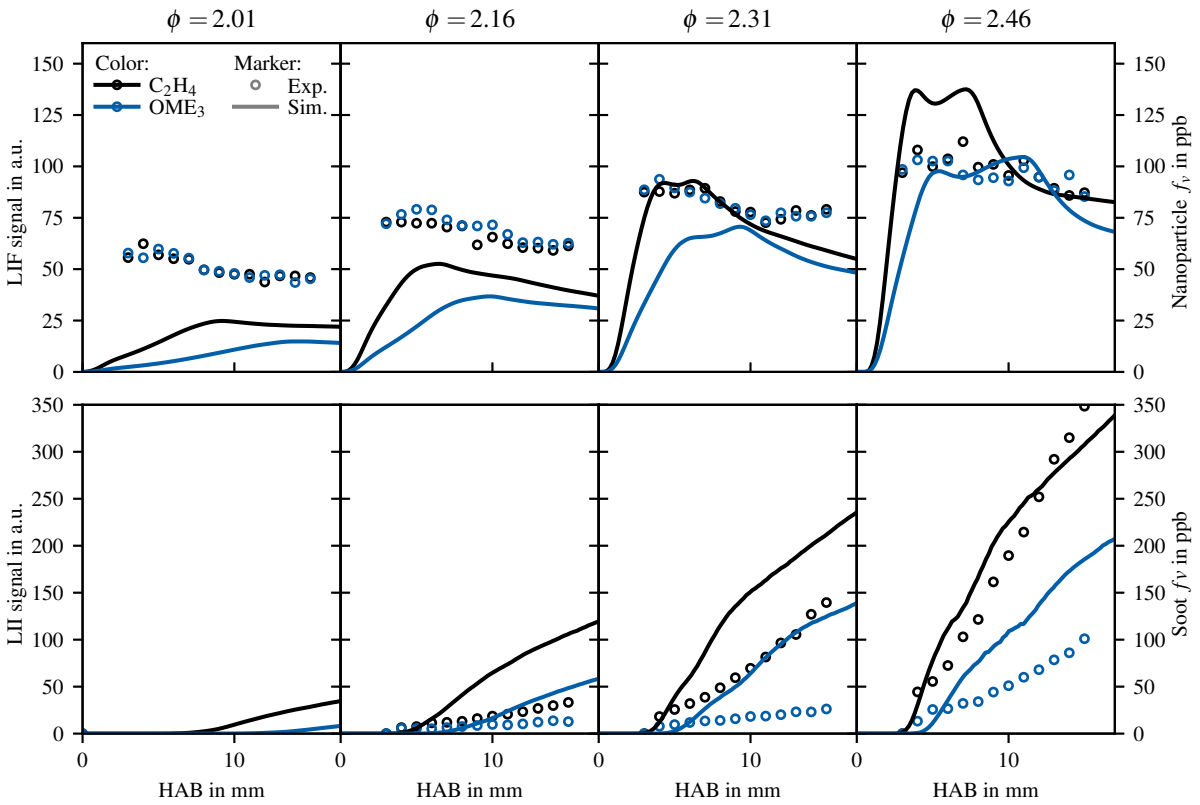

Fig. 3.6: Modeled (lines) nanoparticle volume fraction against experimental LIF signal (symbols) of neat ethylene flames (black) and OME_3-doped flames (blue) for four the four equivalence ratios of $\phi = 2.01$, 2.16, 2.31, and 2.46 (top row). The bottom row shows the modeled soot volume fraction against the experimental LII signal using identical coloring and symbols.

After its reconstruction, the modeled PSD is split into two sections based on the particle diameter d_{split}. The first section contains smaller nanoparticles up to the diameter d_{split}, and the second section has soot particles larger than the diameter d_{split}. The integrated nanoparticle volume fraction of the first section is compared against the measured LIF signal, whereas the integrated soot volume fraction is evaluated based on the corresponding LII signal. Details are explained in P5 with a justification of the choice for the parameter d_{split}. However, no direct information about the

PSD is obtainable from the CQMOM results. Following the approach of entropy maximization [121, 122], distribution functions can be reconstructed for the individual entities tracked in the CQMOM soot model. This method was demonstrated by Salenbauch et al. for the applied soot model [123, 82].

By comparing the amount of nanoparticles between the neat ethylene and OME_3-doped flame in the upper row of Fig. 3.6, no clear difference can be observed in the experimental data. At downstream positions, the modeled nanoparticle volume fraction follows this trend but slightly overpredicts the initial nanoparticle formation for the neat ethylene flame. A slight delay of the nanoparticle formation is present in the OME_3-doped flame, visible through different gradients at lower positions in the flame at approximately $\mathrm{HAB} = 3\,\mathrm{mm}$. Overall, the influence of OME_3 on the formation of nanoparticles can be summarized as marginal since the neat ethylene flames exhibit similar nanoparticle profiles.

The measured LII and modeled soot volume fraction f_v in the lower row of Fig. 3.6 shows a different influence of the OME_3 addition. Considerable differences between the neat ethylene and the OME_3-doped flames are visible. OME_3 reduces the amount of soot in the flame throughout the entire length, hence mainly affecting the larger soot particles. The model reproduces this behavior, whereas the measured and numerical soot reduction differs in quantity. LII results quantify the soot reduction between neat ethylene flame and OME_3-doped flame as $70\,\%$ and the simulation results predict a $44\,\%$ reduction. The exact quantity is largely affected by the CH_2O kinetics, as discussed in P3. An improvement starting from a soot reduction of $25\,\%$ in P5 could be shown for slight changes in the kinetic rates for selected CH_2O reactions, further details are given in P3.

Closer insights are obtained by analyzing the PSD for both fuel types. The normalized PSD at a position in the flame of $\mathrm{HAB} = 15\,\mathrm{mm}$ is plotted in Fig. 3.7 for the four investigated equivalence ratios of $\phi = 2.01$, 2.16, 2.31, and 2.46. Based on the experimental data, one can observe characteristic and quantitative differences between both fuels. The neat ethylene flame features a bimodal shape in the leanest flame condition with an equivalence ratio of $\phi = 2.01$. In contrast, a transition from an unimodal shape to bimodality is seen for the OME_3-doped flame at higher equivalence ratios of $\phi = 2.16$ and above. Soot particles with a diameter smaller than approximately $d_m \leq 4\,\mathrm{nm}$ are very similar in terms of their quantity and size for both fuel types. However, particles of the second mode, mainly consisting of soot aggregates, are reduced in quantity and diameter at their peak value when OME_3 is added to the flame.

In Fig. 3.7, both soot particle entities that are tracked in the CQMOM soot model, $\xi_{type} = cluster$ and $\xi_{type} = aggregate$, are plotted separately. No significant differences in the cluster distributions can be seen for both fuels across all equivalence ratios. Analogously to the experimental data, modeling results of larger particle aggregates deviate, resulting in a smaller peak diameter of the second mode with a reduced peak number density for the OME_3-doped flame. While a transition to bimodality can not be observed for the ethylene flame in the richest condition at the plotted position of $\mathrm{HAB} = 15\,\mathrm{mm}$, it occurs at downstream positions above $\mathrm{HAB} = 16\,\mathrm{mm}$ for the modeling results in the case of the neat ethylene flame whereas no transition is observed for the OME_3-doped flame in the entire modeling domain. As the experimental particle sampling is performed based on a probe volume rather than a point measurement due to the diameter of the sampling tube, considering slight shifts of the positioning between experimental and numerical results for

comparison seems reasonable. However, identical positions for the numerical and experimental data at $\mathrm{HAB} = 15\,\mathrm{mm}$ are chosen for Fig. 3.7 for consistency. At the equivalence ratio of $\phi = 2.16$, aggregates are present for both fuels of the CQMOM.

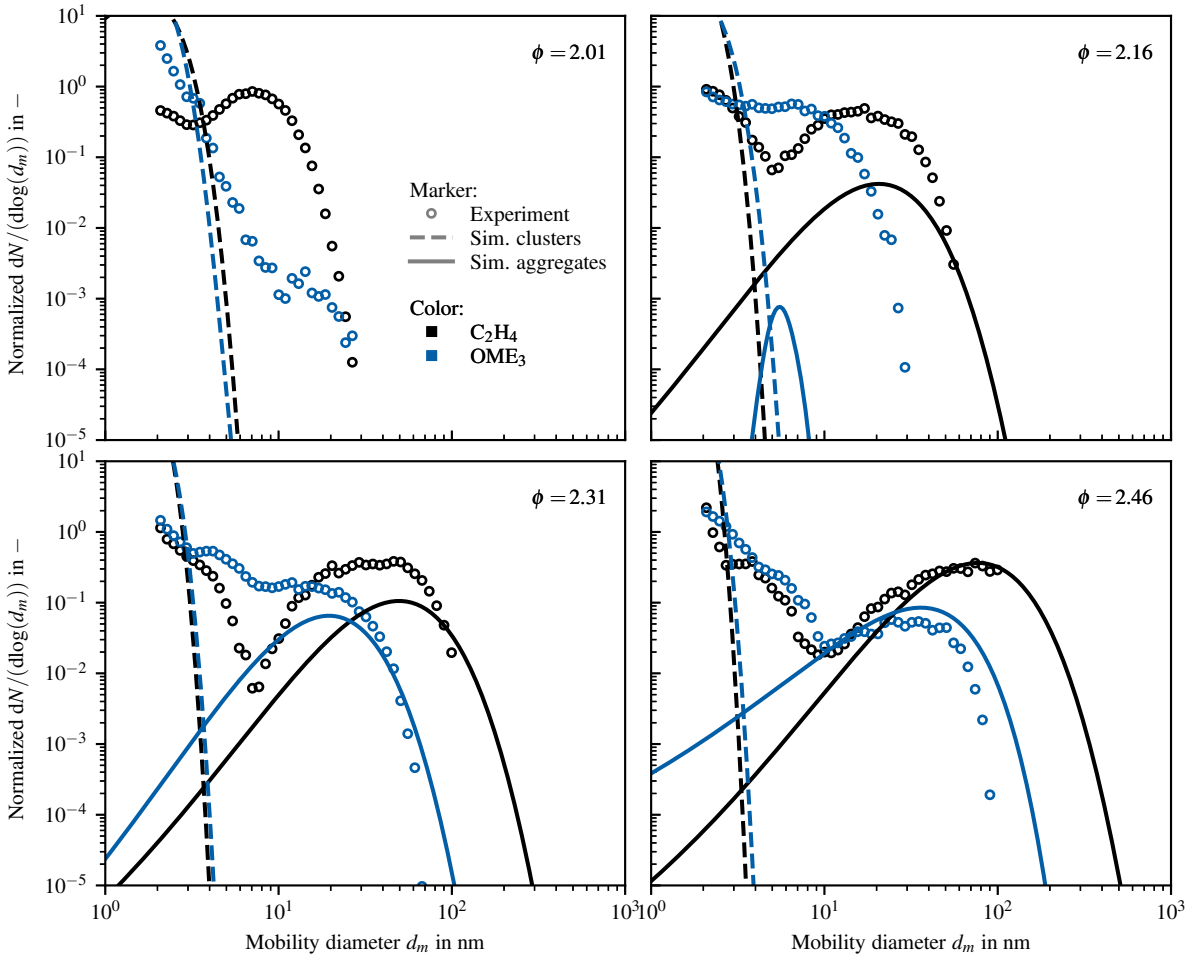

Fig. 3.7: Normalized results of the modeled lines and experimental (symbols) particle size distributions of a pure ethylene flame (black) and a OME_3-doped flame (blue) at a position of $\mathrm{HAB} = 15\,\mathrm{mm}$ for the four equivalence ratios of $\phi = 2.01, 2.16, 2.31$, and 2.46. Simulation data is divided into clusters (dashed line) and aggregates (solid line).

All in all, OME_3 primarily reduces the amount and diameter of larger soot particles such as aggregates. In contrast, OME_3 is found to not influence the nanoparticles significantly. Since comparable amounts of smaller particles are present in flames for both fuel mixtures at a position of $\mathrm{HAB} = 15\,\mathrm{mm}$, the influence of OME_3-doping on the soot inception step is limited. The subsequent particle evolution, on the other hand, is decelerated. Therefore, OME_3 hinders the particle growth processes, such as the HACA mechanism and PAH-condensation. Considerable amounts of incipient, young nanoparticles are still present in the OME-doped flames despite the reduction of aromatic species, as demonstrated in Sec. 3.2. The reduced inception toward nanoparticles seems to be

compensated by a slowed growth process of the nanoparticles due to the mentioned influence on the HACA mechanism or condensation of aromatics. Hence, a similar number of nanoparticles is observed in both flames. With that, the cause-and-effect chain of the influence of OME_3 on the soot formation processes is broken down into its mechanistic steps and unraveled on this basis.

Modeling results using the quadvariate CQMOM captures the main trends observed in the experiments. The main chemical and physical processes are reproduced, while quantitative differences remain. The first steps towards improving the predictability of the nanoparticle and soot volume fraction are performed by adaptations of the underlying kinetics (see P3). Detailed species concentration measurements in the gas phase for rich, sooting OME_3 flames should be conducted for further improvement. In particular, reliable data on soot-relevant PAH species could improve the kinetics and, subsequently, soot formation for OME flames quantitatively. Since embedded oxygen was found in the produced soot as described in P3, oxygenated PAHs could play a role during OME_3 combustion and be a factor in hindering soot formation.

3.4 Influence of OME_3 blending ratios on soot formation and growth

While O2 and O3 consider the influence of OME_3 based on a constant amount of OME_3 in the fuel mixture, O4 evaluates varying blending ratios between ethylene and OME_3 fuel. Different blending ratios are of particular practical and economic interest to optimize the use of this limited availability fuel in the most effective way.

O4 investigates ethylene/OME_3 fuel mixtures from pure ethylene to neat OME_3 with increments of 5 $\%_{carbon}$ for the two equivalence ratios of $\phi = 2.16$ and $\phi = 2.46$. Percentage numbers correspond to the amount of carbon provided through OME_3 compared to the overall carbon in the fuel mixture. For precise mixture compositions, the reader is referred to P1. Similar to objective O2 and O3, the influence of different blending ratios on the species pool, soot precursor species, soot volume fraction, and PSD are evaluated.

Figure 3.8 shows the peak values of the mole fraction profiles over the OME_3 content for selected species. These species are found to have a relevant influence on the decomposition and reaction pathways of OME_3 as well as on the subsequent soot formation pathways, as results of objective O2 suggest. As the OME_3 content rises, also CO_2 and H_2O mole fractions slightly increase linearly, proving a more complete combustion process. This is caused by the decomposition processes of OME_3 as described in objective O2 and confirmed by the corresponding linear increase of the decomposition product CH_2O in Fig. 3.8. CH_4, another species formed by OME_3 fuel fragments, additionally increases for higher contents of OME_3. Although CH_4 can cause the formation of soot-relevant species, C_2H_2 and C_6H_6 are reduced with increasing OME_3 contents. Here, an approximately linear reduction can be seen for C_2H_2, which controls the surface growth of soot particles. Comparing both equivalence ratios, one can see that the sensitivity to the OME_3 content is quantitatively higher in the richer flames since the fuel mixture provides more carbon to the flame. While the quantitative amount of C_2H_2 increases marginally in the richer flame, the amount of C_6H_6 approximately triples.

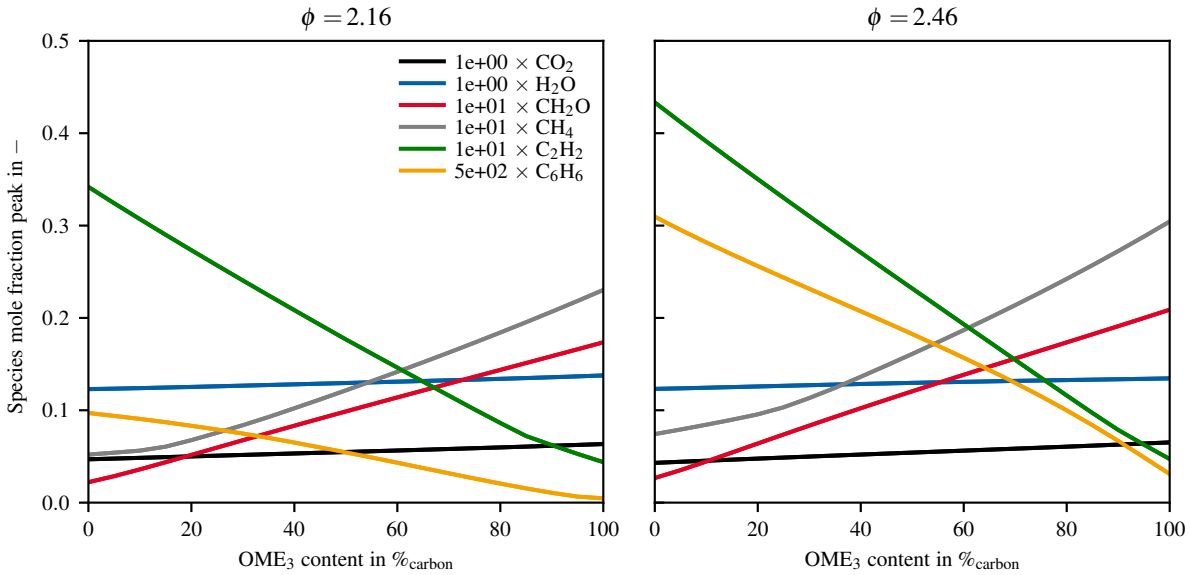

Fig. 3.8: Modeled peak values of the mole fraction profiles for the species CO_2 (black), H_2O (blue), CH_2O (red), CH_4 (gray), C_2H_2 (green), and C_6H_6 (orange) over the OME_3 content with respect to the carbon in the fuel mixture for an equivalence ratio of $\phi = 2.16$ (left) and $\phi = 2.46$ (right).

The resulting particle formation is visualized in Fig. 3.9 based on their nanoparticle and soot volume fraction profiles and their corresponding peak values within the flames for the investigated OME_3/C_2H_4 fuel mixtures. Despite lacking an experimental reference, an identical distinction between nanoparticle and soot volume fraction is applied as in O2 and O3 for consistency. The nanoparticle formation increasingly slows down with higher amounts of OME_3. A complete suppression of nanoparticle formation can be obtained with the combustion of neat OME_3 mixtures for both equivalence ratios. Some positions in the flame, such at $\mathrm{HAB} \geq 10\,\mathrm{mm}$, experience an intermediate increase in nanoparticles for small content of OME_3 but are decreased again for contents above $50\,\%_{\mathrm{carbon}}$ OME_3.

Increasing amounts of OME_3 delay the soot formation process, which is visible through the shift of the starting soot volume fraction increase towards higher HABs in Fig. 3.9. The correlation between soot volume fraction reduction and OME_3 content in the fuel mixture is approximately linear for both flames until a complete soot suppression is obtained for $80\,\%_{\mathrm{carbon}}$ OME_3 in the leaner flame set and $90\,\%_{\mathrm{carbon}}$ OME_3 in the richer flame set, respectively. This proportional relationship can be linked with the linear reduction of C_2H_2 for higher contents of OME_3 and, as a consequence thereof, limitation of the soot growth process through the HACA mechanism. Here, OME_3 replaces the soot-relevant species with soot-ineffective species such as CH_2O and has a dilution effect on the soot growth process. The linkage between nanoparticle volume fraction and involved species in the inception process is more complex since aromatic and PAH species show progressively decreasing, regressively decreasing, or linear decreasing functionalities (depending on their size) with increasing amounts of OME_3 content (see P1).

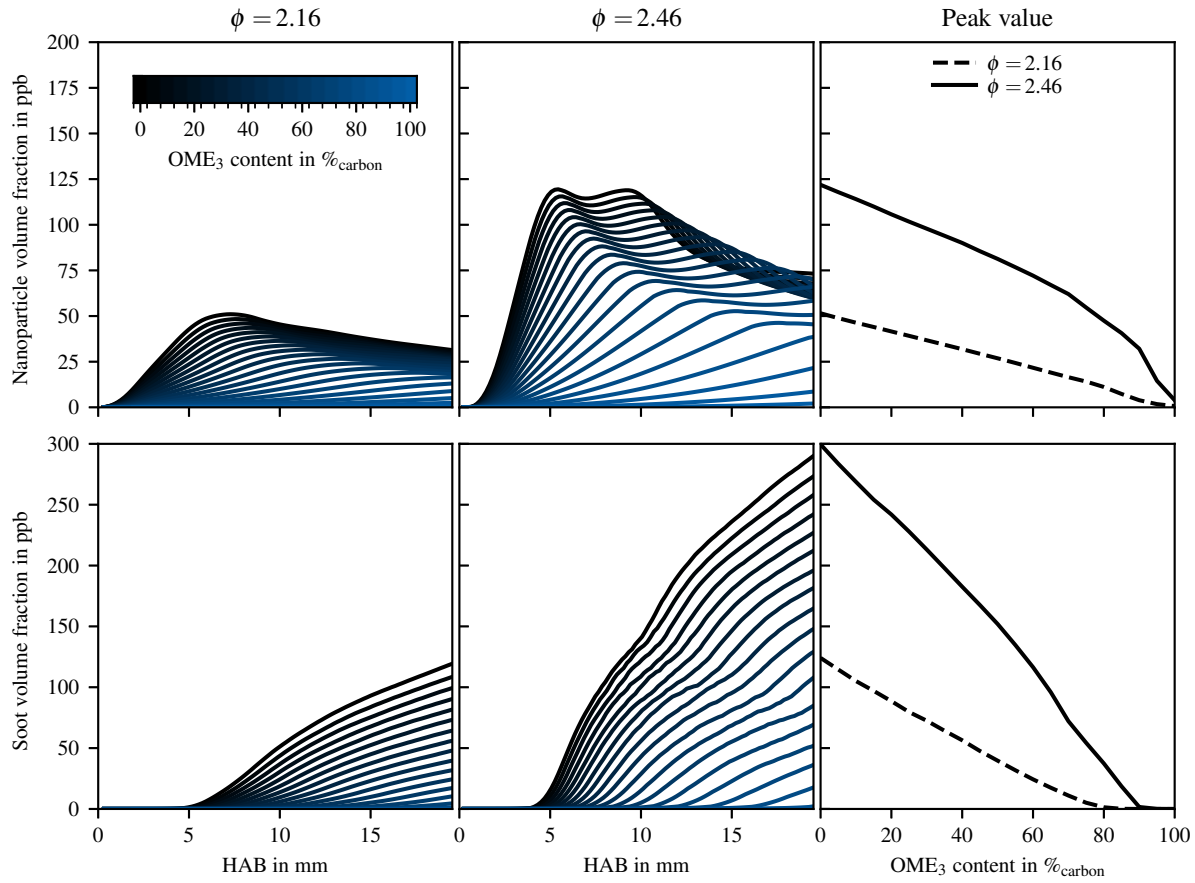

Fig. 3.9: Nanoparticle (top row) and soot volume fraction (bottom row) profiles over HAB (left and center) with their corresponding peak values (right) of fuel mixtures with different OME$_3$ content for the equivalence ratios $\phi = 2.16$ (left) and $\phi = 2.46$ (center).

Figure 3.10 shows the particle size distributions in dependence on the OME$_3$ for increments of $10\,\%_{\mathrm{carbon}}$ OME$_3$ content steps. For both equivalence ratios, no significant change of the smaller particle clusters is observed for blending ratios up to $60\,\%_{\mathrm{carbon}}$ OME$_3$. For OME$_3$ contents above this value, the OME$_3$ reduces these clusters in size and number in the lean flame, whereas an intermediate increase in its number is provoked in the rich flame. Aggregates are completely suppressed for $50\,\%_{\mathrm{carbon}}$ OME$_3$ and above in the flame of equivalence ratio $\phi = 2.16$ or $80\,\%_{\mathrm{carbon}}$ OME$_3$ in the richest flames. Solely for higher OME$_3$ quantities, a reduction of the aggregates' diameter and number is taking place. At the same time, the richer flame shows a reduction mainly in diameter and only for almost neat OME$_3$ also in number with a slight intermediate increase.

Altogether, the correlation between increasing amounts of OME$_3$ and the reduction of smaller particles differs from the behavior of larger particles. Smaller particles get reduced with higher amounts of OME$_3$, although an intermediate increase in number is observed in some areas of very rich flames before negligible amounts of nanoparticles occur for neat OME$_3$. In contrast, the soot

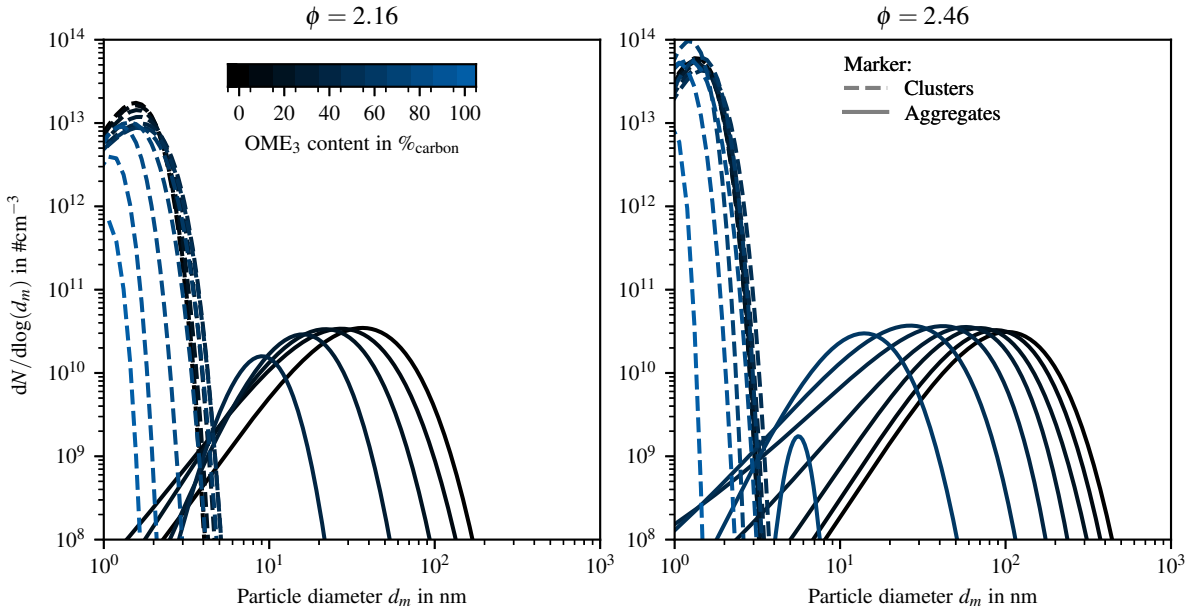

Fig. 3.10: Particle size distributions for varying OME_3 contents in the fuel mixture for the two investigated equivalence ratios $\phi = 2.16$ and $\phi = 2.46$.

volume fraction of larger particles is monotonically reduced proportionally to the amount of OME_3 in the fuel mixture until a complete suppression of aggregates is found for higher amounts of OME_3.

This effect can be assessed in two ways. On the one hand, smaller soot particles represent a higher risk to human health due to their increasing potential to penetrate deeply into the human body, e.g., as smaller soot particles are known to be respirable. On the other hand, smaller particles tend to have larger surface areas related to their mass or volume compared to larger soot aggregates. This aspect allows a faster oxidation process in practical applications. Particle oxidation of smaller soot particles possibly takes place in a combustion system itself directly following their formation after mixing richer, sooting pockets with the remaining fuel/air load. Depending on the exhaust-gas system, this could also happen in later stages of exhaust-gas aftertreatment, such as in diesel particulate filters during their regeneration.

3.5 Influence of OME_n variants - from fuel chemistry to soot evolution

While the objectives O2, O3, and O4 address exclusively the influence of OME_3, additional oxymethylene ethers with longer and shorter molecular structures or a blended mixture featuring multiple OME_n variants are also viable options as alternative fuels, as discussed in Sec. 1.4. Thus, the current objective O5 compares the influence of the two oxymethylene ether variants OME_2 and OME_4 featuring shorter and longer chain lengths than OME_3 with the results and effects

of OME_3. Like O2 and O3, this study focuses on the initial fuel decomposition, resulting species pool, soot precursor creation, soot formation, and soot evolution. The underlying target is to evaluate whether oxymethylene ethers of varying chain lengths induce similar or different effects on the chain of events of the soot formation process.

In P3, individual decomposition pathways of the species OME_2, OME_3, and OME_4 are individually shown. These specific reaction pathways are combined into one single schematic representing the decomposition of a generalized OME_n molecule. The resulting diagram is visualized in Fig. 3.11. This schematic is valid for the three investigated OME_n with $n = 2, 3, 4$ in rich flames at an equivalence ratio of $\phi = 2.46$ according to the mixture compositions stated in Tab. 2.3.

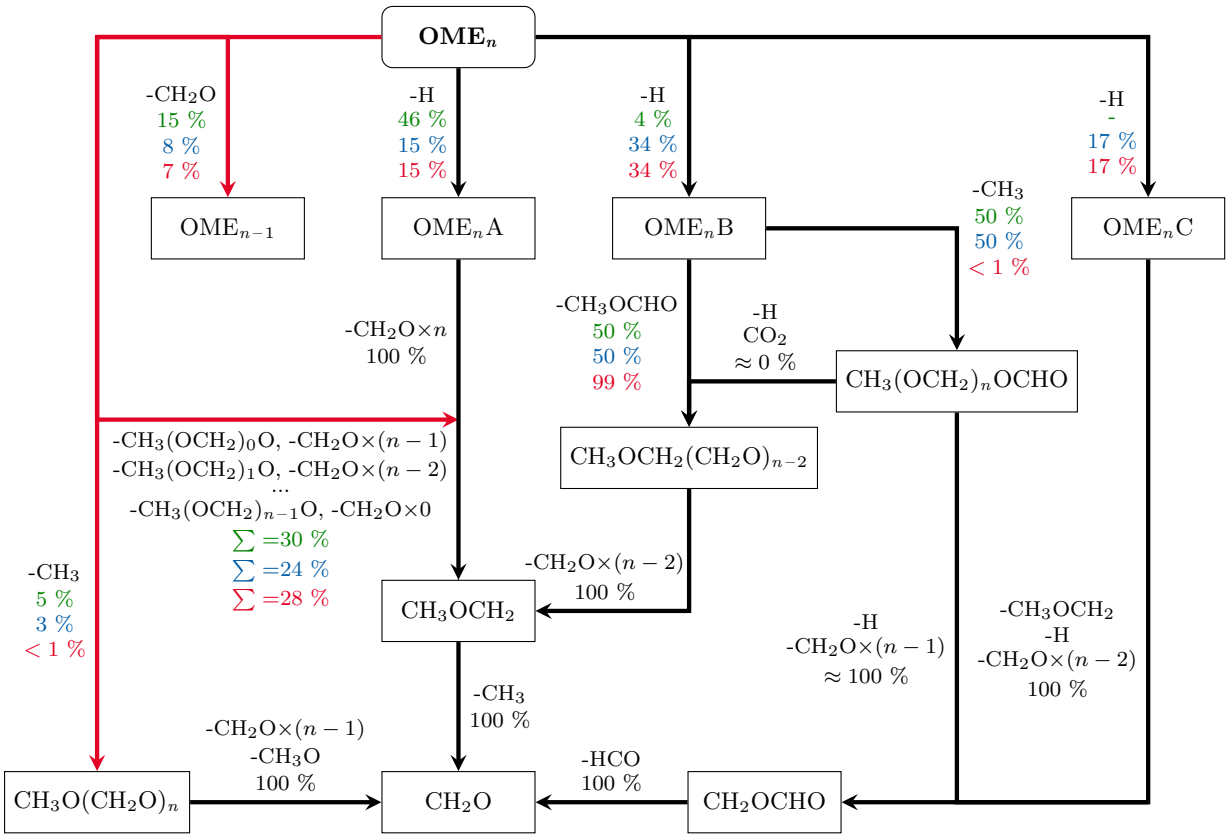

Fig. 3.11: Schematic initial decomposition pathways of the generalized species OME_n derived from OME_2, OME_3, and OME_4 pathways for an equivalence ratio of $\phi = 2.46$. Unimolecular reaction pathways are marked by red arrows. Numbers correspond to the relative carbon fluxes starting from the source specie. Colored numbers represent specific values for OME_2 (green), OME_3 (blue), OME_4 (red), and common numbers (black).

The decomposition routes of these three OMEs are qualitatively equal, except for the apparent presence of additional reaction pathways in dependence on the chain length of the molecule. However, these additional pathways, such as for OME_4, follow identical patterns to smaller OMEs. Additional pathways are expected for OME_n with $n \geq 5$ due to more possible options of the first

H-abstraction reaction pathways. All three OMEs follow similar decomposition pathways with a large share of unimolecular reactions. Nonetheless, slight quantitative differences can be observed for unimolecular and H-abstraction reactions. The weightings of the individual reaction paths differ among the three investigated OMEs. Whether this corresponds to differences regarding the formed fuel fragments and subsequently to deviating influences of the soot precursor formation is evaluated based on the species pool.

A quantitative comparison among the three investigated OMEs and neat ethylene flames based on the mole fraction peak values for a small species selection is shown in Fig. 3.12. Mole fraction peaks are normalized by the maximum mole fraction value across the four fuel mixtures of each plotted species. Fig. 3.12 is limited to the richest flame set of an equivalence ratio of $\phi = 2.46$ since this flame condition features the most significant contrast between the neat ethylene and OME_3-doped flame as described in objective O2.

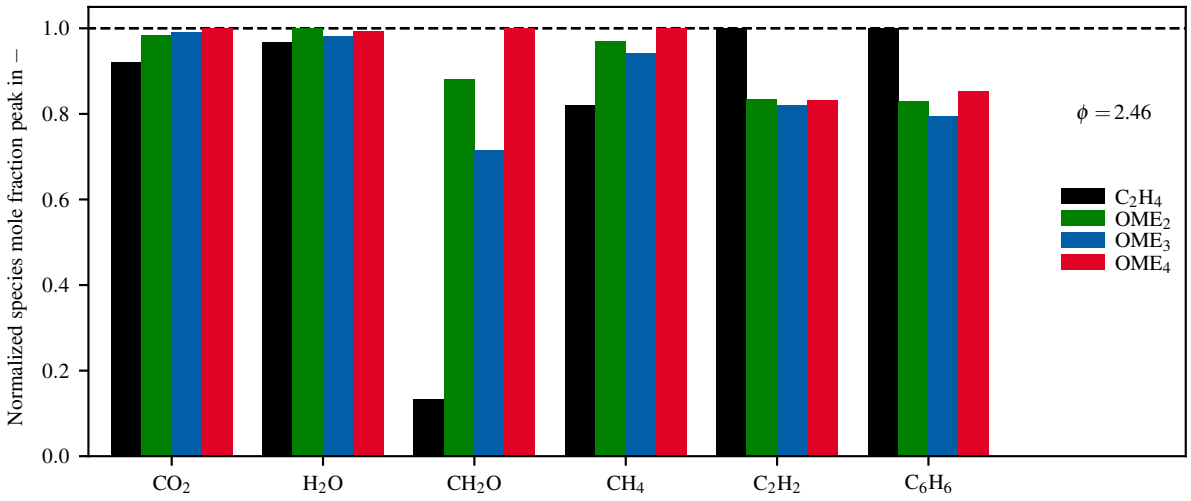

Fig. 3.12: Normalized species mole fraction peaks of the species CO_2, H_2O, CH_2O, CH_4, C_2H_2, and C_6H_6 for the neat C_2H_4 flame and three investigated OME_n variants for the equivalence ratio of $\phi = 2.46$.

All three OME_n variants generate similar trends in the species pool compared to the reference flames of neat ethylene fuel. The species CO_2 and H_2O are slightly increased, indicating a more complete combustion process. The CH_4 mole fraction peaks additionally rise slightly, whereas a strong formation of CH_2O is present across all OME-doped flames, and the C_2H_2 and C_6H_6 formation is reduced. While quantitative deviations among the OMEs can be observed, these differences are assessed as negligible, taking into account the strong quantitative differences between all OME_n flames and the reference flames of neat ethylene. Besides the similarity of these quantitative peak values, species profiles of OME_2, OME_3, and OME_4 also match very closely, as demonstrated in P3. Further details therein also illustrate generally indifferent species pools for OME_n flames at equivalence ratios $\phi = 2.01$, $\phi = 2.16$, and $\phi = 2.31$. These results suggest that OME_n variants featuring different chain lengths do not deviate in their chemical effects on the species pool, at least for these premixed flames, which are based on identical carbon streams.

No monotonic increase or decrease of these species is recognizable with increasing chain length of the OME_n molecule. The general decomposition formula of OME_n into methoxy radicals, methyl radicals, and formaldehyde would suggest a decomposition into the fuel fragments according to the proportion $OME_n = CH_3O + (CH_2O)_n + CH_3$ proposed by Tan et al. [124] in the context of non-premixed flames. Hence, a monotonic increase of formaldehyde and reduction of CH_3 with increasing chain length of the OME_n molecule is expected. While an increase of formaldehyde can be observed for OME_2 towards OME_4 and a reduction of methane from OME_2 to OME_3, which supports this formula, it is not reproduced for all three OMEs simultaneously. However, it has to be reminded that the fuels are compared on the basis of identical carbon streams and consistent OME_n fuel ratios of $20\,\%_{\mathrm{carbon}}$ in the fuel mixture, so the overall concentration of OME_n molecules in the investigated flames decreases with increasing OME_n chain length due to the higher carbon number. Other factors, such as subsequent reactions, additionally outweigh the suggested ratios of this decomposition formula.

The influence of different OME_n variants on soot formation and evolution is analyzed based on Fig. 3.13. This figure presents the normalized PSD for the three investigated OMEs in relation to the reference flames with neat ethylene. While the general trends for OME_3-doping are discussed in objective O1, only similarities and dissimilarities for the different OME_n variants are mentioned and analyzed here.

No obvious difference is noticeable for the smaller particles in either the experimental or numerical results. The investigated OME_n, therefore, all share the influence of delaying the initial soot formation process. Additionally, their effects on aggregates follow common trends as results do not contain qualitative differences for the variants of OME_n-doped flames. The second mode of the PSD containing aggregates is diminished regarding its peak particle number density and also its averaged mobility diameter in flames containing OME_n fuel mixtures. Additionally, OME_n delays the bimodality in comparison to the neat ethylene flames. Modeling results of the aggregates exhibit slightly increased severity of this effect from OME_3 over OME_4 towards OME_2, while the overall differences are assessed as negligible in contrast to the significant dissimilarity when comparing against the neat ethylene flames. Experimental results do not show a consistent ranking of the soot reduction effect for the investigated OME_n throughout the four equivalence ratios, and differences fall within measurement uncertainty.

The studies of the integral nanoparticle volume fraction and soot volume fraction additionally prove the indifferent influence of OME_2, OME_3, and OME_4 on the soot formation and soot growth processes. The nanoparticle and soot particle profiles OME_2 and OME_4 follow the trends of OME_3. (See P3)

All in all, the three investigated OME_n variants are decomposed through similar reaction pathways with minor differences in their allocation. Nevertheless, fuel fragments and subsequent formation of soot-relevant species in the gas phase are almost indifferent to the OME_n variant. Therefore, their chemical effects on the species pool can be summarized to be similar for all three OMEs. This leads to no significant deviations in the PSD among the three OMEs regarding their overall shape, trends, and quantitative properties. As a consequence, the chain length of the OME_n molecule does not alter the influence on the soot formation and evolution processes. Hence, it is justified

to assume that additional findings described in O2, O3, and O4 for OME_3-doped flames are also valid for OME_2 and OME_4 flames.

As a result, no OME_n variant can be favored based on their soot reduction potential for identical carbon streams in these premixed flames.

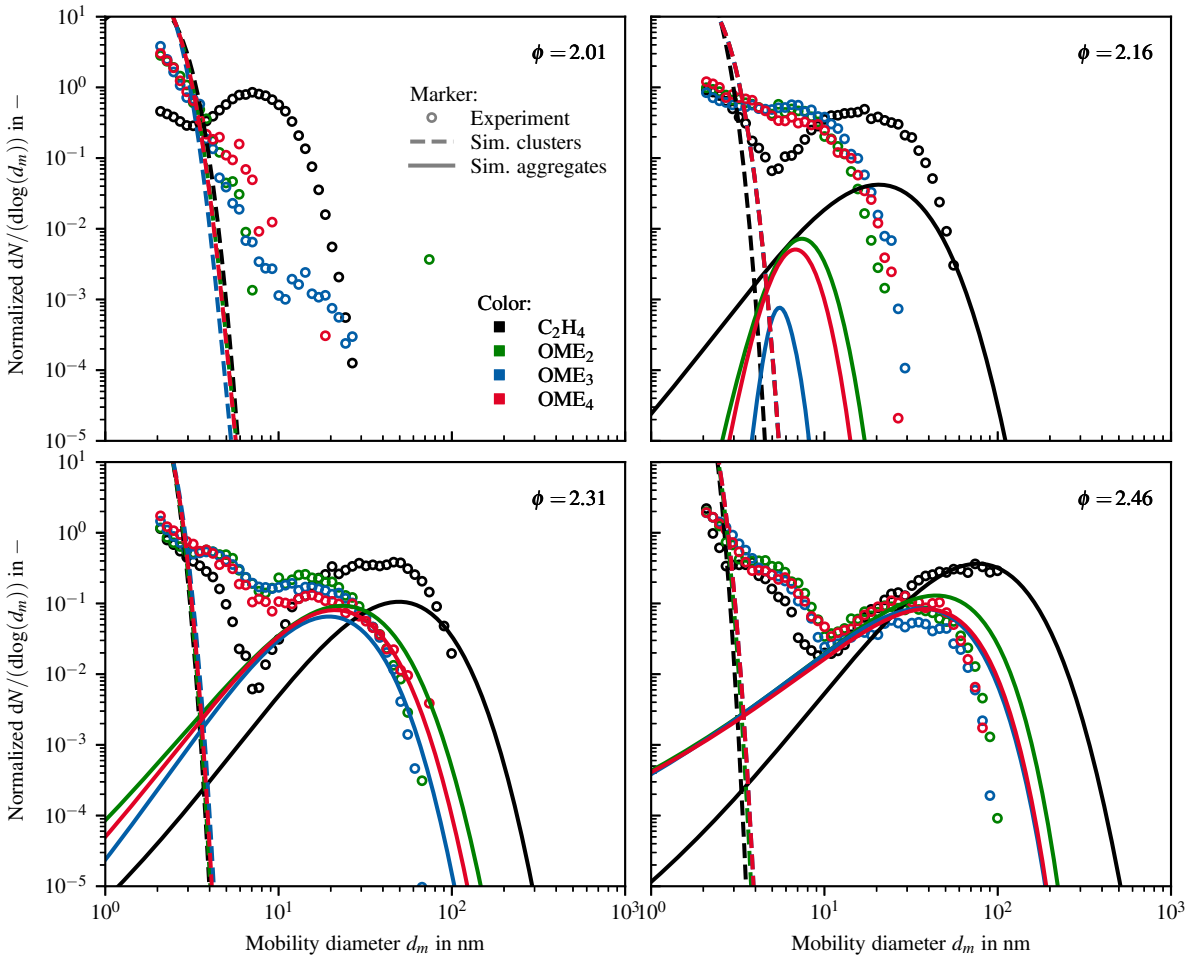

Fig. 3.13: Normalized PSD of the experimental (dots) and modeling results(lines) for the investigated equivalence ratios. Simulations are divided into clusters (dashed line) and aggregates (solid line). Color indicates the fuel mixture containing neat C_2H_4 (black), OME_2 (green), OME_3 (blue), and OME_4 (red).

4 Conclusion and outlook

Soot particle formation is highly affected by the flow field of the gas phase and the resulting mixing processes between fuel and oxidizer. The molecular fuel structure influences the initial composition of smaller fuel fragments in the gas phase. Since these gas-phase fragments affect soot precursor formation and soot sub-processes, fuel structure is another essential factor in controlling soot emissions.

The present work systematically investigates these parameters using quadrature-based moment method soot models. The study of these factors is broken down into six research objectives (O#), individually investigated in correspondingly adapted flame configurations to isolate competing or assisting effects. The following scientific conclusions are obtained:

- **(O0): Validation of the soot modeling approach**
  A prerequisite for all further studies is a validation of both the applied soot modeling approaches against multiple measurement techniques. The model trends are equivalent to the experimental findings. Remaining quantitative differences for OME_3-flames are traced back to the underlying kinetics. Overall, the soot models achieve good quantitative agreement with the experimental data in the context of soot modeling.
- **(O1): Influence of the strain and fuel dilution on soot formation**
  Fuel/oxidizer mixing processes are analyzed in counterflow diffusion flames through variations of the strain rate and dilution of the fuel stream with nitrogen for lightly sooting flames. The strain rate does not significantly alter the soot formation rates, but instead, the particle residence times. In contrast, fuel dilution strongly reduces all soot processes (inception, PAH-deposition, HACA). Both effects result in decreased soot volume fractions overall and a shift of the second mode of the PSD towards smaller diameters for higher strain or dilution ratios.
- **(O2): Influence of OME_3 fuel chemistry on gas-phase species and soot precursor pool**
  The influence of molecular fuel structure on soot particle formation is analyzed. The investigation utilizes the alternative e-fuel oxymethylene ether-3 (OME_3) in burner-stabilized, premixed flames using a detailed quadvariate conditional quadrature method of moments considering physical and chemical soot particle properties. In general, the decomposition of OME_3 strongly favors the formation of aldehydic fuel fragments with no immediate formation pathways toward unsaturated hydrocarbons, which leads to a direct reduction of soot-relevant species such as C_2H_2 or aromatic structures.

- **(O3): Influence of OME_3 on soot formation and growth**
  The subsequent influence of OME_3 on soot particles in ethylene flames mainly affects large particle aggregates, with minor changes of nanoparticles. The soot volume fraction highly decreases, and aggregates reduce in diameter and number. Overall, there is a delay and slowdown of the formation pathways. The cause-and-effect chain for OME_3 reducing soot emissions is, therefore, explained on the basis of chemical and physical principles.
- **(O4): Influence of OME_3 blending ratios on soot formation and growth**
  Increased blending ratios of OME_3 in OME_3/ethylene fuel mixtures result in a linear reduction of C_2H_2, which analogously reduces soot volume fraction by preventing soot growth through the HACA mechanism until completely suppressing the aggregate formation for high OME_3 contents.
- **(O5): Influence of OME_n variants - from fuel chemistry to soot evolution**
  Major effects on the initial species pool, soot precursor formation, and soot evolution, described in objectives O2 and O3, are found to be similar for the investigated OME_n variants OME_2 and OME_4. Therefore, additional findings for OME_3, such as the ones for O4, are also assumed to be valid for OME_2 and OME_4. The results suggest no favorite OME_n variant through their effect on soot emissions for the comparison based on identical carbon streams.

These objectives follow the same overarching goal to deepen the knowledge about influencing factors of particle emissions. The effects of fuel-oxidizer mixing and molecular OME_n fuel structure are analyzed based on the underlying chemical and physical processes. This way, the influence on the complete chain of events, from fuel decomposition to soot evolution, is comprehensively explained and grounded on universal, physical, and chemical mechanisms. The accomplishments are detailed insights into the particle formation and inhibition processes in OME_n flames.

After investigating individual parameters isolated from each other in laminar flame configurations, the interactions of these effects are of interest. Flames with turbulent conditions combine multiple processes of mixing, turbulence, thus exhibiting high intermittency of fuel-rich pockets prone to soot formation, increasing the technical relevance. This approach is pursued with the start of turbulent OME_n flame simulations, in which the influence of OME_n on the gas-phase pool and soot formation is analyzed within a jet flame.

The high sensitivity of the initial OME_n decomposition pathways on soot precursor formation is demonstrated (see P3), which suggests a revision of the OME_n kinetics. Additional experimental studies for OME_n flames should be performed under rich, sooty conditions to quantify species compositions including soot-relevant compounds, precisely. Since embedded oxygen was found in the soot particles of OME_3-doped flames (see P5), the effects of this aspect need to be closely investigated.

Acknowledgment

I would like to express my sincere gratitude to my dissertation supervisor, Prof. Christian Hasse, for his scientific guidance throughout the past years. His unwavering support and effective scientific recommendations have been leading to this dissertation. A special thanks goes to my former group leader, Jun.-Prof. Federica Ferraro for her exceptional teaching, which has been a helpful mentorship in my entire research career. Her trust in my abilities has been instrumental, and I would like to thank her for the outright help, even during late hours. A very fruitful collaboration throughout the years has been established with Italian research groups, for which I am very thankful. First and foremost, Prof. Mariano Sirignano had many scientific ideas and quickly assisted with kinetics and insights into soot formation.

I extend my heartfelt appreciation to my colleagues at STFS and RSM. The mutual assistance and shared experiences have enriched the academic journey we have had together as a group in the past five years. The collective spirit at both institutes, the countless memes, and the pants-widening quantities of cake on Fridays have contributed significantly to the vibrant and collaborative atmosphere that defined our journey. My former students, who turned to colleagues, contributed to the success of several projects through excellent work. I also want to acknowledge my predecessor for his comprehensive achievements in the field of soot modeling, on which this dissertation is heavily based.

In addition to my professional environment, I am enormously grateful to my parents, family, and friends. My parents, in particular, for their encouragement toward the invaluable gift of education and for offering me help that I can trust without hesitation. The collective support of my family and friends has been fundamental in overcoming challenges in academia and all aspects. Last but not certainly not least, I deeply thank my partner, Isabel, for her unrestricted and selfless help, care, and love. She has been a great source of motivation and strength, making the challenging moments more manageable and the successes more meaningful.

Bibliography

[1] Michael Sterner and Ingo Stadler. *Energiespeicher - Bedarf, Technologien, Integration*. Berlin, Heidelberg: Springer Berlin Heidelberg, 2014. ISBN: 978-3-642-37379-4 978-3-642-37380-0. DOI: 10.1007/978-3-642-37380-0.

[2] A. Dreizler et al. "The Role of Combustion Science and Technology in Low and Zero Impact Energy Transformation Processes". In: *Appl. Energy Combust. Sci.* 7 (2021), p. 100040. DOI: 10.1016/j.jaecs.2021.100040.

[3] Katharina Kohse-Höinghaus. "Combustion, Chemistry, and Carbon Neutrality". In: *Chemical Reviews* 123.8 (Apr. 2023), pp. 5139–5219. DOI: 10.1021/acs.chemrev.2c00828.

[4] Rituraj Niranjan and Ashwani Kumar Thakur. "The Toxicological Mechanisms of Environmental Soot (Black Carbon) and Carbon Black: Focus on Oxidative Stress and Inflammatory Pathways". In: *Frontiers in Immunology* 8 (June 2017), p. 763. DOI: 10.3389/fimmu.2017.00763.

[5] J. Lelieveld et al. "Effects of Fossil Fuel and Total Anthropogenic Emission Removal on Public Health and Climate". In: *Proceedings of the National Academy of Sciences* 116.15 (Apr. 2019), pp. 7192–7197. DOI: 10.1073/pnas.1819989116.

[6] Katharina Kohse-Höinghaus. "Combustion in the Future: The Importance of Chemistry". In: *Proceedings of the Combustion Institute* 38.1 (2021), pp. 1–56. DOI: 10.1016/j.proci.2020.06.375.

[7] Jacob W. Martin, Maurin Salamanca, and Markus Kraft. "Soot Inception: Carbonaceous Nanoparticle Formation in Flames". In: *Progress in Energy and Combustion Science* 88 (Jan. 2022), p. 100956. DOI: 10.1016/j.pecs.2021.100956.

[8] Henning Bockhorn et al., eds. *Soot Formation in Combustion: Mechanisms and Models*. Vol. 59. Springer Series in Chemical Physics. Berlin, Heidelberg: Springer Berlin Heidelberg, 1994. ISBN: 978-3-642-85169-8 978-3-642-85167-4. DOI: 10.1007/978-3-642-85167-4.

[9] H Richter and J.B Howard. "Formation of Polycyclic Aromatic Hydrocarbons and Their Growth to Soot—a Review of Chemical Reaction Pathways". In: *Progress in Energy and Combustion Science* 26.4-6 (Aug. 2000), pp. 565–608. DOI: 10.1016/S0360-1285(00)00009-5.

[10] H.F. Calcote. "Mechanisms of Soot Nucleation in Flames—A Critical Review". In: *Combustion and Flame* 42 (Jan. 1981), pp. 215–242. DOI: 10.1016/0010-2180(81)90159-0.

[11] Hai Wang and Michael Frenklach. “A Detailed Kinetic Modeling Study of Aromatics Formation in Laminar Premixed Acetylene and Ethylene Flames”. In: *Combustion and Flame* 110.1-2 (July 1997), pp. 173–221. DOI: 10.1016/S0010-2180(97)00068-0.

[12] Michael Frenklach and Hai Wang. “Detailed Mechanism and Modeling of Soot Particle Formation”. In: *Soot Form. Combust. Mech. Model.* Ed. by Henning Bockhorn. Berlin, Heidelberg: Springer Berlin Heidelberg, 1994, pp. 165–192. ISBN: 978-3-642-85167-4. DOI: 10.1007/978-3-642-85167-4_10.

[13] Henning Richter and Jack B. Howard. “Formation and Consumption of Single-Ring Aromatic Hydrocarbons and Their Precursors in Premixed Acetylene, Ethylene and Benzene flamesElectronic Supplementary Information (ESI) Available: Thermodynamic and Kinetic Property Data. See http://www.rsc.org/suppdata/cp/b1/b110089k/”. In: *Physical Chemistry Chemical Physics* 4.11 (May 2002), pp. 2038–2055. DOI: 10.1039/b110089k.

[14] J A Miller, R J Kee, and C K Westbrook. “Chemical Kinetics and Combustion Modeling”. In: *Annual Review of Physical Chemistry* 41.1 (Oct. 1990), pp. 345–387. DOI: 10.1146/annurev.pc.41.100190.002021.

[15] James A. Miller and Carl F. Melius. “Kinetic and Thermodynamic Issues in the Formation of Aromatic Compounds in Flames of Aliphatic Fuels”. In: *Combustion and Flame* 91.1 (Oct. 1992), pp. 21–39. DOI: 10.1016/0010-2180(92)90124-8.

[16] James A. Miller and Stephen J. Klippenstein. “The Recombination of Propargyl Radicals and Other Reactions on a C_6H_6 Potential”. In: *The Journal of Physical Chemistry A* 107.39 (Oct. 2003), pp. 7783–7799. DOI: 10.1021/jp030375h.

[17] Michael Frenklach and Hai Wang. “Detailed Modeling of Soot Particle Nucleation and Growth”. In: *Symposium (International) on Combustion* 23.1 (Jan. 1991), pp. 1559–1566. DOI: 10.1016/S0082-0784(06)80426-1.

[18] Michael Frenklach. “Reaction Mechanism of Soot Formation in Flames”. In: *Physical Chemistry Chemical Physics* 4.11 (May 2002), pp. 2028–2037. DOI: 10.1039/b110045a.

[19] A. D’Anna and A. Violi. “Detailed Modeling of the Molecular Growth Process in Aromatic and Aliphatic Premixed Flames”. In: *Energy & Fuels* 19.1 (Jan. 2005), pp. 79–86. DOI: 10.1021/ef0499675.

[20] M.B. Colket and D.J. Seery. “Reaction Mechanisms for Toluene Pyrolysis”. In: *Symposium (International) on Combustion* 25.1 (1994), pp. 883–891. DOI: 10.1016/S0082-0784(06)80723-X.

[21] N. M. Marinov et al. “Modeling of Aromatic and Polycyclic Aromatic Hydrocarbon Formation in Premixed Methane and Ethane Flames”. In: *Combustion Science and Technology* 116–117.1-6 (Aug. 1996), pp. 211–287. DOI: 10.1080/00102209608935550.

[22] Anthony M. Dean. “Detailed Kinetic Modeling of Autocatalysis in Methane Pyrolysis”. In: *The Journal of Physical Chemistry* 94.4 (Feb. 1990), pp. 1432–1439. DOI: 10.1021/j100367a043.

[23] Carl F. Melius et al. “Reaction Mechanisms in Aromatic Hydrocarbon Formation Involving the C5H5 Cyclopentadienyl Moiety”. In: *Symposium (International) on Combustion* 26.1 (Jan. 1996), pp. 685–692. DOI: 10.1016/S0082-0784(96)80276-1.

[24] Hai Wang. “Formation of Nascent Soot and Other Condensed-Phase Materials in Flames”. In: *Proceedings of the Combustion Institute* 33.1 (2011), pp. 41–67. DOI: 10.1016/j.proci.2010.09.009.

[25] Edina Reizer, Béla Viskolcz, and Béla Fiser. “Formation and Growth Mechanisms of Polycyclic Aromatic Hydrocarbons: A Mini-Review”. In: *Chemosphere* 291 (Mar. 2022), p. 132793. DOI: 10.1016/j.chemosphere.2021.132793.

[26] Hope A. Michelsen et al. “A Review of Terminology Used to Describe Soot Formation and Evolution under Combustion and Pyrolytic Conditions”. In: *ACS Nano* 14.10 (Oct. 2020), pp. 12470–12490. DOI: 10.1021/acsnano.0c06226.

[27] Mariano Sirignano, Carmela Russo, and Anna Ciajolo. “One-Step Synthesis of Carbon Nanoparticles and Yellow to Blue Fluorescent Nanocarbons in Flame Reactors”. In: *Carbon* 156 (Jan. 2020), pp. 370–377. DOI: 10.1016/j.carbon.2019.09.068.

[28] Mariano Sirignano, John Kent, and Andrea D’Anna. “Detailed Modeling of Size Distribution Functions and Hydrogen Content in Combustion-Formed Particles”. In: *Combustion and Flame* 157.6 (June 2010), pp. 1211–1219. DOI: 10.1016/j.combustflame.2009.11.014.

[29] Henning Bockhorn, ed. *Combustion Generated Fine Carbonaceous Particles: Proceedings of an International Workshop Held in Villa Orlandi, Anacapri, May 13-16, 2007*. Karlsruhe: KIT Scientific Publishing, 2009. ISBN: 978-3-86644-441-6.

[30] Andrea D’Anna. “Combustion-Formed Nanoparticles”. In: *Proceedings of the Combustion Institute* 32.1 (2009), pp. 593–613. DOI: 10.1016/j.proci.2008.09.005.

[31] Dongping Chen et al. “A Fully Coupled Simulation of PAH and Soot Growth with a Population Balance Model”. In: *Proceedings of the Combustion Institute* 34.1 (2013), pp. 1827–1835. DOI: 10.1016/j.proci.2012.06.089.

[32] Mariano Sirignano. “Nanoparticle in High Temperature Environment:” PhD thesis. University of Naples Federico II, 2011.

[33] A. D’Alessio et al. “Precursor Formation and Soot Inception in Premixed Ethylene Flames”. In: *Symposium (International) on Combustion* 24.1 (Jan. 1992), pp. 973–980. DOI: 10.1016/S0082-0784(06)80115-3.

[34] A.D. Abid et al. “Size Distribution and Morphology of Nascent Soot in Premixed Ethylene Flames with and without Benzene Doping”. In: *Proceedings of the Combustion Institute* 32.1 (2009), pp. 681–688. DOI: 10.1016/j.proci.2008.07.023.

[35] L.A Sgro et al. “Detection of Combustion Formed Nanoparticles”. In: *Chemosphere* 51.10 (June 2003), pp. 1079–1090. DOI: 10.1016/S0045-6535(02)00718-X.

[36] S J Harris and A M Weiner. “Chemical Kinetics of Soot Particle Growth”. In: *Annual Review of Physical Chemistry* 36.1 (Oct. 1985), pp. 31–52. DOI: 10.1146/annurev.pc.36.100185.000335.

[37] Richard A. Dobbins and Haran Subramaniasivam. “Soot Precursor Particles in Flames”. In: *Soot Formation in Combustion*. Ed. by Vitalii I. Goldanskii et al. Vol. 59. Berlin, Heidelberg: Springer Berlin Heidelberg, 1994, pp. 290–301. ISBN: 978-3-642-85169-8 978-3-642-85167-4. DOI: 10.1007/978-3-642-85167-4_16.

[38] Stephen J. Harris and Anita M. Weiner. “Surface Growth of Soot Particles in Premixed Ethylene/Air Flames”. In: *Combustion Science and Technology* 31.3-4 (Apr. 1983), pp. 155–167. DOI: 10.1080/00102208308923637.

[39] B. S. Haynes and H. Gg. Wagner. “The Surface Growth Phenomenon in Soot Formation”. In: *Zeitschrift für Physikalische Chemie* 133.2 (Feb. 1982), pp. 201–213. DOI: 10.1524/zpch.1982.133.2.201.

[40] J. Nagle and R.F. Strickland-Constable. “OXIDATION OF CARBON BETWEEN 1000–2000°C”. In: *Proceedings of the Fifth Conference on Carbon*. Elsevier, 1962, pp. 154–164. ISBN: 978-0-08-009707-7. DOI: 10.1016/B978-0-08-009707-7.50026-1.

[41] K.G. Neoh, J.B. Howard, and A.F. Sarofim. “Effect of Oxidation on the Physical Structure of Soot”. In: *Symposium (International) on Combustion* 20.1 (Jan. 1985), pp. 951–957. DOI: 10.1016/S0082-0784(85)80584-1.

[42] K. G. Neoh, J. B. Howard, and A. F. Sarofim. “Soot Oxidation in Flames”. In: *Particulate Carbon*. Ed. by Donald C. Siegla and George W. Smith. Boston, MA: Springer US, 1981, pp. 261–282. ISBN: 978-1-4757-6139-9 978-1-4757-6137-5. DOI: 10.1007/978-1-4757-6137-5_9.

[43] S. Von Gersum and P. Roth. “Soot Oxidation in High Temperature N2O/Ar and NO/Ar Mixtures”. In: *Symposium (International) on Combustion* 24.1 (Jan. 1992), pp. 999–1006. DOI: 10.1016/S0082-0784(06)80118-9.

[44] G. Blanquart, P. Pepiot-Desjardins, and H. Pitsch. “Chemical Mechanism for High Temperature Combustion of Engine Relevant Fuels with Emphasis on Soot Precursors”. In: *Combustion and Flame* 156.3 (Mar. 2009), pp. 588–607. DOI: 10.1016/j.combustflame.2008.12.007.

[45] J. Lahaye. “Mechanisms of Soot Formation”. In: *Polymer Degradation and Stability* 30.1 (Jan. 1990), pp. 111–121. DOI: 10.1016/0141-3910(90)90121-M.

[46] M.E. Mueller, G. Blanquart, and H. Pitsch. “Modeling the Oxidation-Induced Fragmentation of Soot Aggregates in Laminar Flames”. In: *Proceedings of the Combustion Institute* 33.1 (2011), pp. 667–674. DOI: 10.1016/j.proci.2010.06.036.

[47] Mariano Sirignano, John Kent, and Andrea D’Anna. “Modeling Formation and Oxidation of Soot in Nonpremixed Flames”. In: *Energy & Fuels* 27.4 (Apr. 2013), pp. 2303–2315. DOI: 10.1021/ef400057r.

[48] Darson D. Li et al. “Soot: A Review of Computational Models at Different Length Scales”. In: *Experimental and Computational Multiphase Flow* 5.1 (Mar. 2023), pp. 1–14. DOI: 10.1007/s42757-021-0124-4.

[49] Qinghua Zeng, Aibing Yu, and Gaoqing (Max) Lu. “Evaluation of Interaction Forces between Nanoparticles by Molecular Dynamics Simulation”. In: *Industrial & Engineering Chemistry Research* 49.24 (Dec. 2010), pp. 12793–12797. DOI: 10.1021/ie101751v.

[50] Charles A. Schuetz and Michael Frenklach. “Nucleation of Soot: Molecular Dynamics Simulations of Pyrene Dimerization”. In: *Proceedings of the Combustion Institute* 29.2 (Jan. 2002), pp. 2307–2314. DOI: 10.1016/S1540-7489(02)80281-4.

[51] Laura Pascazio et al. “Exploring the Internal Structure of Soot Particles Using Nanoindentation: A Reactive Molecular Dynamics Study”. In: *Combustion and Flame* 219 (Sept. 2020), pp. 45–56. DOI: 10.1016/j.combustflame.2020.04.029.

[52] Laura Pascazio et al. “Aromatic Penta-Linked Hydrocarbons in Soot Nanoparticle Formation”. In: *Proceedings of the Combustion Institute* 38.1 (2021), pp. 1525–1532. DOI: 10.1016/j.proci.2020.09.029.

[53] Angela Violi. “Modeling of Soot Particle Inception in Aromatic and Aliphatic Premixed Flames”. In: *Combustion and Flame* 139.4 (Dec. 2004), pp. 279–287. DOI: 10.1016/j.combustflame.2004.08.013.

[54] I M Khan, C H T Wang, and B E Langridge. “Coagulation and Combustion of Soot Particles in Diesel Engines”. In: *Combustion and Flame* 17.3 (1971), pp. 409–419. DOI: 10.1016/S0010-2180(71)80064-0.

[55] S Brookes and J Moss. “Predictions of Soot and Thermal Radiation Properties in Confined Turbulent Jet Diffusion Flames”. In: *Combustion and Flame* 116.4 (Mar. 1999), pp. 486–503. DOI: 10.1016/S0010-2180(98)00056-X.

[56] A.C.Y. Yuen et al. “Comparison of Detailed Soot Formation Models for Sooty and Non-Sooty Flames in an under-Ventilated ISO Room”. In: *International Journal of Heat and Mass Transfer* 115 (Dec. 2017), pp. 717–729. DOI: 10.1016/j.ijheatmasstransfer.2017.08.074.

[57] Daniele L. Marchisio and Rodney O. Fox. *Computational Models for Polydisperse Particulate and Multiphase Systems*. Cambridge Series in Chemical Engineering. Cambridge ; New York: Cambridge University Press, 2013. ISBN: 978-0-521-85848-9.

[58] Steffen Salenbauch. “Modeling of Soot Formation and Oxidation in Reacting Flows”. PhD thesis. Technical University of Darmstadt, 2018.

[59] Sheldon K. Friedlander. *Smoke, Dust, and Haze: Fundamentals of Aerosol Dynamics*. 2nd ed. Topics in Chemical Engineering. New York: Oxford University Press, 2000. ISBN: 978-0-19-512999-1.

[60] Michael E Mueller. “LARGE EDDY SIMULATION OF SOOT EVOLUTION IN TURBULENT REACTING FLOWS”. PhD thesis. Stanford University, 2012.

[61] Fabian Mauss et al. “Soot Formation in Partially Premixed Diffusion Flames at Atmospheric Pressure”. In: *Soot Formation in Combustion*. Ed. by Vitalii I. Goldanskii et al. Vol. 59. Berlin, Heidelberg: Springer Berlin Heidelberg, 1994, pp. 325–349. ISBN: 978-3-642-85169-8 978-3-642-85167-4. DOI: 10.1007/978-3-642-85167-4_19.

[62] Daniele L. Marchisio and Antonello A. Barresi. “Investigation of Soot Formation in Turbulent Flames with a Pseudo-Bivariate Population Balance Model”. In: *Chemical Engineering Science* 64.2 (Jan. 2009), pp. 294–303. DOI: 10.1016/j.ces.2008.10.020.

[63] Fabrizio Bisetti et al. “On the Formation and Early Evolution of Soot in Turbulent Nonpremixed Flames”. In: *Combustion and Flame* 159.1 (Jan. 2012), pp. 317–335. DOI: 10.1016/j.combustflame.2011.05.021.

[64] Dongyue Li, Zhipeng Li, and Zhengming Gao. “Quadrature-Based Moment Methods for the Population Balance Equation: An Algorithm Review”. In: *Chinese Journal of Chemical Engineering* 27.3 (Mar. 2019), pp. 483–500. DOI: 10.1016/j.cjche.2018.11.028.

[65] M Balthasar and M Kraft. “A Stochastic Approach to Calculate the Particle Size Distribution Function of Soot Particles in Laminar Premixed Flames”. In: *Combustion and Flame* 133.3 (May 2003), pp. 289–298. DOI: 10.1016/S0010-2180(03)00003-8.

[66] Jasdeep Singh et al. “Stochastic Modeling of Soot Particle Size and Age Distributions in Laminar Premixed Flames”. In: *Proceedings of the Combustion Institute* 30.1 (Jan. 2005), pp. 1457–1465. DOI: 10.1016/j.proci.2004.08.120.

[67] Jasdeep Singh et al. “Numerical Simulation and Sensitivity Analysis of Detailed Soot Particle Size Distribution in Laminar Premixed Ethylene Flames”. In: *Combustion and Flame* 145.1-2 (Apr. 2006), pp. 117–127. DOI: 10.1016/j.combustflame.2005.11.003.

[68] Steffen Salenbauch et al. “Modeling Soot Formation in Premixed Flames Using an Extended Conditional Quadrature Method of Moments”. In: *Combustion and Flame* 162.6 (June 2015), pp. 2529–2543. DOI: 10.1016/j.combustflame.2015.03.002.

[69] M.E. Mueller, G. Blanquart, and H. Pitsch. “Hybrid Method of Moments for Modeling Soot Formation and Growth”. In: *Combustion and Flame* 156.6 (June 2009), pp. 1143–1155. DOI: 10.1016/j.combustflame.2009.01.025.

[70] Michael Edward Mueller, Guillaume Blanquart, and Heinz Pitsch. “A Joint Volume-Surface Model of Soot Aggregation with the Method of Moments”. In: *Proceedings of the Combustion Institute* 32.1 (2009), pp. 785–792. DOI: 10.1016/j.proci.2008.06.207.

[71] Achim Wick et al. “Modeling Soot Oxidation with the Extended Quadrature Method of Moments”. In: *Proceedings of the Combustion Institute* 36.1 (2017), pp. 789–797. DOI: 10.1016/j.proci.2016.08.004.

[72] C.S. McEnally et al. “Computational and Experimental Study of Soot Formation in a Coflow, Laminar Ethylene Diffusion Flame”. In: *Symposium (International) on Combustion* 27.1 (1998), pp. 1497–1505. DOI: 10.1016/S0082-0784(98)80557-2.

[73] Pedro Rodrigues et al. “Unsteady Dynamics of PAH and Soot Particles in Laminar Counterflow Diffusion Flames”. In: *Proceedings of the Combustion Institute* 36.1 (2017), pp. 927–934. DOI: 10.1016/j.proci.2016.07.047.

[74] Karl Netzell, Harry Lehtiniemi, and Fabian Mauss. “Calculating the Soot Particle Size Distribution Function in Turbulent Diffusion Flames Using a Sectional Method”. In: *Proceedings of the Combustion Institute* 31.1 (Jan. 2007), pp. 667–674. DOI: 10.1016/j.proci.2006.08.081.

[75] Robert McGraw. “Description of Aerosol Dynamics by the Quadrature Method of Moments”. In: *Aerosol Science and Technology* 27.2 (Jan. 1997), pp. 255–265. DOI: 10.1080/02786829708965471.

[76] C. Yuan, F. Laurent, and R.O. Fox. “An Extended Quadrature Method of Moments for Population Balance Equations”. In: *Journal of Aerosol Science* 51 (Sept. 2012), pp. 1–23. DOI: 10.1016/j.jaerosci.2012.04.003.

[77] Christophe Chalons et al. “Multivariate Gaussian Extended Quadrature Method of Moments for Turbulent Disperse Multiphase Flow”. In: *Multiscale Modeling & Simulation* 15.4 (Jan. 2017), pp. 1553–1583. DOI: 10.1137/16M109209X. arXiv: 1609.00139 [math].

[78] Janine Chungyin Cheng and Rodney O. Fox. “Kinetic Modeling of Nanoprecipitation Using CFD Coupled with a Population Balance”. In: *Industrial & Engineering Chemistry Research* 49.21 (Nov. 2010), pp. 10651–10662. DOI: 10.1021/ie100558n.

[79] C. Yuan and R.O. Fox. “Conditional Quadrature Method of Moments for Kinetic Equations”. In: *Journal of Computational Physics* 230.22 (Sept. 2011), pp. 8216–8246. DOI: 10.1016/j.jcp.2011.07.020.

[80] Daniele L. Marchisio and Rodney O. Fox. “Solution of Population Balance Equations Using the Direct Quadrature Method of Moments”. In: *Journal of Aerosol Science* 36.1 (Jan. 2005), pp. 43–73. DOI: 10.1016/j.jaerosci.2004.07.009.

[81] Steffen Salenbauch et al. “A Numerically Robust Method of Moments with Number Density Function Reconstruction and Its Application to Soot Formation, Growth and Oxidation”. In: *Journal of Aerosol Science* 128 (Feb. 2019), pp. 34–49. DOI: 10.1016/j.jaerosci.2018.11.009.

[82] Steffen Salenbauch et al. “Detailed Modeling of Soot Particle Formation and Comparison to Optical Diagnostics and Size Distribution Measurements in Premixed Flames Using a Method of Moments”. In: *Fuel* 222 (June 2018), pp. 287–293. DOI: 10.1016/j.fuel.2018.02.148.

[83] Federica Ferraro et al. “Soot Particle Size Distribution Reconstruction in a Turbulent Sooting Flame with the Split-Based Extended Quadrature Method of Moments”. In: *Physics of Fluids* 34.7 (July 2022), p. 075121. DOI: 10.1063/5.0098382.

[84] Philipp Koob et al. “Large Eddy Simulation of Soot Formation in a Real Aero-Engine Combustor Using Tabulated Chemistry and a Quadrature-based Method of Moments”. In: *Proceedings of ASME Turbo Expo 2023 (accepted)* (2023).

[85] Trupti Kathrotia et al. “Combustion Kinetics of Alternative Jet Fuels, Part-II: Reaction Model for Fuel Surrogate”. In: *Fuel* 302 (Oct. 2021), p. 120736. DOI: 10.1016/j.fuel.2021.120736.

[86] Andrea D’Anna, Mariano Sirignano, and John Kent. “A Model of Particle Nucleation in Premixed Ethylene Flames”. In: *Combustion and Flame* 157.11 (Nov. 2010), pp. 2106–2115. DOI: 10.1016/j.combustflame.2010.04.019.

[87] D. L. Baulch et al. “Evaluated Kinetic Data for Combustion Modelling”. In: *Journal of Physical and Chemical Reference Data* 21.3 (May 1992), pp. 411–734. DOI: 10.1063/1.555908.

[88] Shengkai Wang et al. “Reaction Rate Constant of $CH_2O + H = HCO + H_2$ Revisited: A Combined Study of Direct Shock Tube Measurement and Transition State Theory Calculation”. In: *The Journal of Physical Chemistry A* 118.44 (Nov. 2014), pp. 10201–10209. DOI: 10.1021/jp5085795.

[89] Z. F. Xu, P. Raghunath, and M. C. Lin. “Ab Initio Chemical Kinetics for the CH $_3$ + O(^{3} P) Reaction and Related Isomerization–Decomposition of CH $_3$ O and CH $_2$ OH Radicals”. In: *The Journal of Physical Chemistry A* 119.28 (July 2015), pp. 7404–7417. DOI: 10.1021/acs.jpca.5b00553.

[90] Gladson De Souza Machado et al. “Prediction of Rate Coefficients for the H $_2$ CO + OH → HCO + H $_2$ O Reaction at Combustion, Atmospheric and Interstellar Medium Conditions”. In: *The Journal of Physical Chemistry A* 124.11 (Mar. 2020), pp. 2309–2317. DOI: 10.1021/acs.jpca.9b11690.

[91] Shucheng Xu, R. S. Zhu, and M. C. Lin. “Ab Initio Study of the OH + CH2O Reaction: The Effect of the OH··OCH2 Complex on the H-abstraction Kinetics”. In: *International Journal of Chemical Kinetics* 38.5 (May 2006), pp. 322–326. DOI: 10.1002/kin.20166.

[92] Venkatesh Vasudevan, David F. Davidson, and Ronald K. Hanson. “Direct Measurements of the Reaction OH + CH2O ? HCO + H2O at High Temperatures”. In: *International Journal of Chemical Kinetics* 37.2 (Feb. 2005), pp. 98–109. DOI: 10.1002/kin.20056.

[93] Robert Schmitz et al. “Numerical and Experimental Investigations on the Particle Formation in Oxymethylene Ethers (OME n , n = 2-4)/Ethylene Premixed Flames”. In: *Fuel* 357 (Feb. 2024), p. 129762. DOI: 10.1016/j.fuel.2023.129762.

[94] Wenyu Sun et al. “Speciation and the Laminar Burning Velocities of Poly(Oxymethylene) Dimethyl Ether 3 (POMDME3) Flames: An Experimental and Modeling Study”. In: *Proceedings of the Combustion Institute* 36.1 (2017), pp. 1269–1278. DOI: 10.1016/j.proci.2016.05.058.

[95] Jakob Burger et al. “Poly(Oxymethylene) Dimethyl Ethers as Components of Tailored Diesel Fuel: Properties, Synthesis and Purification Concepts”. In: *Fuel* 89.11 (Nov. 2010), pp. 3315–3319. DOI: 10.1016/j.fuel.2010.05.014.

[96] *DIN EN 590:2022-05, Kraftstoffe_- Dieselkraftstoff_- Anforderungen Und Prüfverfahren; Deutsche Fassung EN_590:2022*. Tech. rep. Beuth Verlag GmbH. DOI: 10.31030/3337114.

[97] Diana Deutsch et al. “High Purity Oligomeric Oxymethylene Ethers as Diesel Fuels”. In: *Chemie Ingenieur Technik* 89.4 (Apr. 2017), pp. 486–489. DOI: 10.1002/cite.201600158.

[98] Zhi Wang et al. “Homogeneous Charge Compression Ignition (HCCI) Combustion of Polyoxymethylene Dimethyl Ethers (PODE)”. In: *Fuel* 183 (Nov. 2016), pp. 206–213. DOI: 10.1016/j.fuel.2016.06.033.

[99] Haoye Liu et al. “Recent Progress in the Application in Compression Ignition Engines and the Synthesis Technologies of Polyoxymethylene Dimethyl Ethers”. In: *Applied Energy* 233–234 (Jan. 2019), pp. 599–611. DOI: 10.1016/j.apenergy.2018.10.064.

[100] Philipp Demel and Christian Beidl. “CO $_2$ Neutral Fuels in Series Engines - Demonstration of the Potential of OME with Regard to Efficiency and Ultra-Low Emissions”. In: *15th International Conference on Engines & Vehicles*. Sept. 2021, pp. 2021-24–0061. DOI: 10.4271/2021-24-0061.

[101] Zhenbin Yang et al. “Theoretical Predictions of Compatibility of Polyoxymethylene Dimethyl Ethers with Diesel Fuels and Diesel Additives”. In: *Fuel* 307 (Jan. 2022), p. 121797. DOI: 10.1016/j.fuel.2021.121797.

[102] Ahmad Omari et al. “Potential of Long-Chain Oxymethylene Ether and Oxymethylene Ether-Diesel Blends for Ultra-Low Emission Engines”. In: *Applied Energy* 239 (Apr. 2019), pp. 1242–1249. DOI: 10.1016/j.apenergy.2019.02.035.

[103] Alexander D Gelner et al. “Ultra-Low Emissions of a Heavy-Duty Engine Powered with Oxymethylene Ethers (OME) under Stationary and Transient Driving Conditions”. In: *International Journal of Engine Research* 23.5 (May 2022), pp. 738–753. DOI: 10.1177/14680874211047922.

[104] Alexander D. Gelner et al. “Particle Emissions of a Heavy-Duty Engine Fueled with Polyoxymethylene Dimethyl Ethers (OME)”. In: *Environmental Science: Atmospheres* 2.2 (2022), pp. 291–304. DOI: 10.1039/D1EA00084E.

[105] Florian Zacherl et al. “Potential of the Synthetic Fuel Oxymethylene Ether (OME) for the Usage in a Single-Cylinder Non-Road Diesel Engine: Thermodynamics and Emissions”. In: *Energies* 15.21 (Oct. 2022), p. 7932. DOI: 10.3390/en15217932.

[106] Christophe Barro et al. “Neat Polyoxymethylene Dimethyl Ether in a Diesel Engine; Part 2: Exhaust Emission Analysis”. In: *Fuel* 234 (Dec. 2018), pp. 1414–1421. DOI: 10.1016/j.fuel.2018.07.108.

[107] Christophe Barro, Matteo Parravicini, and Konstantinos Boulouchos. “Neat Polyoxymethylene Dimethyl Ether in a Diesel Engine; Part 1: Detailed Combustion Analysis”. In: *Fuel* 256 (Nov. 2019), p. 115892. DOI: 10.1016/j.fuel.2019.115892.

[108] Shuojin Ren et al. “Development of a Reduced Polyoxymethylene Dimethyl Ethers (PODEn) Mechanism for Engine Applications”. In: *Fuel* 238 (Feb. 2019), pp. 208–224. DOI: 10.1016/j.fuel.2018.10.111.

[109] José M García-Oliver et al. “Numerical Analysis of the Combustion Process of Oxymethylene Ethers as Low-Carbon Fuels for Compression Ignition Engines”. In: *International Journal of Engine Research* 24.5 (May 2023), pp. 2175–2186. DOI: 10.1177/14680874221113749.

[110] Yanju Wei et al. “Numerical Optimization of the EGR Rate and Injection Timing with a Novel Cavitation Model in a Diesel Engine Fueled with PODE/Diesel Blends”. In: *Applied Sciences* 12.24 (Dec. 2022), p. 12556. DOI: 10.3390/app122412556.

[111] *International Sooting Flame Workshop*. https://www.adelaide.edu.au/cet/isfworkshop/home (visited on 12/04/2023). Feb. 2023.

[112] Yu Wang and Suk Ho Chung. “Strain Rate Effect on Sooting Characteristics in Laminar Counterflow Diffusion Flames”. In: *Combustion and Flame* 165 (Mar. 2016), pp. 433–444. DOI: 10.1016/j.combustflame.2015.12.028.

[113] Abhijit Kalbhor et al. “Experimental and Numerical Investigation on Soot Formation and Evolution of Particle Size Distribution in Laminar Counterflow Ethylene Flames”. In: *Combustion and Flame* 260 (Feb. 2024), p. 113220. DOI: 10.1016/j.combustflame.2023.113220.

[114] Lei Xu et al. “Experimental and Soot Modeling Studies of Ethylene Counterflow Diffusion Flames: Non-monotonic Influence of the Oxidizer Composition on Soot Formation”. In: *Combustion and Flame* 197 (Nov. 2018), pp. 304–318. DOI: 10.1016/j.combustflame.2018.08.011.

[115] Yiqing Wang et al. “A Systematic Analysis of Chemical Mechanisms for Ethylene Oxidation and PAH Formation”. In: *Combustion and Flame* 253 (July 2023), p. 112784. DOI: 10.1016/j.combustflame.2023.112784.

[116] Stephan Kruse et al. “Experimental and Numerical Study of Soot Formation in Counterflow Diffusion Flames of Gasoline Surrogate Components”. In: *Combustion and Flame* 210 (Dec. 2019), pp. 159–171. DOI: 10.1016/j.combustflame.2019.08.013.

[117] Fabian P. Hagen et al. “From Molecular to Sub-Mm Scale: The Interplay of Precursor Concentrations, Primary Particle Size, and Carbon Nanostructure during Soot Formation in Counter-Flow Diffusion Flames”. In: *Combustion and Flame* 258 (Dec. 2023), p. 112729. DOI: 10.1016/j.combustflame.2023.112729.

[118] Nina Gaiser et al. “Oxidation of Oxymethylene Ether (OME0-5): An Experimental Systematic Study by Mass Spectrometry and Photoelectron Photoion Coincidence Spectroscopy”. In: *Fuel* 313 (Apr. 2022), p. 122650. DOI: 10.1016/j.fuel.2021.122650.

[119] Zeyan Qiu et al. “An Experimental and Modeling Study on Polyoxymethylene Dimethyl Ether 3 (PODE3) Oxidation in a Jet Stirred Reactor”. In: *Fundamental Research* 2.5 (Sept. 2022), pp. 738–747. DOI: 10.1016/j.fmre.2021.09.005.

[120] Yann Fenard and Guillaume Vanhove. “A Mini-Review on the Advances in the Kinetic Understanding of the Combustion of Linear and Cyclic Oxymethylene Ethers”. In: *Energy & Fuels* 35.18 (Sept. 2021), pp. 14325–14342. DOI: 10.1021/acs.energyfuels.1c01924.

[121] C E Shannon. “A Mathematical Theory of Communication”. In: *The Bell System Technical Journal* 27 (July, October, 1948), pp. 379–423, 623–656.

[122] Lawrence R. Mead and N. Papanicolaou. “Maximum Entropy in the Problem of Moments”. In: *Journal of Mathematical Physics* 25.8 (Aug. 1984), pp. 2404–2417. DOI: 10.1063/1.526446.

[123] Steffen Salenbauch et al. “Detailed Particle Nucleation Modeling in a Sooting Ethylene Flame Using a Conditional Quadrature Method of Moments (CQMOM)”. In: *Proceedings of the Combustion Institute* 36.1 (2017), pp. 771–779. DOI: 10.1016/j.proci.2016.08.003.

[124] Yong Ren Tan et al. “Sooting Characteristics of Polyoxymethylene Dimethyl Ether Blends with Diesel in a Diffusion Flame”. In: *Fuel* 224 (July 2018), pp. 499–506. DOI: 10.1016/j.fuel.2018.03.051.

[125] *CC BY 4.0 Deed | Attribution 4.0 International | Creative Commons*. https://creativecommons.org/licenses/by/4.0/ (visited on 12/04/2023).

[126] Robert Schmitz et al. “Numerical Investigation on the Effect of the Oxymethylene Ether-3 (OME3) Blending Ratio in Premixed Sooting Ethylene Flames”. In: *Frontiers in Mechanical Engineering* 7 (Aug. 2021), p. 744172. DOI: 10.3389/fmech.2021.744172.

[127] Liz Allen, Alison O'Connell, and Veronique Kiermer. "How Can We Ensure Visibility and Diversity in Research Contributions? How the Contributor Role Taxonomy (CRediT) Is Helping the Shift from Authorship to Contributorship". In: *Learned Publishing* 32.1 (Jan. 2019), pp. 71–74. DOI: 10.1002/leap.1210.

[128] *Permissions | Elsevier Policy*. https://www.elsevier.com/about/policies-and-standards/copyright/permissions (visited on 12/04/2023).

[129] Robert Schmitz et al. "Effect of Oxymethylene Ether-2-3-4 (OME2-4) on Soot Particle Formation and Chemical Features". In: *Fuel* 324 (Sept. 2022), p. 124617. DOI: 10.1016/j.fuel.2022.124617.

[130] Federica Ferraro et al. "Experimental and Numerical Study on the Effect of Oxymethylene Ether-3 (OME3) on Soot Particle Formation". In: *Fuel* 286 (Feb. 2021), p. 119353. DOI: 10.1016/j.fuel.2020.119353.

Publications

List of publications

During my research time as a doctoral candidate at the institute Simulation of reactive Thermo-Fluid Systems (STFS) of the Technical University of Darmstadt (TUDa), I mainly investigated soot formation processes. The scientific findings lead to several publications (P), which are published in journals of an international audience and recognition. The catalog of publications created during my studies at the TUDa reads as follows:

Publications (first authorship)

- P1: **R. Schmitz**, M. Sirignano, C. Hasse, and F. Ferraro, "Numerical Investigation on the Effect of the Oxymethylene Ether-3 (OME_3) Blending Ratio in Premixed Sooting Ethylene Flames," Front. Mech. Eng., vol. 7, p. 744172, Aug. 2021, doi: 10.3389/fmech.2021.744172.
- P2: **R. Schmitz**, C. Russo, F. Ferraro, B. Apicella, C. Hasse, and M. Sirignano, "Effect of oxymethylene ether-2-3-4 (OME_{2-4}) on soot particle formation and chemical features," Fuel, vol. 324, p. 124617, Sep. 2022, doi: 10.1016/j.fuel.2022.124617.
- P3: **R. Schmitz**, F. Ferraro, M. Sirignano, and C. Hasse, "Numerical and experimental investigations on the particle formation in oxymethylene ethers (OME_n , n = 2-4)ethylene premixed flames," Fuel, vol. 357, p. 129762, Feb. 2024, doi: 10.1016/j.fuel.2023.129762.
- P4: A. Kalbhor*, **R. Schmitz***, A. Ramirez, P. Vlavakis, F. P. Hagen, F. Ferraro, M. Braun-Unkhoff, T. Kathrotia, U. Riedel, D. Trimis, J. van Oijen, C. Hasse, D. Mira„ "Experimental and numerical investigation on soot formation and evolution of particle size distribution in laminar counterflow ethylene flames," Combustion and Flame, vol. 260, p. 113220, Feb. 2024, doi: 10.1016/j.combustflame.2023.113220. *Joint first authors

Additional publication

- P5: F. Ferraro, C. Russo, **R. Schmitz**, C. Hasse, and M. Sirignano, "Experimental and numerical study on the effect of oxymethylene ether-3 (OME_3) on soot particle formation," Fuel, vol. 286, p. 119353, Feb. 2021, doi: 10.1016/j.fuel.2020.119353.

The publications P1-P5 are accepted by the doctoral committee of the Department of Mechanical Engineering (TUDa) for this dissertation.

P1 Front. Mech. Eng. 7 (2021), 744172

R. Schmitz, M. Sirignano, C. Hasse, and F. Ferraro, "Numerical Investigation on the Effect of the Oxymethylene Ether-3 (OME_3) Blending Ratio in Premixed Sooting Ethylene Flames," Front. Mech. Eng., vol. 7, p. 744172, Aug. 2021, doi: 10.3389/fmech.2021.744172.

Author contributions

Tab. P.1: Author contributions to publication [126] following CRediT [127]

Robert Martin Schmitz	Conceptualization of the numerical setup and investigations (equal) Conduction of detailed numerical simulations Interpretation and discussion of the numerical results (lead) Data analysis and visualization Writing – Original draft Main and corresponding author
Mariano Sirignano	Conceptualization of the investigations (equal) Interpretation and discussion of the numerical results (equal)
Christian Hasse	Conceptualization of the investigation (equal) Supervision (equal) Funding acquisition
Federica Ferraro	Conceptualization of the numerical setup and investigations (equal) Supervision (equal) Interpretation and discussion of the numerical results (equal)
All co-authors	Writing – Review & Editing

Use of publication contents in finalized and ongoing dissertations

This publication is part of the ongoing dissertation of Robert Martin Schmitz at the Institute for Simulation of reactive Thermo-Fluid Systems at the Technical University of Darmstadt, Germany.

frontiers in Mechanical Engineering

ORIGINAL RESEARCH
published: 27 August 2021
doi: 10.3389/fmech.2021.744172

Numerical Investigation on the Effect of the Oxymethylene Ether-3 (OME3) Blending Ratio in Premixed Sooting Ethylene Flames

Robert Schmitz[1]*, *Mariano Sirignano*[2], *Christian Hasse*[1] and *Federica Ferraro*[1]

[1]Institute for Simulation of Reactive Thermo-Fluid Systems (STFS), Technical University of Darmstadt, Darmstadt, Germany, [2]Dipartimento di Ingegneria Chimica, dei Materiali e della Produzione Industriale, Università degli Studi di Napoli Federico II, Napoli, Italy

OPEN ACCESS

Edited by:
Raul Payri,
Universitat Politècnica de València, Spain

Reviewed by:
Vasudevan Raghavan,
Indian Institute of Technology Madras, India
Dong Han,
Shanghai Jiao Tong University, China
Chun Lou,
Huazhong University of Science and Technology, China

***Correspondence:**
Robert Schmitz
schmitz@stfs.tu-darmstadt.de

Specialty section:
This article was submitted to Engine and Automotive Engineering, a section of the journal Frontiers in Mechanical Engineering

Received: 19 July 2021
Accepted: 16 August 2021
Published: 27 August 2021

Citation:
Schmitz R, Sirignano M, Hasse C and Ferraro F (2021) Numerical Investigation on the Effect of the Oxymethylene Ether-3 (OME3) Blending Ratio in Premixed Sooting Ethylene Flames. Front. Mech. Eng 7:744172. doi: 10.3389/fmech.2021.744172

Synthetic fuels, especially oxygenated fuels, which can be used as blending components, make it possible to modify the emission properties of conventional fossil fuels. Among oxygenated fuels, one promising candidate is oxymethylene ether-3 (OME_3). In this work, the sooting propensity of ethylene (C_2H_4) blended with OME_3 is numerically investigated on a series of laminar burner-stabilized premixed flames with increasing amounts of OME_3, from pure ethylene to pure OME_3. The numerical analysis is performed using the Conditional Quadrature Method of Moments combined with a detailed physico-chemical soot model. Two different equivalence ratios corresponding to a lightly and a highly sooting flame condition have been investigated. The study examines how different blending ratios of the two fuels affect soot particle formation and a correlation between OME_3 blending ratio and corresponding soot reduction is established. The soot precursor species in the gas-phase are analyzed along with the soot volume fraction of small nanoparticles and large aggregates. Furthermore, the influence of the OME_3 blending on the particle size distribution is studied applying the entropy maximization concept. The effect of increasing amounts of OME_3 is found to be different for soot nanoparticles and larger aggregates. While OME_3 blending significantly reduces the amount of larger aggregates, only large amounts of OME_3, close to pure OME_3, lead to a considerable suppression of nanoparticles formed throughout the flame. A linear correlation is identified between the OME_3 content in the fuel and the reduction in the soot volume fraction of larger aggregates, while smaller blending ratios may lead to an increased number of nanoparticles for some positions in the flame for the richer flame condition.

Keywords: oxymethylene ether-3 (OME3), PODE3, soot particle formation, soot modeling, alternative fuels, Quadrature Method of Moments (QMOM)

1 INTRODUCTION

The ongoing tightening of emissions legislation is resulting in increasingly vigorous efforts to control the pollutants formed in hydrocarbon combustion systems in the transportation and power generation sectors. Synthetic fuels produced with renewable energy and, in particular, oxygenated fuels can improve both the overall carbon balance and local emissions, such as soot particles, without extensively modifying the present combustion devices. Oxymethylene ethers

(OMEs), which are promising synthetic fuel candidates (Kohse-Höinghaus, 2021), deployable e.g. in self-ignition engines, have been proven in recent studies (Ferraro et al., 2021; Tan et al., 2021) to significantly reduce the sooting tendency of blended fuel flames. Compared to other alternative and oxygenated fuel candidates such as biodiesels and alcohols, oxymethylene ethers combine high oxygenation of around 50% by mass (Wang et al., 2016) with high propensity for self-ignition (Lumpp et al., 2011; Wang et al., 2016). While the combustion of pure OMEs exhibits almost the complete suppression of soot, an application as a blending fuel is a more realistically viable scenario in the short and medium term. The good miscibility of oxymethylene ethers in fossil diesel (Lin et al., 2019; Omari et al., 2019) supports this scenario. OME_3 to OME_5 in particular exhibit properties favourable to their use as fuel blends in compression ignition applications. For instance, the cetane number of OME_3 to OME_5 is in the range of 72–93 (Lautenschütz et al., 2016; 2017; Deutsch et al., 2017) and the flash, boiling and melting points are comparable to those of diesel fuel (Zheng et al., 2013; Omari et al., 2019). These suitable characteristics explain the recent research interest in this specific group of oxygenated fuels in the field of kinetic mechanism development (Sun et al., 2017; He et al., 2018; Cai et al., 2019; Li et al., 2020; Bai et al., 2021; Niu et al., 2021), their application in engine simulations (Lin et al., 2019; Lv et al., 2019; Ren et al., 2019) or for different synthesis methods (Gierlich et al., 2020; Klokic et al., 2020), and the assessment of the overall carbon impact (Mahbub et al., 2019; Bokinge et al., 2020). The application of oxymethylene ethers in engines in combination with their emission propensity has been investigated in several studies (Pellegrini et al., 2013; Barro et al., 2018; Huang et al., 2018; Liu et al., 2019; Ren et al., 2019; LeBlanc et al., 2020; Parravicini et al., 2020; Pélerin et al., 2020), while fewer investigations have been conducted, notably, into soot formation for pure or blended OMEs in canonical flames (Ferraro et al., 2021; Tan et al., 2021). Hence, this work addresses the potential of oxymethylene ether-3 (OME_3) and its effect on soot particle formation and growth to deeply understand the soot suppression phenomenon in a simple configuration and in blending with a well-known fuel such as ethylene. While studies containing small amounts of OME_3 blended into C_2H_4 have been performed for both premixed flames (Ferraro et al., 2021) and diffusion flames (Tan et al., 2021), the effects of blending increased amounts of OME_3 has not been investigated yet. Additionally, a systematic assessment between the blending ratio of OME_n fuels and their effects on the overall soot reduction and especially on the individual maturation steps in the soot evolution process is unknown to the authors. Detailed knowledge of the soot reduction potential including possible saturation effects for higher blending ratios is needed for an efficient application of synthetic fuels. Therefore, this study aims to analyze these aspects for OME_3 combustion. The correlation between the OME_3 blending ratio and the soot reduction will be numerically investigated. The analysis systematically evaluates the complete range of OME_3 blending ratios using detailed chemistry combined with a quadrivariate soot model enabling a deeper understanding of the effects of different amounts of OME_3 blending on the entire soot formation process.

Simulations are performed on a series of laminar burner-stabilized premixed flames burning ethylene blended with increasing amounts of OME_3 up to a pure OME_3/air flame at constant equivalence ratios. Detailed chemical kinetics in combination with the Conditional Quadrature Method of Moments (CQMOM) (Salenbauch et al., 2017, 2018), based on the physico-chemical soot model by D'Anna et al. (2010), are chosen to model soot formation, particle surface growth and other occurring particle processes. This approach enables a detailed investigation of the soot suppression behavior of OME_3 regarding the smaller carbon chemistry, and of different particle size classes, such as large polycyclic aromatic hydrocarbons, spherical clusters and larger aggregates including their chemical properties. The effect that increasing amounts of OME_3 exert on soot formation is evaluated in terms of both the total soot volume fraction and the particle size distribution. Additionally, the relationship between the OME_3 to ethylene blending ratio and the subsequent soot reduction is analyzed to verify whether OME_3 has only a dilution effect on the mixture or if it also has an active kinetic effect in the formation of soot gas-phase precursors, nano-organic carbon and soot particles. Finally, the range of OME_3 blending ratios yielding a soot suppression effect is identified to assess the overall potential of this oxygenated fuel. This study is performed for two different equivalence ratios covering lightly to highly sooting flame conditions.

2 NUMERICAL MODELING

The numerical modeling includes a description of the gas-phase chemistry and of the soot particle formation and evolution. The gas-phase chemistry is modeled by a detailed kinetic mechanism accounting for 141 species and 674 reactions in total. The decomposition and oxidation reactions of OME_3 (41 species and 213 reactions) are taken from Sun et al. (2017). The reactions of smaller and larger carbon species up to polycyclic aromatic hydrocarbons (PAHs) are described by the kinetic mechanism by D'Anna et al. (2010), Sirignano et al. (2010, 2013), and Conturso et al. (2017).

To describe the soot particle evolution, the physico-chemical soot formation model (D'Anna et al., 2010) is combined with the Conditional Quadrature Method of Moments. The numerical approach was developed in Salenbauch et al. (2017) and has been successfully applied in atmospheric premixed flames (Salenbauch et al., 2017, 2018; Ferraro et al., 2021). A short summary is described in the following. The gas-phase kinetics consider species up to pyrene, while larger PAHs are treated as lumped species. The soot model distinguishes between three different particle structures based on their state of aggregation (D'Anna et al., 2010). Soot precursors with a molecular mass larger than pyrene (*molecules or large PAHs*) are classified separately from the spherically shaped, solid soot particles which are formed through the inception step of several PAHs (*clusters*), and *aggregates*. These in turn are formed due to the agglomeration of several clusters with subsequent soot maturation steps leading

to strongly bonded fractal-shaped particles. The physico-chemical nature of the soot model allows an assessment to be carried out based not only on the size and shape of the particles but also on their chemical properties such as the carbon to hydrogen ratio and their chemical reactivity. The soot processes are formulated based on Arrhenius-rate laws and include growth processes such as the H-Abstraction-C_2H_2-Addition (HACA) mechanism, the resonantly stabilized free radical mechanism or surface growth due to chemical processes. Surface growth and oxidation reactions are applied for all the three entities that describe the soot evolution such as large PAH, clusters and aggregates. Additionally, nucleation steps for different-sized large PAHs are accounted for, resulting in clusters with varying chemical properties as well as soot oxidation and oxidation-induced fragmentation, dehydrogenation and aggregation processes of several clusters, resulting in aggregates shaped like snowflakes, fractals or chains.

Due to the variety of the soot particles involved, classification and bundling similar to lumped species is necessary. The evolution of the chemical and physical properties of each particle class is described by the population balance equation (PBE) for the number density function (NDF) $f(\underline{\xi}; \underline{x}, t)$, which depends on the spatial coordinates $\underline{x}$, the time information t and the internal property vector $\underline{\xi} = [\xi_{nc}, \xi_{H/C}, \xi_{stat}, \xi_{typ}]^T$. This vector contains two continuous properties ξ_{nc}, indicating the number of carbon atoms with $\xi_{nc} \in [0, \infty)$, and $\xi_{H/C}$ describing the carbon to hydrogen ratio with $\xi_{H/C} \in [0, 1]$. ξ_{typ} and ξ_{stat} are discrete dimensions representing the type of entities $\xi_{typ} \in A$, $A = \{large\ PAHs, clusters, aggregates\}$, and ξ_{stat} the chemical reactivity with $\xi_{stat} \in B$, $B = \{stable, radical\}$. Applying Bayes's decomposition, the quadrivariate number density function $f(\underline{\xi}; \underline{x}, t)$ reads as follows

$$f(\underline{\xi}) = f_{H/C}\left(\xi_{H/C}|\xi_{nc}, \xi_{stat}, \xi_{typ}\right) \cdot f_{nc}\left(\xi_{nc}|\xi_{stat}, \xi_{typ}\right) \cdot n\left(\xi_{stat}, \xi_{typ}\right), \tag{1}$$

where the time and spatial dependencies are omitted for brevity.

Here, the distributions $f_{H/C}$ and f_{nc} are conditioned on the state $(\xi_{nc}, \xi_{stat}, \xi_{typ})$ and (ξ_{stat}, ξ_{typ}), respectively. The joint bivariate distribution $n(\xi_{stat}, \xi_{typ})$ can have only six values for the different possible combinations (u, v) of the two discrete particle properties $\xi_{stat} = \xi_{stat,u}$ and $\xi_{typ} = \xi_{typ,v}$. The reader may be referred to Salenbauch (2018) for further details. This simplification can be exploited in combination with the conditional density function definition to transform **Eq. 1** into a system of six bivariate NDFs $\Pi_{(u,v)}$

$$\Pi_{(u,v)}(\xi_{nc}, \xi_{H/C}) = f^{u,v}_{H/C}(\xi_{H/C}|\xi_{nc}) \cdot f^{u,v}_{nc}(\xi_{nc}) \cdot n_{u,v}, \tag{2}$$

in which the conditional distribution $f^{u,v}_{H/C}(\xi_{H/C}|\xi_{nc})$ and the marginal distribution $f^{u,v}_{nc}(\xi_{nc})$ are evaluated for each of the six combinations of (u, v).

The set of NDFs is not solved directly but only for a set of its statistical moments closed with the CQMOM approach. In this work, for all six combinations (u, v) two quadrature nodes are used for the internal coordinate ξ_{nc} and a single quadrature node for $\xi_{H/C}$ conditioned on ξ_{nc}. The system of six bivariate NDFs is therefore represented by 36 additional moment transport equations. The numerical calculations have been performed with the in-house universal Laminar Flame (ULF) solver (Zschutschke et al., 2017), which includes the QMOM library (Salenbauch, 2018). The conservation equations for each individual species in the gas-phase and the equations of the moments representing the solid-phase are solved using a segregated approach. Small PAH species, from benzene to pyrene, and the species involved in the surface growth, oxidation and dehydrogenation reactions (H, OH, H_2, H_2O, C_2H_2, HCO, CO, O_2) are required for the calculation of the soot moments and their gas-phase chemistry is coupled with the soot chemistry. Herein, constant species and temperature fields are applied when evaluating the soot moments, while a constant set of moments and species consumption rate due to soot processes are employed when solving for the gas-phase. Coupling of the equations is ensured by iteratively solving and updating both sets of equations until convergence is reached. Due to the stiffness of the system of equations, a pseudo-time step procedure is applied to solve the one-dimensional stationary flame to ensure numerical stability. Additionally, the spatial coordinate of the one-dimensional flame can be transformed into a residence time (Blanquart, 2008; Salenbauch, 2018) allowing to solve the set of moment equations in terms of a homogeneous zero-dimensional reactor prescribing the species fields and thermophysical properties of the gas-phase in dependence of the residence time.

The CQMOM method does not provide access to the PSD information but it reconstructs the moments of the NDF using weighted Dirac-delta functions. Following Salenbauch et al. (2018), the entropy maximization (EM) concept is used here in post-processing to evaluate a continuous distribution of the particle sizes from a given number of moments, without prescribing the distribution shape. The idea from Mead and Papanicolaou (1984) is to find a univariate continuous distribution function $f(\xi_1)$ that maximizes the entropy (Shannon, 1948) $H(f)$, being ξ_1 the internal coordinate

$$H(f) = -\int_{\Omega_{\xi_1}} f(\xi_1) \ln\left(f(\xi_1)\right) \mathrm{d}\xi_1. \tag{3}$$

Mead and Papanicolaou (1984) formulated the entropy for the unknown distribution function using Lagrangian multipliers and specified the moment set as constraints. This allows an explicit expression of the distribution function, which can be iteratively calculated by searching for its maximum. Further details on the numerical approach can be found in Salenbauch et al. (2017, 2018) and references therein.

3 INVESTIGATED FLAMES

In this section, the numerical setup and the investigated flames are described. A burner-stabilized flat flame is employed in this work. The flame configuration is adopted from previous experimental studies (Salamanca et al., 2012; Sirignano et al., 2014; Conturso et al., 2017; Russo et al., 2019; Ferraro et al., 2021) which used a capillary burner with an inner diameter of 5.8 cm

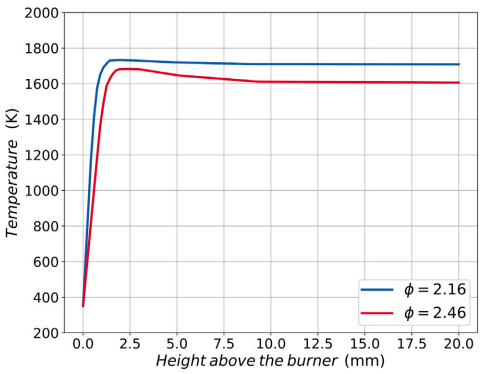

FIGURE 1 | Prescribed temperature profiles as a function of the height above the burner for the two different investigated equivalence ratios $\phi = 2.16$ and $\phi = 2.46$. Profiles adapted from Russo et al. (2019) for pure ethylene flames.

including a stainless steel plate located 30 mm above the burner exit for flame stabilization. The combustion parameters are kept constant in both sets of flames investigated, varying only the blending ratio of OME_3 and ethylene. Laminar, premixed conditions at atmospheric pressure and a cold gas velocity of 0.1 m/s are considered, allowing a one-dimensional simulation approach. Two equivalence ratios, $\phi = 2.16$ and $\phi = 2.46$, are investigated based on neat ethylene flames investigated in a previous study (Ferraro et al., 2021), representing lightly and highly sooting conditions. More specifically, for neat ethylene fuel, the flame at $\phi = 2.16$ presents minor formation of soot aggregates, while the flame at $\phi = 2.46$ presents a significant amount of soot aggregate and a distinct bimodality of the PSD.

Temperature profiles experimentally measured in Russo et al. (2019) for the pure ethylene flames at corresponding equivalence ratios, are prescribed for all the simulations and are plotted in **Figure 1**. As with other alternative fuels (Conturso et al., 2017), the effect that adding smaller amounts of OME_3 up to 30% exerts on the flame temperature is assumed to be insignificant, while major effects are expected when higher percentages are used. Here, this procedure is adopted to separate the thermal effects of OME_3 blending from the chemical effects in the numerical simulations.

The mixture compositions at the inlet of the flames are stated in **Table 1**. Fuel compositions are investigated ranging from pure ethylene up to pure OME_3 with intermediate blending steps. The fuel is blended by keeping the overall carbon stream constant for all flames, while the relative amount of carbon atoms provided as OME_3 compared to the overall carbon fed to the flame is specified in the table. The oxygen (O_2) stream is adapted to match the equivalence ratios of $\phi = 2.16$ and $\phi = 2.46$. The fuel and oxygen streams are diluted with nitrogen (N_2) which is adapted to ensure there is an identical cold gas velocity in all the flames. Since the combustion parameters are kept constant for all flames in this study, all the changes regarding the soot formation can be

TABLE 1 | Inflow mixture compositions of the investigated flames. Entries for 15 to 90 $\%_{carbon}$ of OME_3 blending are omitted for brevity.

ϕ	OME_3 blending ratio	Inflow composition in mole fractions			
	in $\%_{carbon}$	C_2H_4	O_2	N_2	OME_3
	0	0.131	0.182	0.686	0.000
	5	0.125	0.181	0.692	0.003
	10	0.118	0.179	0.698	0.005
2.16	5% steps	...	...	...	...
	95	0.007	0.148	0.796	0.050
	100	0.000	0.146	0.802	0.053
	0	0.147	0.179	0.674	0.000
	5	0.140	0.177	0.680	0.003
	10	0.132	0.176	0.686	0.006
2.46	5% steps	...	...	...	...
	95	0.007	0.145	0.792	0.056
	100	0.000	0.143	0.798	0.059

associated with the difference in the fuel composition and fuel structure. While a previous study Ferraro et al. (2021) compared the numerical model against experimental data, this study extends the variation of the investigated parameters and sets its focus on the blending ratio between OME_3 and C_2H_4 using the same modeling approach. In Ferraro et al. (2021), the soot reduction trends of OME_3 observed in the experiments on flames with different equivalence ratios have been well captured by the numerical method. Additionally, this burner configuration has been employed to evaluate several oxygenated fuels and their sooting characteristics (Salamanca et al., 2012; Sirignano et al., 2014; Conturso et al., 2017; Russo et al., 2019), enabling cross-comparisons to be made.

4 RESULTS AND DISCUSSION

4.1 Gas-phase

In this section, the simulation results for the gas-phase are first analyzed. **Figure 2** shows the species mole fraction profiles for C_2H_2 and C_6H_6 based on the example of two different blending ratios of pure ethylene and 50% OME_3 blending ratio with equivalence ratios of $\phi = 2.16$ in **Figure 2A** and $\phi = 2.46$ in **Figure 2B**. It is observed that 50% OME_3 blending significantly reduces the mole fraction profiles of C_2H_2 and C_6H_6 for both equivalence ratios. In the OME_3 blended flame, both species are reduced by a factor of approximately 40–50% compared to the pure ethylene flame. Additionally, the shape of the C_6H_6 profile changes in the richer flame configuration since the peak visible in the pure ethylene flame vanishes with 50% OME_3 blending.

To investigate the whole range of blending ratios, only the maximum values of the species profiles are considered in the following. In **Figure 3** the maximum value of the calculated mole fraction profiles for acetylene (C_2H_2), benzene (C_6H_6), naphthalene ($C_{10}H_8$) and pyrene ($C_{16}H_{10}$) are plotted against increasing amounts of OME_3 blended into the ethylene flame for both equivalence ratios, $\phi = 2.16$ and $\phi = 2.46$. These species have been selected because of their important role in particle inception

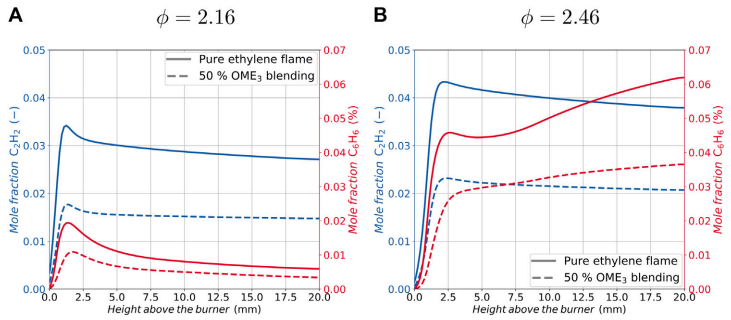

FIGURE 2 | Species mole fraction profiles of acetylene (C_2H_2, blue lines) and benzene (C_6H_6, red lines) as a function of the height above the burner with an equivalence ratio of ϕ = 2.16 **(A)** and ϕ = 2.46 **(B)** for pure ethylene flames (solid lines) and 50% OME_3 blending ratio (dashed lines).

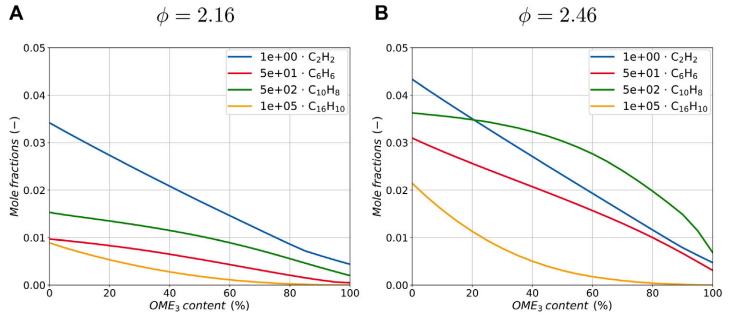

FIGURE 3 | Maximum peak of species mole fractions in the flame with an equivalence ratio of ϕ = 2.16 **(A)** and ϕ = 2.46 **(B)** for different OME_3 blending ratios. The peak values of the aromatic species C_6H_6, $C_{10}H_8$ and $C_{16}H_{10}$ are scaled by the factors of 5.0e1, 5.0e2 and 1.0e5 for better clarity.

and surface growth processes. Since the evolution of larger PAHs is accounted for by the statistical soot model as described above, here only small aromatic species are plotted for both flame configurations. Acetylene can be formed from ethylene by thermal decomposition through the cleavage of two hydrogen atoms within only a few reactions, thus resulting in higher mole fractions of acetylene with increasing amounts of ethylene in the fuel. OME_3 by contrast, does not feature direct single or double carbon-to-carbon bonds in the molecule and there is no direct pathway from OME_3 forming alkenes (He et al., 2018). This results in lower mole fractions of acetylene due to OME_3 blending in both flame configurations and overall higher quantities of acetylene in the richer flame. Following C_2H_2 profiles, aromatic species are also reduced with OME_3 blending. Comparing the results for the two equivalence ratios, it can be observed that the absolute amount of C_2H_2 does not change significantly, while the flame at an equivalence ratio ϕ = 2.16 lacks aromatic species. Therefore, it is assumed that the soot formation in the richer flame is mainly dominated by surface growth through the HACA mechanism, while the soot formation in the leaner flame is mainly limited by the initial inception step and therefore by the amount of PAH formation.

4.2 Soot Formation

Following previous works (Salenbauch et al., 2017, 2018; Ferraro et al., 2021), the simulated PSD obtained with CQMOM and EM is split in a post-processing step to account for nanoparticles with diameters $d_p < d_{p,split}$ and aggregates with diameters $d_p > d_{p,split}$. The separation between nanoparticles and aggregates allows a more detailed analysis of the blending effect on the formation of incipient young soot particles and larger soot particles. To lower the sensitivity of this splitting diameter $d_{p,split}$, the calculations are performed for $d_{p,split}$ = 2 nm and for $d_{p,split}$ = 7 nm, but only the average of the two quantities is plotted in the following graphs for better clarity.

Figure 4 shows the soot volume fraction over the height above the burner for different blending ratios of OME_3 for both equivalence ratios, ϕ = 2.16 (left) and ϕ = 2.46 (right). The soot volume fraction of smaller nanoparticles is plotted in the two upper graphs (**Figures 4A,B**), while the soot volume fraction

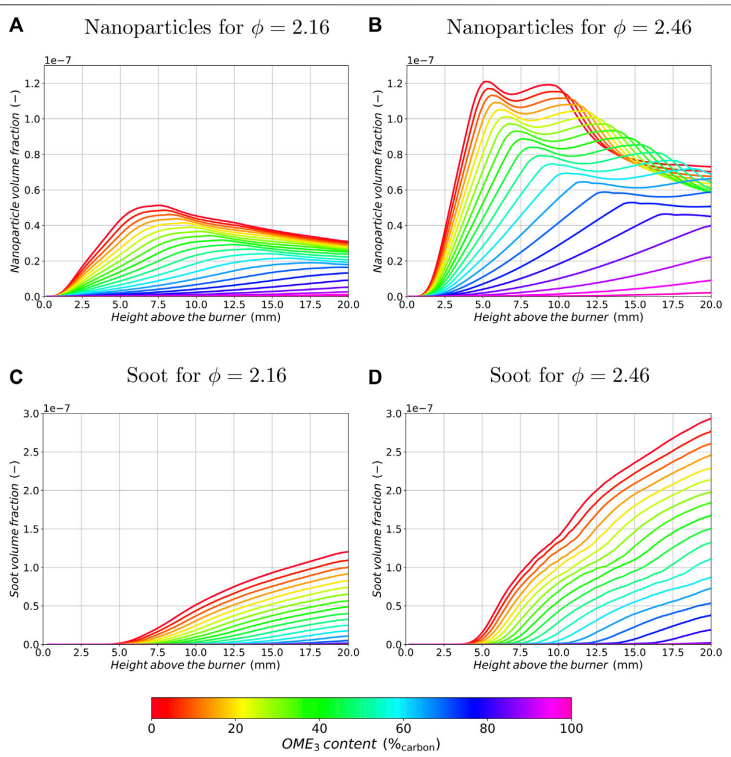

FIGURE 4 | Nanoparticle **(A,B)** and soot **(C,D)** volume fraction profiles as a function of the height above the burner for different OME_3 blending ratios and equivalence ratios of ϕ = 2.16 **(A,C)** and ϕ = 2.46 **(B,D)**.

originating from larger soot aggregates is visualized in the lower ones (**Figures 4C,D**). It can be observed that the nanoparticle volume fraction in **Figures 4A,B** increases rapidly for the pure ethylene flame until a maximum is reached at HAB = 5 mm to HAB = 7 mm depending on the equivalence ratio. Starting from HAB = 7 mm in the leaner and HAB = 10 mm in the richer flame, the particle growth becomes predominant over the inception processes resulting in a decreasing nanoparticle volume fraction further downstream in the flame. With increasing OME_3 blending in the fuel, the initial nanoparticle volume fraction decreases and the position of the peak value is shifted downstream. For HAB >10 mm, even a small increase in the nanoparticle volume fraction can be observed for OME_3 blending in the richer condition, which is consistent with the findings in (Ferraro et al., 2021). For instance, OME_3 blending results in a slightly increased amount of nanoparticles at HAB = 12.5 mm in **Figure 4B** for blending ratios between 0 and 50% OME_3. Overall, the formation of nanoparticles is slowed down with OME_3 blending until no significant nanoparticle formation can be identified for pure OME_3 combustion. The amount of nanoparticles formed in the flames follows the amount of soot precursors such as PAHs and C_2H_2 formed in the gas-phase according to the above findings.

A plateau of the nanoparticle volume fraction can be identified in the richer configuration between HAB = 5 mm and HAB = 10 mm, whereas the leaner configuration exhibits a single peak with a monotonic reduction in nanoparticle volume fraction for HAB > 7.5 mm for the pure ethylene flame. Closer investigation of the richer configuration shows that the plateau with the two peaks for smaller OME_3 blending ratios can not be explained by a single soot process alone, but is the result of coexisting soot processes. Nucleation and surface growth reactions are competing against coagulation and aggregation mechanisms in this flame region. The species profile of C_6H_6 in **Figure 2B** suggests that a significant amount of PAH species is present in this region of the flame, resulting in a high nucleation rate not only close to the flame sheet at approx. HAB = 2 mm but also further downstream. **Figure 2A** shows a single peak of C_6H_6 with a monotonic reduction until the end of the domain for the leaner flame configuration indicating that

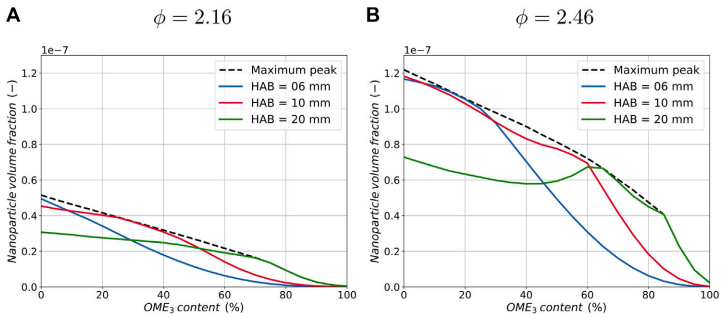

FIGURE 5 | Correlation between nanoparticle volume fraction and blending ratio of OME_3 for three different positions in the flame and the maximum peak in the flame for an equivalence ratio of ϕ = 2.16 **(A)** and ϕ = 2.46 **(B)**.

nucleation is predominant close to the flame sheet and plays a limited role in the post-flame zone, where condensation followed by coagulation and aggregation contribute to the soot evolution.

Furthermore, in **Figures 4C,D** it can be seen that the position where aggregates start to form is shifted downstream with increasing OME_3 blending ratios and the volume fraction of large particles is significantly decreased at both equivalence ratios. Therefore, OME_3 blending results in a monotonically decreasing amount of aggregates. The slowing down of the particle formation processes follows the decrease and delay of nanoparticle formation and is also similar to other biofuels such as ethanol or dimethyl ether (Salamanca et al., 2012; Sirignano et al., 2014).

Figure 5 shows the correlation between the nanoparticle volume fraction and the OME_3 content in the fuel for three different positions in the flame for both equivalence ratios. Additionally, the maximum value of the nanoparticle volume fraction of the whole flame is added in the graphs, which allows the results to be analyzed regardless of the position in the flame.

At a position of HAB = 6 mm and HAB = 10 mm, the nanoparticle volume fraction evolves similarly for both equivalence ratio flames. It is monotonically reduced with increasing OME_3 blending ratios. In contrast, at a position of HAB = 20 mm, a non-monotonic evolution of the nanoparticle reduction with increasing blending ratios can be observed in the richer flame configuration, while the leaner flame configuration exhibits no substantial change unless high blending ratios close to neat OME_3 are burnt. Here, no substantial change in nanoparticle volume fraction can be identified for OME_3 contents between 0% and approximately 70% for both equivalence ratios. Further increasing the OME_3 content reduces the nanoparticle volume fraction again. Comparing the three curves of the different positions in the flames for both equivalence ratios, they are all seen to share a flat gradient for smaller blending ratios and a steep decline in nanoparticle volume fraction for increasing blending ratios at increased HABs. These results indicate that even if the nanoparticles decrease locally, the number of nanoparticles downstream along the flame does not decrease substantially, so the particle formation is slowed down. Additionally, the maximum peak of nanoparticles in the flame indicates that a significant reduction in the amount of nanoparticles, equivalent to a larger gradient of the maximum peak, can only be obtained for larger blending ratios. A monotonic reduction in the maximum peak can be observed in both flames, with a rapid drop for blending ratios larger than approximately 70% OME_3 blending. This effect is true for both configurations, whereas the overall reduction in nanoparticles due to OME_3 blending is larger in the richer configuration. Meanwhile, only a small reduction can be observed in the lean configuration for the same OME_3 percentages.

Figure 6 shows the soot volume fraction originating from large aggregates over the OME_3 blending ratio of three locations along both flame configurations. At all three positions in the flame, OME_3 blending reduces the formation of aggregates until a complete suppression is observed for a specific flame position in both flame configurations. The quantitative correlation between the amount of OME_3 in the fuel and soot volume fraction is approximately linear in the case of the rich flame configuration in **Figure 6B**. Additionally, the gradient of the three curves changes for the different positions in the flame, resulting in a larger soot reduction further downstream in the flame when the same amount of OME_3 is added. For soot (large particles and aggregates), there is a direct correlation with the C_2H_2 concentration, since surface growth plays a dominant role at the investigated equivalence ratio of ϕ = 2.46.

At the lower equivalence ratio, **Figure 6A**, a decreasing aggregate reduction effect can be observed with increasing amounts of OME_3 blending. This results in slightly regressively declining soot volume fraction slopes compared to the almost linear behavior of the rich conditions. This is thought to be due to the leaner conditions, in which nucleation is one of the limiting factors in the soot formation process. Therefore, the shape of the curves follows the shape of larger PAHs such as pyrene and is less heavily influenced by surface growth reactions of C_2H_2. Overall, both configurations show a significant reduction in soot aggregates for OME_3 blending with a monotonic effect for all ratios throughout the flame.

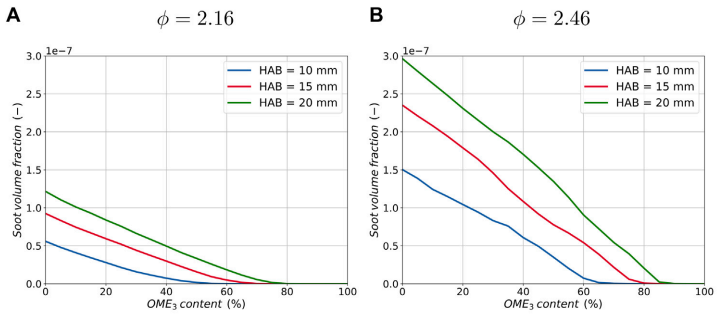

FIGURE 6 | Correlation between soot volume fraction and the blending ratio of OME_3 for three different positions in the flame and for an equivalence ratio of $\phi = 2.16$ **(A)** and $\phi = 2.46$ **(B)**.

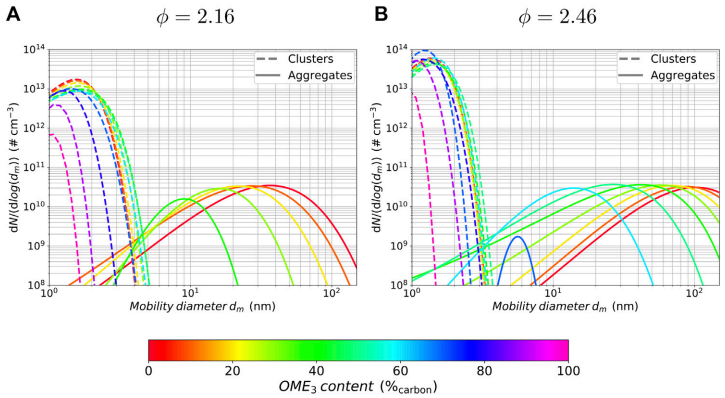

FIGURE 7 | Particle size distributions of clusters and aggregates at a flame position of HAB = 20 mm for different OME_3 blending ratios and equivalence ratios of $\phi = 2.16$ **(A)** and $\phi = 2.46$ **(B)**.

To evaluate the effect of different OME_3 blending ratios on the particle sizes and their distribution, **Figure 7** shows the particle size distribution (PSD) that is obtained by the entropy maximization process at HAB = 20 mm. Blending steps with $10\%_{carbon}$ are used and larger PAHs are omitted to enhance readability. A distinction is made between spherical clusters and fractal-shaped aggregates, which are plotted over the mobility diameter d_m. The mobility diameter d_m considers the fractal-like shape of larger soot aggregates in contrast to the spherical diameter d_p, which assumes a purely spherical particle. The mobility diameter is derived from the collision diameter d_c with $d_m \equiv d_c = d_p(n_p)^{1/D_f}$ (Kruis et al., 1993). A fractal dimension D_f equal to 1.8 and a primary particle diameter of d_p = 15 nm are applied and the number of primary particles n_p is derived from the mass ratio of an aggregate and the corresponding primary particles. This procedure, previously used in (Ferraro et al., 2021), is applied here to allow for a consistent comparison with our previous studies. Note that the selected parameters are comparable with the common values used in the literature (Kruis et al., 1993).

It can be seen that the distribution of the particle clusters is not substantially changed for an OME_3 blending ratio between 0 and 60% in both flame configurations. Further increasing the OME_3 content for the rich condition results in a higher number of particles with smaller diameters, and further on, in a significant decrease in the number and size of the clusters for conditions close to neat OME_3 combustion, while no such large intermediate increase in the number of clusters is visible in the leaner flame configuration of $\phi = 2.16$ in **Figure 7A**. This difference is consistent with the findings of the nanoparticle volume fraction in **Figures 4A,B** at a height of HAB = 15 mm, in which the leaner flame configuration shows a monotonic decrease of nanoparticle volume fraction with increasing OME_3 blending, whereas the

richer configuration exhibits a non-monotonic behaviour with an intermediate increase in nanoparticle volume fraction. Similar non-monotonic behavior was found previously for premixed propene flames blended with ethylene (Lin et al., 2018), in which small amounts of ethylene addition led to an intermediate increase in soot formation while larger amounts decreased the amount of soot. It was found that this effect is due to a synergistic effect of the two fuels by the acetylene addition and propargyl recombination/addition pathways (Lin et al., 2018).

The distribution of aggregates in the richer configuration in **Figure 7B** indicates that there are significant changes regarding the overall number and particle diameter with an increasing OME_3 content. A considerable amount of aggregate formation occurs for OME_3 blending ratios of ≤ 70%, while higher contents of OME_3 in the fuel delay the soot formation and suppress aggregate formation to a negligible level. The distribution function therefore changes from a bimodal to a unimodal shape. While the number of aggregates differs only slightly in the range of 60–0% OME_3, with a maximum at approximately 50% OME_3, the size of the particles changes significantly from an average mobility diameter of approx. 15 nm to 100 nm. For blending percentages above 60%, the number of aggregates is additionally reduced. In contrast to that, the aggregates show a simultaneous reduction in number and diameter even for small blending ratios of OME_3 in the leaner flame configuration, with a suppression to negligible levels for blending ratios of above 40% OME_3.

Further investigations at upstream positions in the flame show that the PSD changes its shape, from bimodal to unimodal, for lower levels of the OME_3 blending ratio.

5 CONCLUSION

A numerical study is performed simulating two series of laminar premixed burner-stabilized flames burning a mixture of C_2H_4 and OME_3 for two equivalence ratios, corresponding to highly and lightly sooting flame conditions. The sets cover flames with increasing blending ratios of OME_3 reaching from pure ethylene to pure OME_3 at a constant equivalence ratio and identical carbon streams. The soot precursors in the gas-phase, soot formation and PSD are analyzed using a detailed physico-chemical soot model.

The effects of OME_3 blending are found to be different for nanoparticles compared to larger aggregates. While the formation of larger aggregates is approximately linearly reduced for increasing amounts of OME_3 throughout the flame, the nanoparticle formation shows a non-monotonic correlation to the blending ratio and is mainly suppressed for higher amounts of OME_3, similarly to the combustion of pure OME_3.

The particle size distribution is reconstructed with the concept of entropy maximization at a fixed height above the burner of HAB = 20 mm. A substantially unchanged distribution of clusters for OME_3 blending ratios between approximately 0 and 60% and a decreasing number of particles for higher blending percentages can be identified for both equivalence ratios with a slight, intermediate increase in the particle number for the richer flame condition at around 70% OME_3 in the fuel, whereas the leaner configuration shows a monotonic reduction in the particle number. While the number of aggregates in the richer configuration is not significantly affected by smaller amounts of OME_3 blending, their particle size is mainly reduced, but a simultaneous reduction in the particle number and particle diameter is observed for the leaner configuration at this position in the flame.

These findings indicate that OME_3 blending mainly delays the soot formation processes and, as a consequence, suppresses the formation of larger aggregates at a specific position in the flame. This is due to the absence of direct carbon-to-carbon bonds in OME_3, which leads to a more complete oxidation process and therefore subtracts carbon from the soot growth pathways. The linear correlation for aggregate reduction suggests a predominant dilution effect rather than an active kinetic effect.

DATA AVAILABILITY STATEMENT

The raw data supporting the conclusion of this article will be made available by the authors, without undue reservation.

AUTHOR CONTRIBUTIONS

RS, MS and FF contributed to conceptualization, writing - review and editing. CH contributed to conceptualization, review - editing and funding acquisition.

FUNDING

The authors gratefully acknowledge the funding by the German Federal Ministry of Education and Research (BMBF) as part of the NAMOSYN Project (project number 03SF0566R0).

REFERENCES

Bai, J., Geeson, R., Farazi, F., Mosbach, S., Akroyd, J., Bringley, E. J., et al. (2021). Automated Calibration of a Poly(oxymethylene) Dimethyl Ether Oxidation Mechanism Using the Knowledge Graph Technology. *J. Chem. Inf. Model.* 4, 1701–1717. doi:10.1021/acs.jcim.0c01322

Barro, C., Parravicini, M., Boulouchos, K., and Liati, A. (2018). Neat polyoxymethylene dimethyl ether in a diesel engine; part 2: Exhaust emission analysis. *Fuel* 234, 1414–1421. doi:10.1016/j.fuel.2018.07.108

Blanquart, G. G. (2008). *Chemical and Statistical Soot modeling*. California: Ph.D. thesis, Stanford University.

Bokinge, P., Heyne, S., and Harvey, S. (2020). Renewable OME from biomass and electricity-Evaluating carbon footprint and energy performance. *Energy Sci. Eng.* 8, 2587–2598. doi:10.1002/ese3.687

Cai, L., Jacobs, S., Langer, R., vom Lehn, F., Heufer, K. A., and Pitsch, H. (2020). Auto-ignition of oxymethylene ethers (OMEn, n = 2-4) as promising synthetic e-fuels from renewable electricity: shock tube experiments and automatic mechanism generation. *Fuel* 264, 116711. doi:10.1016/j.fuel.2019.116711

Conturso, M., Sirignano, M., and D'Anna, A. (2017). Effect of 2,5-dimethylfuran doping on particle size distributions measured in premixed ethylene/air flames. *Proc. Combustion Inst.* 36, 985–992. doi:10.1016/j.proci.2016.06.048

D'Anna, A., Sirignano, M., and Kent, J. (2010). A model of particle nucleation in premixed ethylene flames. *Combust. Flame* 157, 2106–2115. doi:10.1016/j.combustflame.2010.04.019

Deutsch, D., Oestreich, D., Lautenschütz, L., Haltenort, P., Arnold, U., and Sauer, J. (2017). High Purity Oligomeric Oxymethylene Ethers as Diesel Fuels. *Chem. Ingenieur Technik* 89, 486–489. doi:10.1002/cite.201600158

Ferraro, F., Russo, C., Schmitz, R., Hasse, C., and Sirignano, M. (2021). Experimental and numerical study on the effect of oxymethylene ether-3 (OME3) on soot particle formation. *Fuel* 286, 119353. doi:10.1016/j.fuel.2020.119353

Gierlich, C. H., Beydoun, K., Klankermayer, J., and Palkovits, R. (2020). Challenges and Opportunities in the Production of Oxymethylene Dimethylether. *Chem. Ingenieur Technik* 92, 116–124. doi:10.1002/cite.201900187

He, T., Wang, Z., You, X., Liu, H., Wang, Y., Li, X., et al. (2018). A chemical kinetic mechanism for the low- and intermediate-temperature combustion of Polyoxymethylene Dimethyl Ether 3 (PODE3). *Fuel* 212, 223–235. doi:10.1016/j.fuel.2017.09.080

Huang, H., Liu, Q., Teng, W., Pan, M., Liu, C., and Wang, Q. (2018). Improvement of combustion performance and emissions in diesel engines by fueling n-butanol/diesel/PODE3-4 mixtures. *Appl. Energ.* 227, 38–48. doi:10.1016/j.apenergy.2017.09.088

Klokic, S., Hochegger, M., Schober, S., and Mittelbach, M. (2020). Investigations on an efficient and environmentally benign poly(oxymethylene) dimethyl ether (OME3-5) fuel synthesis. *Renew. Energ.* 147, 2151–2159. doi:10.1016/j.renene.2019.10.004

Kohse-Höinghaus, K. (2021). Combustion in the future: The importance of chemistry. *Proc. Combustion Inst.* 38, 1–56. doi:10.1016/j.proci.2020.06.375

Kruis, F. E., Kusters, K. A., Pratsinis, S. E., and Scarlett, B. (1993). A Simple Model for the Evolution of the Characteristics of Aggregate Particles Undergoing Coagulation and Sintering. *Aerosol Sci. Tech.* 19, 514–526. doi:10.1080/02786829308959656

Lautenschütz, L., Oestreich, D., Seidenspinner, P., Arnold, U., Dinjus, E., and Sauer, J. (2016). Physico-chemical properties and fuel characteristics of oxymethylene dialkyl ethers. *Fuel* 173, 129–137. doi:10.1016/j.fuel.2016.01.060

LeBlanc, S., Sandhu, N., Yu, X., Han, X., Wang, M., Tjong, J., et al. (2020). "An Investigation Into OME3 on a High Compression Ratio Engine,"in ASME 2020 Internal Combustion Engine Division Fall Technical Conference. Internal Combustion Engine Division Fall Technical Conference. doi:10.1115/ICEF2020-2983 Available at: https://asmedigitalcollection.asme.org/ICEF/proceedings-pdf/ICEF2020/84034/V001T02A007/6603497/v001t02a007-icef2020-2983.pdf

Li, R., Herreros, J. M., Tsolakis, A., and Yang, W. (2020). Chemical kinetic study on ignition and flame characteristic of polyoxymethylene dimethyl ether 3 (PODE3). *Fuel* 279, 118423. doi:10.1016/j.fuel.2020.118423

Lin, B., Gu, H., Ni, H., Guan, B., Li, Z., Han, D., et al. (2018). Effect of mixing methane, ethane, propane and ethylene on the soot particle size distribution in a premixed propene flame. *Combustion and Flame* 193, 54–60. doi:10.1016/j.combustflame.2018.03.002

Lin, Q., Tay, K. L., Zhou, D., and Yang, W. (2019). Development of a compact and robust Polyoxymethylene Dimethyl Ether 3 reaction mechanism for internal combustion engines. *Energ. Convers. Manag.* 185, 35–43. doi:10.1016/j.enconman.2019.02.007

Liu, H., Wang, Z., Li, Y., Zheng, Y., He, T., and Wang, J. (2019). Recent progress in the application in compression ignition engines and the synthesis technologies of polyoxymethylene dimethyl ethers. *Appl. Energ.* 233-234, 599–611. doi:10.1016/j.apenergy.2018.10.064

Lumpp, B., Rothe, D., Pastötter, C., Lämmermann, R., and Jacob, E. (2011). Oxymethylene Ethers as Diesel Fuel Additives of the Future. *MTZ Worldw* 72, 34–38. doi:10.1365/s38313-011-0027-z

Lv, D., Chen, Y., Chen, Y., Guo, X., Chen, H., and Huang, H. (2019). Development of a reduced diesel/PODEn mechanism for diesel engine application. *Energ. Convers. Manag.* 199, 112070. doi:10.1016/j.enconman.2019.112070

Mahbub, N., Oyedun, A. O., Zhang, H., Kumar, A., and Poganietz, W.-R. (2019). A life cycle sustainability assessment (LCSA) of oxymethylene ether as a diesel additive produced from forest biomass. *Int. J. Life Cycle Assess.* 24, 881–899. doi:10.1007/s11367-018-1529-6

Mead, L. R., and Papanicolaou, N. (1984). Maximum entropy in the problem of moments. *J. Math. Phys.* 25, 2404–2417. doi:10.1063/1.526446

Niu, B., Jia, M., Chang, Y., Duan, H., Dong, X., and Wang, P. (2021). Construction of reduced oxidation mechanisms of polyoxymethylene dimethyl ethers (PODE1-6) with consistent structure using decoupling methodology and reaction rate rule. *Combustion and Flame* 232, 111534. doi:10.1016/j.combustflame.2021.111534

Omari, A., Heuser, B., Pischinger, S., and Rüdinger, C. (2019). Potential of long-chain oxymethylene ether and oxymethylene ether-diesel blends for ultra-low emission engines. *Appl. Energ.* 239, 1242–1249. doi:10.1016/j.apenergy.2019.02.035

Parravicini, M., Barro, C., and Boulouchos, K. (2020). Compensation for the differences in LHV of diesel-OME blends by using injector nozzles with different number of holes: Emissions and combustion. *Fuel* 259, 116166. doi:10.1016/j.fuel.2019.116166

Pélerin, D., Gaukel, K., Härtl, M., Jacob, E., and Wachtmeister, G. (2020). Potentials to simplify the engine system using the alternative diesel fuels oxymethylene ether OME1 and OME3–6 on a heavy-duty engine. *Fuel* 259, 116231. doi:10.1016/j.fuel.2019.116231

Pellegrini, L., Marchionna, M., Patrini, R., and Florio, S. (2013). "Emission performance of neat and blended polyoxymethylene dimethyl ethers in an old light-duty diesel car,"in *SAE 2013 World Congress & Exhibition* SAE International 2, 1–12. doi:10.4271/2013-01-1035

Ren, S., Wang, Z., Li, B., Liu, H., and Wang, J. (2019). Development of a reduced polyoxymethylene dimethyl ethers (PODEn) mechanism for engine applications. *Fuel* 238, 208–224. doi:10.1016/j.fuel.2018.10.111

Russo, C., D'Anna, A., Ciajolo, A., and Sirignano, M. (2019). The effect of butanol isomers on the formation of carbon particulate matter in fuel-rich premixed ethylene flames. *Combustion and Flame* 199, 122–130. doi:10.1016/j.combustflame.2018.10.025

Salamanca, M., Sirignano, M., Commodo, M., Minutolo, P., and D'Anna, A. (2012). The effect of ethanol on the particle size distributions in ethylene premixed flames. *Exp. Therm. Fluid Sci.* 43, 71–75. doi:10.1016/j.expthermflusci.2012.04.006

Salenbauch, S. (2018). *Modeling of Soot Formation and Oxidation in Reacting Flows*. TU Darmstadt: Ph.D. thesis.

Salenbauch, S., Sirignano, M., Marchisio, D. L., Pollack, M., D'Anna, A., and Hasse, C. (2017). Detailed particle nucleation modeling in a sooting ethylene flame using a Conditional Quadrature Method of Moments (CQMOM). *Proc. Combustion Inst.* 36, 771–779. doi:10.1016/j.proci.2016.08.003

Salenbauch, S., Sirignano, M., Pollack, M., D'Anna, A., and Hasse, C. (2018). Detailed modeling of soot particle formation and comparison to optical diagnostics and size distribution measurements in premixed flames using a method of moments. *Fuel* 222, 287–293. doi:10.1016/j.fuel.2018.02.148

Shannon, C. E. (1948). A Mathematical Theory of Communication. *Bell Syst. Tech. J.* 27, 379–423. doi:10.1002/j.1538-7305.1948.tb01338.x

Sirignano, M., Kent, J., and D'Anna, A. (2010). Detailed modeling of size distribution functions and hydrogen content in combustion-formed particles. *Combustion and Flame* 157, 1211–1219. doi:10.1016/j.combustflame.2009.11.014

Sirignano, M., Kent, J., and D'Anna, A. (2013). Modeling formation and oxidation of soot in nonpremixed flames. *Energy Fuels* 27, 2303–2315. doi:10.1021/ef400057r

Sirignano, M., Salamanca, M., and D'Anna, A. (2014). The role of dimethyl ether as substituent to ethylene on particulate formation in premixed and counter-flow diffusion flames. *Fuel* 126, 256–262. doi:10.1016/j.fuel.2014.02.039

Sun, W., Wang, G., Li, S., Zhang, R., Yang, B., Yang, J., et al. (2017). Speciation and the laminar burning velocities of poly(oxymethylene) dimethyl ether 3 (POMDME3) flames: An experimental and modeling study. *Proc. Combustion Inst.* 36, 1269–1278. doi:10.1016/j.proci.2016.05.058

Tan, Y. R., Salamanca, M., Pascazio, L., Akroyd, J., and Kraft, M. (2021). The effect of poly(oxymethylene) dimethyl ethers (PODE3) on soot formation in ethylene/PODE3 laminar coflow diffusion flames. *Fuel* 283, 118769. doi:10.1016/j.fuel.2020.118769

Wang, Z., Liu, H., Ma, X., Wang, J., Shuai, S., and Reitz, R. D. (2016). Homogeneous charge compression ignition (HCCI) combustion of

polyoxymethylene dimethyl ethers (PODE). *Fuel* 183, 206–213. doi:10.1016/j.fuel.2016.06.033

Zheng, Y., Tang, Q., Wang, T., Liao, Y., and Wang, J. (2013). Synthesis of a green fuel additive over cation resins. *Chem. Eng. Technol.* 36, 1951–1956. doi:10.1002/ceat.201300360

Zschutschke, A., Messig, D., Scholtissek, A., and Hasse, C. (2017). *Universal Laminar Flame Solver (ULF)* Freiberg. Available at: https://figshare.com/articles/ULF_code_pdf/5119855.

Conflict of Interest: The authors declare that the research was conducted in the absence of any commercial or financial relationships that could be construed as a potential conflict of interest.

Publisher's Note: All claims expressed in this article are solely those of the authors and do not necessarily represent those of their affiliated organizations, or those of the publisher, the editors and the reviewers. Any product that may be evaluated in this article, or claim that may be made by its manufacturer, is not guaranteed or endorsed by the publisher.

P2 Fuel 324 (2022), 124617

R. Schmitz, C. Russo, F. Ferraro, B. Apicella, C. Hasse, and M. Sirignano, "Effect of oxymethylene ether-2-3-4 (OME_{2-4}) on soot particle formation and chemical features," Fuel, vol. 324, p. 124617, Sep. 2022, doi: 10.1016/j.fuel.2022.124617.

As the author of this Elsevier article, I retain the right to include this article in this manuscript [128]. The original source is available under the digital object identifier above.

Author contributions

Tab. P.2: Author contributions to publication [129] following CRediT [127]

Robert Martin Schmitz	Conceptualization of the numerical setup and investigations (equal) Conduction of detailed numerical simulations Interpretation and discussion of the numerical results (lead) Data curation Data analysis and visualization (equal) Writing – Original draft Main author
Carmela Russo	Conduction of experimental investigations (equal) Interpretation and discussion of the experimental results (equal) Corresponding author
Federica Ferraro	Conceptualization of the numerical setup and investigations (equal) Supervision (equal) Interpretation and discussion of the numerical results (support) Interpretation and discussion of the experimental results (equal)
Barbara Apicella	Conduction of experimental investigation (equal) Interpretation and discussion of the experimental results (equal) Data analysis and visualization (equal)
Christian Hasse	Conceptualization of the numerical setup and investigations (equal) Supervision (equal) Funding acquisition
Mariano Sirignano	Conceptualization of the investigations (equal) Conceptualization of the design of experiments Interpretation and discussion of the numerical results (support)
All co-authors	Writing – Review & Editing

Use of publication contents in finalized and ongoing dissertations

This publication is part of the ongoing dissertation of Robert Martin Schmitz at the Institute for Simulation of reactive Thermo-Fluid Systems at the Technical University of Darmstadt, Germany.

Fuel 324 (2022) 124617

Contents lists available at ScienceDirect

Fuel

journal homepage: www.elsevier.com/locate/fuel

Full Length Article

Effect of oxymethylene ether-2-3-4 (OME_{2-4}) on soot particle formation and chemical features

Robert Schmitz [a,1], Carmela Russo [b,*,1], Federica Ferraro [a], Barbara Apicella [b], Christian Hasse [a], Mariano Sirignano [c]

[a] Institute for Simulation of Reactive Thermo-Fluid Systems (STFS), Technische Universität Darmstadt, Otto-Berndt-Straße 2, Darmstadt 64287, Germany
[b] Istituto di Scienze e Tecnologie per l'Energia e la Mobilità Sostenibili (STEMS)– CNR – P.le V. Tecchio 80, 80125 Napoli, Italy
[c] Dipartimento di Ingegneria Chimica, dei Materiali e della Produzione Industriale – Università degli Studi di Napoli Federico II, P.le Tecchio 80, 80125 Napoli, Italy

ARTICLE INFO

Keywords:
Oxymethylene ether-2–3-4 (OME_{2-4})
Biofuels
Soot
Premixed flames
Quadrature Method of Moments (QMOM)
Soot nanostructure

ABSTRACT

The reduction of carbon emissions is leading to alternative and renewable energy sources. Solar or wind sources can only be regulated to a limited extent and fluctuate considerably due to environmental conditions, which could be overcome by chemical energy storage solutions.

Synthetic fuels are chemical energy carriers that can be produced using excess renewable electrical energy and can be directly used or easily stored. Different synthetic fuels have been investigated recently as a potential alternative or additive for fossil diesel and gasoline. Of the synthetic fuels, oxymethylene ethers (OMEs) have proven to be suitable candidates for compression-ignition engines while additionally reducing soot emissions when used either as a neat fuel or blended with fossil fuels. However, the effect of varying OME chain length on this soot reduction effect and the structure of the particulate matter has not yet been systematically investigated.

This study therefore compares the soot reduction potential and analyzes the physicochemical particle features in laminar premixed flames fueled with pure ethylene and ethylene/OME_{2-4} flames at four equivalence ratios, from lightly to heavily sooting conditions. Particle size distribution (PSD) measurements and numerical investigations (Conditional Quadrature Method of Moments—CQMOM) were conducted to study particle formation and growth. The results indicate a reduction in the total number and size of particles at all equivalence ratios, while the number of nanoparticles remains almost unchanged. The CQMOM model predicts the general shape of the experimentally measured PSD for both ethylene and OME-blended flames. Further, carbon particulate matter was thermophoretically sampled and its chemical structure was analyzed. The nanostructure of soot was investigated using ultraviolet–visible and Raman spectroscopy, revealing slightly higher aromaticity for the pure ethylene soot, whereas OME_{2-4} particles exhibited increased reactivity, as evidenced by thermogravimetric analysis. Fourier-Transform Infrared (FTIR) spectroscopy analysis showed that carbon particulate matter produced from OME_{2-4}-doped flames contained higher amounts of oxygen, mainly as C = O. Mass spectrometry confirmed the presence of oxygen-containing functional groups in OME_{2-4} particulate only.

1. Introduction

The search for clean and, where possible, net-carbon-free sources of energy has pushed research towards renewable and alternative sources such as the sun or wind. However, one of the common issues with renewable sources is the intrinsic intermittency of their availability and/or the energy production process [1,2]. Hence, besides the pursuit of finding a clean source of energy, ongoing research is investigating different alternatives for energy storage. In addition to batteries and other traditional energy storage systems, one of the most interesting and promising possibilities involves the usage of chemical storage. This process would involve storing the energy produced with solar cells, wind, hydroelectric or other renewable sources in chemical energy carriers [3] that can be produced locally, close to the energy source. Having been distributed to places with a high energy demand, the energy could be released in a controlled manner when required. Hydrogen

* Corresponding author at: Istituto di Scienze e Tecnologie per l'Energia e la Mobilità Sostenibili (STEMS) – CNR – P.le V. Tecchio, 80 – 80125 Napoli, Italy.
E-mail address: carmela.russo@stems.cnr.it (C. Russo).
[1] Joint first authors.

https://doi.org/10.1016/j.fuel.2022.124617
Received 25 February 2022; Received in revised form 28 April 2022; Accepted 13 May 2022
Available online 21 May 2022

is one of the most promising sustainable chemical energy carriers. It can be produced directly from water hydrolysis, and some of the infrastructure used for other gaseous compounds such as methane can be retrofitted for its use, in terms of both transportation and energy conversion systems. However, the risks linked with hydrogen are considerably high, thus a new method has been explored that includes hydrogen as a starting point for chemical energy storage. The e-fuels are liquid hydrocarbons that can be produced on the basis of hydrogen (and other renewable feedstocks) [4,5]. Their role could become crucial in the near future, first as they can be used in almost all the present energy conversion systems and secondly as they can even be produced using CO_2 captured from other energy conversion systems working with carbon-based fuels [6–9].

Oxymethylene ethers (OMEs), also known as polyoxymethylene dimethyl ethers (PODEs), have the chemical formula $CH_3O(CH2O)_nCH_3$, with n indicating the length of the chain in the abbreviation OME_n. They have proven to be promising candidates for chemical storage. As well as being produced on the basis of renewable sources, they can also be synthesized using methanol from waste biomass at market prices [10–14]. They are non-toxic and miscible with diesel fuel and thus can be part of a carbon–neutral combustion process, both as additives or substitutes in diesel engines [10,15]. Similarly to other biofuels, OMEs have a high oxygen content, but interestingly they do not contain any C–C bonds. This latter aspect is highly important for reducing the formation of undesired carbon byproducts, including small hydrocarbons, PAHs, and carbonaceous particles [10].

The effect of OMEs has been already investigated in compression ignition engines, revealing a reduction in the emission of gases including CO, CO_2, and NO_x — as well as particles [16–20].

The development of reduced and detailed kinetic mechanisms is currently limited to smaller OMEs such as $OME_{1\text{-}3}$ [10,21–23] and $OME_{2\text{-}4}$ [24], with validation based on experimental data obtained for the ignition delay time [10,24–26] and laminar flame speed [22,27].

However, some of the compounds belonging to the homologous OME series have proven more suitable for direct application in present energy conversion systems when used as an additive rather than as a fuel alternative. OME_1 and OME_2 have a cetane number that is too low (24 and 64 [28] respectively) to be selected as a fuel additive and a flash point below the ambient temperature [28], which increases the risk associated with their use. By contrast, OME_4 seems to have physical features that make it harder to use (melting point above − 10 °C and boiling point above 202 °C [28]). OME_3 was identified as a perfect candidate as a fuel additive. Another key point that needs to be considered is the OME production process. Several synthesis routes have been investigated in terms of economic or ecological criteria [14] and each favors a different OME composition in the blendstock formed. This composition of the blendstock can be partially changed by manipulating the synthesis route.

Recently, several studies have been published on OME fuel sooting propensity and on the particulate emission of OME/fuel blends in general [29–31].

We recently focused our attention on OME_3 [29,30], experimentally and numerically studying its effect on particulate emissions in premixed flames. In this study, we extend the investigation to include OME_2 and OME_4, concentrating on two aspects:

1. clarifying whether there is a significant advantage in terms of particle emissions in using OME_3 compared with OME_2 and OME_4,
2. determining whether there is a similarity in the chemical features of the soot particles produced with the different OMEs that may be generically linked with the fuel structure.

Experimental investigations include ex-situ measurements of the particle size distribution (PSD) and the characterization of particulate in terms of composition and nanostructure utilizing UV–Visible (UV–Vis), Raman, and Fourier-Transform Infrared (FTIR) spectroscopy, thermogravimetric analysis, and mass spectrometry. Simulations are performed with the detailed physicochemical soot model proposed by D'Anna et al. [32,33] integrated into a conditional quadrature-based method of moments (CQMOM) approach [34,35]. $OME_{1\text{-}3}$ gas-phase kinetics from Sun et al. [22] have been included to account for the fuel-specific oxidation reactions. The kinetic mechanism has recently been extended to include OME_4 for the conditions investigated [36]. Following [35], PSDs have been reconstructed in this work, using the entropy maximization approach on a suitably selected set of transported moments.

Table 1
Flame conditions. Inflow mixture composition is given in mole fraction. Inlet gas velocity @STP = 10 cm/s.

φ	Species	Fuel composition in terms of carbon provided by each fuel			
		100 % C_2H_4	20 % OME_2 + 80 % C_2H_4	20 % OME_3 + 80 % C_2H_4	20 % OME_4 + 80 % C_2H_4
2.01	C_2H_4	0.1234	0.0987	0.0987	0.0987
	O_2	0.1841	0.1780	0.1767	0.1759
	N_2	0.6925	0.7110	0.7147	0.7172
	OME_n	0	0.0123	0.0099	0.0082
2.16	C_2H_4	0.1313	0.1051	0.1051	0.1051
	O_2	0.1824	0.1763	0.1751	0.1743
	N_2	0.6862	0.7055	0.7093	0.7119
	OME_n	0	0.0131	0.0105	0.0088
2.31	C_2H_4	0.1392	0.1114	0.1114	0.1114
	O_2	0.1808	0.1747	0.1735	0.1727
	N_2	0.6800	0.7000	0.704	0.7066
	OME_n	0	0.0139	0.0111	0.0093
2.46	C_2H_4	0.1469	0.1175	0.1175	0.1175
	O_2	0.1792	0.1732	0.172	0.1712
	N_2	0.6739	0.6949	0.6987	0.7015
	OME_n	0	0.0147	0.0118	0.0098

2. Experimental setup

The experimental setup proposed in this work has been used to study other alternative fuels such as butanols [37], furans [38], ethanol [39], dimethyl ether [40], and most recently OME_3 [30]. Details of the experimental setup can be found in previous papers and are reported briefly here. Atmospheric pressure, premixed ethylene/air flames with equivalence ratios, φ, equal to 2.01, 2.16, 2.31, and 2.46, which represent lightly to heavily sooting conditions, are stabilized on a capillary burner [41]. These flames are the reference cases for studying the effect of $OME_{2\text{-}4}$ blending on soot particle formation and growth. $OME_{2\text{-}4}$ was added by replacing some of the ethylene (20 % of the total carbon) fed to the reference ethylene/air flames. The combustion conditions investigated in this work are reported in Table 1.

PSDs were measured by sampling from the flames at a height above the burner (HAB) of = 15 mm where soot reaches steady properties using a horizontal probe [42–47] with an inner diameter of ID = 1.2 mm, a wall thickness of 0.5 mm, and a pinhole diameter of 0.8 mm. A two-stage dilution system with 3 Nl/min (at 273 K) for the first dilution stage and 45 Nl/min for the second stage guaranteed an overall dilution of 350; enough to achieve critical dilution conditions. A nano-DMA (TapCon 3/150 Differential Mobility Analyzer with a nominal size range of 2–100 nm, equipped with a Faraday cup electrometer) fitted with a Soft X-Ray Advanced Aerosol Neutralizer (TSI model 3088) was used to detect particles. The PSDs obtained with the DMA were corrected for losses in the pinhole and the probe following the procedure reported in the literature [48–50] and the particle diameter was determined using the correlation proposed by Singh et al. [51]. PSD uncertainty derives from the evaluation of the wall losses and the coagulation of the small particles onto the large ones in the probing system.

Particles were also collected on a 75 × 25 × 1 mm glass plate arranged horizontally, following a consolidated procedure for mass

collection for batch analysis, i.e. multiple insertions 2 s into the flame and successively cooled at room temperature for 10 s [52,53]. The physiochemical analysis was carried out on carbon particulate matter collected at 15 mm HAB and $\varphi = 2.46$ in the pure ethylene and ethylene/OME flames.

Samples deposited on the glass plate were analyzed by Raman spectroscopy using a Horiba XploRA Raman microscope system (Horiba Jobin Yvon, Japan) equipped with a frequency-doubled Nd:YAG solid-state laser ($\lambda = 532$ nm). For each flame condition, four glass plates covered by carbon particulate matter were analyzed by means of Raman spectroscopy. For each glass plate, two spectra were acquired within an investigated sample area of 2 cm^2. To perform other diagnostic techniques, it was necessary to gently remove the samples from the glass plates with a laboratory spatula. Carbon particulate matter samples were mixed and ground to make KBr pellets (0.2–0.3 wt%) and analyzed by FTIR spectroscopy in the 3400–600 cm^{-1} range using a Nicolet iS10 spectrophotometer. Carbon samples were dissolved in N-methyl-2-pyrrolidinone (NMP, with a concentration of 10 mg/L) and analyzed using UV–Vis spectroscopy in a quartz cuvette with a 1-cm path length using an Agilent UV–Vis 8453 spectrophotometer. Thermogravimetric analysis (TGA) was also performed with a PerkinElmer Pyris 1 thermogravimetric analyzer. Approximately 1 mg of sample was used for each measurement; this was heated in air (flow of 30 mL min^{-1}) from 50 to 750 °C at a rate of 10 °C min^{-1}. In the experimental conditions used with the described thermogravimetric apparatus, the temperature error was calculated to be +/-20 °C.

Laser desorption ionization time-of-flight mass spectrometry (LDI-TOFMS) spectra were recorded in positive reflectron mode on a SCIEX TOF/TOF™ 5800 system using a N2 laser ($\lambda = 337$ nm). The target was prepared by depositing the carbon particulate matter suspended in NMP on a standard stainless-steel plate and heating it at about 100 °C for a few minutes to evaporate the solvent. The addition of matrices to the investigated samples is not necessary for their ionization, since they are able to absorb the laser beam at 337 nm and to act as a "self-matrix" [54–56]. Each spectrum represents the sum of 12,000 laser pulses per sample position, from randomly chosen spots. The obtained spectra were quantitatively analyzed using Fast Fourier Transform (FFT) analysis and graphing software (Origin). More details on the method as applied to mass spectra are reported in [57].

3. Numerical modeling

3.1. Gas-phase kinetic mechanism and soot model

To model the gas-phase and soot particle evolution, a kinetic mechanism is combined with a detailed soot model described by D'Anna et al. [32]. The kinetic mechanism developed by D'Anna and coworkers in [32,33,38,58] is employed as a base mechanism taking into account the reactions of the smaller hydrocarbon chemistry and the formation of soot precursors. The mechanism described by Sun et al. [22], which originally captures oxidation reactions between OME_1 and OME_3, was extended to include reactions modeling the combustion of OME_4 [36]. Reaction pathways for OME_4 were added as with OME_3. Therefore, a total of 154 species and 757 reactions are incorporated in the kinetic mechanism, of which 54 species and 286 reactions relate to $OME_{2\text{-}4}$ cleavage and oxidation processes.

This procedure of taking similar rate rules to those used with smaller OMEs and applying them to OME_4 is justified because of the homologous structure of the $OME_{2\text{-}4}$ series and the identical functional groups dominating the decomposition and oxidation processes. The principle of generating reaction-class-based mechanisms was similarly applied in [24] for $OME_{2\text{-}4}$ based on OME_1 reaction kinetics.

The formation and evolution of soot particles and PAHs larger than pyrene are not tracked by the kinetic gas-phase mechanism but by a detailed statistical soot model. The modeling approach developed by [58] was successfully applied previously for premixed laminar ethylene flames [34,35] and OME_3-doped ethylene flames [29,30]. It is therefore only briefly described here.

The kinetic mechanism contains PAHs with up to four rings, pyrene being the largest molecule. The transition from gas-phase PAHs to larger PAHs, which was included in the statistical soot model through lumping, arises from the reactions of two gas-phase PAHs. The physicochemical soot model subdivides the soot precursor formation of the larger PAHs and the soot particle evolution process into three stages to cover the specific properties of the individual particle entity. Therefore, the soot model tracks larger PAHs, which are still gaseous or peri-condensed molecules (named *large PAHs* in the following) separated from incipient soot particles exhibiting a spherical shape (*clusters*). The third stage represents fully evolved soot particles (*aggregates*) in fractal form after several clusters have aggregated. The maturation of each entity is represented by the number of carbon atoms in a particle and by the carbon-to-hydrogen ratio.

With all three entities, particle growth occurs through surface reactions caused by the addition of C_2H_2 or the condensation of aromatics, while larger PAHs can additionally adsorb onto clusters and aggregates and grow due to the resonance-stabilized free radical (RSFR) mechanism. Coalescence and aggregation processes, along with further processes that alter the particulate matter, such as oxidation and dehydrogenation, are modeled using Arrhenius rate laws as with the kinetic gas-phase equations.

Taking both physical and chemical properties into consideration leads to a multivariate description of the particles ξ_- with four independent parameters $\xi_- = \left[\xi_{nc}, \xi_{H/C}, \xi_{stat}, \xi_{typ}\right]^T$. ξ_{typ} represents the structure of the entity with the three discrete values $\xi_{typ} \in A, A = \{large\ PAHs, clusters, agglomerates\}$ and ξ_{stat} the reactivity of the particles with $\xi_{stat} \in B, B = \{stable, radical\}$. ξ_{nc} and $\xi_{H/C}$ are the number of carbon particles and the hydrogen-to-carbon ratio of a particle, respectively. Both are continuous properties that can vary in the range of $\xi_{nc} \in [0, \infty)$ and $\xi_{H/C} \in [0, 1]$.

3.2. Conditional Quadrature Method of Moments—CQMOM

The population balance equation quantifies the evolution of the particle property distribution in terms of the quadrivariate number density function (NDF) $f\left(\xi_-; x_-, t\right)$ for the internal coordinate vector ξ_- in space x_- and time t. The last two dependencies are neglected in the following for brevity. The NDF can be reformulated as a conditional density function.

$$f\left(\xi_-\right) = f_{H/C}\left(\xi_{H/C}|\xi_{nc}, \xi_{stat}, \xi_{typ}\right) \cdot f_{nc}\left(\xi_{nc}|\xi_{stat}, \xi_{typ}\right) \cdot n\left(\xi_{stat}, \xi_{typ}\right), \tag{1}$$

in which the distribution $f_{H/C}$ of the hydrogen-to-carbon ratio $\xi_{H/C}$ depends on the specific condition $(\xi_{nc}, \xi_{stat}, \xi_{typ})$ and the distribution f_{nc} of the carbon atoms in a particle ξ_{nc} depends on the state (ξ_{stat}, ξ_{typ}). The joint bivariate distribution $n\left(\xi_{stat}, \xi_{typ}\right)$ holds six possible combinations (u, v) of the discrete particle properties $\xi_{stat} = \xi_{stat,u}$ and $\xi_{typ} = \xi_{typ,v}$. Thus, it can be simplified as a set of six bivariate NDFs $\Pi_{(u,v)}$

$$\Pi_{(u,v)}\left(\xi_{nc}, \xi_{H/C}\right) = f_{H/C}^{u,v}\left(\xi_{H/C}|\xi_{nc}\right) \cdot f_{nc}^{u,v}\left(\xi_{nc}\right) \cdot n_{u,v}, \tag{2}$$

in which the dependency of the distribution function $f_{H/C}^{u,v}$ is reduced to solely the number of carbon atoms ξ_{nc} and $f_{nc}^{u,v}$, resulting in a marginal distribution function of the subset ξ_{nc}, both for each combination (u, v).

The set of NDFs is discretized by its statistical moments using the CQMOM approach, as described in more detail in [29,35]. In this work, the integer-order moments are transformed into fractional-order moments $m_{u,v}^{\frac{k_1}{z},k_2}$ following [59] with $z = 3$ in terms of ξ_{nc}, resulting in.

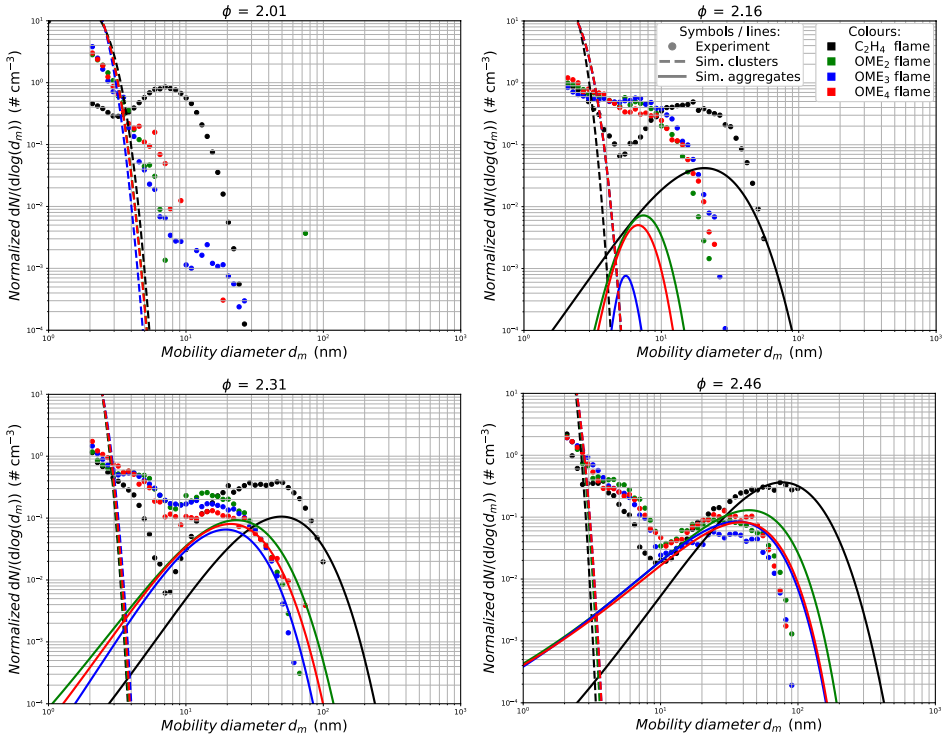

Fig. 1. Particle size distributions determined with EM on the CQMOM simulation results (dashed lines for clusters and solid lines for aggregates) compared with the experimental SMPS measurements (dots) at HAB = 15 mm for flames with different equivalence ratios of 2.01, 2.16, 2.31, and 2.46: pure ethylene flame (black), $OME_{2\text{-}4}$-doped ethylene flame (green for OME_2, blue for OME_3 and red for OME_4). (For interpretation of the references to colour in this figure legend, the reader is referred to the web version of this article.)

$$m_{u,v}^{\frac{k_1}{-},k_2} = \int_0^\infty \int_0^1 \xi_{nc}^{\frac{k_1}{-}} \xi_{H/C}^{k_2} \Pi_{(u,v)} \left(\xi_{nc}, \xi_{H/C}\right) \mathrm{d}\xi_{H/C} \mathrm{d}\xi_{nc}. \tag{3}$$

The distribution of the internal coordinates ξ_{nc} is discretized using two quadrature nodes and one for the carbon-to-hydrogen ratio $\xi_{H/C}$, resulting in a total of 36 moment transport equations for the system of six bivariate NDFs $\Pi_{(u,v)}$. Since the CQMOM approach uses weighted Dirac-delta functions to approximate the NDF, no continuous information about the distribution of the internal coordinates is given by the moments.

An entropy maximization (EM) approach is applied in a post-processing step, producing the particle size distribution that is successfully applied in Salenbauch et al. [35] and additionally described in references therein. In the current study, a continuous distribution function $f(\xi_1)$ is sought without prescribing its shape for the internal coordinate ξ_1 which maximizes the entropy [60] $H(f)$

$$H(f) = -\int_{\Omega_{\xi_1}} f(\xi_1) \ln(f(\xi_1)) \mathrm{d}\xi_1, \tag{4}$$

under the constraint of the moment set using Lagrangian multipliers.

To take into account the fractal particle shape, the mobility diameter is used in this study for the evaluation of the aggregates.

The solution of fractional moments provides the additional advantage that it is possible to directly evaluate the PSD using the EM concept. Given the expression between the equivalent-volume sphere diameter d_p and the coordinate ξ_{nc}

$$d_p = \left(\frac{6W_c}{\pi\rho_s}\right)^{1/3} \xi_{nc}^{1/3} = L^{1/3} \xi_{nc}^{1/3}, \tag{5}$$

where W_c is the mass of a single carbon atom and ρ_s the soot density, the diameter-based moments $\left\langle m_{u,v}^{k_1} \right\rangle$ can be obtained from the transported fractional moments $m_{u,v}^{\frac{k_1}{-},0}$

$$\left\langle m_{u,v}^{k_1} \right\rangle = \int_0^\infty d_p^{k_1} f_{d_p}(d_p) \mathrm{d}d_p = L^{k_1/3} \int_0^\infty \xi_{nc}^{k_1/3} f_{nc}(\xi_{nc}) \mathrm{d}\xi_{nc} = L^{k_1/3} m_{u,v}^{\frac{k_1}{-},0}. \tag{6}$$

Finally, examining the particle aggregates, the simulated PSDs are expressed as a function of the mobility diameter d_m, here equal to the collision diameter d_c as in [61], $d_m \equiv d_c = d_p n_p^{1/D_f}$, where n_p is the number of primary particles in an aggregate calculated on the basis of the ratio between the mass of the aggregate and the mass of the primary particle. Similarly to [29], a fractal dimension D_f equal to 1.8 and a primary particle diameter d_p equal to 15 nm were assumed here.

3.3. Numerical setup

The laminar premixed flames are modeled using one-dimensional simulations with imposed temperature profiles. For each equivalence

ratio, a constant temperature profile is applied whatever fuel is used (pure ethylene or OME_{2-4}/ethylene blends). The four temperature profiles were experimentally measured in [37] for pure ethylene flames under consistent conditions.

The close similarity of the temperature profiles when comparing the pure ethylene flame and the flame with substitute justifies the applied approach; this is consistent with the experimental observations for other biofuels [37–40,52,62–64]. The flame temperature in the current configuration is indeed strongly influenced by the heat losses between the flame and the burner. The temperature profile measured for pure flames was also used for doped flames, as with other biofuels investigated before [37–40,52,62–64].

Two-way coupling between the gas-phase and the particle phase is implemented. A segregated approach is utilized in the numerical in-house Universal Laminar Flame (ULF) solver [65], which solves the gas-phase and the moment transport equations of the particulate matter. The coupling includes the species involved in the transition to larger PAHs and the condensation process onto soot particles extending from benzene up to the four-ring member pyrene. Surface growth, oxidation and dehydrogenation are based on the species H, OH, H_2, H_2O, C_2H_2, HCO, CO, and O_2, which are therefore required to evaluate the moments. Further information about the solution strategy can be found in [30,35]. An increasing soot density between 1000 and 1800 kg/m^3 is assumed for the particulate matter depending on the H/C ratio. Molecular soot diffusion and thermophoresis effects are neglected, as they are known to be of minor importance in this flame configuration [66].

4. Results and discussion

Below, the results are presented for the flames fueled with pure ethylene and with OME_{2-4}/ethylene blends at different equivalence ratios φ (see Table 1).

4.1. Soot evolution

Fig. 1 shows the PSDs measured at a HAB of 15 mm for the four equivalence ratios investigated, with and without the addition of OME_{2-4}, together with modeling results from the EM procedure applied to the CQMOM flame solutions.

The effect of OMEs on the PSD is evident: starting from an equivalence ratio of $\phi = 2.01$, the bimodality of the PSD is lost when OMEs are added. Moving to higher equivalence ratios, larger particles are still formed with OME blending but are significantly reduced in terms of their number and their diameter. Conversely, smaller particles ($d_p < 5$ nm) are present in large amounts in all the conditions and the addition of OME_n does not lead to a significant reduction of smaller particles or even a slight increase as for the flames with an equivalence ratio of $\phi = 2.01$, as previously investigated in [29] for OME_3 blending. It appears that with all equivalence ratios, the effect of different OMEs on small particles and large soot aggregates is the same. All the investigated OMEs exhibit a delay in the soot formation process that mainly reduces larger aggregates while the number of smaller particles is not significantly affected or even slightly increased. Therefore, none of the investigated OMEs shows a significant advantage over the others in terms of soot emissions, at least in the investigated laminar premixed flames, which are based on identical carbon contents.

The model proposed here is able to capture the trend with the equivalence ratio and the substantial indifference with respect to the OME chain length found experimentally in terms of soot reduction. As in previous works, the model also overpredicts the number concentration of smaller particles with a diameter smaller than approx. 3 nm. This can be partially attributed to the undermeasurement of small particles due to losses in the experimental sampling line [41,67]. While smaller clusters are overpredicted by the model, particles with a diameter between 3 nm and 10 nm are underpredicted, indicating a deviation from the experimental distribution of particles smaller than 10 nm with a focus on the smallest clusters. With regard to the density of the normalized total number of particles with a diameter smaller than 10 nm, the modeling results and experimental data are comparable and within the same order of magnitude.

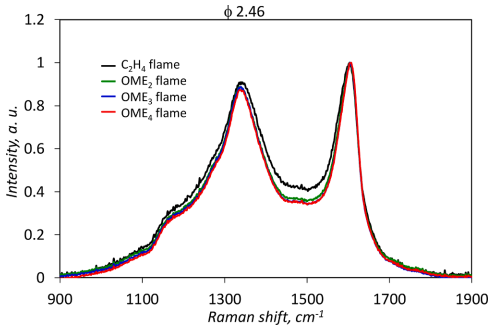

Fig. 2. Raman spectra of soot particles sampled at 15 nm HAB and ϕ = 2.46 in ethylene/air and ethylene/OME_{2-4} /air flames (For interpretation of the references to colour in this figure legend, the reader is referred to the web version of this article.).

Since the number of nanoparticles of the OME_n-doped flames is in the same order of magnitude as with the pure ethylene flame, the reduction might be due to limited particle growth and therefore a delay in the soot evolution process. This suggests that the principal mechanism that involves OMEs in inhibiting particle formation relies on the particles' interaction with the gas-phase and on the gas-phase itself. A thorough discussion of the changes in the gas-phase species with OME_3 addition to ethylene flames is given in [30], which investigated the reduction of acetylene and PAH species, supporting this assumption. The reactions that lead to OME oxidation and are likely also responsible for removing carbon from the molecular growth path are also fast enough to overcome the effect of the chain length and corresponding differences in the OME_{2-4} decomposition.

In general, OMEs have a similar effect in terms of particle reduction compared to other oxygenated fuels. Dimethyl ether (DME) fuel has proven to be the most reducing fuel in the conditions investigated [40] and also shares the absence of C–C bonds. In [40], DME-doped ethylene flames are investigated in a similar flame configuration with a DME content of 20 % in terms of carbon fed to the flame, allowing a quantitative comparison of the soot reduction effect for OME_n and DME flames. The reduction of soot volume fraction for a flame containing 20 % DME is between 90 % and 80 % compared to the pure ethylene flames, with an increasing equivalence ratio from φ = 2.16 to φ = 2.46 [40]. From a similar flame configuration [29], the reduction due to OME_3 doping can be quantified as 75 % to 65 % for the same equivalence ratios. Since flames doped with OME_2 and OME_4 exhibit similar PSDs to those doped with OME_3, similar quantities of soot reduction are also expected for flames doped with OME_2 and OME_4. Therefore, DME seems to be slightly more effective than OME_n fuel in reducing the soot formation in this premixed flame configuration.

4.2. Soot structure analysis

A detailed physicochemical analysis of the thermophoretically collected samples was performed to verify the effect exerted by OME on particulate properties. The investigation was carried out on carbon particulate matter collected on a glass plate at 15 mm HAB and φ = 2.46 in the pure ethylene and ethylene/OME flames.

Carbon particulate matter was firstly analyzed with Raman spectroscopy, a diagnostic technique widely used to characterize the sp^2

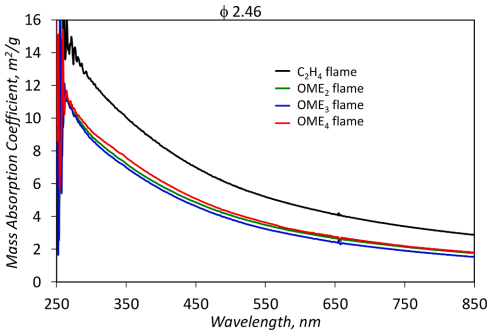

Fig. 3. UV–Vis absorption spectra of particulate collected at 15 mm HAB in the ethylene/air and ethylene/OME_{2-4} /air flame at $\phi = 2.46$ (For interpretation of the references to colour in this figure legend, the reader is referred to the web version of this article.).

phase of ordered and amorphous carbon materials [68]. In Fig. 2, the Raman spectra of the soot samples collected in the ethylene/air and ethylene/OME_{2-4}/air are reported. The Raman spectrum of sp^2-carbon-rich material with any level of disorder is characterized by the predominance of two peaks: the G band, located at about 1600 cm^{-1}, and the D band, located at about 1350 cm^{-1} [69].

The G band is due to the stretching vibration of pairs of sp^2 carbon atoms. The D peak is a disorder-induced band arising from the presence of defects that initiate the breathing modes of sp^2 carbon atoms in aromatic ring systems [69]. This mode thus necessarily requires the presence of aromatic rings. The ratio between the intensity of these two peaks is the Raman parameter most used to study soot, since it can be used to derive the size of the aromatic layers comprising the particles [70–75]. An accurate spectral deconvolution procedure was developed to study the contributions and features of these two peaks that strongly overlap in the soot samples [76]. Breit–Wigner–Fano and Lorentzian curves were used to fit the G and the D peaks, respectively. Two Lorentzian lines were used to fit the features at 1100–1300 cm^{-1}, while a Gaussian line shape was chosen for a band around 1500 cm^{-1}. More details on the deconvolution procedure are reported in a previous work [76]. As can be seen in Fig. 2, the Raman features of the OME samples are very similar. The results obtained after the deconvolution are comparable and differ from those of the ethylene soot. The I(D)/I(G) ratio calculated for the OME samples has an average value of 0.79 with a standard deviation of 0.035, whereas the ethylene sample has an average value of 0.83 with a standard deviation of 0.03. In highly disordered carbons, the development of a D peak indicates ordering, exactly the opposite of what happens in more ordered materials such as microcrystalline graphite [69]. Therefore, ethylene soot, which has a higher I(D)/I(G) ratio, presents longer aromatic islands in comparison to OME soot. As the I(D)/I(G) ratio increases, the bandwidths also increase, as previously found for soot collected from premixed flames [53,76], suggesting that as the layer length increases, distortions in the bond angle and aromatic planes occur to a larger extent.

The G band in the OME samples is located at higher Raman shifts (about 1603 cm^{-1}) than the ethylene flame (1600 cm^{-1}), indicating a higher abundance of olefinic bonds and/or smaller aromatic layers [77].

UV–Vis spectroscopy was performed on samples consisting in NMP suspensions of carbon particulate matter. The mass absorption coefficients (MACs) in the UV–Vis range are reported in Fig. 3. As already found with Raman spectroscopy, the UV–Vis spectra of OME samples are very similar to one another and differ from ethylene soot, which has higher MACs. In particular, at 550 nm, ethylene soot has a MAC of 5.2 m^2/g, whereas OME particles have an average value of 3.4 m^2/g, significantly far outside the range of values lying between 5 and 13 m^2/g as reported in an extensive review on the absorbing properties of soot and carbon black [78]. This comparison of the UV–Vis data confirms the higher aromaticity of ethylene soot, which absorbs more visible light.

Particulate reactivity was assessed by TGA analysis. It can be seen from the thermogravimetric profiles reported in Fig. 4 that OME samples have a higher oxidation reactivity; indeed, their oxidation starts at 410 °C and is almost completed at 600 °C, whereas for ethylene soot the temperature range for particle oxidation is shifted to higher temperature values, namely 470–650 °C. Consequently, the temperatures at which the highest oxidation rate occurs are also different: 630 °C for ethylene soot and in the range 585–597 °C for OME soot samples. Slightly higher temperature values are experienced by OME_4 soot during its oxidation. This small difference was found to be within the range of experimental error of the TGA apparatus and thus could be attributed to instrumental

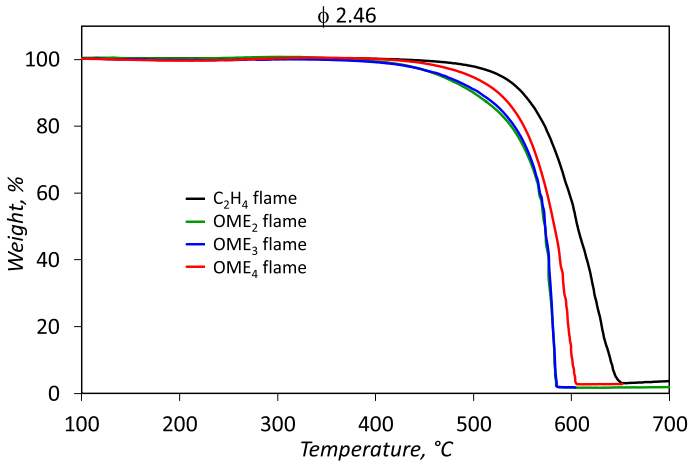

Fig. 4. Thermogravimetric profiles measured for particulate collected at 15 mm HAB in the ethylene/air and ethylene/OME_{2-4} /air flame at $\phi = 2.46$ (For interpretation of the references to colour in this figure legend, the reader is referred to the web version of this article.).

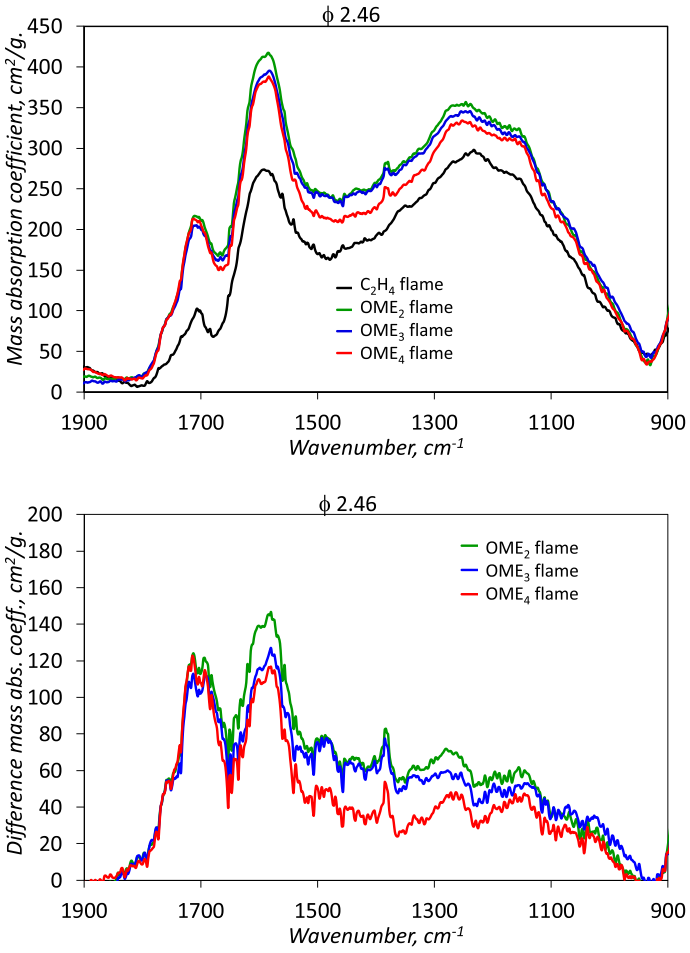

Fig. 5. Infrared mass absorption coefficients (upper panel) of particulate collected at 15 mm HAB in the ethylene/air and ethylene/OME_{2-4} /air flame at ϕ = 2.46. Difference (lower panel) between the infrared mass absorption coefficients in the 900–1900 cm^{-1} wavenumber range of carbon particulate matter at 15 mm HAB and φ = 2.46 in the ethylene/OME_{2-4} /air flame and ethylene/air flame (For interpretation of the references to colour in this figure legend, the reader is referred to the web version of this article.).

reproducibility. This conclusion seems to be supported by the fact that nanostructural and compositional features of all the OME_{2-4} soot described so far and in the following are found to be very similar, hence this result could not be attributed to a particular feature of OME_4 soot, at least among those investigated.

FTIR spectroscopy has been performed to analyze soot particle compositions. The spectra were acquired in the same conditions, i.e., the same carbon concentration within the KBr disk and disk thickness, to compare the results and calculate the mass absorption coefficient. The infrared mass absorption coefficients of soot samples are reported in the upper panel of Fig. 5. The spectra have been deprived of the absorption continuum to better visualize and compare the vibrational modes arising from the different functional groups. The spectra in the 4000–2500 cm^{-1} spectral region were not reported since they were very similar. Several peaks can be seen in the 500–2000 wavenumber range. The peak located at 1720 cm^{-1} is due to the stretching of carbonyl C = O groups. At this wavenumber value, no other peak occurs, thus an absorption signal in this region is clear and undeniable evidence of the presence of oxygen bonds within the carbon nanostructure. The 1600 cm^{-1} peak is due to the aromatic C = C stretching mode and is usually strengthened by dissymmetry of the aromatic systems, which can be caused by any kind of ring substitution [79,80]. In particular, it was found that if the structural irregularity is caused by the presence of oxygen, the increase in the dipole moment strongly enhances the intensity of the C = C stretching peak [81]. As can be observed in Fig. 5, complex carbonaceous materials such as soot are characterized by a broad absorption in the 1000–1500 cm^{-1} region [82–84] where aliphatic C–H bending and C–O stretching also occur. In the wavenumber region between 900 and 600 cm^{-1}, peaks occur due to the out-of-plane (OPLA) bending of aromatic hydrogen [85]. The differences in the FTIR signal intensity are shown more clearly in the lower panel of Fig. 5, which shows the spectra obtained as the difference between the infrared mass absorption coefficients of carbon particulate of OME-doped flames and those of the pure ethylene flame. OME samples present a higher concentration of carbonyl groups, which could be responsible for the higher intensity of the C = C 1600 cm^{-1} peak. All the region from 1500 to 100 cm^{-1}

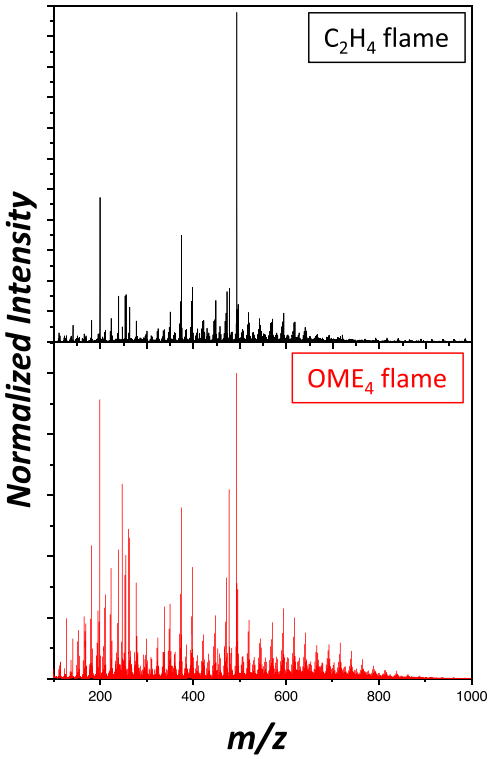

Fig. 6. LDI-TOF mass spectra of particulate collected at 15 mm HAB in the ethylene/air flame (upper panel) and the ethylene/OME_4 /air flame (lower panel) at $\phi = 2.46$.

presents slightly higher absorption coefficients for the OME samples, with no clearly distinguishable peaks. Moreover, the OPLA signals are higher, suggesting the presence of a more hydrogenated aromatic layer comprising OME soot nanostructure, supporting the hypothesis of a less ordered structure.

The LDI mass spectrum of the ethylene sample is contrasted in Fig. 6 with the spectrum of OME_4 (representative of all the OME spectra, which are all very similar). Both the spectra extend over the 100–1000 m/z range and appear very complex and crowded with peaks, as usually occurs for carbon particulate spectra [86]. The OME_4 spectrum is richer in peaks, especially in the region below m/z 300. The application of a mathematical tool is very useful for extrapolating quantitative information from such complex spectra, demonstrating the periodic mass differences of peaks and therefore the main chemical functionalities of the mass sequences and growth paths [57]. The FFT analysis was carried out in two selected mass ranges ($m/z < 300$ and $300 < m/z < 900$) of the spectra since all samples present some sort of bimodality with a change in the mass spectral distribution above m/z 300. Fig. 7 reports the height-normalized FFT profiles evaluated based on the spectra of all the particulate samples.

The FFT analysis reveals that in all the samples, mass differences of 12 and 14 predominate, with a prevalence of 14. The 14 difference can be traced back to homologous series increasing by a CH_2 group (structures with aliphatic moieties such as those featuring C_5-PAHs). The presence of a smaller peak at m/z 24 (higher in the case of ethylene) is indicative, along with 12, of PAH growth sequences. It is due to the organic fraction present in the particulate [86]. One notable feature is the presence, only in the case of OME samples, of a mass difference of 16, which suggests the occurrence of species growing through the addition of oxygen. The peak at 16 is completely absent in pure ethylene, confirming the presence of oxygenated functionalities found only in OME particulate. Above m/z 300, for all samples, the FFT mass differences are restricted to 12 and 24. With the prevalence of 24, this is indicative of the presence of carbon clusters that are not ascribable to the typical fullerene cluster series [84].

The pathways that lead to oxygen being incorporated in the particles are still not clear. The FTIR spectra indicate the presence of a very specific oxygenated functionality, namely C = O, which should be given serious consideration. When particles coming from the same experimental apparatus and generated in flames fueled with different oxygenated compounds—ethanol [63], butanols [37], DMF [52]—were analyzed, all different oxygen functionalities were detected. This peculiarity of particles coming from OME combustion hence suggests that kinetic pathways leading to the formation of specific intermediate compounds are enhanced. Looking at the kinetic pathways of the oxidation decomposition of the OMEs shown in the literature [24,36], aldehydes, and particularly formaldehyde (HCHO), are likely to play a dominant role in the formation of C = O functionality incorporated in the particles. Future investigation of rich flames doped with formaldehyde could shed light on this point. At present, models for particle prediction do not consider these pathways, kinetics are not available, and in general, do not account for the role of oxygenated compounds in particle formation. In [87], a significant reduction of the PAH concentration was found due to the formation of oxygenated PAHs including C = O bonds while the concentration of these oxygenated PAHs was too low to be considered in the nucleation step of soot particles. The FTIR results and especially the presence of C = O functionalities in the soot particles suggest to consider oxygenated PAHs in other soot processes such as surface growth.

Overall, the effect of oxygenated intermediate species on the total amount of particles or even on the PSD could be considered negligible with respect to other combustion and kinetic parameters. However, considering that the surface growth becomes effective and predominant as the combustion process evolves, covering up and undoing the original effect that fuel structure has on the particle features, the possibility of there being a more obvious effect and/or presence of oxygen functionalities on the particle in the first part of the flames is reasonable. Further studies will have to explore this topic in more detail, taking into consideration the impact that oxygenated functionalities can have on particle reactivity in after-treatment systems and on biological systems.

5. Conclusions

The combustion of $OME_{2\text{-}3\text{-}4}$ has been investigated to assess whether their fuel structure, namely the length of the fuel chain, could have a significantly different effect on particle formation. The paper has also explored the effect of fuel structure on particle features, particularly regarding the presence of oxygen functional groups incorporated in particles. Premixed flames fueled with pure ethylene and ethylene/OME blends were investigated experimentally with ex-situ online measurements (SMPS) and batch measurements (UV–Vis, Raman and FTIR spectroscopy, TGA, mass spectrometry), and numerically with a CQMOM approach. $OME_{2\text{-}4}$ were used as a substituent for 20 % of the total carbon while keeping the cold gas velocity constant, and four equivalence ratios were investigated: 2.01, 2.16, 2.31, and 2.46.

A reduction in the number and size of the soot particles in all $OME_{2\text{-}4}$-blended flames was found with PSD analysis, similar to that previously found for OME_3-blended flames. OME_2 and OME_4 also follow the behavior of OME_3 in that they have a negligible effect on small particles. Overall, the differences found between the different OMEs can be considered negligible, suggesting that the chain length plays a minor

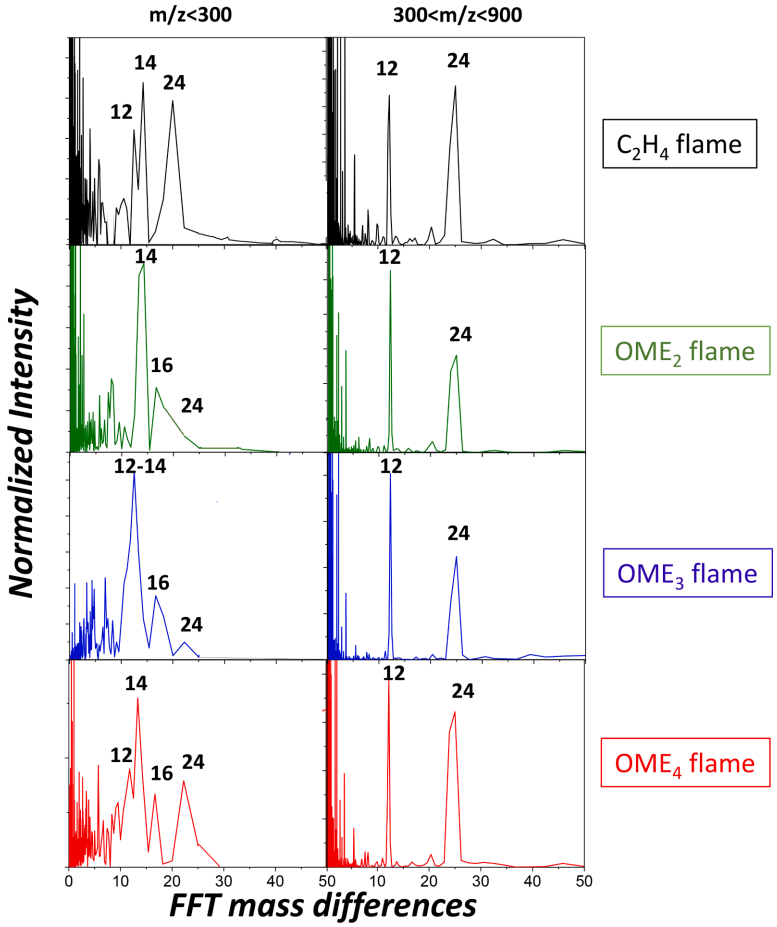

Fig. 7. Mass differences evaluated based on the FFT of particulate soot sampled at 15 mm HAB and $\phi = 2.46$ in ethylene/air and ethylene/$OME_{2\text{-}3\text{-}4}$ /air flames.

role. This behavior can be attributed to the important role of oxidation reactions at high temperatures: they overcome the effect of chain length and are very effective in removing carbon from the molecular growth pathway. The model was able to predict all particle formation trends for the different OMEs, particularly the minor effect of the chain length over the fuel structure, suggesting that the absence of C–C bonds plays a major role in particle reduction.

The effect of $OME_{2\text{-}3\text{-}4}$ addition on the chemical features of carbon particulate matter at the highest equivalence ratio was investigated in terms of aromaticity, reactivity and composition. On one hand, $OME_{2\text{-}4}$ soot properties as a function of the chain length were found to be invariant. On the other hand, clear differences were found when $OME_{2\text{-}4}$ soot were compared with ethylene soot. UV–Vis and Raman spectroscopy analysis revealed a slightly lower degree of aromatization in the carbon particulate matter produced in the OME-doped flames. A higher presence of C = O functionalities in $OME_{2\text{-}4}$ samples was found by analyzing the FTIR spectra of the particles. Mass spectrometric analysis confirm the presence of oxygenated functionalities for $OME_{2\text{-}4}$ particulate which might significantly impact the oxidation features of the particles in after-treatment systems and their interaction with living beings, i.e., their toxicity. Thermogravimetric analysis substantially confirmed results obtained with other techniques showing that the $OME_{2\text{-}4}$ samples were more highly reactive, which was attributed both to the higher presence of oxygenated functionalities and to the smaller size of the aromatic layers, making them more dominated by edge positions. The measured FTIR spectra suggest that the oxygenated intermediate species coming from OME oxidation/decomposition may be closely related to the presence of C = O functionality in particles. Aldehydes and particularly formaldehyde are quite likely to be responsible for this. Future investigation of rich flames doped with formaldehyde could shed light on this point. Moreover, to show the role and presence of oxygen functionality, combustion conditions should be investigated where surface growth has not already played a dominant role, such as the early stage of rich premixed flames. Finally, a reduction in the particle size along with an increase in oxygen content can be critical determinants of carbon nanomaterial toxicity. This aspect must be further investigated and taken into account in the formulation of new fuels.

CRediT authorship contribution statement

Robert Schmitz: Conceptualization, Writing – review & editing. **Carmela Russo:** Conceptualization, Writing – review & editing. **Federica Ferraro:** Conceptualization, Writing – review & editing. **Barbara Apicella:** Writing – review & editing. **Christian Hasse:** Conceptualization, Funding acquisition. **Mariano Sirignano:** Conceptualization, Writing – review & editing.

Declaration of Competing Interest

The authors declare that they have no known competing financial interests or personal relationships that could have appeared to influence the work reported in this paper.

Acknowledgments

The authors gratefully acknowledge the funding by the German Federal Ministry of Education and Research (BMBF) as part of the NAMOSYN Project (project number 03SF0566R0).

References

[1] Grubler A. Energy transitions research: Insights and cautionary tales. Energy Policy 2012;50:8–16. https://doi.org/10.1016/j.enpol.2012.02.070.
[2] Moriarty P, Honnery D. Rise and Fall of the Carbon Civilisation. 1st ed. London: Springer London; 2011. https://doi.org/10.1007/978-1-84996-483-8.
[3] Dreizler A, Pitsch H, Scherer V, Schulz C, Janicka J. The role of combustion science and technology in low and zero impact energy transformation processes. Appl Energy Combust Sci 2021;7:100040. https://doi.org/10.1016/j.jaecs.2021.100040.
[4] Olah GA, Goeppert A, Prakash GKS. Chemical recycling of carbon dioxide to methanol and dimethyl ether: From greenhouse gas to renewable, environmentally carbon neutral fuels and synthetic hydrocarbons. J Org Chem 2009;74:487–98. https://doi.org/10.1021/jo801260f.
[5] Deutz S, Bongartz D, Heuser B, Kätelhön A, Schulze Langenhorst L, Omari A, et al. Cleaner production of cleaner fuels: Wind-to-wheel-environmental assessment of CO2-based oxymethylene ether as a drop-in fuel. Energy Environ Sci 2018;11(2):331–43.
[6] Masri AR. Challenges for turbulent combustion. Proc Combust Inst 2021;38:121–55. https://doi.org/10.1016/j.proci.2020.07.144.
[7] Global Alliance Powerfuels. Powerfuels: Missing link to a successful global energy transition 2021.
[8] Li B, Li Y, Liu H, Liu F, Wang Z, Wang J. Combustion and emission characteristics of diesel engine fueled with biodiesel/PODE blends. Appl Energy 2017;206:425–31. https://doi.org/10.1016/j.apenergy.2017.08.206.
[9] Cao W, Zhang J, Li H. Batteries with high theoretical energy densities. Energy Storage Mater 2020;26:46–55. https://doi.org/10.1016/j.ensm.2019.12.024.
[10] He T, Wang Z, You X, Liu H, Wang Y, Li X, et al. A chemical kinetic mechanism for the low- and intermediate-temperature combustion of Polyoxymethylene Dimethyl Ether 3 (PODE3). Fuel 2018;212:223–35.
[11] Lumpp B, Rothe D, Pastotter C, Lämmermann R, Jacob E. Oxymethylene Ethers As Diesel Fuel. Mtz Worldw 2011;78:34–8.
[12] Fleisch TH, Sills RA. Large-scale gas conversion through oxygenates: Beyond GTL-FT. Stud Surf Sci Catal 2004;147:31–6. https://doi.org/10.1016/s0167-2991(04)80023-5.
[13] Emenike O, Michailos S, Hughes KJ, Ingham D, Pourkashanian M. Techno-economic and environmental assessment of BECCS in fuel generation for FT-fuel, bioSNG and OMEx. Sustain Energy Fuels 2021;5:3382–402. https://doi.org/10.1039/d1se00123j.
[14] Mantei F, Ali RE, Baensch C, Voelker S, Haltenort P, Burger J, et al. Techno-economic assessment and carbon footprint of processes for the large-scale production of oxymethylene dimethyl ethers from carbon dioxide and hydrogen. Sustain Energy Fuels 2022;6(3):528–49.
[15] Yang Z, Ren C, Jiang S, Xin Y, Hu Y, Liu Z. Theoretical predictions of compatibility of polyoxymethylene dimethyl ethers with diesel fuels and diesel additives. Fuel 2022;307:121797. https://doi.org/10.1016/j.fuel.2021.121797.
[16] Sanfilippo D, Patrini R, Marchionna M. Use of an oxygenated product as a substitute of gas oil in diesel engines. US 2007;7235113:B2.
[17] Omari A, Heuser B, Pischinger S. Potential of oxymethylenether-diesel blends for ultra-low emission engines. Fuel 2017;209:232–7. https://doi.org/10.1016/j.fuel.2017.07.107.
[18] Zhou D, Zhang H, Yang S. A Robust Reacting Flow Solver with Computational Diagnostics Based on OpenFOAM and Cantera. A Robust Reacting Flow Solver with Computational Diagnostics Based on OpenFOAM and Cantera 2022;9(2):102.
[19] Pélerin D, Gaukel K, Härtl M, Jacob E, Wachtmeister G. Potentials to simplify the engine system using the alternative diesel fuels oxymethylene ether OME1 and OME3-6 on a heavy-duty engine. Fuel 2020;259:116231. https://doi.org/10.1016/j.fuel.2019.116231.
[20] Liu H, Wang Z, Wang J, He X. Improvement of emission characteristics and thermal efficiency in diesel engines by fueling gasoline/diesel/PODEn blends. Energy 2016;97:105–12. https://doi.org/10.1016/j.energy.2015.12.110.
[21] Ren S, Wang Z, Li B, Liu H, Wang J. Development of a reduced polyoxymethylene dimethyl ethers (PODEn) mechanism for engine applications. Fuel 2019;238:208–24. https://doi.org/10.1016/j.fuel.2018.10.111.
[22] Sun W, Wang G, Li S, Zhang R, Yang B, Yang J, et al. Speciation and the laminar burning velocities of poly(oxymethylene) dimethyl ether 3 (POMDME3) flames: An experimental and modeling study. Proc Combust Inst 2017;36(1):1269–78.
[23] Fenard Y, Vanhove G. A Mini-Review on the Advances in the Kinetic Understanding of the Combustion of Linear and Cyclic Oxymethylene Ethers. Energy Fuels 2021;35:14325–42. https://doi.org/10.1021/acs.energyfuels.1c01924.
[24] Cai L, Jacobs S, Langer R, vom Lehn F, Heufer KA, Pitsch H. Auto-ignition of oxymethylene ethers (OMEn, n = 2–4) as promising synthetic e-fuels from renewable electricity: shock tube experiments and automatic mechanism generation. Fuel 2020;264:116711. https://doi.org/10.1016/j.fuel.2019.116711.
[25] Ngugi JN, Richter S, Braun-Unkhoff M, Naumann C, Köhler M, Riedel U. A Study on Fundamental Combustion Properties of Oxymethylene Ether-2. vol. Volume 6:, 2021. https://doi.org/10.1115/GT2021-60078.
[26] Ngügi JM, Richter S, Braun-Unkhoff M, Naumann C, Riedel U. A study on fundamental combustion properties of oxymethylene ether-1, the primary reference fuel 90, and their blend: Experiments and modeling. Combust Flame 2022;111996. https://doi.org/10.1016/j.combustflame.2022.111996.
[27] Eckart S, Cai L, Fritsche C, vom Lehn F, Pitsch H, Krause H. Laminar burning velocities, CO, and NOx emissions of premixed polyoxymethylene dimethyl ether flames. Fuel 2021;293:120321. https://doi.org/10.1016/j.fuel.2021.120321.
[28] Omari A, Heuser B, Pischinger S, Rüdinger C. Potential of long-chain oxymethylene ether and oxymethylene ether-diesel blends for ultra-low emission engines. Appl Energy 2019;239:1242–9. https://doi.org/10.1016/j.apenergy.2019.02.035.
[29] Ferraro F, Russo C, Schmitz R, Hasse C, Sirignano M. Experimental and numerical study on the effect of oxymethylene ether-3 (OME3) on soot particle formation. Fuel 2021;286:119353. https://doi.org/10.1016/j.fuel.2020.119353.
[30] Schmitz R, Sirignano M, Hasse C, Ferraro F. Numerical Investigation on the Effect of the Oxymethylene Ether-3 (OME3) Blending Ratio in Premixed Sooting Ethylene Flames. Front Mech Eng 2021;7:1–11. https://doi.org/10.3389/fmech.2021.744172.
[31] Tan YR, Salamanca M, Pascazio L, Akroyd J, Kraft M. The effect of poly (oxymethylene) dimethyl ethers (PODE3) on soot formation in ethylene/PODE3 laminar coflow diffusion flames. Fuel 2021;283:118769. https://doi.org/10.1016/j.fuel.2020.118769.
[32] D'Anna A, Sirignano M, Kent J. A model of particle nucleation in premixed ethylene flames. Combust Flame 2010;157:2106–15. https://doi.org/10.1016/j.combustflame.2010.04.019.
[33] Sirignano M, Kent J, D'Anna A. Detailed modeling of size distribution functions and hydrogen content in combustion-formed particles. Combust Flame 2010;157:1211–9. https://doi.org/10.1016/j.combustflame.2009.11.014.
[34] Salenbauch S, Sirignano M, Marchisio DL, Pollack M, Anna AD, Hasse C. Detailed particle nucleation modeling in a sooting ethylene flame using a Conditional Quadrature Method of Moments (CQMOM). Proc Combust Inst 2016;36:1–9. https://doi.org/10.1016/j.proci.2016.08.003.
[35] Salenbauch S, Sirignano M, Pollack M, D'Anna A, Hasse C. Detailed modeling of soot particle formation and comparison to optical diagnostics and size distribution measurements in premixed flames using a method of moments. Fuel 2018;222:287–93. https://doi.org/10.1016/j.fuel.2018.02.148.
[36] Schmitz R, Ferraro F, Sirignano M, Hasse C. Particle formation in oxymethylene ethers (OMEn, n = 2-4) / ethylene premixed flames 2022. https://doi.org/https://doi.org/10.48550/arXiv.2204.10733.
[37] Russo C, D'Anna A, Ciajolo A, Sirignano M. The effect of butanol isomers on the formation of carbon particulate matter in fuel-rich premixed ethylene flames. Combust Flame 2019;199:122–30. https://doi.org/10.1016/j.combustflame.2018.10.025.
[38] Conturso M, Sirignano M, D'Anna A. Effect of 2,5-dimethylfuran doping on particle size distributions measured in premixed ethylene/air flames. Proc Combust Inst 2017;36:985–92. https://doi.org/10.1016/j.proci.2016.06.048.
[39] Salamanca M, Sirignano M, Commodo M, Minutolo P, D'Anna A. The effect of ethanol on the particle size distributions in ethylene premixed flames. Exp Therm Fluid Sci 2012;43:71–5. https://doi.org/10.1016/j.expthermflusci.2012.04.006.
[40] Sirignano M, Salamanca M, D'Anna A. The role of dimethyl ether as substituent to ethylene on particulate formation in premixed and counter-flow diffusion flames. Fuel 2014;126:256–62. https://doi.org/10.1016/j.fuel.2014.02.039.
[41] Sirignano M, Bartos D, Conturso M, Dunn M, D'Anna A, Masri AR. Detection of nanostructures and soot in laminar premixed flames. Combust Flame 2017;176:299–308. https://doi.org/10.1016/j.combustflame.2016.10.009.
[42] Sirignano M, D'Anna A. Coagulation of combustion generated nanoparticles in low and intermediate temperature regimes: An experimental study. Proc Combust Inst 2013;34:1877–84. https://doi.org/10.1016/j.proci.2012.06.119.
[43] Zhao B, Yang Z, Johnston MV, Wang H, Wexler AS, Balthasar M, et al. Measurement and numerical simulation of soot particle size distribution functions in a laminar premixed ethylene-oxygen-argon flame. Combust Flame 2003;133(1-2):173–88.
[44] Maricq MM. A comparison of soot size and charge distributions from ethane, ethylene, acetylene, and benzene/ethylene premixed flames. Combust Flame 2006;144(4):730–43.

[45] Zhao B, Yang Z, Li Z, Johnston MV, Wang H. Particle size distribution function of incipient soot in laminar premixed ethylene flames: Effect of flame temperature. Proc Combust Inst 2005;30:1441–8. https://doi.org/10.1016/j.proci.2004.08.104.

[46] Thierley M, Grotheer H-H, Aigner M, Yang Z, Abid A, Zhao B, et al. On existence of nanoparticles below the sooting threshold. Proc Combust Inst 2007;31(1):639–47.

[47] Sgro LA, De Filippo A, Lanzuolo G, D'Alessio A. Characterization of nanoparticles of organic carbon (NOC) produced in rich premixed flames by differential mobility analysis. Proc Combust Inst 2007;31(1):631–8.

[48] Hinds WC. Properties, Behavior, and Measurement ofAirborne Particles. J Aerosol Sci 1999. https://doi.org/10.1016/0021-8502(83)90049-6.

[49] Sgro LA, D'Anna A, Minutolo P. Charge distribution of incipient flame-generated particles. Aerosol Sci Technol 2010;44:651–62. https://doi.org/10.1080/02786826.2010.483701.

[50] Minutolo P, D'Anna A, D'Alessio A. On detection of nanoparticles below the sooting threshold. Combust Flame 2008;152:287–92. https://doi.org/10.1016/j.combustflame.2007.09.007.

[51] Singh J, Patterson RIA, Kraft M, Wang H. Numerical simulation and sensitivity analysis of detailed soot particle size distribution in laminar premixed ethylene flames. Combust Flame 2006;145:117–27. https://doi.org/10.1016/j.combustflame.2005.11.003.

[52] Russo C, D'Anna A, Ciajolo A, Sirignano M. Analysis of the chemical features of particles generated from ethylene and ethylene/2,5 dimethyl furan flames. Combust Flame 2016;167:268–73. https://doi.org/10.1016/j.combustflame.2016.02.003.

[53] Sirignano M, Russo C, Ciajolo A. One-step synthesis of carbon nanoparticles and yellow to blue fluorescent nanocarbons in flame reactors. Carbon N Y 2020;156:370–7. https://doi.org/10.1016/j.carbon.2019.09.068.

[54] Przybilla L, Brand JD, Yoshimura K, Räder HJ, Müllen K. MALDI-TOF mass spectrometry of insoluble giant polycyclic aromatic hydrocarbons by a new method of sample preparation. Anal Chem 2000;72:4591–7. https://doi.org/10.1021/ac000372q.

[55] Rizzi A, Cosmina P, Flego C, Montanari L, Seraglia R, Traldi P. Laser desorption/ionization techniques in the characterization of high molecular weight oil fractions. Part 1: Asphaltenes. J Mass Spectrom 2006;41:1232–41. https://doi.org/10.1002/jms.1095.

[56] Apicella B, Carpentieri A, Alfè M, Barbella R, Tregrossi A, Pucci P, et al. Mass spectrometric analysis of large PAH in a fuel-rich ethylene flame. Proc Combust Inst 2007;31(1):547–53.

[57] Apicella B, Bruno A, Wang X, Spinelli N. Fast Fourier Transform and autocorrelation function for the analysis of complex mass spectra. Int J Mass Spectrom 2013;338:30–8. https://doi.org/10.1016/j.ijms.2013.01.003.

[58] Sirignano M, Kent J, D'Anna A. Modeling formation and oxidation of soot in nonpremixed flames. Energy Fuels 2013;27:2303–15. https://doi.org/10.1021/ef400057r.

[59] McGraw R, Wright DL. Chemically resolved aerosol dynamics for internal mixtures by the quadrature method of moments. J Aerosol Sci 2003;34:189–209. https://doi.org/10.1016/S0021-8502(02)00157-X.

[60] Shannon CE. A Mathematical Theory of Communication. Bell Syst Tech J 1948;27:379–423. https://doi.org/10.1002/j.1538-7305.1948.tb01338.x.

[61] Kruis FE, Kusters KA, Pratsinis SE, Scarlett B. A Simple Model for the Evolution of the Characteristics of Aggregate Particles Undergoing Coagulation and Sintering. Aerosol Sci Technol 1993;19:514–26. https://doi.org/10.1080/02786829308959656.

[62] Conturso M, Sirignano M, D'Anna A. Effect of furanic biofuels on particles formation in premixed ethylene-air flames: An experimental study. Fuel 2016;175:137–45. https://doi.org/10.1016/j.fuel.2016.02.038.

[63] Sirignano M, Ciajolo A, D'Anna A, Russo C. Chemical Features of Particles Generated in an Ethylene/Ethanol Premixed Flame. Energy Fuels 2017;31:2370–7. https://doi.org/10.1021/acs.energyfuels.6b02372.

[64] Salamanca M, Sirignano M, Danna A. Particulate formation in premixed and counter-flow diffusion ethylene/ethanol flames. Energy Fuels 2012;26:6144–52. https://doi.org/10.1021/ef301081q.

[65] Zschutschke, Axel; Messig, Danny; Scholtissek, Arne; Hasse C. Universal Laminar Flame Solver (ULF). Figshare Poster 2017.

[66] Xu F, Sunderland B, Faeth GM. Soot formation in laminar premixed ethylene/air flames at atmospheric pressure. Combust Flame 1997;108:471–93. https://doi.org/10.1016/S0010-2180(96)00200-3.

[67] Sirignano M, Ciajolo A, D'Anna A, Russo C. Particle formation in premixed ethylene-benzene flames: An experimental and modeling study. Combust Flame 2019;200:23–31. https://doi.org/10.1016/j.combustflame.2018.11.006.

[68] Ferrari AC, Basko DM. Raman spectroscopy as a versatile tool for studying the properties of graphene. Nat Nanotechnol 2013;8:235–46. https://doi.org/10.1038/nnano.2013.46.

[69] Ferrari AC, Robertson J. Interpretation of Raman spectra of disordered and amorphous carbon. Phys Rev B 2000;61:14095–107. https://doi.org/10.1103/PhysRevB.61.14095.

[70] Al-Qurashi K, Boehman AL. Impact of exhaust gas recirculation (EGR) on the oxidative reactivity of diesel engine soot. Combust Flame 2008;155:675–95. https://doi.org/10.1016/j.combustflame.2008.06.002.

[71] Lapuerta M, Oliva F, Agudelo JR, Boehman AL. Effect of fuel on the soot nanostructure and consequences on loading and regeneration of diesel particulate filters. Combust Flame 2012;159:844–53. https://doi.org/10.1016/j.combustflame.2011.09.003.

[72] Dippel B, Jander H, Heintzenberg J. NIR FT Raman spectroscopic study of flame soot. Phys Chem Chem Phys 1999;1:4707–12. https://doi.org/10.1039/a904529e.

[73] Ivleva NP, Messerer A, Yang X, Niessner R, Pöschl U. Raman microspectroscopic analysis of changes in the chemical structure and reactivity of soot in a diesel exhaust aftertreatment model system. Environ Sci Technol 2007;41:3702–7. https://doi.org/10.1021/es0612448.

[74] Minutolo P, Commodo M, Santamaria A, De Falco G, D'Anna A. Characterization of flame-generated 2-D carbon nano-disks. Carbon N Y 2014;68:138–48. https://doi.org/10.1016/j.carbon.2013.10.073.

[75] Apicella B, Pré P, Rouzaud JN, Abrahamson J, Wal RLV, Ciajolo A, et al. Laser-induced structural modifications of differently aged soot investigated by HRTEM. Combust Flame 2019;204:13–22.

[76] Russo C, Ciajolo A. Effect of the flame environment on soot nanostructure inferred by Raman spectroscopy at different excitation wavelengths. Combust Flame 2015;162:2431–41. https://doi.org/10.1016/j.combustflame.2015.02.011.

[77] Russo C, Giarracca L, Stanzione F, Apicella B, Tregrossi A, Ciajolo A. Sooting structure of a premixed toluene-doped methane flame. Combust Flame 2018;190:252–9. https://doi.org/10.1016/j.combustflame.2017.12.004.

[78] Bond TC, Bergstrom RW. Light absorption by carbonaceous particles: An investigative review. Aerosol Sci Technol 2006;40:27–67. https://doi.org/10.1080/02786820500421521.

[79] Galvez A, Herlin-Boime N, Reynaud C, Clinard C, Rouzaud JN. Carbon nanoparticles from laser pyrolysis. Carbon N Y 2002;40:2775–89. https://doi.org/10.1016/S0008-6223(02)00195-1.

[80] Akhter MS, Chughtai AR, Smith DM. The Structure of Hexane Soot I: Spectroscopic Studies. Appl Spectrosc 1985;39(1):143–53.

[81] Fuente E, Menéndez JA, Díez MA, Suárez D, Montes-Morán MA. Infrared spectroscopy of carbon materials: A quantum chemical study of model compounds. J Phys Chem B 2003;107:6350–9. https://doi.org/10.1021/jp027482g.

[82] Llamas-Jansa I, Jäger C, Mutschke H, Henning T. Far-ultraviolet to near-infrared optical properties of carbon nanoparticles produced by pulsed-laser pyrolysis of hydrocarbons and their relation with structural variations. Carbon N Y 2007;45:1542–57. https://doi.org/10.1016/j.carbon.2007.02.032.

[83] Russo C, Stanzione F, Tregrossi A, Ciajolo A. Infrared spectroscopy of some carbon-based materials relevant in combustion: Qualitative and quantitative analysis of hydrogen. Carbon N Y 2014;74:127–38. https://doi.org/10.1016/j.carbon.2014.03.014.

[84] Odeh AO. Qualitative and quantitative ATR-FTIR analysis and its application to coal char of different ranks. Ranliao Huaxue Xuebao/Journal Fuel Chem Technol 2015;43:129–37. https://doi.org/10.1016/s1872-5813(15)30001-3.

[85] Centrone A, Brambilla L, Renouard T, Gherghel L, Mathis C, Müllen K, et al. Structure of new carbonaceous materials: The role of vibrational spectroscopy. Carbon N Y 2005;43(8):1593–609.

[86] Apicella B, Russo C, Carpentieri A, Tregrossi A, Ciajolo A. PAHs and fullerenes as structural and compositional motifs tracing and distinguishing organic carbon from soot. Fuel 2022;309:122356. https://doi.org/10.1016/j.fuel.2021.122356.

[87] Liu P, Chen B, Li Z, Bennett A, Sioud S, Sarathy SM, et al. Evolution of oxygenated polycyclic aromatic hydrocarbon chemistry at flame temperatures. Combust Flame 2019;209:441–51.

P3 Fuel 357 (2024), 129762

R. Schmitz, F. Ferraro, M. Sirignano, and C. Hasse, "Numerical and experimental investigations on the particle formation in oxymethylene ethers (OME_n , n = 2-4)ethylene premixed flames," Fuel, vol. 357, p. 129762, Feb. 2024, doi: 10.1016/j.fuel.2023.129762.

As the author of this Elsevier article, I retain the right to include this article in this manuscript [128]. The original source is available under the digital object identifier above.

Author contributions

Tab. P.3: Author contributions to publication [93] following CRediT [127]

Robert Martin Schmitz	Conceptualization of the numerical setup and investigations (equal) Conduction of detailed numerical simulations Conduction of sensitivity studies Conduction of reaction pathway analysis Interpretation and discussion of the numerical results (lead) Data analysis and visualization (equal) Writing – Original draft Main author
Federica Ferraro	Conceptualization of the numerical setup and investigations (equal) Interpretation and discussion of the numerical results (support) Data analysis and visualization (equal) Supervision (equal) Joint corresponding author
Mariano Sirignano	Conceptualization of the investigations (equal) Interpretation and discussion of the numerical results (support) Interpretation and discussion of the experimental results (equal) Joint corresponding author
Christian Hasse	Conceptualization of the numerical setup and investigations (equal) Supervision (equal) Funding acquisition
All co-authors	Writing – Review & Editing

Use of publication contents in finalized and ongoing dissertations

This publication is part of the ongoing dissertation of Robert Martin Schmitz at the Institute for Simulation of reactive Thermo-Fluid Systems at the Technical University of Darmstadt, Germany.

Fuel 357 (2024) 129762

Contents lists available at ScienceDirect

Fuel

journal homepage: www.elsevier.com/locate/fuel

Full length article

Numerical and experimental investigations on the particle formation in oxymethylene ethers (OME_n, n = 2–4)/ethylene premixed flames

Robert Schmitz [a], Federica Ferraro [a,*], Mariano Sirignano [b], Christian Hasse [a]

[a] Technical University of Darmstadt, Department of Mechanical Engineering, Simulation of reactive Thermo-Fluid Systems, Otto-Berndt-Str. 2, Darmstadt, 64287, Germany

[b] Dipartimento di Ingegneria Chimica, dei Materiali e della Produzione Industriale – Università degli Studi di Napoli Federico II, P. le Tecchio 80, Napoli, 80125, Italy

ARTICLE INFO

Keywords:
Oxymethylene ether (OMEn)
Polyoxymethylene dimethyl ether (PODEn)
Soot formation
Alternative fuel
Quadrature Method of Moments (QMOM)

ABSTRACT

Alternative synthetic fuels can be produced by renewable energy sources and represent a potential route for solving long-term energy storage. Among them, oxygenated fuels have the advantage of significantly reducing pollutant emissions and can therefore be used as carbon-neutral substitute fuels for transportation. In this work, the sooting propensity of different oxymethylene ethers (OMEs) is investigated using a combined experimental and numerical study on a series of burner-stabilized premixed flames under mild to severe sooting conditions. Herein, mixtures of ethylene in combination with the three individual oxymethylene ether (OME_n) for $n = 2, 3, 4$ are compared in terms of soot formation behavior with pure ethylene flames. The kinetic mechanism from Sun et al. (Proc. Combust. Inst. 36 (2017) 1269–1278) for OME_n combustion with $n = 1, 2, 3$ is extended to include OME_4 decomposition and combustion kinetics. It is combined with a detailed quadvariate soot model, which uses the Conditional Quadrature Method of Moments (CQMOM), and the soot simulation results are validated with Laser-Induced Fluorescence (LIF) and Laser-Induced Incandescence (LII) measurements. It is observed that the three investigated OME_n with $n = 2, 3, 4$ show similar sooting behavior, mainly reducing larger aggregates while not significantly affecting the formation of smaller particles. Furthermore, the extent of soot reduction is comparable among the three OME_n. The trends and overall reduction are captured very well by the model. The modeling results are analyzed through reaction pathway analyses and sensitivity studies that show the importance of OME_n decomposition and the formation of formaldehyde (CH_2O) under rich conditions for reducing species relevant for soot precursor formation. These findings are based on the negligible differences in soot formation between the different OME_n fuels observed in this study.

1. Introduction

Oxygenated synthetic fuels can support the decarbonization of practical combustion devices by reducing pollutant emissions, especially in hard-to-electrify sectors such as maritime, heavy-duty, and air transportation. Oxymethylene ethers (OMEs [1]), $CH_3O(CH_2O)_nCH_3$, also known as polyoxymethylene dimethyl ethers (POMDMEs [2], PODEs [3], or DMMs [4]), are promising fuel candidates and are currently being investigated for self-ignition engine applications. They can be produced by renewable energy sources [5] to yield a neutral greenhouse gas balance. Recent studies, e.g., [6–11], have shown that OME fuels, pure or in blends, can significantly reduce carbon monoxide (CO), unburned hydrocarbons, and soot particles. Their molecular structure exhibits no C–C bonds, resulting in a fast oxidation process, smaller amounts of gas-phase particle precursors, and reduced particle formation.

Although the combustion of pure OMEs yields an almost complete soot suppression [9,12], its application would require a redesign of available combustion systems to exploit its full potential. Therefore, several studies are investigating an optimized injection and combustion strategy with software or hardware changes, adaptations of the injector nozzles, or the required exhaust gas after-treatment systems for the combustion of pure OMEs and reveal the possibility for an efficiency increase combined with a reduction of soot particles, nitrogen oxides (NO_x), and other regulated pollutants [12–15]. Due to its low availability of carbon-neutrally produced OMEs, using OMEs as a blend component in combination with available fossil fuels is a more feasible pathway in the near future to reduce the emissions of certain pollutants while simultaneously decreasing the carbon footprint by retrofitting available combustion systems. Expensive production costs [16] also

* Corresponding author.
E-mail addresses: ferraro@stfs.tu-darmstadt.de (F. Ferraro), mariano.sirignano@unina.it (M. Sirignano).

https://doi.org/10.1016/j.fuel.2023.129762
Received 31 May 2023; Received in revised form 3 August 2023; Accepted 7 September 2023
Available online 19 September 2023

make this an economically more practical option to maximize the environmental effect than pure OME_n combustion [17].

OMEs show good miscibility in fossil diesel [18,19] with decreasing solubility for increasing chain length [20]. The cetane number of OME_2 to OME_5 [21–23], as well as the flash, boiling, and melting points are comparable to values of diesel fuel [19,24], indicating their preferable use as fuel blends in compression ignition applications.

OME blends have been studied under practical conditions in high-pressure vessels [25,26] and by engine simulations [27–30]. Investigations on soot formation for pure or blended OMEs in canonical flames have been conducted by other groups in [10,31,32] under highly controlled conditions. The application of oxymethylene ethers in self-ignition engines in combination with their soot emission propensity has been studied in several works summarized in [33] and more recent work [13,34,35,35–37] showing that soot emissions are reduced drastically with neat OME_n combustion or combined with conventional diesel fuel while breaking the tradeoff between soot and NO_x emission. The exhaust gas recirculation parameter (EGR) is varied in some of these studies [35,36,38] to characterize the simultaneous soot and NO_x formation in more detail. Due to the lower heating value of OME fuel, adapted injectors or injection strategies need to be applied to maintain the engine performance compared to fossil fuel combustion, which is investigated in [34,35,37] with subsequent effects on pollutant emissions. Ren et al. [28] explained the soot reduction effect for OME combustion in engines with a higher ratio of premixed combustion for OME and higher content of oxygen embedded in the fuel. In Huang et al. [39], engine investigations are combined with kinetic studies to investigate the OME pyrolysis suggesting that the C–O bonds of the OME-molecule break and result in formaldehyde formation. It can be summarized for internal combustion engines, that OMEs allow for overcoming prior limitations of the combustion strategy and designing new concepts with a broader optimization range, focusing on the reduction of other pollutants, or overall combustion efficiency [13].

Recently, reduced and detailed kinetic models have been developed for OME_n with $n = 1$–3 [3,4,40–44], $n = 1$–4 [1], and $n = 1$–6 [45] and validated against experimental data for ignition delay time [1,3,46,47], laminar flame speed [32,40,47], and species data from jet-stirred reactors [4,48]. While the main combustion properties and concentration of intermediate and major combustion species are adequately reproduced by the kinetics, an accurate prediction of soot precursor species under sooty conditions was not the main focus of their development.

In our previous work [8], 20 % of OME_3 blended with ethylene in premixed flames has been found to significantly affect the total number and the size of the particles produced. Specifically, the number of small particles with a diameter $d_p < 5\,\mathrm{nm}$ has been observed to remain unchanged or slightly increase, while the total amount of larger particles and aggregates with a diameter $d_p > 20\,\mathrm{nm}$ decreased drastically. Similar trends are also found for OME_2 and OME_4 in our recent work [11], suggesting the soot reduction effect to be independent of the OME chain length. Furthermore, soot structure has been investigated finding a slightly higher aromaticity for the pure ethylene soot. Particles produced from OME_3-doped flames contained increased amounts of oxygen, mainly in the form of C=O bonds [8].

Previous studies focused on OME_3 pure and in blends with traditional fuels (e.g., [8,9,28,31,40,49]) due to its better low-temperature fluidity and volatility compared with OME_4 or larger compounds. OME_n with n > 5 exhibit a too-high melting point, i.e., 18 °C for OME_5 [19], while OME_1 is too volatile as a diesel additive [49]. However, OME production is achieved by multiple processes, which lead to a mix of OME_n at different levels of polymerization [35,50]. A commercially available OME mixture, with properties suitable for diesel applications, will therefore contain besides short-chain OME_n compounds also up to 30 wt% $OME_{\geq 5}$ [19]. Hence, understanding the behavior of the different OME_n compounds is of highly practical relevance. Despite that, previous studies have only provided limited insights into the chemical effects of OME_n fuels on gas-phase chemistry, particularly soot precursors, and their subsequent influence on soot formation processes. Additionally, the similarities or differences in the effects of different OME_n variants are not thoroughly understood.

This work focuses, therefore, on the following three objectives: (i) to compare the sooting propensity of OME_n fuels with $n = 2, 3, 4$ using quantitative, experimental data based on LIF and LII measurements; (ii) to achieve a deeper understanding of the underlying processes by extending this analysis with simulations using a detailed, physicochemical soot model; (iii) to investigate the OME_n decomposition pathways and their effect on the gas-phase species pool, soot precursor formation, and consequently reduced sooting tendency of different OME_n fuels.

This study was performed on laminar, premixed flames for a systematic variation between lightly to highly sooting conditions burning a fuel mixture of ethylene and OME_n. Laser-based, in situ measurements characterized the formation of large polycyclic hydrocarbons and smaller nanoparticles by the LIF and the presence of matured soot particles by the LII technique. Similar to [8,9], numerical investigations of the sooting flames were conducted with the Conditional Quadrature Method of Moments (CQMOM) [51,52], based on the quadvariate soot model by D'Anna et al. [53]. The soot model was combined and coupled with detailed kinetics for a comprehensive description of the whole process chain. This method allows a detailed analysis of the physical and chemical soot formation pathways starting from the initial step, the fuel decomposition, to the soot growth processes. Detailed kinetic analyses are conducted to obtain more insights into the evolution of OME fuels in flames and to identify the main reaction pathways of OME_n decomposition and oxidation, which affect the formation of gas-phase precursors and species relevant for soot formation processes.

2. Experimental setup

Premixed flames burning ethylene (C_2H_4) as pure fuel and blended with 20 % of OME_2, OME_3, and OME_4 with equivalence ratios of $\phi = 2.01$, 2.16, 2.31, and 2.46 are stabilized on a water-cooled capillary burner with a diameter of 58 mm. A steel plate positioned 30 mm above the burner exit and water-recirculating cooled from a water bath of a temperature of 80 °C was used to stabilize the flame. Further details of this atmospheric flat flame burner setup can be found in [54–56].

OME_n, for $n = 2, 3, 4$, are added by replacing some of the ethylene (20 % of the total carbon fed), being ethylene/air flames the reference. Equivalence ratio, a cold gas velocity at room temperature (25 °C) of $u = 0.1\,\mathrm{ms^{-1}}$ at the inlet, and total carbon flow rate are kept constant while C_2H_4 is partially substituted by OME_n. In order to achieve this, nitrogen (N_2) and oxygen (O_2) streams are adapted accordingly. All flames of one equivalence ratio, therefore, feature identical carbon concentration and carbon flow rates to prevent any dilution of the carbon content across different fuel compositions. A blending ratio of 20 % is selected because substituting small amounts of ethylene with an oxygenated fuel proved to not significantly change temperature profiles when preserving the flame parameters as described above, which is demonstrated in [54,57–62] for other oxygenated fuels in a similar burner configuration. Additionally, practical considerations described in the introduction support the investigation of blending ratios containing only small amounts of OME_n. The summarized flame conditions investigated in this work are reported in Table 1.

Constant carbon yield due to identical carbon streams and equivalence ratio, similar temperature profile, and similar residence time of the soot particles due to identical cold gas flow rates ensure a fair comparison between the investigated fuels. Other studies investigating fuel effects differentiate between dilution effects, thermal effects, and chemical effects [63–65]. In the current study, any differences in the gas-phase precursors or regarding the soot processes can be attributed to chemical effects due to the molecular structure of the OME_n fuel since thermal effects and dilution effects regarding the carbon content are negligible or not present due to the choice of flame conditions and mixture compositions as described above.

Table 1
Flame inflow conditions given in mole fractions. OME_n indicates the mole fraction of OME_2, OME_3 and OME_4 in the corresponding flames, respectively.

ϕ		$C_2H_4/O_2/N_2$	$C_2H_4/OME_2/O_2/N_2$	$C_2H_4/OME_3/O_2/N_2$	$C_2H_4/OME_4/O_2/N_2$
2.01	OME_n	–	0.0123	0.0099	0.0082
	C_2H_4	0.1234	0.0987	0.0987	0.0987
	N_2	0.6925	0.7110	0.7147	0.7172
	O_2	0.1841	0.1780	0.1767	0.1759
2.16	OME_n	–	0.0131	0.0105	0.0088
	C_2H_4	0.1313	0.1051	0.1051	0.1051
	N_2	0.6862	0.7055	0.7093	0.7119
	O_2	0.1824	0.1763	0.1751	0.1743
2.31	OME_n	–	0.0139	0.0111	0.0093
	C_2H_4	0.1392	0.1114	0.1114	0.1114
	N_2	0.6800	0.7000	0.7040	0.7066
	O_2	0.1808	0.1747	0.1735	0.1727
2.46	OME_n	–	0.0147	0.0118	0.0098
	C_2H_4	0.1469	0.1175	0.1175	0.1175
	N_2	0.6739	0.6946	0.6987	0.7015
	O_2	0.1792	0.1732	0.1720	0.1712

Laser-Induced Emission (LIE) measurements in the 200 nm to 550 nm range are applied to detect particles in the flame, using the fourth harmonic of an Nd:YAG laser at 266 nm as the excitation source [8,57]. The emitted spectra are collected with an intensified charge-coupled device (ICCD) camera with a gate of 100 ns, allowing to distinguish between the broad LIF signal, ranging between 300 nm and 400 nm, and the LII following a blackbody curve and evaluated at 550 nm. Experimental uncertainty of the LIF and LII measurements is estimated to be approximately ±5 % of the measurement value. This quantification is derived from uncertainties due to oscillations of the laser source (less than 1 %) and variations in the applied mass flow (less than 1 %). A more detailed description of the systems is given in [54,66,67].

3. Numerical modeling

3.1. Gas-phase kinetics

In this work, the kinetic mechanism employed in [8,9], constituted by the detailed mechanism from D'Anna and co-workers [53] combined with the $OME_{1\text{-}3}$ kinetics from Sun et al. [40], is further developed.

The kinetic mechanism is extended to cover the decomposition and combustion reactions of OME_4. Reaction pathways for OME_4 analogous to smaller OMEs are added following the same reaction coefficients, similar to the approach adopted by Sun et al. [40]. In Tab. S2 of the supplementary material, reactions added for OME_4 are reported. Similarly to other OMEs, both formation of radicals and unimolecular decomposition are considered. Small fragments from OME_4 decomposition follow reaction pathways already established in previous mechanisms [8,40]. In addition, following considerations made in [8], a revised oxidation of CH_2O is proposed according to reaction rates found in the literature [68–73]. Further details on the modified reaction rate coefficients are reported in Tab. S1 in the supplementary material. The gas-phase kinetic mechanism extended for the OME_4 fuel consists of 758 reactions in total involving 154 species. It is worth noting that changes in CH_2O oxidation do not change the general trend found for different OME_n compounds (See Fig. S2 in the supplementary material). Further details are discussed hereon.

Experimentally quantified temperature profiles [60] for the pure ethylene flames at the four different equivalence ratios of consistent conditions are imposed in the simulations and also for OME_n doped flames, similarly to the approach applied in [8].

3.2. Soot modeling

A detailed physicochemical soot formation model [53] combined with the CQMOM is employed to study the sooting properties from OME_2 to OME_4. The numerical approach developed in [51] has been successfully applied in several atmospheric premixed flames [8,51,52]. The gas-phase kinetics account for species up to pyrene ($C_{16}H_{10}$), whereas PAH compounds with a molecular weight larger than pyrene are not treated as individual species but considered as lumped species (*large PAHs*). The CQMOM describes the evolution of their distribution. The soot model distinguishes between three different particle structures based on their state of aggregation [53]: *large PAHs*, *clusters*, and *aggregates*. *Clusters* are spherically shaped, solid soot particles formed by the inception steps involving *large PAHs*. *Aggregates* are fractal-shaped particles generated by the aggregation of several *clusters*.

The evolution of the chemical and physical properties of each particle class is described by the population balance equation (PBE) for the number density function (NDF) $f(\underline{\xi}; \underline{x}, t)$, which depends on the spatial coordinates $\underline{x}$, the time t, and the internal property vector $\underline{\xi} = [\xi_{nc}, \xi_{H/C}, \xi_{stat}, \xi_{typ}]^T$. $\underline{\xi}$ contains two continuous properties ξ_{nc}, indicating the number of carbon atoms with $\xi_{nc} \in [0, \infty)$, and $\xi_{H/C}$ describing the carbon to hydrogen ratio with $\xi_{H/C} \in [0, 1]$. ξ_{typ} and ξ_{stat} are discrete dimensions representing the type of entities $\xi_{typ} \in A, A = \{$*large PAHs, clusters, aggregates*$\}$, and ξ_{stat} the chemical reactivity with $\xi_{stat} \in B, B = \{$*stable, radical*$\}$.

The CQMOM is used to solve the quadrivariate NDF. Following [51], the quadrivariate NDF is reformulated in six bivariate NDFs and a set of 36 statistical moments is solved to account for the soot particle evolution. Further details on the numerical approach can be found in [51,52].

The soot processes, which provide the moment source terms, are formulated based on Arrhenius-rate laws and include growth processes such as the H-Abstraction-C_2H_2-Addition (HACA) mechanism, the resonantly stabilized free radical mechanism, or surface growth due to chemical processes. Nucleation steps for different-sized large PAHs are accounted for, resulting in clusters with various chemical properties as well as oxidation and oxidation-induced fragmentation, dehydrogenation, and aggregation processes of several clusters, resulting in chain-like formed aggregates.

The gas-phase kinetics with its largest species $C_{16}H_{10}$ and the CQMOM, which models the distribution of the (*large PAHs*) and particles (clusters and aggregates), are bidirectionally coupled through all species that are involved in the formation and growth of large PAHs and the soot maturation processes namely the aromatic species (C_6H_6 to $C_{16}H_{10}$) and additionally H, OH, H_2, H_2O, C_2H_2, HCO, CO, and O_2. Nucleation accounts for several dimerization reactions by several *large PAHs*.

The system of transport equations, chemical source terms, evaluation of thermodynamic properties, and soot modeling by the CQMOM is solved with the in-house solver Universal Laminar Flame solver (ULF) [74].

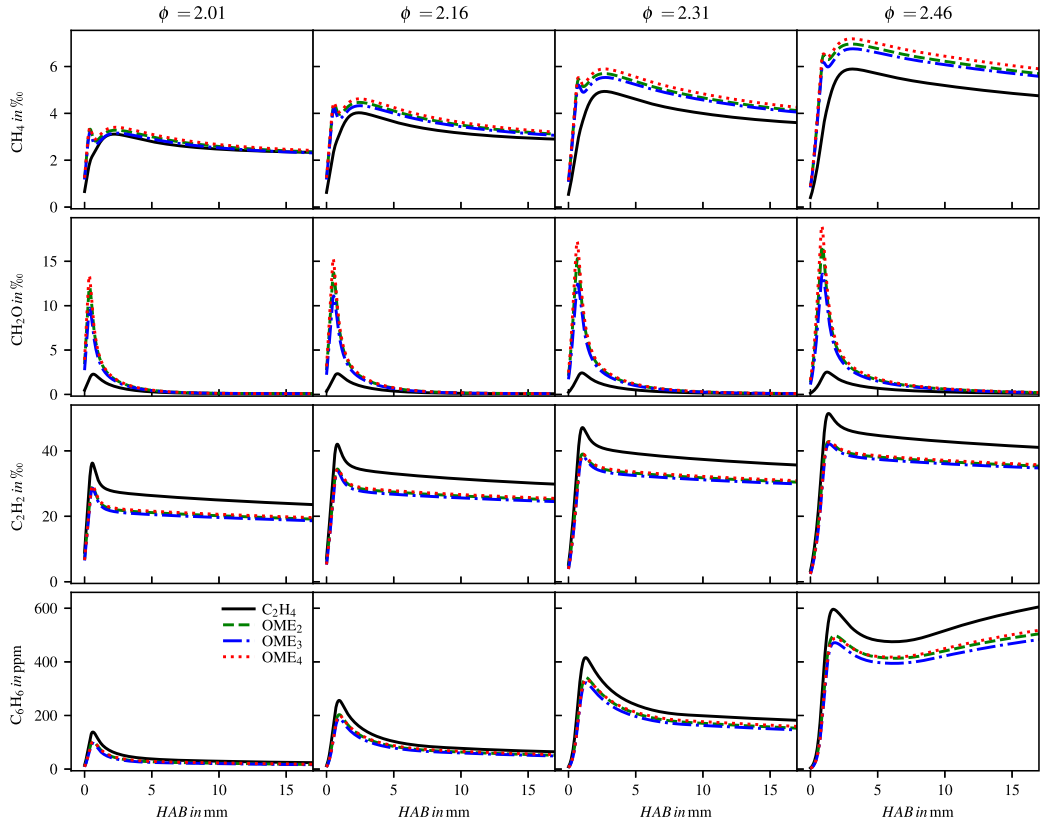

Fig. 1. Simulated species mole fraction profiles of CH_4, CH_2O, C_2H_2, and C_6H_6 as a function of height above the burner HAB obtained for pure ethylene and OME_n/ethylene blended mixtures for $n = 2, 3, 4$ at different equivalence ratios.

4. Results

Firstly, experimental and numerical results for gas-phase species and soot formation in ethylene and ethylene/OME_n flames are presented. Then, reaction pathways flux analyses are performed for the richest condition $\phi = 2.46$ to characterize the decomposition of the investigated OME_n. Additionally, the influence of selected OME_n reactions on formaldehyde formation is evaluated through a sensitivity study.

4.1. Gas-phase analysis and soot formation in OME_2, OME_3, and OME_4 blended flames

The investigated flames with pure ethylene fuel and OME_n/ethylene blended mixtures are analyzed based on simulation results of the mole fraction profiles for the main combustion products, major intermediate species, oxygenated products of the OME_n decomposition, and soot precursor species. Graphs of selected species are plotted in Fig. 1, while additional species are not shown here for brevity but are attached (see Fig. S4 and Fig. S5 in the supplementary material).

The mole fraction profiles of H_2O, CO, H, and H_2 are almost insensitive to the OME_n blending, while a slightly higher amount of CO_2 forms when adding OME_n compounds due to a more complete combustion as expected. This finding agrees well with experimental data measured in two laminar premixed configurations burning neat OME_n with $n = 0, 1, 2, 3, 4$ at leaner conditions with equivalence ratios of $\phi = 1.0$ and $\phi = 1.7$ from Gaiser et al. [75]. There, the species pool was almost independent of the OME chain length.

Generally, a better oxidation mechanism for OME_n is expected due to the absence of C–C bonds in the fuel structure. Methane (CH_4) and formaldehyde (CH_2O), which are principal species during the decomposition process of OME_n, as well as the important soot precursor species acetylene (C_2H_2) and benzene (C_6H_6) are plotted in Fig. 1 for the four equivalence ratios and fuel mixtures against the height above the burner (HAB). As expected, CH_4 and CH_2O increase for higher equivalence ratios due to higher carbon content in the flame. An additional increase is visible in the OME_n-doped flames compared to the pure ethylene flames. In particular, CH_4 is significantly higher in concentration in OME_n-doped flames as equivalence ratios increase, suggesting a more effective decomposition process. The CH_2O profile contains a distinct peak close to the inlet again because of fast oxidation/decomposition pathways. Then CH_2O quickly decomposes further downstream to even smaller species. In general, the preferential pathways leading to the formation of CH_2O suggest a fast decomposition and a more complete combustion process when OME_n is used compared to pure ethylene. Further oxygenated species are reported in Fig. S5 in the supplementary material.

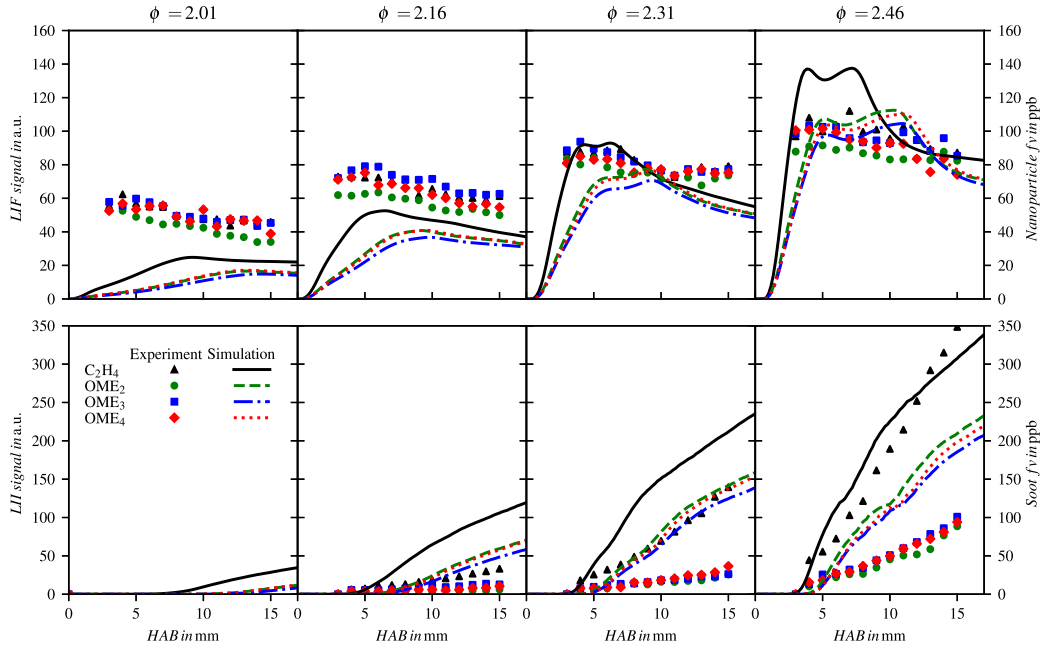

Fig. 2. Comparison of the simulated nanoparticle volume fraction against the measured LIF signal (top row) and the simulated soot volume fraction against the measured LII signal (bottom row) for the four investigated equivalence ratios and fuel compositions. Lines indicate predicted profiles simulated using the quadvariate CQMOM model whereas dots represent experimental data. The pure ethylene flame is colored black and the OME_n-doped flames are colored green, blue and red representing OME_2, OME_3, and OME_4 fuel addition to the flame. (For interpretation of the references to color in this figure legend, the reader is referred to the web version of this article.)

Measurements in laminar flow reactors investigating flames burning pure OME_n with n = 0–5 at equivalence ratios of $\phi = 0.8, 1.2, 2.0$ with an electron ionization molecular-beam mass spectrometer for species quantification [76] suggest that oxygenated intermediates are dominating the species pool. In the current simulations, the doping of 20 % OME_n ($n = 2, 3, 4$) to ethylene flames results in a significant increase of oxygenated species such as CH_2O, which indicates that conclusions of the experimental findings [76] are also valid for richer and therefore soot-relevant conditions at $\phi = 2.01, 2.16, 2.31, 2.46$.

OME doping inhibits the formation of species relevant for particle formation and growth, such as C_2H_2 and C_6H_6. These species lead to the formation of intermediate soot precursors and directly contribute to soot formation processes due to surface growth by the HACA process or deposition onto the particle surface (by C_6H_6 or larger PAHs). The C_2H_2 mole fraction is constantly higher in pure ethylene flames across all the equivalence ratios because it mostly comes from ethylene dehydrogenation pathways. Hence, C_2H_2 mainly depends on the amount of ethylene present in the blend disregarding the equivalence ratio investigated. The effect of OME_n is indeed of the first order on this species and an even more pronounced effect on particle formation is expected at higher equivalence ratios, where surface growth plays a major role. On the other hand, the reduction of C_6H_6 increases at higher equivalence ratios due to the relation of C_6H_6 formation to intermediate C_3 and C_4 compounds. The effect of C_6H_6 on particles is more complex to follow since it directly influences PAH formation, thus slowing down the inception process. This is likely to have a significant effect also at lower equivalence ratios where inception is the controlling step for the soot evolution and growth process. Overall, it is interesting that both the profile shape and the mole fraction values for all the key species plotted show negligible differences for the different OME_n at all the equivalence ratios. These findings suggest similar soot formation behavior of the investigated OME_n compounds.

Fig. 2 shows the modeling results for particles compared with experimentally measured nanoparticles and soot particles for the investigated equivalence ratios and different OME_n-blended mixtures. As done in previous works [8,9,11,52], here LIF signal is associated with aromatic hydrocarbons in the condensed-phase, i.e., nanoparticles [66], whereas the LII signal arises from the larger, solid soot particles and aggregates. In order to better compare modeling results with experimental data, following previous studies [8,52], the total amount of all particles modeled of the state cluster and aggregate is split depending on particle diameter. Specifically, nanoparticle volume fraction includes particles smaller than the split diameter $d_{p,split}$, while soot volume fraction includes particles with a diameter larger than $d_{p,split}$. The splitting process here is performed by varying the value of split particle diameter, i.e., for $d_{p,split}$ = 2 nm and $d_{p,split}$ = 7 nm, to reduce the sensitivity of the results on the selected value. The plotted volume fraction fv is obtained as the average of both splitting processes. The error bars are not reported here for the sake of clarity. However, as shown in previous works [8,52], the choice of $d_{p,split}$ is not affecting the profile shape nor the absolute value of the volume fraction reduction by OME_n addition.

In previous studies [8,9], it has been found that OME_3 addition reduces the formation of large soot aggregates significantly, while the formation of smaller nanoparticles is less affected. The LIF measurements in Fig. 2 suggest similar trends for OME_2 and OME_4-doped flames. There is indeed no noticeable difference in the LIF signal for the pure C_2H_4 flame compared to OME_3 and OME_4-doped flames, the OME_2-doped flame exhibits the smallest signal value while still being close to the other results and within the measurement uncertainty. The simulation results of the nanoparticle formation show minor differences

in OME_n compounds and therefore reproduce the trends observed in the experiments. The model captures a slowing down of the particle formation process. Despite the model slightly overpredicting the nanoparticle peak in the richest ethylene flame, it reproduces the trend of nanoparticle concentration for ethylene and OME_n blends. Overall it is interesting to note that all the OMEs behave similarly to other oxygenated fuels [57], having a minor impact on the total formation of small nanoparticles, which dominate particle size distribution in terms of number [8]. In Richter et al. [32], the sooting propensity of OME_n-doped laminar premixed diesel flames with $n = 3, 4, 5$ were measured and compared at which equivalence ratio the OME_n mixture starts to soot. Similar sooting thresholds were found for the individual OME_n, which agrees with the current quantitative investigations. The LII measurements of this study show the onset of soot formation at an equivalence ratio of $\phi = 2.16$ for all OME_n mixtures, while no soot is measured for $\phi = 2.01$. Furthermore, the quantitative soot reduction for the three investigated OME_n compounds at higher equivalence ratios is comparable. Thus, the experimental results indicate that the reduction of large aggregates is similar for mixtures blended with OME_2, OME_3, and OME_4. Regarding the simulation results, the significant reduction of large particles due to OME_2, OME_3, and OME_4 addition is well captured by the model. Nevertheless, the overall soot reduction predicted by the model is less than the amount observed in the experiments.

In our previous work [8], a soot reduction of up to 70 % is experimentally observed for the OME_3-doped flames relative to neat ethylene flames. Compared to the previous modeling results of the OME_3-doped flame simulations, the formaldehyde decomposition of the base mechanism has been revised in this work. These changes improve the numerically obtained soot reduction from approx. 25 % in [8] to 44 % for the richest OME_3 flame and 33 % for the OME_4 flame of this work, which is significantly closer to the measurements. Furthermore, these results confirm the validity of the approach of extending the gas-phase kinetics, originally developed by Sun et al. [40] for OME_n with $n = 1, 2, 3$, with the kinetics of OME_4 similar to its smaller counterparts for the investigated conditions.

4.2. Reaction analysis

The gas-phase kinetics is further analyzed to identify the main reaction pathways under rich flame conditions and better understand the reaction pathways for different OME_n. Fig. 3 schematically displays the reaction pathways of the OME_3 decomposition to smaller species for a mixture of $C_2H_4/OME_3/O_2/N_2$ at an equivalence ratio of $\phi = 2.46$ and temperature $T = 1500$ K, which corresponds to a position of approximately $HAB = 0.001$ m within the premixed flames. The composition of the gas-phase is according to Table 1. The carbon flux indicates that for OME_3, oxidation/decomposition pathways lead rapidly to CH_2O formation. The importance of this latter in OME_n-doped, rich combustion is hence crucial, and its oxidation/decomposition determines the overall particle reduction. Furthermore, it is observed that in the fuel-rich conditions analyzed in this study, the unimolecular pathways, almost irrelevant (<1 %) in the leaner conditions analyzed by Sun et al. (See Fig. 5 in [40]), are here significant. Approximately 35 % of the carbon contained in the OME_3 fuel indeed decomposes through unimolecular decomposition reactions. Similar trends have been observed in the reaction pathway analysis for OME_2 (≈50 %) and OME_4 (≈36 %), shown in Fig. 4 and Fig. 5. Large amounts of CH_2O and other aldehydic compounds are formed during OME_n combustion, whereas almost no other oxygenated species are produced. This could be linked to the presence of a specific oxygen functionality on particles found experimentally [8].

Molecular dynamics simulations for OME_3, OME_4, and OME_5 pyrolysis at high temperatures combined with calculation of bond dissociation energies of the corresponding individual C–O bonds of the OME_n molecule found CH_3, CH_3O, and CH_2O to be the decomposition products of the largest quantity [77]. C-H breaking and initial H-abstraction were found not to be the dominating reaction pathways for OME_n pyrolysis [77]. Among the unimolecular reactions, the ones breaking the inner C–O bonds were the ones favored over the dissociation of outer C–O bonds in the OME_n molecules [77]. Both studies, Zhu et al. [77] and the current one, suggest that unimolecular reaction pathways mostly affect the initial reactions under rich or pyrolytic conditions. Other studies, e.g., [40,48] focused on slightly lean to slightly rich flames and found H-abstraction reactions to mainly decompose the initial OME_n molecules under these conditions. Further investigation on the unimolecular reaction pathways for the context of soot formation is needed.

Finally, Fig. 6 shows the sensitivity of the mole fraction peaks of the species CH_2O, C_2H_2, C_6H_6, and $C_{16}H_{10}$ in the richest OME_3 flame with an equivalence ratio of $\phi = 2.46$ for a small change ($k = 0.5$ %) of the reaction rate coefficients of selected reactions decomposing OME_3 into radicals and smaller species. Sensitivity analysis confirms the general picture seen in reaction pathway analysis for CH_2O formation. The formation of the OME_3A radical and the breaking of OME_3 into small fragments strongly favor CH_2O formation. On the other side, OME_3B radicals and even more OME_3C radicals have a negative impact on the CH_2O formation, slowing down the process. OME_3B eventually decomposing into small fragments (R648) would recover its capability of fast-producing CH_2O. Similar results are obtained for OME_2 and OME_4 (see Fig. S2 and Fig. S3 in the supplemental material). Sensitivity analysis for OME_2 shows a strong preference for OME_2A radical for CH_2O formation without a possibility of recovering for OME_2B. On the other side, for OME_4, the only radical that inhibits CH_2O formation is OME_4C, whereas OME_4B quickly breaks into small fragments and favors CH_2O formation.

The subsequent effect on soot precursor formation is additionally shown in Fig. 6 through the soot-relevant species C_2H_2, and the aromatic and PAH species benzene and pyrene, C_6H_6 and $C_{16}H_{10}$, respectively. The sensitivities of their mole fraction peaks are scaled by a factor of 2, 6, and 16, respectively, which represent the number of carbon atoms of each molecule to demonstrate the sensitivity of the carbon streams. Fig. 6 illustrates that the C_2H_2 peak is not significantly affected by the initial decomposition reactions of the OME_3 fuel. In the investigated flames, the largest contribution to C_2H_2 formation seems not to be originating from OME_3 fuel but due to the C_2H_4 decomposition. On the other hand, C_6H_6 and $C_{16}H_{10}$ peaks are highly affected by small changes in the initial OME_3 decomposition reactions. Direct decomposition of OME_3 to smaller fragments, such as reactions R621, R622, R623, and R624, slightly favors the formation of aromatic species, with the impact being generally small. OME_3B decomposition shows a clear trend. Here, the decomposition of OME_3B to a methyl radical (R647) increases the aromatics formation, while decomposition into smaller fragments (R648) significantly reduces their peaks. The two reactions with the highest sensitivity on the benzene and pyrene peak (R647, R648) suggest a correlation between the CH_2O peak increase and the reduction of aromatic species. The remaining reactions show an overall quite small sensitivity on the formation of aromatics and PAHs. Here, additional aspects seem to superpose the formation of benzene and pyrene and to have counteracting effects on their formation.

Results for the OME_2 and OME_4 flames are attached (see Fig. S2 and Fig. S3 in the supplementary material). Similar trends can be observed for OME_2 and OME_4. For instance, the reaction R691, which decomposes OME_4, is favoring CH_2O formation and simultaneously reduces the benzene and pyrene peak, and R692 shows the inverse effect with a reduction of CH_2O and an increase in C_6H_6 and $C_{16}H_{10}$ for a decomposition toward OME_4C. The current results demonstrate the high impact of the initial decomposition pathways of the OME_n molecules on the formation of CH_2O and subsequent soot precursors.

It can be concluded that the chemical effect of OME_n relies upon a delay of the soot formation process due to the formation of CH_2O

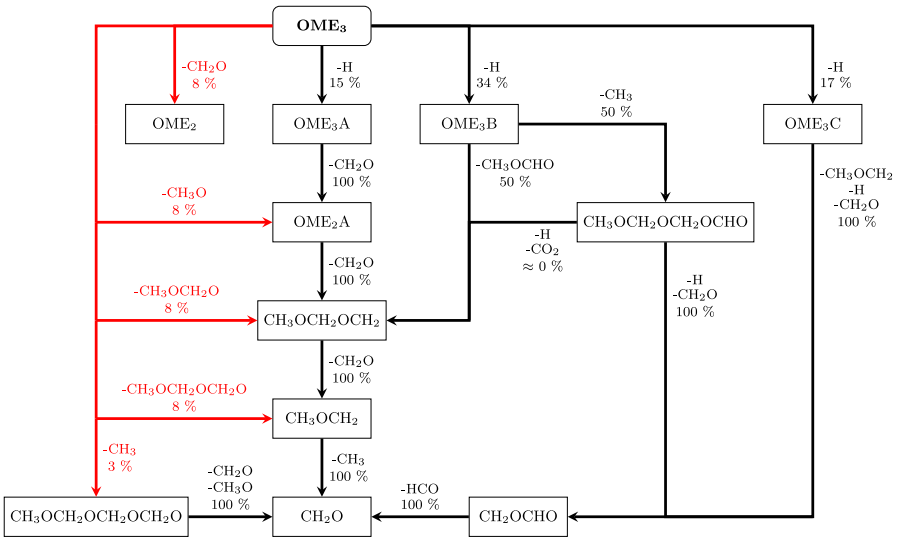

Fig. 3. Reaction pathways for OME_3 based on the integrated carbon flux for the $C_2H_4/OME_3/O_2/N_2$ mixture at ϕ = 2.46. The numbers are the flux percent contribution relative to the species on the source side. The red lines indicate the unimolecular decomposition pathways. According to [40], OME_3A: $CH_3OCH_2OCH_2OCH_2OCH_2$; OME_3B: $CH_3OCH_2OCH_2OCHOCH_3$; OME_3C: $CH_3OCH_2OCHOCH_2OCH_3$; OME_2A: $CH_3OCH_2OCH_2OCH_2$. (For interpretation of the references to color in this figure legend, the reader is referred to the web version of this article.)

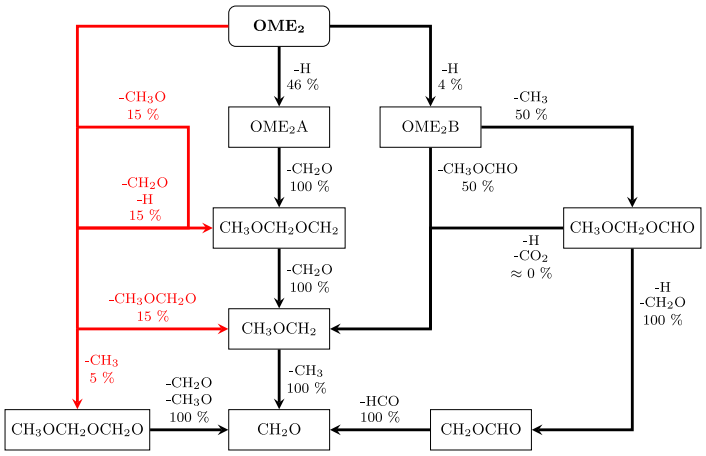

Fig. 4. Reaction pathways for OME_2 based on the integrated carbon flux for the $C_2H_4/OME_2/O_2/N_2$ mixture at ϕ = 2.46. The numbers are the flux percent contribution relative to the species on the source side. The red lines indicate the unimolecular decomposition pathways. According to [40], OME_2A: $CH_3OCH_2OCH_2OCH_2$; OME_2B: $CH_3OCH_2OCHOCH_3$. (For interpretation of the references to color in this figure legend, the reader is referred to the web version of this article.)

subtracting carbon from the formation pathways of aromatic species. The abstraction of methyl radicals CH_3 seems to represent the only major pathway that could lead to the formation of aromatic structures via subsequent acetylene formation or propargyl recombination mechanisms during the initial decomposition process of the OME_n fuel. In comparison, the decomposition of C_2H_4 leads to an immediate formation of C_2H_2 due to dehydrogenation and subsequent rapid formation of PAH species.

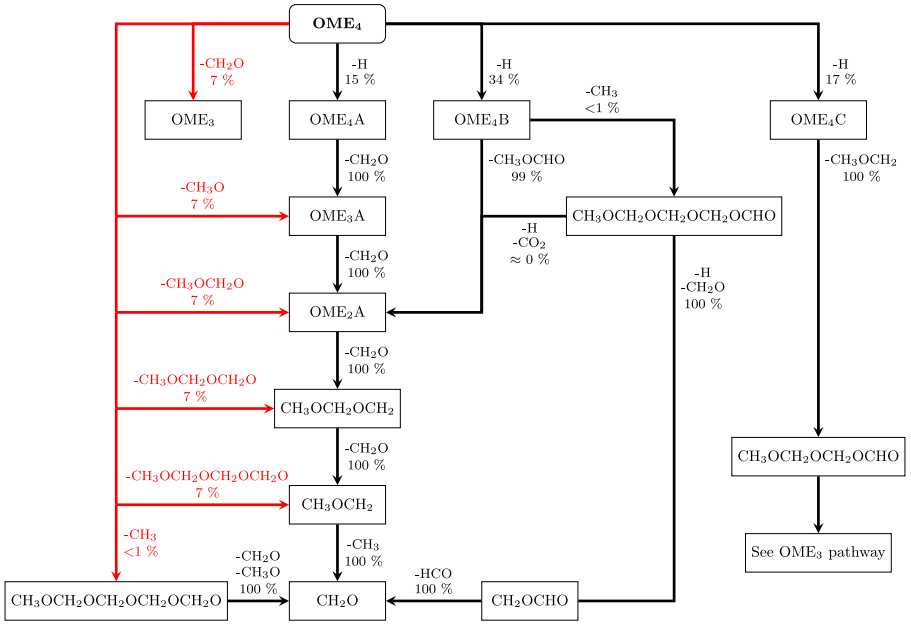

Fig. 5. Reaction pathways for OME_4 based on the integrated carbon flux for the $C_2H_4/OME_4/O_2/N_2$ mixture at $\phi = 2.46$. The numbers are the flux percent contribution relative to the species on the source side. The red lines indicate the unimolecular decomposition pathways. According to [40], OME_4: $CH_3OCH_2OCH_2OCH_2OCH_2OCH_3$; OME_4A: $CH_3OCH_2OCH_2OCH_2OCH_2OCH_2$; OME_4B: $CH_3OCH_2OCH_2OCH_2OCHOCH_3$; OME_4C: $CH_3OCH_2OCH_2OCHOCH_2OCH_3$; OME_3A: $CH_3OCH_2OCH_2OCH_2OCH_2$; OME_3B: $CH_3OCH_2OCH_2OCHOCH_3$; OME_3C: $CH_3OCH_2OCHOCH_2OCH_3$; OME_2A: $CH_3OCH_2OCH_2OCH_2$. (For interpretation of the references to color in this figure legend, the reader is referred to the web version of this article.)

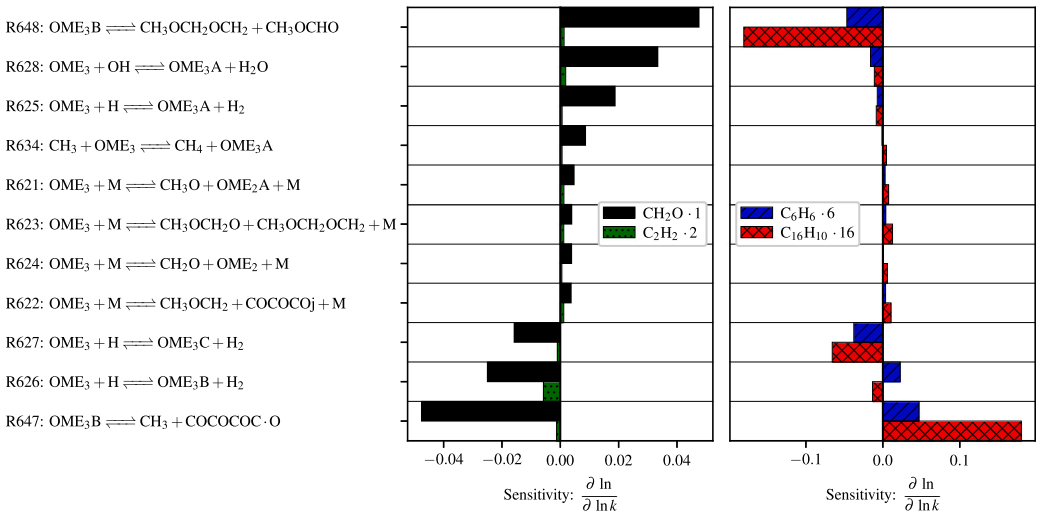

Fig. 6. Sensitivity of the mole fraction peaks of the species CH_2O, C_2H_2, C_6H_6, and $C_{16}H_{10}$ for small perturbations of different reaction rates in the richest OME_3 flame at $\phi = 2.46$. Sensitivities are scaled by the number of carbon atoms present in the corresponding species. According to [40], OME_3: $CH_3OCH_2OCH_2OCH_2OCH_3$; OME_3A: $CH_3OCH_2OCH_2OCH_2OCH_2$; OME_3B: $CH_3OCH_2OCH_2OCHOCH_3$; OME_3C: $CH_3OCH_2OCHOCH_2OCH_3$; OME_2: $CH_3OCH_2OCH_2OCH_3$; OME_3A: $CH_3OCH_2OCH_2OCH_2$; COCOCOj: $CH_3OCH_2OCH_2O$; COCOCOC·O: $CH_3OCH_2OCH_2OCHO$.

5. Conclusions

The sooting propensity of different OME_n compounds for $n = 2, 3, 4$ was investigated by combining experimental measurements with numerical simulations. Ethylene flames with equivalence ratios of $\phi = 2.01, 2.16, 2.31, 2.46$ blended with 20 % OME_n compounds of different chain lengths were studied. Experimental LIF and LII measurements for these flames were performed, which exhibited similar trends for the soot formation properties of the three OME_n investigated. Adding all OME_n compounds leads primarily to a reduction of soot aggregates compared to pure ethylene flames, which was observed in the numerical results and confirmed by the LII measurements. On the other hand, LIF measurements and modeling suggest that nanoparticles are less affected. A comparable total amount of soot particle reduction for the three OME_n was observed. Furthermore, the kinetic mechanism from Sun et al. [40] for OME_{1-3} was extended with OME_4 kinetics to study the gas-phase species under fuel-rich conditions. Numerical simulations were performed using the detailed kinetic mechanism in combination with the CQMOM soot model. The modeling reproduces the experimentally observed trends of the soot reduction very well for all OME_n compounds. Reaction pathway analyses and sensitivity studies for the OME_n show the importance of fuel decomposition under the investigated conditions for CH_2O formation. Overall, the different OME_n showed similar soot formation under the conditions investigated, suggesting that some differences could arise when the initial steps of oxidation/decomposition become slow enough to be the controlling steps.

CRediT authorship contribution statement

Robert Schmitz: Writing – review & editing, Writing – original draft, Visualization, Investigation, Data curation, Conceptualization. **Federica Ferraro:** Writing – review & editing, Writing – original draft, Supervision, Conceptualization. **Mariano Sirignano:** Writing – review & editing, Writing – original draft, Investigation, Data curation, Conceptualization. **Christian Hasse:** Writing – review & editing, Supervision, Funding acquisition, Conceptualization.

Declaration of competing interest

The authors declare that they have no known competing financial interests or personal relationships that could have appeared to influence the work reported in this paper.

Data availability

Data will be made available on request.

Acknowledgments

The authors gratefully acknowledge the funding by the German Federal Ministry of Education and Research (BMBF) as part of the NAMOSYN Project (project number 03SF0566R0).

Appendix A. Supplementary data

Supplementary material related to this article can be found online at https://doi.org/10.1016/j.fuel.2023.129762.

References

[1] Cai L, Jacobs S, Langer R, Vom Lehn F, Heufer KA, Pitsch H. Auto-ignition of oxymethylene ethers (OMEn, n=2–4) as promising synthetic e-fuels from renewable electricity: Shock tube experiments and automatic mechanism generation. Fuel 2020;264:116711. http://dx.doi.org/10.1016/j.fuel.2019.116711.

[2] Burger J, Siegert M, Ströfer E, Hasse H. Poly(Oxymethylene) dimethyl ethers as components of tailored diesel fuel: Properties, synthesis and purification concepts. Fuel 2010;89(11):3315–9. http://dx.doi.org/10.1016/j.fuel.2010.05.014.

[3] He T, Wang Z, You X, Liu H, Wang Y, Li X, et al. A chemical kinetic mechanism for the low- and intermediate-temperature combustion of polyoxymethylene dimethyl ether 3 (PODE3). Fuel 2018;212:223–35. http://dx.doi.org/10.1016/j.fuel.2017.09.080.

[4] Wang H, Yao Z, Zhong X, Zuo Q, Zheng Z, Chen Y, et al. Experimental and kinetic modeling studies on low-temperature oxidation of polyoxymethylene dimethyl ether (DMM1-3) in a jet-stirred reactor. Combust Flame 2022;245:112332. http://dx.doi.org/10.1016/j.combustflame.2022.112332.

[5] Fenard Y, Vanhove G. A mini-review on the advances in the kinetic understanding of the combustion of linear and cyclic oxymethylene ethers. Energy Fuels 2021;35(18):14325–42. http://dx.doi.org/10.1021/acs.energyfuels.1c01924.

[6] Wang Z, Liu H, Ma X, Wang J, Shuai S, Reitz RD. Homogeneous charge compression ignition (HCCI) combustion of polyoxymethylene dimethyl ethers (PODE). Fuel 2016;183:206–13. http://dx.doi.org/10.1016/j.fuel.2016.06.033.

[7] Liu H, Wang Z, Wang J, He X. Improvement of emission characteristics and thermal efficiency in diesel engines by fueling gasoline/diesel/PODEn blends. Energy 2016;97:105–12. http://dx.doi.org/10.1016/j.energy.2015.12.110.

[8] Ferraro F, Russo C, Schmitz R, Hasse C, Sirignano M. Experimental and numerical study on the effect of oxymethylene ether-3 (OME3) on soot particle formation. Fuel 2021;286:119353. http://dx.doi.org/10.1016/j.fuel.2020.119353.

[9] Schmitz R, Sirignano M, Hasse C, Ferraro F. Numerical investigation on the effect of the oxymethylene ether-3 (OME3) blending ratio in premixed sooting ethylene flames. Front Mech Eng 2021;7:744172. http://dx.doi.org/10.3389/fmech.2021.744172.

[10] Tan YR, Salamanca M, Pascazio L, Akroyd J, Kraft M. The effect of poly(Oxymethylene) dimethyl ethers (PODE3) on soot formation in ethylene/PODE3 laminar coflow diffusion flames. Fuel 2021;283:118769. http://dx.doi.org/10.1016/j.fuel.2020.118769.

[11] Schmitz R, Russo C, Ferraro F, Apicella B, Hasse C, Sirignano M. Effect of oxymethylene ether-2-3-4 (OME2-4) on soot particle formation and chemical features. Fuel 2022;324:124617. http://dx.doi.org/10.1016/j.fuel.2022.124617.

[12] Gelner AD, Rothe D, Kykal C, Irwin M, Sommer A, Pastoetter C, et al. Particle emissions of a heavy-duty engine fueled with polyoxymethylene dimethyl ethers (OME). Environ Sci Atmos 2022;2(2):291–304. http://dx.doi.org/10.1039/D1EA00084E.

[13] Zacherl F, Wopper C, Schwanzer P, Rabl H-P. Potential of the synthetic fuel oxymethylene ether (OME) for the usage in a single-cylinder non-road diesel engine: thermodynamics and emissions. Energies 2022;15(21):7932. http://dx.doi.org/10.3390/en15217932.

[14] Saupe C, Atzler F. Potentials of oxymethylene-dimethyl-ether in diesel engine combustion. Autom Engine Technol 2022;7(3–4):331–42. http://dx.doi.org/10.1007/s41104-022-00117-5.

[15] Gelner AD, Beck HA, Pastoetter C, Härtl M, Wachtmeister G. Ultra-low emissions of a heavy-duty engine powered with oxymethylene ethers (OME) under stationary and transient driving conditions. Int J Engine Res 2022;23(5):738–53. http://dx.doi.org/10.1177/14680874211047922.

[16] Mantei F, Ali RE, Baensch C, Voelker S, Haltenort P, Burger J, et al. Techno-economic assessment and carbon footprint of processes for the large-scale production of oxymethylene dimethyl ethers from carbon dioxide and hydrogen. Sustain Energy Fuels 2022;6(3):528–49. http://dx.doi.org/10.1039/D1SE01270C.

[17] Voelker S, Deutz S, Burre J, Bongartz D, Omari A, Lehrheuer B, et al. Blend for all or pure for few? Well-to-wheel life cycle assessment of blending electricity-based OME_{3-5} with fossil diesel. Sustain Energy Fuels 2022;6(8):1959–73. http://dx.doi.org/10.1039/D1SE01758F.

[18] Lin Q, Tay KL, Zhou D, Yang W. Development of a compact and robust Polyoxymethylene Dimethyl Ether 3 reaction mechanism for internal combustion engines. Energy Convers Manage 2019;185:35–43. http://dx.doi.org/10.1016/j.enconman.2019.02.007.

[19] Omari A, Heuser B, Pischinger S, Rüdinger C. Potential of long-chain oxymethylene ether and oxymethylene ether-diesel blends for ultra-low emission engines. Appl Energy 2019;239:1242–9. http://dx.doi.org/10.1016/j.apenergy.2019.02.035.

[20] Yang Z, Ren C, Jiang S, Xin Y, Hu Y, Liu Z. Theoretical predictions of compatibility of polyoxymethylene dimethyl ethers with diesel fuels and diesel additives. Fuel 2022;307:121797. http://dx.doi.org/10.1016/j.fuel.2021.121797.

[21] Lautenschütz L, Oestreich D, Seidenspinner P, Arnold U, Dinjus E, Sauer J. Physico-chemical properties and fuel characteristics of oxymethylene dialkyl ethers. Fuel 2016;173:129–37. http://dx.doi.org/10.1016/j.fuel.2016.01.060.

[22] Lautenschütz L, Oestreich D, Seidenspinner P, Arnold U, Dinjus E, Sauer J. Corrigendum to "Physico-chemical properties and fuel characteristics of oxymethylene dialkyl ethers" [Fuel 173 (2016) 129–137]. Fuel 2017;209:812. http://dx.doi.org/10.1016/j.fuel.2017.07.083.

[23] Deutsch D, Oestreich D, Lautenschütz L, Haltenort P, Arnold U, Sauer J. High purity oligomeric oxymethylene ethers as diesel fuels. Chem Ing Tech 2017;89(4):486–9. http://dx.doi.org/10.1002/cite.201600158.

[24] Zheng Y, Tang Q, Wang T, Liao Y, Wang J. Synthesis of a green fuel additive over cation resins. Chem Eng Technol 2013;36(11):1951–6. http://dx.doi.org/10.1002/ceat.201300360.

[25] Wiesmann F, Strauß L, Rieß S, Manin J, Wan K, Lauer T. Numerical and experimental investigations on the ignition behavior of OME. Energies 2022;15(18):6855. http://dx.doi.org/10.3390/en15186855.

[26] Goeb D, Davidovic M, Cai L, Pancharia P, Bode M, Jacobs S, et al. Oxymethylene ether – n-dodecane blend spray combustion: Experimental study and large-eddy simulations. Proc Combust Inst 2021;38(2):3417–25. http://dx.doi.org/10.1016/j.proci.2020.08.017.

[27] Lv D, Chen Y, Chen Y, Guo X, Chen H, Huang H. Development of a reduced diesel/PODEn mechanism for diesel engine application. Energy Convers Manage 2019;199:112070. http://dx.doi.org/10.1016/j.enconman.2019.112070.

[28] Ren S, Wang Z, Li B, Liu H, Wang J. Development of a reduced polyoxymethylene dimethyl ethers (PODEn) mechanism for engine applications. Fuel 2019;238:208–24. http://dx.doi.org/10.1016/j.fuel.2018.10.111.

[29] Wei Y, Zhang C, Zhu Z, Zhang Y, He D, Liu S. Numerical optimization of the EGR rate and injection timing with a novel cavitation model in a diesel engine fueled with PODE/Diesel blends. Appl Sci 2022;12(24):12556. http://dx.doi.org/10.3390/app122412556.

[30] García-Oliver JM, Novella R, Micó C, De Leon-Ceriani D. Numerical analysis of the combustion process of oxymethylene ethers as low-carbon fuels for compression ignition engines. Int J Engine Res 2023;24(5):2175–86. http://dx.doi.org/10.1177/14680874221113749.

[31] Liu Y, Cheng X, Ya Y, Wang B, Zhang P, Zhang K, et al. Impact of PODE3 on soot oxidation reactivity at different stages in N-heptane/toluene diffusion flames. Fuel 2023;331:125672. http://dx.doi.org/10.1016/j.fuel.2022.125672.

[32] Richter S, Kathrotia T, Braun-Unkhoff M, Naumann C, Köhler M. Influence of Oxymethylene Ethers (OMEn) in mixtures with a diesel surrogate. Energies 2021;14(23):7848. http://dx.doi.org/10.3390/en14237848.

[33] Liu H, Wang Z, Li Y, Zheng Y, He T, Wang J. Recent progress in the application in compression ignition engines and the synthesis technologies of polyoxymethylene dimethyl ethers. Appl Energy 2019;233–234:599–611. http://dx.doi.org/10.1016/j.apenergy.2018.10.064.

[34] Parravicini M, Barro C, Boulouchos K. Compensation for the differences in LHV of diesel-OME blends by using injector nozzles with different number of holes: Emissions and combustion. Fuel 2020;259:116166. http://dx.doi.org/10.1016/j.fuel.2019.116166.

[35] Pélerin D, Gaukel K, Härtl M, Jacob E, Wachtmeister G. Potentials to simplify the engine system using the alternative diesel fuels oxymethylene ether OME1 and OME3-6 on a heavy-duty engine. Fuel 2020;259:116231. http://dx.doi.org/10.1016/j.fuel.2019.116231.

[36] LeBlanc S, Sandhu N, Yu X, Han X, Wang M, Tjong J, et al. An investigation into OME3 on a high compression ratio engine. In: ASME 2020 Internal combustion engine division fall technical conference. Virtual, Online: American Society of Mechanical Engineers; 2020, http://dx.doi.org/10.1115/ICEF2020-2983, V001T02A007.

[37] Pastor JV, García A, Micó C, Lewiski F. Simultaneous high-speed spectroscopy and 2-color pyrometry analysis in an optical compression ignition engine fueled with OMEX-diesel blends. Combust Flame 2021;230:111437. http://dx.doi.org/10.1016/j.combustflame.2021.111437.

[38] Barro C, Parravicini M, Boulouchos K, Liati A. Neat polyoxymethylene dimethyl ether in a diesel engine; Part 2: Exhaust emission analysis. Fuel 2018;234:1414–21. http://dx.doi.org/10.1016/j.fuel.2018.07.108.

[39] Huang H, Liu Q, Teng W, Pan M, Liu C, Wang Q. Improvement of combustion performance and emissions in diesel engines by fueling N-butanol/diesel/PODE3–4 mixtures. Appl Energy 2018;227:38–48. http://dx.doi.org/10.1016/j.apenergy.2017.09.088.

[40] Sun W, Wang G, Li S, Zhang R, Yang B, Yang J, et al. Speciation and the laminar burning velocities of poly(oxymethylene) dimethyl ether 3 (POMDME3) flames: An experimental and modeling study. Proc Combust Inst 2017;36(1):1269–78. http://dx.doi.org/10.1016/j.proci.2016.05.058.

[41] Li R, Herreros JM, Tsolakis A, Yang W. Chemical kinetic study on ignition and flame characteristic of polyoxymethylene dimethyl ether 3 (PODE3). Fuel 2020;279:118423. http://dx.doi.org/10.1016/j.fuel.2020.118423.

[42] Zhao Y, Li N, Xie Y, Cheng Y, Wang X. Study on chemical kinetic mechanisms of polyoxymethylene dimethyl ethers ($PODE_n$). IOP Conf Ser Mater Sci Eng 2020;768(2):022056. http://dx.doi.org/10.1088/1757-899X/768/2/022056.

[43] Lin Q, Tay KL, Zhao F, Yang W. Enabling robust simulation of polyoxymethylene dimethyl ether 3 ($PODE_3$) combustion in engines. Int J Engine Res 2022;23(9):1522–42. http://dx.doi.org/10.1177/14680874211018363.

[44] Shrestha KP, Eckart S, Drost S, Fritsche C, Schießl R, Seidel L, et al. A comprehensive kinetic modeling of oxymethylene ethers (OMEn, N=1–3) oxidation - laminar flame speed and ignition delay time measurements. Combust Flame 2022;246:112426. http://dx.doi.org/10.1016/j.combustflame.2022.112426.

[45] Niu B, Jia M, Chang Y, Duan H, Dong X, Wang P. Construction of reduced oxidation mechanisms of polyoxymethylene dimethyl ethers (PODE1–6) with consistent structure using decoupling methodology and reaction rate rule. Combust Flame 2021;232:111534. http://dx.doi.org/10.1016/j.combustflame.2021.111534.

[46] De Ras K, Kusenberg M, Vanhove G, Fenard Y, Eschenbacher A, Varghese RJ, et al. A detailed experimental and kinetic modeling study on pyrolysis and oxidation of oxymethylene ether-2 (OME-2). Combust Flame 2022;238:111914. http://dx.doi.org/10.1016/j.combustflame.2021.111914.

[47] Ngugi JM, Richter S, Braun-Unkhoff M, Naumann C, Köhler M, Riedel U. A study on fundamental combustion properties of oxymethylene ether-2. J Eng Gas Turb Power 2022;144(1):011014. http://dx.doi.org/10.1115/1.4052097.

[48] Qiu Z, Zhong A, Huang Z, Han D. An experimental and modeling study on polyoxymethylene dimethyl ether 3 (PODE3) oxidation in a jet stirred reactor. Fundam Res 2022;2(5):738–47. http://dx.doi.org/10.1016/j.fmre.2021.09.005.

[49] Lumpp B, Rothe D, Pastötter C, Lämmermann R, Jacob E. Oxymethylene ethers as diesel fuel additives of the future. MTZ Worldwide 2011;72(3):34–8. http://dx.doi.org/10.1365/s38313-011-0027-z.

[50] Emenike O, Michailos S, Hughes KJ, Ingham D, Pourkashanian M. Techno-economic and environmental assessment of BECCS in fuel generation for FT-fuel, bioSNG and OME *x*. Sustain Energy Fuels 2021;5(13):3382–402. http://dx.doi.org/10.1039/D1SE00123J.

[51] Salenbauch S, Sirignano M, Marchisio DL, Pollack M, D'Anna A, Hasse C. Detailed particle nucleation modeling in a sooting ethylene flame using a conditional quadrature method of moments (CQMOM). Proc Combust Inst 2017;36(1):771–9. http://dx.doi.org/10.1016/j.proci.2016.08.003.

[52] Salenbauch S, Sirignano M, Pollack M, D'Anna A, Hasse C. Detailed modeling of soot particle formation and comparison to optical diagnostics and size distribution measurements in premixed flames using a method of moments. Fuel 2018;222:287–93. http://dx.doi.org/10.1016/j.fuel.2018.02.148.

[53] D'Anna A, Sirignano M, Kent J. A model of particle nucleation in premixed ethylene flames. Combust Flame 2010;157(11):2106–15. http://dx.doi.org/10.1016/j.combustflame.2010.04.019.

[54] Salamanca M, Sirignano M, D'Anna A. Particulate formation in premixed and counter-flow diffusion ethylene/Ethanol flames. Energy Fuels 2012;26(10):6144–52. http://dx.doi.org/10.1021/ef301081q.

[55] Sgro L, Basile G, Barone A, D'Anna A, Minutolo P, Borghese A, et al. Detection of combustion formed nanoparticles. Chemosphere 2003;51(10):1079–90. http://dx.doi.org/10.1016/S0045-6535(02)00718-X.

[56] Salamanca M, Sirignano M, Commodo M, Minutolo P, D'Anna A. The effect of ethanol on the particle size distributions in ethylene premixed flames. Exp Therm Fluid Sci 2012;43:71–5. http://dx.doi.org/10.1016/j.expthermflusci.2012.04.006.

[57] Conturso M, Sirignano M, D'Anna A. Effect of furanic biofuels on particles formation in premixed ethylene–air flames: An experimental study. Fuel 2016;175:137–45. http://dx.doi.org/10.1016/j.fuel.2016.02.038.

[58] Conturso M, Sirignano M, D'Anna A. Effect of 2,5-dimethylfuran doping on particle size distributions measured in premixed ethylene/air flames. Proc Combust Inst 2017;36(1):985–92. http://dx.doi.org/10.1016/j.proci.2016.06.048.

[59] Russo C, D'Anna A, Ciajolo A, Sirignano M. Analysis of the chemical features of particles generated from ethylene and ethylene/2,5 dimethyl furan flames. Combust Flame 2016;167:268–73. http://dx.doi.org/10.1016/j.combustflame.2016.02.003.

[60] Russo C, D'Anna A, Ciajolo A, Sirignano M. The effect of butanol isomers on the formation of carbon particulate matter in fuel-rich premixed ethylene flames. Combust Flame 2019;199:122–30. http://dx.doi.org/10.1016/j.combustflame.2018.10.025.

[61] Sirignano M, Salamanca M, D'Anna A. The role of dimethyl ether as substituent to ethylene on particulate formation in premixed and counter-flow diffusion flames. Fuel 2014;126:256–62. http://dx.doi.org/10.1016/j.fuel.2014.02.039.

[62] Sirignano M, Ciajolo A, D'Anna A, Russo C. Chemical features of particles generated in an ethylene/ethanol premixed flame. Energy Fuels 2017;31(3):2370–7. http://dx.doi.org/10.1021/acs.energyfuels.6b02372.

[63] Liu D. Kinetic analysis of the chemical effects of hydrogen addition on dimethyl ether flames. Int J Hydrogen Energy 2014;39(24):13014–9. http://dx.doi.org/10.1016/j.ijhydene.2014.06.072.

[64] Tran L-S, Carstensen H-H, Lamoureux N, Foo KK, Gosselin S, El Bakali A, et al. Exploring the flame chemistry of C_5 tetrahydrofuranic biofuels: Tetrahydrofurfuryl alcohol and 2-methyltetrahydrofuran. Energy Fuels 2021;35(22):18699–715. http://dx.doi.org/10.1021/acs.energyfuels.1c01949.

[65] Liu D, Santner J, Togbé C, Felsmann D, Koppmann J, Lackner A, et al. Flame structure and kinetic studies of carbon dioxide-diluted dimethyl ether flames at reduced and elevated pressures. Combust Flame 2013;160(12):2654–68. http://dx.doi.org/10.1016/j.combustflame.2013.06.032.

[66] Sirignano M, Bartos D, Conturso M, Dunn M, D'Anna A, Masri AR. Detection of nanostructures and soot in laminar premixed flames. Combust Flame 2017;176:299–308. http://dx.doi.org/10.1016/j.combustflame.2016.10.009.
[67] D'Anna A. Combustion-formed nanoparticles. Proc Combust Inst 2009;32(1):593–613. http://dx.doi.org/10.1016/j.proci.2008.09.005.
[68] Baulch DL, Cobos CJ, Cox RA, Esser C, Frank P, Just T, et al. Evaluated kinetic data for combustion modelling. J Phys Chem Ref Data 1992;21(3):411–734. http://dx.doi.org/10.1063/1.555908.
[69] Wang S, Dames EE, Davidson DF, Hanson RK. Reaction rate constant of CH_2O + H = HCO + H_2 revisited: A combined study of direct shock tube measurement and transition state theory calculation. J Phys Chem A 2014;118(44):10201–9. http://dx.doi.org/10.1021/jp5085795.
[70] Xu ZF, Raghunath P, Lin MC. Ab initio chemical kinetics for the CH_3 + $O(^3P)$ reaction and related isomerization–Decomposition of CH_3O and CH_2OH radicals. J Phys Chem A 2015;119(28):7404–17. http://dx.doi.org/10.1021/acs.jpca.5b00553.
[71] De Souza Machado G, Martins EM, Baptista L, Bauerfeldt GF. Prediction of rate coefficients for the H_2CO + OH → HCO + H_2O reaction at combustion, atmospheric and interstellar medium conditions. J Phys Chem A 2020;124(11):2309–17. http://dx.doi.org/10.1021/acs.jpca.9b11690.
[72] Xu S, Zhu RS, Lin MC. Ab initio study of the OH + CH2O reaction: The effect of the OH··OCH2 complex on the H-abstraction kinetics. Int J Chem Kinet 2006;38(5):322–6. http://dx.doi.org/10.1002/kin.20166.
[73] Vasudevan V, Davidson DF, Hanson RK. Direct measurements of the reaction OH + CH2O = HCO + H2O at high temperatures. Int J Chem Kinet 2005;37(2):98–109. http://dx.doi.org/10.1002/kin.20056.
[74] Zschutschke A, Messig D, Scholtissek A, Hasse C. Universal laminar flame solver (ULF). 2017, p. 4893736. http://dx.doi.org/10.6084/M9.FIGSHARE.5119855.V2, figshare.
[75] Gaiser N, Bierkandt T, Oßwald P, Zinsmeister J, Kathrotia T, Shaqiri S, et al. Oxidation of oxymethylene ether (OME0-5): An experimental systematic study by mass spectrometry and photoelectron photoion coincidence spectroscopy. Fuel 2022;313:122650. http://dx.doi.org/10.1016/j.fuel.2021.122650.
[76] Gaiser N, Zhang H, Bierkandt T, Schmitt S, Zinsmeister J, Kathrotia T, et al. Investigation of the combustion chemistry in laminar, low-pressure oxymethylene ether flames (OME0–4). Combust Flame 2022;243:112060. http://dx.doi.org/10.1016/j.combustflame.2022.112060.
[77] Zhu Q, Wang F, Lyu J-Y, Li Y, Chen D, Yang W. Molecular dynamics simulation on the pyrolysis process of PODE3-5. Processes 2022;10(11):2378. http://dx.doi.org/10.3390/pr10112378.

Numerical and experimental investigations on the particle formation in oxymethylene ethers (OME_n, n = 2-4) / ethylene premixed flames (Supplementary material)

Robert Schmitz[a], Federica Ferraro[a], Mariano Sirignano[b], and Christian Hasse[a]

[a]*Technical University of Darmstadt, Department of Mechanical Engineering, Simulation of reactive Thermo-Fluid Systems, Otto-Berndt-Str. 2, 64287 Darmstadt, Germany*
[b]*Dipartimento di Ingegneria Chimica, dei Materiali e della Produzione Industriale – Universidà degli Studi di Napoli Federico II, P. le Tecchio 80, 80125 Napoli, Italy*

Abstract

This supplementary material complements the article and provides additional information on the applied kinetic mechanism, species profiles, and reaction sensitivity analyses.

Contents

Supplement A Rate coefficients of CH_2O decomposition and effects on soot formation

Table S 1: Changes to the reactions describing the formaldehyde breakdown. Reaction rate expression is $k = AT^n \exp(-E_a/RT)$. Units are expressed in s^{-1}, cm^3 and $\mathrm{cal\,mol}^{-1}$.

No.	Reaction	A	n	E_a
Mech. A (this work) [1–3]	$CH_2O + H \rightleftharpoons H_2 + HCO$	2.29E+08	1.05	3280.2
Mech. A (this work) [1, 4–6]	$CH_2O + OH \rightleftharpoons H_2O + HCO$	3.43E+07	1.18	-447.3
Mech. B ([7] + OME_4 reactions from Tab. S2)	$CH_2O + H \rightleftharpoons H_2 + HCO$	2.29E+10	1.05	3280.2
Mech. B ([7] + OME_4 reactions from Tab. S2)	$CH_2O + OH \rightleftharpoons H_2O + HCO$	3.43E+09	1.18	-447.3

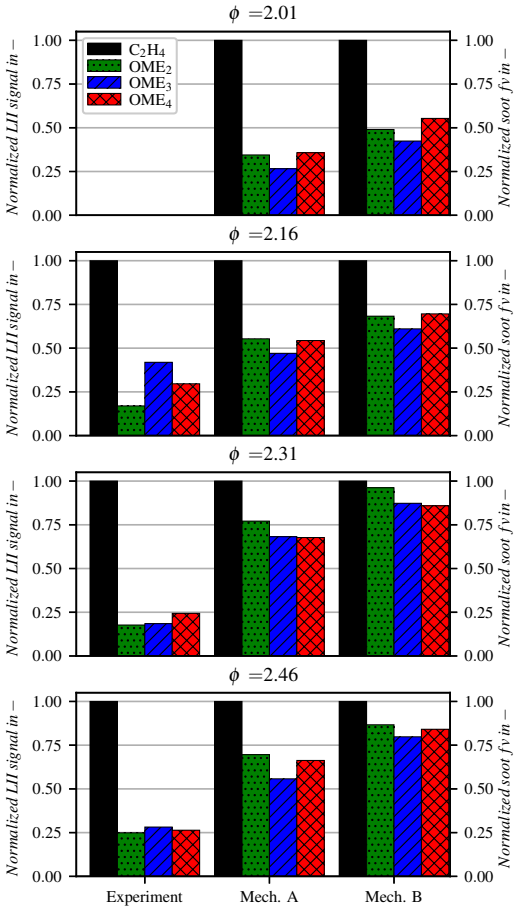

Fig. S 1: Normalized (to the corresponding value of the pure ethylene flame) soot volume fraction for the investigated equivalence ratios at $HAB = 15\,\mathrm{mm}$. Comparison of experimental LII signal with the modeling results of the soot volume fraction using mechanism A and mechanism B.

Supplement B Sensitivity analysis for OME_2 and OME_4

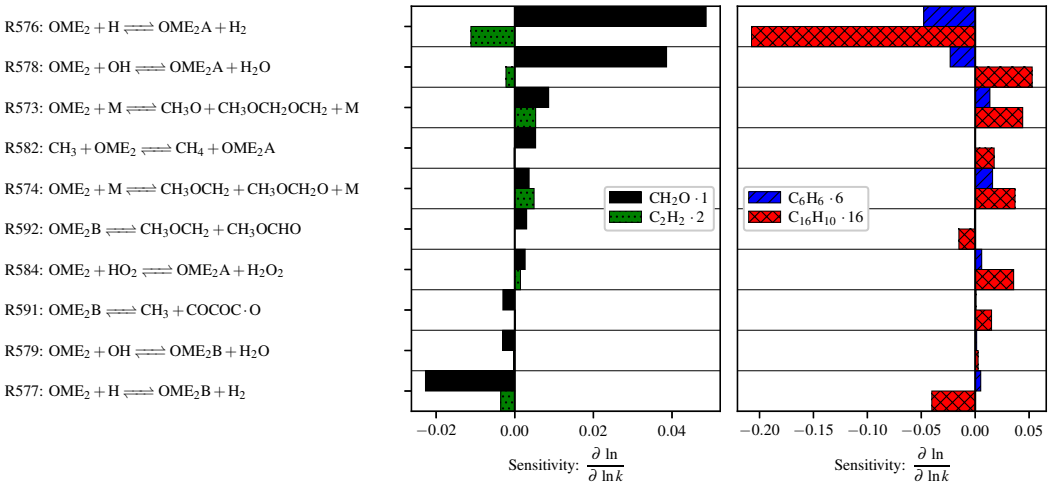

Fig. S 2: Sensitivity of the mole fraction peaks of the species CH_2O, C_2H_2, C_6H_6, and $C_{16}H_{10}$ for small perturbations of different reaction rates in the OME_2 flame at $\phi = 2.46$. Sensitivities are scaled by the number of carbon atoms present in the corresponding species. According to [8], OME_2: $CH_3OCH_2OCH_2OCH_3$; OME_2A: $CH_3OCH_2OCH_2OCH_2$; OME_2B: $CH_3OCH_2OCHOCH_3$; $COCOC \cdot O$: CH_3OCH_2OCHO.

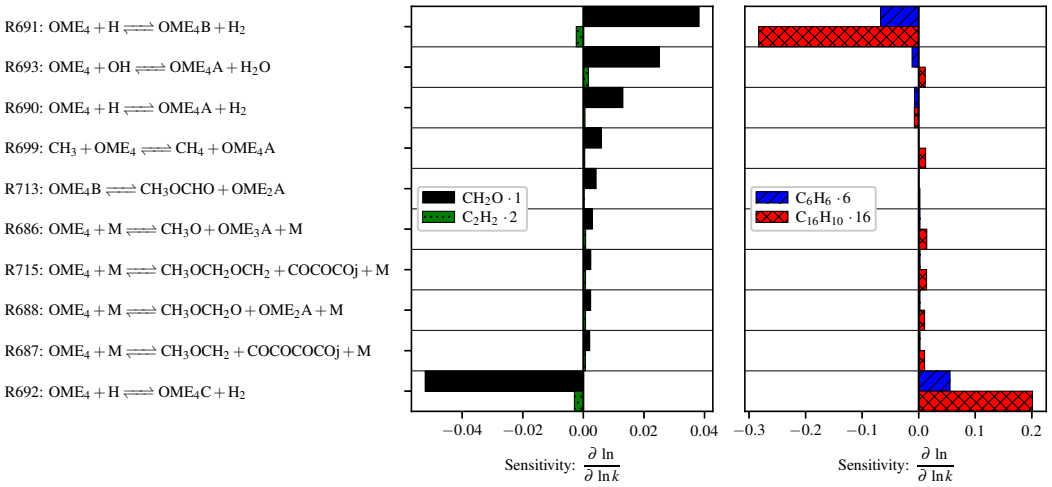

Fig. S 3: Sensitivity of the mole fraction peaks of the species CH_2O, C_2H_2, C_6H_6, and $C_{16}H_{10}$ for small perturbations of different reaction rates in the OME_4 flame at $\phi = 2.46$. Sensitivities are scaled by the number of carbon atoms present in the corresponding species. According to [8], OME_4: $CH_3OCH_2OCH_2OCH_2OCH_2OCH_3$; OME_4A: $CH_3OCH_2OCH_2OCH_2OCH_2OCH_2$; OME_4B: $CH_3OCH_2OCH_2OCH_2OCHOCH_3$; OME_4C: $CH_3OCH_2OCH_2OCHOCH_2OCH_3$; OME_3A: $CH_3OCH_2OCH_2OCH_2OCH_2$; OME_2A: $CH_3OCH_2OCH_2OCH_2$; COCOCOCOj: $CH_3OCH_2OCH_2OCH_2O$; COCOCOj: $CH_3OCH_2OCH_2O$.

Supplement C Additional species mole fraction profiles

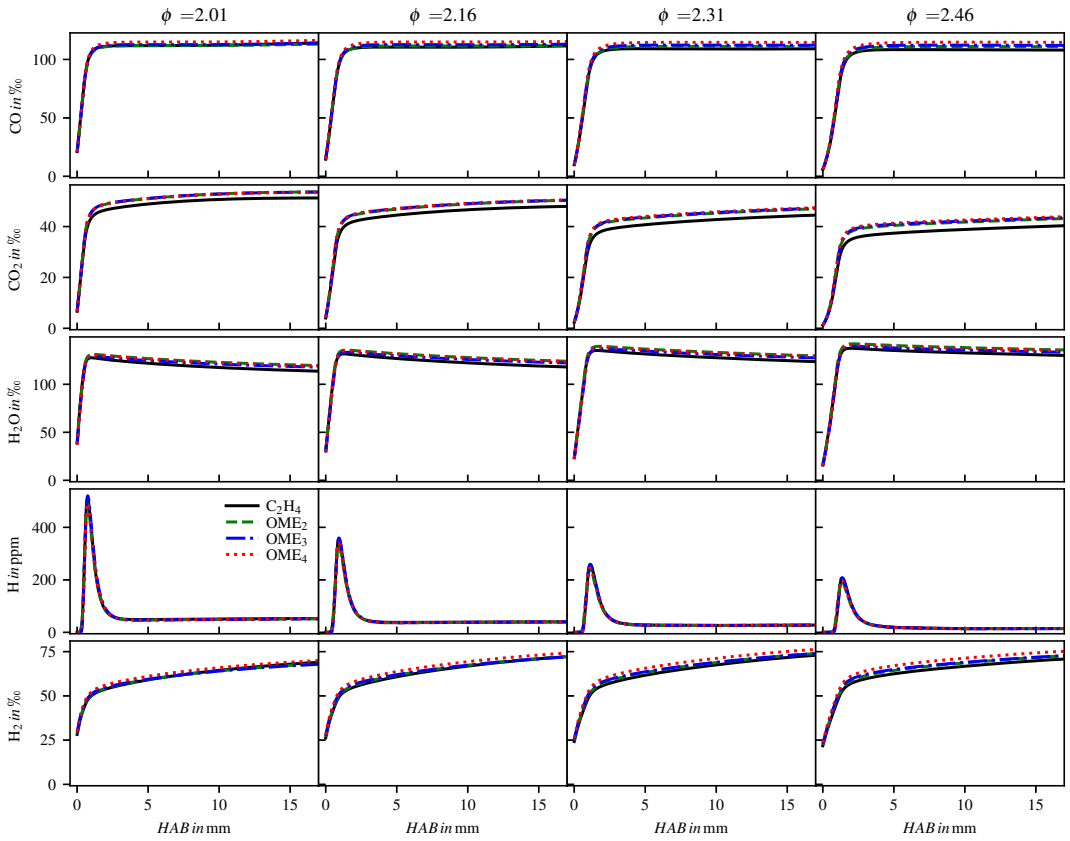

Fig. S 4: Simulated species mole fraction profiles of CO, CO_2, H_2O, H and H_2 as a function of height above the burner HAB obtained for pure ethylene and OME_n/ethylene blended mixture for n = 2, 3, 4 at different equivalence ratios.

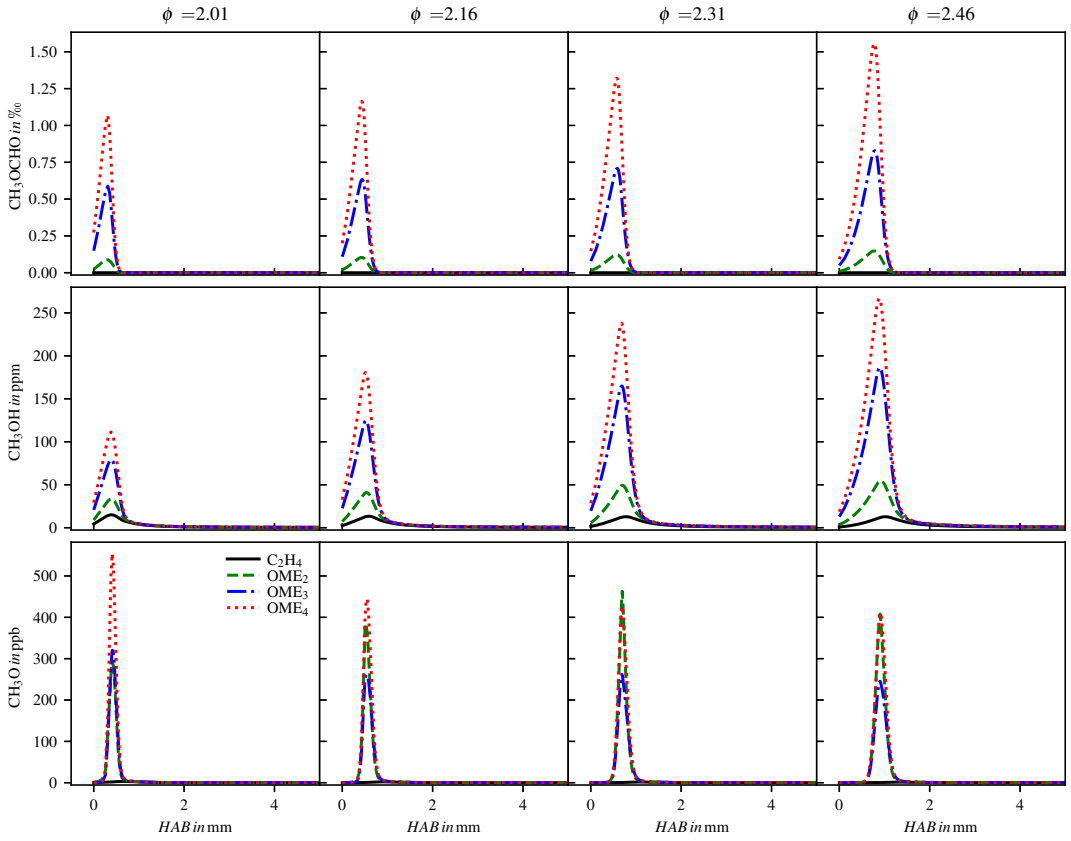

Fig. S 5: Simulated species mole fraction profiles of CH_3OCHO, CO_2, CH_3OH, and CH_3O as a function of height above the burner HAB obtained for pure ethylene and OME_n/ethylene blended mixture for n = 2, 3, 4 at different equivalence ratios.

Supplement D OME_4 sub-mechanism reactions

Table S 2: Selected reactions of the OME_4 sub-mechanism derived from the OME_3 mechanism from Sun et al. [8]. Reaction rate expression is $k = AT^n \exp(-E_a/RT)$. Units are expressed in s^{-1}, cm^3 and $\mathrm{cal\,mol}^{-1}$.

No.	Reaction		A	n	E_a
1	OME4+M = COCOCOCOCOj+CH3+M		2.33E+19	-0.66	84139.5
		LOW	1.72E+59	-11.40	93295.6
		TROE	1.0	1.0E-30	880
		H2/3.0/ H2O/9.0/ CH4/3.0/ CO/2.25/ CO2/3.0/ C2H6/4.5/ Ar/1.0			
2	OME4+M = OME3A+M+CH3O		1.24E+25	-2.29	85330
		LOW	3.55E+83	-18.70	98640
		TROE	9.0E-6	506	1.14E+10 2470
3	OME4+M = COCOCOCOj+CH3OCH2+M		1.24E+25	-2.29	85330
		LOW	3.55E+83	-18.70	98640
		TROE	9.0E-6	506	1.14E+10 2470
4	OME4+M = OME2A+CH3OCH2O+M		1.24E+25	-2.29	85330
		LOW	3.55E+83	-18.70	98640
		TROE	9.0E-6	506	1.14E+10 2470
5	OME4+M = OME3+CH2O+M		1.0E+14	0.00	65210
		LOW	5.72E+96	-23.0	80813
		TROE	1.17E-3	379	1.58E+7 4730
6	OME4+H = OME4A+H2		3.940E+00	4.13	1.780E+03
7	OME4+H = OME4B+H2		7.400E+14	0.00	3.170E+03
8	OME4+H = OME4C+H2		3.700E+14	0.00	3.170E+03
9	OME4+OH = OME4A+H2O		1.954E+07	1.89	-3.656E+02
10	OME4+OH = OME4B+H2O		2.260E+03	2.93	4.040E+03
11	OME4+OH = OME4C+H2O		1.130E+03	2.93	4.040E+03
12	OME4+O = OME4A+OH		2.689E+07	2.00	2.632E+03
13	OME4+O = OME4B+OH		1.600E+13	0.00	3.038E+03
15	OME4+O = OME4C+OH		8.000E+12	0.00	3.038E+03
16	OME4+CH3 = OME4A+CH4		1.019E+01	3.78	9.688E+03
17	OME4+CH3 = OME4B+CH4		9.993E+11	0.00	9.767E+03
18	OME4+CH3 = OME4C+CH4		4.997E+11	0.00	9.767E+03
19	OME4+HO2 = OME4A+H2O2		1.680E+03	0.00	1.769E+04
20	OME4+HO2 = OME4B+H2O2		2.950E+04	2.60	1.390E+04
21	OME4+HO2 = OME4C+H2O2		1.475E+04	2.60	1.390E+04
22	OME4+O2 = OME4A+HO2		2.000E+13	0.00	4.560E+04
23	OME4+O2 = OME4B+HO2		6.660E+12	0.00	4.354E+04
24	OME4+O2 = OME4C+HO2		3.330E+12	0.00	4.354E+04
25	OME4+CH3O = OME4A+CH3OH		6.020E+11	0.00	4.074E+03
26	OME4+CH3O = OME4B+CH3OH		1.000E+12	0.00	4.552E+03
27	OME4+CH3O = OME4C+CH3OH		5.000E+11	0.00	4.552E+03
28	OME4A = OME3A+CH2O		4.450E+14	-0.22	2.727E+04
29	OME4B = COCOCOCOC*O+CH3		2.860E+15	-0.24	1.017E+04
30	OME4B = OME2A+CH3OCHO		2.860E+15	-0.24	1.017E+04
31	OME4C = COCOCOC*O+CH3OCH2		5.720E+15	-0.24	1.017E+04
32	OME4+M = CH3OCH2OCH2+COCOCOj+M		1.240E+25	-2.29	85330
		LOW	3.55E+83	-18.70	98640
		TROE	9.0E-6	506	1.14E+10 2470

Note: OME4: $CH_3OCH_2OCH_2OCH_2OCH_2OCH_3$; OME4A: $CH_3OCH_2OCH_2OCH_2OCH_2OCH_2$; OME4B: $CH_3OCH_2OCH_2OCH_2OCHOCH_3$; OME4C: $CH_3OCH_2OCH_2OCHOCH_2OCH_3$; OME3: $CH_3OCH_2OCH_2OCH_2OCH_3$; OME3A: $CH_3OCH_2OCH_2OCH_2OCH_2$; OME2A: $CH_3OCH_2OCH_2OCH_2$; COCOCOCOCOj: $CH_3OCH_2OCH_2OCH_2OCH_2O$; COCOCOCOj: $CH_3OCH_2OCH_2OCH_2O$; COCOCOj: $CH_3OCH_2OCH_2O$; COCOCOCOC*O: $CH_3OCH_2OCH_2OCH_2OCHO$; COCOCOC*O: $CH_3OCH_2OCH_2OCHO$.

References

[1] D. L. Baulch, C. J. Cobos, R. A. Cox, C. Esser, P. Frank, Th. Just, J. A. Kerr, M. J. Pilling, J. Troe, R. W. Walker, J. Warnatz, Evaluated Kinetic Data for Combustion Modelling, Journal of Physical and Chemical Reference Data 21 (1992) 411–734. doi:10.1063/1.555908.

[2] S. Wang, E. E. Dames, D. F. Davidson, R. K. Hanson, Reaction Rate Constant of $CH_2O + H = HCO + H_2$ Revisited: A Combined Study of Direct Shock Tube Measurement and Transition State Theory Calculation, The Journal of Physical Chemistry A 118 (2014) 10201–10209. doi:10.1021/jp5085795.

[3] Z. F. Xu, P. Raghunath, M. C. Lin, Ab Initio Chemical Kinetics for the $CH_3 + O(^3P)$ Reaction and Related Isomerization–Decomposition of CH_3O and CH_2OH Radicals, The Journal of Physical Chemistry A 119 (2015) 7404–7417. doi:10.1021/acs.jpca.5b00553.

[4] G. De Souza Machado, E. M. Martins, L. Baptista, G. F. Bauerfeldt, Prediction of Rate Coefficients for the $H_2CO + OH \rightarrow HCO + H_2O$ Reaction at Combustion, Atmospheric and Interstellar Medium Conditions, The Journal of Physical Chemistry A 124 (2020) 2309–2317. doi:10.1021/acs.jpca.9b11690.

[5] S. Xu, R. S. Zhu, M. C. Lin, Ab initio study of the OH + CH2O reaction: The effect of the OH··OCH2 complex on the H-abstraction kinetics, International Journal of Chemical Kinetics 38 (2006) 322–326. doi:10.1002/kin.20166.

[6] V. Vasudevan, D. F. Davidson, R. K. Hanson, Direct measurements of the reaction OH + CH2O ? HCO + H2O at high temperatures, International Journal of Chemical Kinetics 37 (2005) 98–109. doi:10.1002/kin.20056.

[7] F. Ferraro, C. Russo, R. Schmitz, C. Hasse, M. Sirignano, Experimental and numerical study on the effect of oxymethylene ether-3 (OME3) on soot particle formation, Fuel 286 (2021) 119353. doi:10.1016/j.fuel.2020.119353.

[8] W. Sun, G. Wang, S. Li, R. Zhang, B. Yang, J. Yang, Y. Li, C. K. Westbrook, C. K. Law, Speciation and the laminar burning velocities of poly(oxymethylene) dimethyl ether 3 (POMDME3) flames: An experimental and modeling study, Proceedings of the Combustion Institute 36 (2017) 1269–1278. doi:10.1016/j.proci.2016.05.058.

P4 Combustion and Flame 260 (2024), 113220

A. Kalbhor*, **R. Schmitz***, A. Ramirez, P. Vlavakis, F. P. Hagen, F. Ferraro, M. Braun-Unkhoff, T. Kathrotia, U. Riedel, D. Trimis, J. van Oijen, C. Hasse, D. Mira„ “Experimental and numerical investigation on soot formation and evolution of particle size distribution in laminar counterflow ethylene flames,” Combustion and Flame, vol. 260, p. 113220, Feb. 2024, doi: 10.1016/j.combustflame.2023.113220.
*Joint first authors

Author contributions

Tab. P.4: Author contributions to publication [113] following CRediT [127]

Abhijit Kalbhor	Conceptualization of the investigations (equal) Conduction of detailed numerical soot simulations with DSM model Validation of soot modeling (equal) Interpretation and discussion of the results (equal) Visualization of results Writing – Original draft (lead) Joint first and corresponding author
Robert Martin Schmitz	Conceptualization of the investigations (equal) Software implementation Conduction of detailed numerical soot simulations with S-EQMOM model Validation of soot modeling (equal) Interpretation and discussion of the results (equal) Writing – Original draft (lead) Joint first author
Astrid Ramirez	Development of kinetic mechanism Validation of kinetics Interpretation and discussion of the results (equal) Visualization of results Writing – Original draft (support)
Petros Vlavakis	Conceptualization of the design of experiments (equal) Conceptualization of the investigations (equal) Conduction of experimental investigations (equal) Writing – Original draft (support)
Fabian P. Hagen	Conceptualization of the design of experiments (equal) Conduction of experimental investigations (equal) Writing – Original draft (support)
Federica Ferraro	Conceptualization of the investigations (equal) Supervision (equal)

Table continues on next page

Marina Braun-Unkhoff	Conceptualization of the kinetic mechanism (equal) Conceptualization of the investigations (equal) Funding acquisition Supervision (equal)
Trupti Kathrotia	Methodology and development of the kinetic mechanism
Uwe Riedel	Conceptualization of the kinetic mechanism (equal) Supervision (equal) Funding acquisition
Dimosthenis Trimis	Conceptualization of the experimental investigations (equal) Supervision (equal) Funding acquisition
Jeroen van Oijen	Conceptualization of the investigations (equal) Supervision (equal) Funding acquisition
Christian Hasse	Conceptualization of the investigations (equal) Supervision (equal) Funding acquisition
Daniel Mira	Conceptualization of the investigations (equal) Project administration Funding acquisition
All co-authors	Writing – Review & Editing

Use of publication contents in finalized and ongoing dissertations

This publication is part of the ongoing dissertation of Robert Martin Schmitz at the Institute for Simulation of reactive Thermo-Fluid Systems at the Technical University of Darmstadt, Germany.

Combustion and Flame 260 (2024) 113220

Contents lists available at ScienceDirect

Combustion and Flame

journal homepage: www.sciencedirect.com/journal/combustion-and-flame

Experimental and numerical investigation on soot formation and evolution of particle size distribution in laminar counterflow ethylene flames

Abhijit Kalbhor [a,*], Robert Schmitz [b,1], Astrid Ramirez [c,g], Petros Vlavakis [d], Fabian P. Hagen [d], Federica Ferraro [b], Marina Braun-Unkhoff [c,g], Trupti Kathrotia [g], Uwe Riedel [f], Dimosthenis Trimis [d], Jeroen van Oijen [a], Christian Hasse [b], Daniel Mira [e]

[a] Eindhoven University of Technology, Eindhoven, The Netherlands
[b] Technical University of Darmstadt, Department of Mechanical Engineering, Simulation of reactive Thermo-Fluid Systems, Otto-Berndt-Str. 2, 64287 Darmstadt, Germany
[c] University of Stuttgart, Stuttgart, Germany
[d] Karlsruhe Institute of Technology (KIT), Karlsruhe, Germany
[e] Barcelona Supercomputing Centre, Barcelona, Spain
[f] German Aerospace Center, Cottbus, Germany
[g] German Aerospace Center, Stuttgart, Germany

ARTICLE INFO

Keywords:
Soot formation
Counterflow non-premixed flames
Discrete sectional method
Split-based extended quadrature method of moments
Particle size distribution

ABSTRACT

A detailed investigation of the process of soot formation in ethylene-fueled laminar counterflow diffusion flames is conducted using dedicated experiments and numerical simulations. Two different strategies based on the Discrete Sectional Method (DSM) and the Split-based Quadrature Method of Moments (S-EQMOM) are considered to model the evolution of soot particle size distributions, and their comparative assessment is carried out for soot formation prediction and particle growth. A consistent chemical reaction mechanism describing the oxidation of hydrocarbon fuels and the prediction of soot precursors with the growth of polycyclic aromatic hydrocarbons (PAHs) up to pyrene ($C_{16}H_{10}$) is examined. Experiments for various strain rates and fuel compositions are performed to assess the sensitivity of soot production to these two parameters. The results show that both modeling strategies captured well the qualitative trends of soot volume fraction under variations in strain rate and mixture composition, with slight over-prediction of the peak values. For both soot models, a higher sensitivity of soot formation is noticed by changes in mixture composition compared to those of strain rate variation. Additionally, the soot models demonstrated promising performance in capturing the experimentally observed evolution of the soot particle size distribution (PSD).

1. Introduction

The emission of particulate matter (predominantly soot) from combustion systems is one of the major concerns due to its harmful effects on human health and the environment. Soot particles can range from large sizes that tend to precipitate by gravity, to small sizes that remain in the atmosphere causing more adverse issues such as respiratory problems. Especially soot particles emitted by aero-engines, typically in higher altitudes, absorb sunlight and affect cloud formation when acting as condensation nuclei leading to contrails [1]. For all these reasons, current emission regulations in both air and road transportation are targeting not only soot volume fraction but also particle size distributions [2]. The present-day emission legislation is based on integral values such as soot particle number density or soot particle mass concentration. In fact, the physical and chemical processes associated with soot formation depend on the size distribution of the particles themselves, especially, soot oxidation, which significantly influences the final particle concentrations during subsequent processes in non-premixed flames [3,4]. Therefore, incorporating the size distribution in addition to integral quantities, such as soot volume fraction, is of significant interest to further understand the soot formation process and develop appropriate models for predicting their characteristics.

Soot chemistry is characterized by slower time scales than that of fuel oxidation [5,6]. Therefore, soot formation may be appreciably influenced by characteristics of flow time scales that alter the residence time of particles in a flame [7]. In practical combustion devices, which often operate under turbulent conditions, the soot formation

* Corresponding author.
E-mail address: a.j.kalbhor@tue.nl (A. Kalbhor).
[1] Joint First Authors.

https://doi.org/10.1016/j.combustflame.2023.113220
Received 3 April 2023; Received in revised form 13 November 2023; Accepted 24 November 2023

process is highly affected by complex interactions of reactive flow, flame, and soot. Therefore, understanding soot response to flow variations is an important research topic concerning predictive soot model development.

In this context, the counterflow diffusion flame is an attractive configuration for systematic studies analyzing flow time effects on soot formation through strain rate variations. Several experimental [8–12] and numerical investigations [11–13] have addressed soot sensitivity to strain rate for different fuels in counterflow configurations. It is shown that increased strain rates inhibit soot formation (indicated by soot volume fraction and PAH concentrations, e.g., pyrene concentration) as a consequence of the lower residence times. While these studies have contributed to understanding physical and chemical mechanisms associated with interactions between flow and soot in more detail, the systematic investigation of strain rate effects on the evolution of soot particle size distribution in a counterflow configuration remains limited. In addition, this configuration is suitable to investigate the sooting tendencies of different fuels in the form of a limit curve [14], as fuel composition can be manipulated with the dilution of non-hydrocarbon gases such as nitrogen. Fuel dilution with nitrogen has been shown to affect the sooting tendency through variation mainly of the flame temperature or the concentration of soot precursors [15–17].

For these reasons, we perform numerical simulations with two different state-of-the-art soot modeling strategies from recently measured counterflow flames [18] to investigate their sooting characteristics. These modeling approaches include the discrete sectional method (DSM) [19] and the split-based extended quadrature method of moments (S-EQMOM) [20], which provide direct information on the soot particle size distribution (PSD). Sets of different mixture compositions and strain rate variations are investigated with lightly and moderately sooting conditions which extends the data pool for this configuration with systematic parameter variations. The present study uniquely features detailed measurements of the soot formation by including soot volume fraction and PSD in combination with the comparison of two different soot models. Furthermore, a new comprehensive chemical kinetic mechanism referred to as ESTiMatE-Mech [21] (abbreviated name as EST3) is introduced for modeling the PAH formation chemistry. This mechanism was developed with a focus on the prediction of the PAH formation during the combustion of ethylene and a wide range of jet fuel surrogates.

Considering the rich experimental database and the different modeling approaches, the objectives of the present study are: (1) to systematically investigate the strain rate sensitivity of soot formation and the effects of fuel dilution in laminar ethylene counterflow flames by using new experiments and computations; (2) to study the evolution of soot particle size distribution under strain rate variation and fuel dilution; (3) to introduce a new chemical kinetic mechanism and validate its performance for soot prediction in laminar ethylene counterflow flames; and (4) to perform a comparative assessment of the predictive capabilities of two soot modeling strategies concerning soot formation characteristics.

The manuscript is organized as follows: the experimental setup and measurement techniques for the species, temperature, and soot quantities are described. Subsequently, the modeling study is presented in two parts. First, the kinetic mechanism is presented including validation with species and temperature profiles measured within the counterflow flames using ethylene as a fuel. Second, the performance of the two soot models in the soot prediction in counterflow flames from Wang and Chung [11] is evaluated by comparing the new reaction mechanism EST3 with the well-established KM2 mechanism [22]. The main investigation is performed on a series of ethylene counterflow diffusion flames with varying strain rates and fuel compositions [23]. The experimental data sets for soot formation and PSD evolution are compared against the simulation results. A detailed analysis of the soot formation sub-processes is provided by comparing the numerical results for both soot models. Finally, the concluding remarks and perspectives are given.

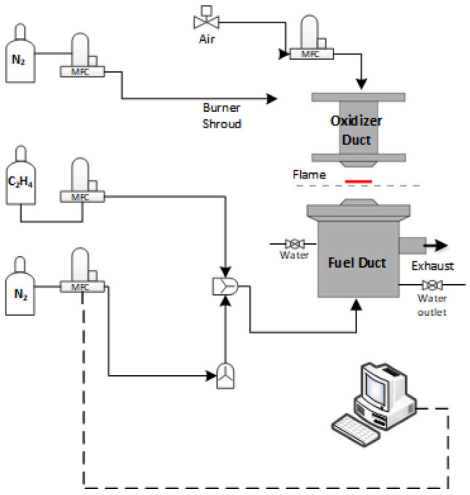

Fig. 1. Schematic of the counterflow burner.

2. Experimental approach

The counterflow setup employed in the present work is based on the burner design described in [24,25]. The details of the experimental setup consisting of intrusive particle sampling coupled with differential mobility particle sizing, i.e., a scanning mobility particle sizer (SMPS), two-color time-resolved laser-induced incandescence (2C-TiRe-LII), and fuel/oxidizer flow control systems can be found in the work of Hagen et al. [18,23]. The burner consists of two concentrically placed identical ducts with inner diameters of 25 mm, configured as opposed to each other, with a separation distance of 12.5 mm. The bottom duct (fuel duct) is surrounded by two concentric annular ducts. Nitrogen gas shielding is applied through the inner annular gap to avoid ambient air interference and the formation of secondary edge flames. To facilitate the suction of product gases, an outermost annular duct is connected to an exhaust system. Similar to the fuel duct, the oxidizer duct is also shrouded by nitrogen. To ensure plug-flow type boundary conditions, multiple stainless steel wire screens (200 meshes/inch) are placed at the nozzle exit. The flow rates are adjusted by thermal mass flow controllers (MFC) with an uncertainty of less than 1%. The schematic of the counterflow burner setup is shown in Fig. 1.

In the present experiments, ethylene with a purity of > 99.9% is used as fuel diluted with nitrogen, while synthetic air (21% O_2/79% N_2 by volume) is used as an oxidizer. For the shielding and dilution of the fuel, nitrogen with a purity of > 99.999% is used. The fuel and oxidizer are maintained at 300 K ambient temperature under atmospheric pressure. In the experiments, a momentum balance is imposed to ensure the stagnation plane formed by the reactant streams lies approximately in the central region between the two ducts. In the counterflow burner, the global strain rate of the oxidizer is defined as:

$$K = \frac{2|u_o|}{L}\left(1 + \frac{|u_f|\sqrt{\rho_f}}{|u_o|\sqrt{\rho_o}}\right), \tag{1}$$

where u denotes the flow velocity of reactants, L represents nozzle separation distance, and ρ is the gas density. Subscripts f and o indicate the fuel and oxidizer streams, respectively. Under the momentum balance ($\rho_f u_f^2 = \rho_o u_o^2$), global strain rate simplifies to $K = 4u_o/L$. In the current study, variation in global strain rate and stoichiometric

Table 1
Strain rates and fuel compositions of the investigated ethylene-air counterflow flames.

Flame	C_2H_4 mass fraction in fuel ($Y_{F,f}$) [–]	Strain rate (K) [s^{-1}]
1	0.20	60
2	0.25	60
3	0.30	50
4	0.30	60
5	0.30	70
6	0.35	60
7	0.25	100

mixture composition is achieved by altering the nozzle exit velocities of reactants and the mass fraction of ethylene in the fuel stream ($Y_{F,f}$). The experimental conditions of the investigated flames are summarized in Table 1.

In this study, temperature, concentrations of gaseous species, soot volume fractions f_v and mobility particle size distributions $P(d_m)$ are measured along the flame axis to obtain the profiles as a function of the height above the fuel duct (HAB for brevity). Temperatures were determined using a 300 μm wire diameter (after coating) S-type thermocouple that was built in-house and is described in detail in [25]. Taking into account the standard deviation of the measurement and the uncertainties imposed by the radiation correction [26], the highest level of uncertainty of the reported temperatures is 80 K [18,25]. The influence of soot deposits on radiation correction can be neglected since the residence time of the thermocouple in the low-sooting counterflow flames was chosen to be less than three seconds.

Gas chromatography coupled with mass spectrometry (GC/MS) is used to quantify gas species concentrations in the examined flames via probing gas phase species. The used sampling system consisting of a chemically inert, deactivated aluminum oxide (Al_2O_3) tube (ID 0.3 mm/OD 0.5 mm, 25 mm length) is explained in [24,25]. This microprobe is connected to a 1/16″ stainless steel tube, which in turn is fixed through a reducer fitting to a 6 mm stainless steel tube. The transfer line connecting the flame probe to the gas GC/MS is heated up to 423 K in order to prevent condensation of species from the flame probe. The GC/MS is equipped with a Thermal Conductivity Detector (TCD) for quantifying permanent gases (CO, CO_2, O_2, H_2O, and H_2) and two Flame Ionization Detectors (FID) for hydrocarbons. Details of the GC/MS, the probe as well as the sampling system used for these investigations are given in the work from Sentko et al. [27].

The GC/MS was calibrated with gaseous and liquid mixtures. Gas calibration of the GC/MS is performed with calibration reference gas mixtures consisting of CO, CO_2, O_2, H_2, N_2, CH_4, C_2H_2, and C_6H_6. On the other hand, higher hydrocarbons and PAHs were calibrated with liquid reference mixtures fed to the GC/MS using a calibration unit consisting of a syringe pump and a direct vaporizer, or by liquid injection. Both methods showed excellent agreement and were used for different concentration levels. To ensure accurate quantification, all species subjected to quantitative analysis were calibrated at least at two different concentration levels, i.e., in a two-point calibration. The overall uncertainty on the reported concentrations is ± 3%–10% for the major species (N_2, O_2, H_2, CO, CO_2, and CH_4), ± 5%–30% for light and heavy hydrocarbons, which include several soot precursors (i.e., styrene, ethylbenzene, naphthalene, pyrene, etc.), and ± 20% for water. These values correspond to the largest uncertainty of the species in the flames studied, taking into account the standard deviations of three repeated measurements and the uncertainties from the calibration procedures. The latter includes the uncertainties in concentrations of reference gases and liquids. Note that there is an additional error in the measured mole fractions arising from the non-isokinetic sampling, which has already been discussed in [28]. The limit of detection (LOD) for the higher PAHs, i.e., the three- and four-ring systems, is 1 ppm.

For the measurement of volume fraction f_v and mobility size distribution $P(d_m)$ of soot particles formed in the investigated counterflow flames, a particle sampling system coupled with differential mobility particle sizing, i.e. SMPS, described in detail in [23], is employed. Aerosol sampling features a tailored probe that is traversed through the flame in combination with a two-stage dilution system. The dual-port probe consists of a double-walled quartz tube with a wall thickness of 1.0 mm, an inner diameter of 6.0 mm for the outer tube, and 3.0 mm for the inner tube, respectively. The outer tube narrows down to an inner diameter at the tip of 0.2 mm to reduce flow perturbance and minimize heat losses from the flame. The extracted aerosol sample is rapidly diluted with nitrogen in two stages to prevent further surface growth, coagulation, and oxidation processes of the particles. The resulting dilution ratio (DR) of the particle-laden flame gas sample was $DR \approx 2 \times 10^3$ [23], which simultaneously corresponds to the maximum values of [29]. To demonstrate the performance of the particle sampling system, f_v and $P(d_m)$ derived via differential mobility sizing were compared in [23] with those obtained by non-intrusive laser-based diagnostics, i.e. 2C-TiRe-LII. Thereby, excellent agreement was found. Further, a threshold for the developed probe was discussed, beyond which no influence of DR on $P(d_m)$ and f_v was observed. In this study, the dilution ratio DR exceeded this threshold. A sketch of the aerosol probe and a description of the methods used to determine and control DR is given in [23]. The approach for correcting $P(d_m)$ for particle losses in the probe and tubes is also provided in [23]. For differential mobility sizing, an electrostatic classifier (EC), a soft X-ray neutralizer, a nano-differential mobility analyzer (nano-DMA), and a condensation particle counter (CPC) have been used. Details of the instrumentation can be found in [30]. As reported in [23,31], uncertainties in the dilution ratio, perturbations of the flame, sampling from a volume rather than a point source, and particle deposition in the probe lead to unavoidable uncertainties in the measurement of f_v and $P(d_m)$ of ±30%.

3. Gas-phase modeling

Complementary to the experimental study, numerical simulations of the measured ethylene flames are performed to compare the ability of the models to predict the main features of the flame and their sooting characteristics. The modeling assessment of the two-phase flow (solid-gas) can be divided into two main parts: gas-phase validation and soot prediction. In this section, the reaction mechanism used to describe the chemistry of the gas phase is introduced, and numerical simulations with detailed chemistry (without soot) are conducted to validate the chemical kinetic mechanism. Dedicated experiments for non-sooting conditions are used to examine the accuracy of the new reaction mechanism EST3 to reproduce the concentrations of major species and PAHs prior to the sooting flame calculations. The description of the gas-phase reaction kinetic approach, along with its validation based on experimental species and temperature data, is detailed below.

3.1. Chemical-kinetic reaction mechanism for soot formation

The chemical-kinetic reaction mechanism EST3 [21,32] is used to describe the chemical breakdown and oxidation of the ethylene fuel. In addition to the kinetics of ethylene, the EST3 mechanism was developed to model the combustion of different compositions of jet fuel surrogates as well as their components [21]. For modeling surrogates of complex practical fuels, EST3 can handle several different *iso*-alkanes up to *iso*-octane, *n*-alkanes up to *n*-dodecane, and *cyclo*-alkanes up to *cyclo*-hexane. Moreover, EST3 includes the kinetics of different potential candidates to represent the aromatics in a jet fuel surrogate formulation, such as toluene, *n*-propylbenzene, *m*-xylene, and 1,3,5-trimethylbenzene. The EST3 mechanism has been developed with a focus on the formation of PAHs up to pyrene (A4), which is considered the key precursor for soot nucleation within the employed soot models. The EST3 mechanism consists of 214 chemical species and 1539 elementary reactions.

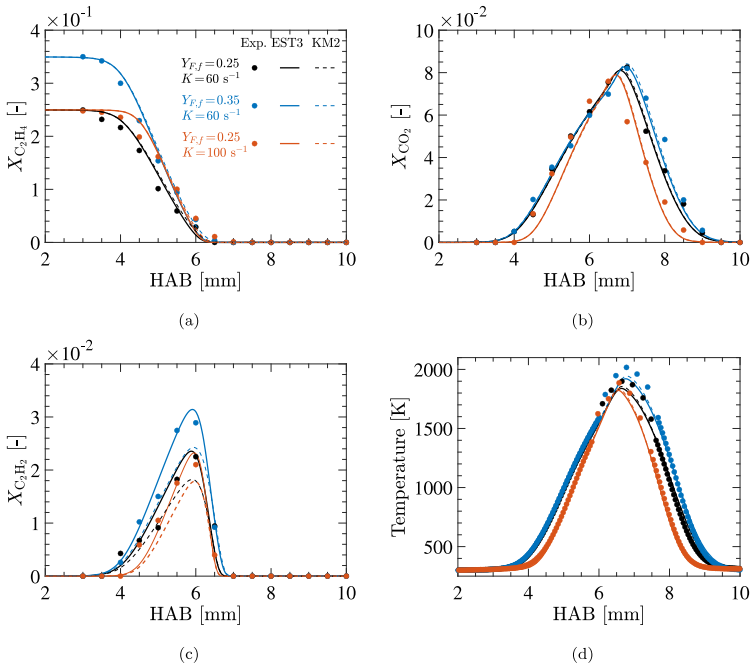

Fig. 2. Comparison between experimental (symbols) and modeling results (curves) obtained with EST3 [21,32] (solid) and KM2 [22] (dashed) mechanisms for C_2H_4, CO_2, and C_2H_2 mole fractions and temperature profiles in counterflow ethylene flames 2, 6, and 7.

In the development of EST3, a recently updated and extensively validated reaction mechanism for kerosene surrogate was selected as a base mechanism, the DLR Concise [33,34]. DLR Concise is a compact modular mechanism that encompasses the kinetics of many *n*-paraffins, *iso*-paraffins, *cyclo*-paraffins, and aromatics. To generate EST3, species that were not considered molecules of interest to be part of jet fuel surrogates were removed from the base mechanism (e.g. larger *iso*-paraffins iC > 8 and larger *n*-alkanes nC > 12). In addition, chemical kinetic sub-models of species of interest that were not yet considered in DLR Concise were developed and incorporated, such as *m*-xylene and 1,3,5-trimethylbenzene [21].

Furthermore, the chemical mechanism was updated taking into account a new detailed experimental database obtained from a counterflow burner [32]. In this counterflow burner, different fuels such as *iso*-octane, 1,3,5-trimethylbenzene, a jet A-1 surrogate, and ethylene were evaluated. This new experimental database allowed for validating and refining the mechanism, taking into account different fuels, strain rates, and fuel mass fractions. A description of the kinetics of these fuel components is omitted here for brevity; for more information, see Ref. [32]. To assure good predictability of species profiles of various PAHs within the combustion of a wide range of fuel components, some modifications based on reaction pathway (ROP) and sensitivity analysis were made, including analyses of the base mechanism [21]. Therefore, EST3 offers the capability to analyze a wide range of hydrocarbons, from lighter compounds such as ethylene to the kinetics of kerosene surrogates. It allows for consistent modeling of PAH formation that aligns well with the applied soot model. This enables efficient studies on soot formation across a diverse range of hydrocarbon fuels, including ethylene.

3.1.1. Validation of the chemical-kinetic reaction mechanism EST3

The proposed chemical-kinetic reaction mechanism of ethylene is validated for multiple PAH species including benzene (A1), toluene ($A1CH_3$), styrene (C_8H_8), indene (C_9H_8), naphthalene (A2), and acenaphthylene (A2R5). Experimental data for larger PAHs, such as phenanthrene (A3) and pyrene (A4), were unavailable as their concentrations were below their detection limits. In Fig. 2, the modeling results obtained with the EST3 mechanism are compared against the measurements for three counterflow ethylene flames with different strain rates and fuel compositions. The counterflow burner was modeled with Cantera [35] to solve the governing equations of the 1-D flame. The species diffusive mass fluxes were computed according to the multi-component formulation. The simulations are carried out for gas-phase description without the coupling of any soot model.

The spatial profiles for temperature and concentration (in mole fraction X) of major species (C_2H_4, CO_2, and C_2H_2) are shown in Fig. 2. The results from the reference mechanism, KM2 [22], are also included for completeness. As observed in Fig. 2, the profiles of major species and temperature are well captured by the EST3 mechanism. Especially, the concentration of C_2H_2, a key precursor species in soot formation, is well predicted by EST3 as compared to KM2. Besides major species, modeling results for the aromatics, such as benzene (A1), toluene ($A1CH_3$), naphthalene (A2), and pyrene (A4) are also presented in Fig. 3. The EST3 model reveals a good qualitative and quantitative predictability of benzene and naphthalene. Especially for flames with lower dilution levels, EST3 mechanism shows better quantitative prediction of toluene (Fig. 3(b)) and A2 (Fig. 3(c)) species. It is important to note that, as introduced above, the EST3 mechanism is designed to be applicable to a wide range of hydrocarbon fuels, not limited to C_1–C_4 fuels like the KM2 mechanism. However, there might be limitations in

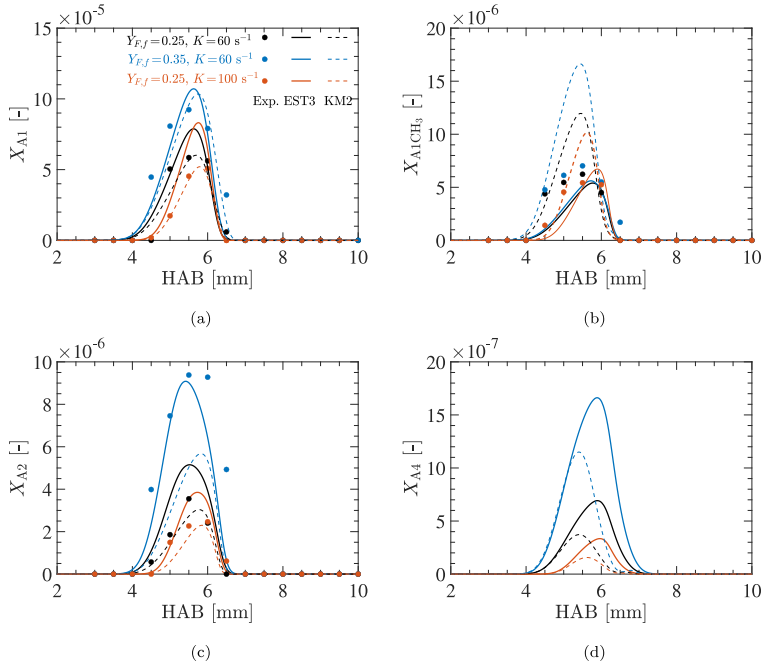

Fig. 3. Comparison between experimental (symbols) and modeling results (curves) obtained with EST3 [21,32] (solid) and KM2 [22] (dashed) mechanisms for benzene (A1), toluene ($A1CH_3$), naphthalene (A2), and pyrene (A4) mole fraction profiles in counterflow ethylene flames 2, 6, and 7.

accurately predicting each gas-phase species under certain conditions. For instance, for higher dilution and higher strain rates, these aromatic species by EST3 mechanism are overpredicted, compared to KM2.

The computed profiles of A4 are also included in Fig. 3 for analysis. However, no experimental data were available for pyrene (A4) since its concentration fell below the detection limits in this set of experiments. Compared to KM2, a higher A4 concentration is obtained with the EST3 mechanism, with a wider spatial distribution and shifted peak locations. This difference follows the expected trends since the reaction network of A4 is formulated in a way that it includes also one of all larger PAHs in the EST3 mechanism. Considering the model uncertainties associated with the reaction rate expressions for aromatic species, the predictive capabilities of the EST3 mechanism are promising. For the rest of the sections, EST3 is selected for numerical simulations.

4. Soot modeling approach

In this section, the soot formation and the evolution of particle size distribution are described using two soot models that rely on a moment-based and on a discrete representation of the population balance equations, respectively. Both models applied in this study describe a univariate evolution of the soot particles and mainly differ in the representation and approximation of the particle number density function (NDF). These models are based on the discrete sectional method (DSM) [19] and the split-based extended quadrature method of moments (S-EQMOM) [20] for describing the soot particle dynamics. The modeling approaches assume purely spherical soot particles, neglecting aggregation processes. However, the flames considered in this study are predominantly lightly to moderately sooting, hence with low levels of chain-like soot aggregates, which justifies this assumption.

4.1. Discrete sectional method (DSM)

In DSM, soot particle volume ranges are divided into a finite number of sections (using a geometric progression here). For each section, i, the governing equation for the soot mass fraction $Y_{s,i}$ is solved by taking into account flow convection, diffusion (for numerical stability), thermophoresis, and soot formation rates. The sectional soot transport equation can be formulated along the flame-normal coordinate x using a quasi-1D approximation and is given by Eq. (2):

$$\frac{\partial(\rho Y_{s,i})}{\partial t}+\frac{\partial}{\partial x}\left(\rho\left[u+v_T\right]Y_{s,i}\right)=\frac{\partial}{\partial x}\left(\rho D_{s,i}\frac{\partial Y_{s,i}}{\partial x}\right)+\rho_s\dot{Q}_{s,i},\quad \forall\, i\in\left[1,N_{sec}\right] \tag{2}$$

where ρ_s is the density of soot particles (assumed to be 1860 kg/m^3 [19]). In the transport equation, $\dot{Q}_{s,i}$ is the sectional soot source term, and v_T is the thermophoretic velocity given by Friendlander et al. [36] as:

$$v_T=-0.55\frac{\nu}{T}\frac{\partial T}{\partial x}, \tag{3}$$

where ν is the kinematic viscosity and T is the local temperature. The diffusion coefficient of soot particles of class i is given by $D_{s,i}$. The sectional source terms $\dot{Q}_{s,i}$ include the contributions from the chemical and physical processes associated with the soot formation such as nucleation, condensation, surface growth, soot oxidation, and particle–particle coagulation.

The nucleation process is modeled through PAH (pyrene molecules here) dimerization. The reaction networks of the larger species are lumped within the gas-phase kinetics, resulting in pyrene serving as the sole surrogate species in the transition pathway from gas-phase to

young soot particles. The PAH condensation is considered as the coalescence of a PAH molecule at a soot particle surface. The growth and oxidation of soot particles by surface reactions are represented through the hydrogen-abstraction-C_2H_2-addition (HACA) mechanism [37] with rate coefficients given by Appel et al. [38]. In the surface growth model, the fraction of sites available for hydrogen abstraction is assumed to be a function of the thermal age, and particle size history [38]. The soot oxidation is considered through surface reactions involving O_2 and OH molecules with soot. The coagulation of soot particles is described following the model proposed by Kumar and Ramkrishna [39]. The morphological description of particles is not considered for simplicity. The DSM model has been validated for soot prediction in laminar flames in earlier works [19,40,41]. A detailed description of the soot model used in this study can be found in Hoerlle and Pereira [19].

4.2. Split-based extended quadrature method of moments (S-EQMOM)

In S-EQMOM [20], the number density function of the particles is approximated by its statistical properties and their moments, so it does not solve for the distribution of the particles directly. The univariate particle distribution is described using the volume V of the particles leading to the definition of the moment m_k of order k as:

$$m_k = \int_{V=V_{\min}}^{\infty} V^k n(t,x;V)\mathrm{d}V. \tag{4}$$

Herein, $n(t,x;V)$ defines the NDF of particles in space x and time t. Transport equations given in Eq. (5) for the low-order moments are considered including thermophoresis effects on soot:

$$\frac{\partial m_k}{\partial t} + \frac{\partial}{\partial x}\left(\left[u + v_T\right]m_k\right) = \dot{m}_k \tag{5}$$

The term $\dot{m}_k$ represents the sum of source terms arising due to physical and chemical soot processes such as nucleation, surface growth by the HACA-mechanism or PAH adsorption, coagulation, and oxidation analogously to the ones described in Section 4.1 for DSM. Following the approach of the Extended Quadrature Method of Moments of Yuan et al. [42], kernel density functions (KDF) of a known shape are used to approximate the PSD and therefore, enable a closure for the calculation of the moment source terms based on the distribution itself.

While in the standard EQMOM, the NDF is calculated based on the sum of the kernel density functions, and the inversion process is performed for the entire NDF, S-EQMOM splits this inversion procedure up for every sub-NDF [20]. In S-EQMOM, the moments of several coupled sub-NDFs are treated individually before the entire NDF is composed again by the sum of all sub-NDFs. This method results in an individual moment inversion step for every sub-NDF leading to a unique solution for every sub-NDF, enhanced robustness, and more stability of the inversion algorithm. The NDF $n(V)$ as the sum of individual sub-NDFs n_{s_i} is defined as:

$$n(V) = \sum_{j=1}^{N_s} n_{s_i}(V) \approx \sum_{j=1}^{N_s} w_{s_i}\delta_{\sigma_{s_i}}(V, V_{s_i}). \tag{6}$$

The sub-NDFs $n_{s_i}(V)$ in Eq. (6) are approximated by the sum of weighted sub-NDFs $\delta_{\sigma_{s_i}}$ of a defined shape following the work of Salenbauch et al. [20]. In the current study, the entire NDF is approximated with three sub-NDFs each with a gamma function shape. The individual shape parameters σ_{s_i}, weights w_{s_i}, and node positions V_{s_i} of the three applied sub-NDFs can be obtained based on the three lower-order moments of each sub-NDF. This leads to nine transported moments for reconstructing the entire particle NDF through superposition. In contrast, moments of the entire NDF get transported in the standard EQMOM. An extensive evaluation of the required number of sub-NDFs and the impact of different shapes for the sub-NDFs is provided in [20, 43]. The modeling performance of S-EQMOM has been demonstrated for premixed flames [20] and turbulent jet flames [44].

In both DSM and S-EQMOM modeling frameworks, a two-way coupling between soot chemistry and gas-phase chemistry is incorporated into the conservation equations to ensure mass/energy balance. The solvers and soot models used in this study have been rigorously verified and validated in prior research [19,20,43].

5. Assessment of the combined kinetic and soot modeling approaches

Before addressing the sooting flames from the experimental setup, we assess the combination of the kinetic scheme EST3 and the corresponding coupling with the different soot modeling strategies. This step is crucial since the soot precursor formation depends on the underlying gas-phase chemistry, and therefore subsequent soot formation results strongly depend on the used gas-phase kinetics as demonstrated in [45]. Details of the validation of the individual soot models are provided for the DSM in [19,40] and for the S-EQMOM in [20,43].

For this assessment, the counterflow ethylene flames under different strain rates, studied by Wang and Chung [11] (referred to as KAUST flames), are considered. In these flames, the fuel is C_2H_4 and the oxidizer is composed of 25% of O_2 and 75% of N_2 (on a molar basis). The reactant streams are separated with a distance of 8 mm. The flow velocities for both the fuel and oxidizer streams are varied from 15 cm/s to 30 cm/s corresponding to four global strain rates K (75 s^{-1}, 100 s^{-1}, 125 s^{-1}, and 150 s^{-1}). Simulations of counterflow flames are conducted using a steady, 1-D formulation of reacting flow equations with plug-flow type boundary conditions for the inlet streams. The 1-D laminar flamelet solvers CHEM1D [46,47] and Universal Laminar Flame solver (ULF) [48] are used for computing sooting flames with DSM and S-EQMOM models, respectively. The investigated flames are SF (soot formation) type flames, in which the flame (or reacting layer) resides on the oxidizer side of the stagnation plane. Therefore, soot particles, nucleated on the fuel-rich side of the flame, are convected away from the flame towards the stagnation plane.

Computed profiles of soot volume fraction with the DSM and S-EQMOM soot models are compared against the experimental data for different strain rates in Fig. 4. In DSM, the soot volume fraction is obtained by multiplying the total soot mass fraction with the ratio of gas and soot density, assuming a constant soot density. On the other hand, in S-EQMOM, the soot volume fraction is determined using the first moment of the Number Density Function (NDF). Simulations are performed using the EST3 kinetic mechanism introduced earlier. In addition, modeling results for the KM2 mechanism [22] are added for comparison. As it can be observed, both DSM and S-EQMOM soot modeling strategies capture the spatial distribution and the lowered peak f_v values against strain rate reasonably well. Consistent with the experimental observations, numerical profiles show that the sooting zone thickness decreases with increasing strain rates. The measured soot volume fraction is underestimated in simulations for both models, DSM and S-EQMOM, and the disparity between numerical and experimental values decreases with the strain rate. Compared to the DSM method, S-EQMOM predicts a wider sooting zone starting closer to the flame front which is in good agreement with experimental observations. On the other hand, compared to S-EQMOM, the skewness of the f_v distribution is better reproduced by DSM. At the particle stagnation position, the diffusion transport and source term for soot balance leads to a sharp decrement in f_v, which is consistent with the experimentally observed leakage of soot through the stagnation plane. Both DSM and S-EQMOM strategies favorably predict the strain rate influence of soot formation for the reference flames, confirming the validity of the employed soot modeling techniques as well as of the kinetic scheme EST3 introduced in the present study.

6. Results and discussion

The previous section has shown that both DSM and S-EQMOM modeling approaches tend to perform similarly for the KAUST flames [11] using the new reaction mechanism EST3, specifically designed to use

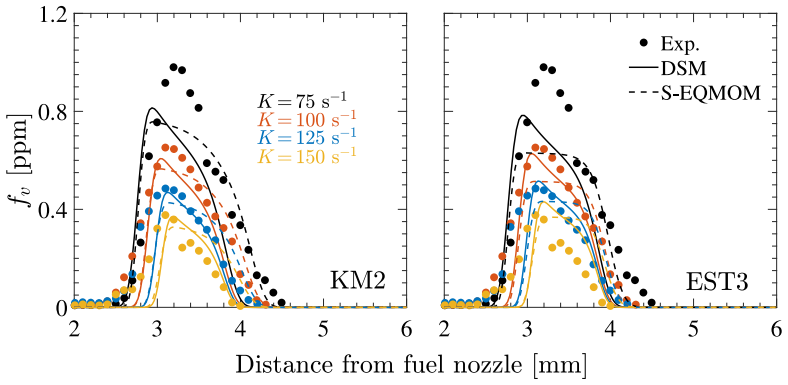

Fig. 4. Comparison between the numerical (curves) and experimental (symbols) profiles for soot volume fraction (f_v) with DSM (solid) and S-EQMOM (dashed) models for KM2 [22] (left) and EST3 (right) kinetic schemes. Experimental data are from Wang and Chung [11].

pyrene as lumped PAH species for particle nucleation. Therefore, these modeling strategies are adopted to investigate the new set of counter-flow diffusion flames measured at Karlsruhe Institute of Technology (KIT) [23]. The predictive capabilities of these modeling approaches are evaluated for strain rate sensitivity and dilution effects of soot formation by comparing the computed results against the measured soot volume fraction profiles and particle size distribution data. To the best of our knowledge, this is the first time such a comparison has been made on the same datasets. Additionally, the sub-processes of the soot formation are analyzed based on both modeling strategies. The flames under investigation are listed in Table 1.

6.1. Evaluation of soot volume fraction profiles

The measured (symbols) and computed (curves) profiles of soot volume fraction f_v are compared in Fig. 5 for strain rates $50\,s^{-1}$, $60\,s^{-1}$, and $70\,s^{-1}$ at a constant fuel mass fraction of $Y_{F,f} = 0.30$. Both soot models predict the qualitative trend of the reduced f_v with increasing strain rate. The measured flames exhibit soot formation type counterflow flames, where soot particles, incepted on the fuel-rich side of the flame, are convected towards the stagnation plane. Compared to DSM, higher f_v values are obtained with the S-EQMOM model. However, the width of the sooting zone is well predicted with the S-EQMOM model compared to DSM. A detailed analysis of different soot formation sub-processes will be presented later to investigate the differences in the modeling results for the two retained methodologies. While quantitative f_v predictions are maintained within the same order of magnitude in simulations, both models predict a lower sensitivity of f_v to strain rate compared to the experiments.

The modeled soot volume fraction profiles for varying levels of fuel mass fraction $Y_{F,f}$ at a constant strain rate of $K = 60\,s^{-1}$ are compared in Fig. 6 against measured SMPS data. An increase in f_v for higher ethylene concentration is obtained experimentally as well as in the modeling results. For the $Y_{F,f} = 0.35$, the S-EQMOM slightly overpredicts the soot formation, while the DSM model matches the measuring results fairly well. However, the reduction of soot formation with reduced ethylene mass fractions is stronger in the measurements as compared to the computed results for both models. Apparently, the soot formation is highly sensitive to the ethylene content in the fuel as 5% of decrement in ethylene mass fraction from $Y_{F,f} = 0.35$ leads to approximately 71% reduction in f_v measured at HAB = 5.5 mm. In the DSM model, such a drop in f_v values is obtained at 15% of reduction in $Y_{F,f} = 0.35$. Comparing the soot models, the S-EQMOM predicts higher amounts of soot volume fraction than the DSM model

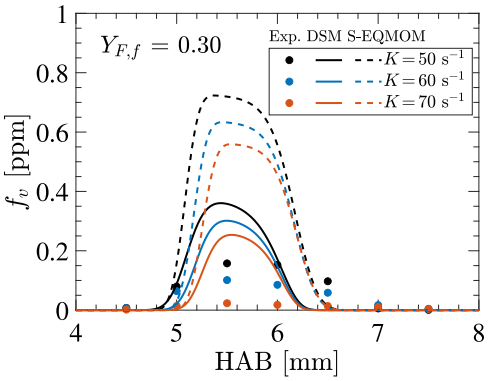

Fig. 5. Comparison between the numerical (curves) and experimental (symbols) soot volume fraction profiles for varying strain rates at a fuel mass fraction of $Y_f = 0.30$.

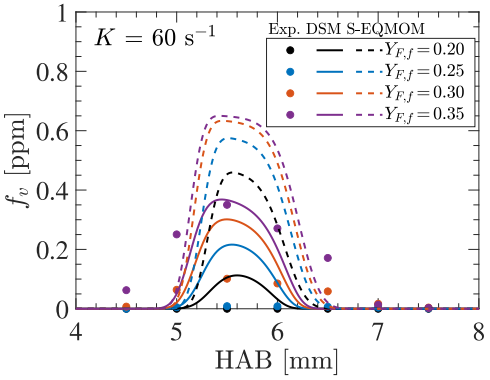

Fig. 6. Comparison between the numerical (curves) and experimental (symbols) soot volume fraction profiles for varying fuel mass fraction at a strain rate of $K = 60\,s^{-1}$.

in all investigated flame configurations. While the position of the peak value and particle stagnation plane agree well, the position of the soot formation zone in the S-EQMOM is displaced to higher HAB positions. Overall, the results are reasonably close to the experimental data taking into account the large uncertainties associated with the predictions of larger PAH concentrations in the EST3 mechanism.

The discrepancy between experimental data and modeling results in counterflow diffusion flames is a common observation in the literature across various modeling approaches [12,13,45,49,50]. These deviations are particularly observed near the stagnation plane. One possible reason for this discrepancy is the variation in the prediction of the flame stagnation position by the models, as measurements for velocity were not conducted and no scaling or numerical shift of the profiles was applied. In cases where the conditions of the studied flames align closely with those of other publications, a better agreement between the soot formation zones is observed, as is the case in the current study. The absolute misalignment between experimental data and models roughly scales with the distance between the fuel and oxidizer ducts, which in the current study is relatively large. The observed diffusion of soot in fuel-rich regions may also be attributed to experimental limitations. However, the exact cause of this systematic misalignment in some flames remains unclear, and further investigation is needed to determine its source.

Additionally, it is important to note, that the soot models were not specifically tuned for the investigated flames. For highly sooting conditions ($Y_{F,f} = 1$ as in KAUST flames), the predictive accuracy of both soot models is reasonably good, though, a stronger variability on the two soot models is observed for these challenging conditions with high fuel dilution and low soot formation. This is because, in flames with high fuel dilution that exhibit low-sooting conditions, the soot formation process is primarily limited by the initial inception step. While the bi-directional coupling between the gas-phase and soot model has a significant effect on the pyrene concentration profile in the gas phase (due to its very low concentration), the concentration of C_2H_2 (a primary contributor for HACA) is not significantly affected due to its overall high value. The sensitivity of the inception process to the gas phase conditions often makes it challenging to accurately capture the initial step and subsequent soot formation process.

6.2. Analyses of the soot sub-processes

To better understand the predictive capabilities of soot models an analysis of the different sub-processes is conducted. The contribution to the soot growth by nucleation, condensation, and HACA surface growth are compared in Fig. 7 for varying strain rates at a constant fuel mass fraction of $Y_{F,f} = 0.30$. Both modeling results show a decreasing peak value for the nucleation, condensation, and surface growth rates for increasing strain rates. The DSM and S-EQMOM models agree on the overall trends and also on the shape of the soot formation rate profiles. While the soot volume fraction profiles in Fig. 5 contain a significant sensitivity for strain rate variations, only small differences in the underlying soot production rates can be observed. The computed rate profiles for different sub-processes mainly differ in the peak position and quantitative values. The condensation and, in the case of the S-EQMOM method, also the nucleation process is markedly influenced by strain rate variations while the difference in the surface growth reactions is almost negligible. Comparing the nucleation rates between the models, it can be seen, that only minor differences are present at the start of the soot formation at HAB = 7 mm up to approximately HAB = 6.2 mm since the nucleation process is solely depending on the underlying gas-phase and on the amount of the PAH species pyrene that initiates the inception step within both soot models. The condensation and surface growth processes on the other hand depend additionally on the modeled PSD, leading to larger deviations between both models. Due to the bi-directional coupling between the gas phase and the particle model, small deviations in some of these processes are also

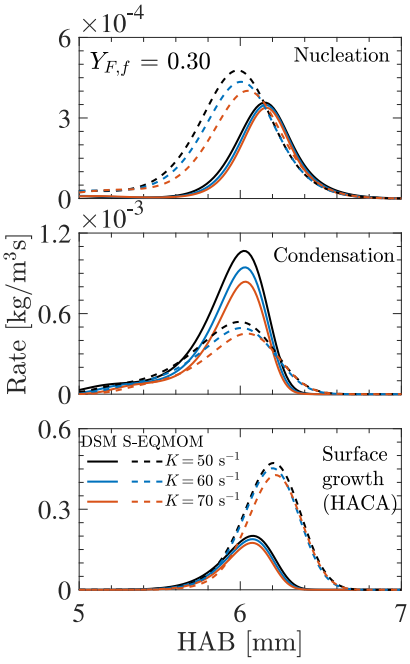

Fig. 7. Computed profiles of soot growth sub-processes with the DSM (solid) and S-EQMOM soot model (dashed) for varying strain rates (indicated by color) at a fuel mass fraction of $Y_f = 0.30$.

altering the underlying gas-phase composition. In fact, the nucleation and condensation processes reduce the pyrene concentration in the gas phase. Hence, larger deviations in nucleation can be observed at lower HAB positions, when condensation and surface growth processes are dominantly affecting the gas-phase chemistry. Fig. 2 demonstrates that the acetylene profile (which impacts the surface growth) is primarily influenced by fuel dilution and only slightly decreases for higher strain rates. However, increased strain rates significantly reduce the residence time of particles in the flame due to higher gas phase velocities. Consequently, despite similar surface growth rates, the variation in residence times leads to different soot volume fractions. Considering relatively small variations in the soot formation rates, the difference in the amount of soot formed for different strain rates can be mainly attributed to varying flow velocities and subsequently the change in the residence times of soot particles.

The rate profiles of different soot sub-processes for varying fuel mass fractions at a constant strain rate of $K = 60\,s^{-1}$ are shown in Fig. 8. The rates for all the sub-processes are significantly increased at higher fuel mass fractions in the fuel stream at a constant strain rate (and thus similar residence times). The increase in soot volume fractions at increasing ethylene content in fuel, as observed in Fig. 6, can therefore be mainly ascribed to the increment in soot formation rates through HACA surface reactions, and higher concentration of soot precursors (not shown) affecting soot inception rates. Again, both DSM and S-EQMOM models follow similar trends and agree in the overall shape; however, quantitative deviations and a shift of the profiles can be observed. In both studies, Figs. 7 and 8, the DSM model leads on one hand to higher condensation rates than the S-EQMOM model, while on the other hand, nucleation rates are reduced which can be

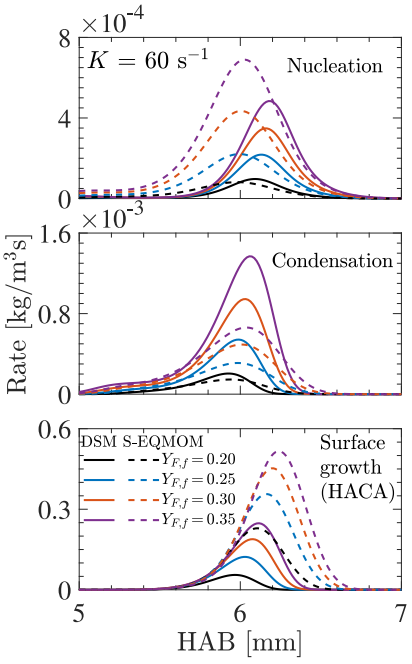

Fig. 8. Computed profiles of soot growth sub-processes with the DSM (solid) and S-EQMOM soot model (dashed) for varying fuel mass fraction (indicated by color) at a strain rate of $K = 60\,s^{-1}$.

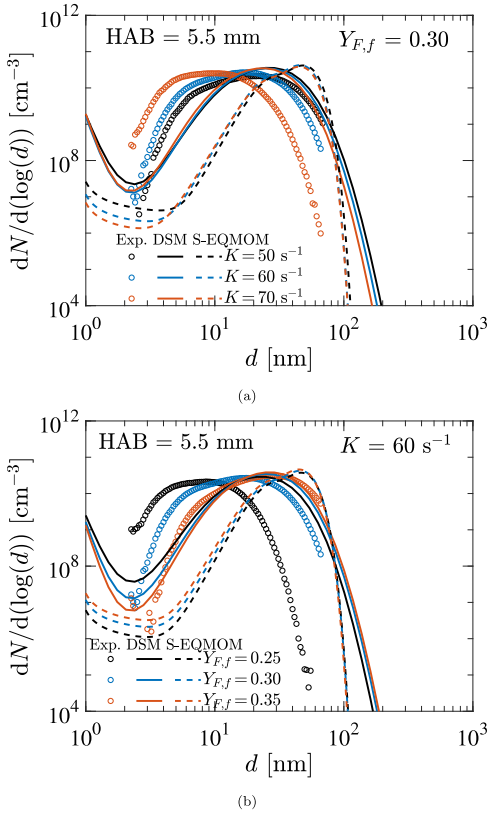

Fig. 9. Comparison between the numerical (curves) and experimental (symbols) PSD for varying strain rates at a fuel mass fraction of $Y_{F,f} = 0.30$ (a), and for varying fuel mass fraction at a strain rate of $K = 60\,s^{-1}$ (b).

explained by the dependence of both processes on the amount of pyrene. These results clearly highlight the competing processes. The S-EQMOM exhibits higher HACA surface growth rates leading also to higher soot volume fractions due to surface growth, which is the largest contributor to soot formation.

Overall, the surface growth mechanism through the HACA pathway contributes significantly to the overall soot loading in terms of soot volume or mass, surpassing the contribution of the inception process or PAH deposition onto the particle surface by several orders of magnitude (as identified in earlier works [11,49] for flames at atmospheric pressure). This is attributed to the large differences in concentration between the C_2H_2 and PAH species, which play key roles in the respective soot processes. However, it is important to note that surface growth is not the sole factor influencing the final soot profile. Other factors, such as residence time due to varying strain rates, the profile and peak concentration of gas-phase precursors, and the position of the flame relative to the stagnation plane, also strongly influence soot formation in the investigated counterflow configurations.

6.3. Evaluation of particle size distributions

In addition to the volume fraction, particle size distributions (PSD) were measured for the investigated flames. The experimental and modeling results of PSDs at a height above the burner of HAB = 5.5 mm (location of highest f_v value in the measurements) are compared in Fig. 9. The experimental SMPS measurement range is limited to particles with a mobility diameter (d_m) between $2\,nm \leqslant d_m \leqslant 79\,nm$, and consists mainly of the log-normal mode of PSD referring to larger particles, while the inception mode is only partially visible at the smallest detectable diameters. Furthermore, it should be noted that there is a significant loss of particles smaller than 10 nm in the probe, tubes, and mobility sizer, resulting in increased experimental uncertainties for the small particle sizes [23]. PSD profiles for a constant fuel mass fraction of $Y_{F,f} = 0.30$ with varying strain rates are displayed in Fig. 9(a), whereas in Fig. 9(b), results for varying fuel mass fractions at a constant strain rate of $K = 60\,s^{-1}$ are presented.

The current soot modeling approaches are based on the volume equivalent particle diameter d_p, whereas measurement data represent mobility sizes (d_m) of particles. A scaling is applied to convert d_m to d_p as proposed in the Refs. [51,52]. Since the current modeling approach assumes the spherical nature of soot particles, the conversion of particle sizes using empirical scaling may be ambiguous, considering the limitations of the empirical Cunningham slip correction transformation, uncertainty of the number of primary particles per aggregate when converting mobility sizes (d_m) to spherical particle sizes (d_p). To address these considerations and avoid ambiguity, the particle diameter in Fig. 9 is generalized with the symbol d and should be interpreted as d_m for measurements and d_p for simulations.

As evident in Fig. 9(a), the median diameter of the log-normal mode shifts to larger particle diameters for decreasing strain rates at constant

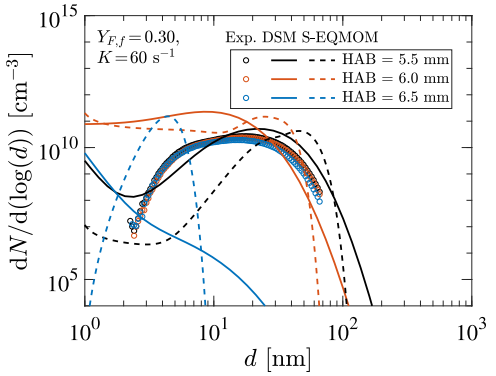

Fig. 10. Comparison between the numerical (curves) and experimental (symbols) PSD profiles at different HAB positions (indicated by color) for the flame with $Y_{F,f} = 0.30$ and $K = 60\,s^{-1}$.

fuel mass fraction. A similar shift towards larger diameters is also noticed in PSDs for higher ethylene mass fractions at constant strain rates (see Fig. 9(b)). However, the number density at this peak position of PSD is not significantly affected by a strain rate or fuel mass fraction variation. Only a slight reduction in number density is observed with a decrement in strain rate or ethylene content in the fuel. The computed profiles by DSM and S-EQMOM strategies favorably capture the shape of PSD for varied strain rates and fuel compositions. The stronger shift in the PSD profiles can be observed in the measurements as a consequence of the high sensitivity of soot volume fraction to strain rate and fuel composition variations for the investigated flames. The simulated profiles, on the other hand, show only a marginal shift in the median diameter of PSD as the soot sensitivity is under-predicted in the simulations.

The modeling results are dominated by the log-normal mode as well indicating that the soot inception area is placed at a higher HAB. The particle evolution is mainly influenced by particle growth and coagulation events during its convection to the particle stagnation plane at smaller HAB. The shape of the DSM results matches the experimentally observed profile quite closely, also the qualitative trends in PSD shift are captured well by the DSM model. The S-EQMOM profiles are dominated by a peak at a diameter of 50 nm in Fig. 9(a). Here, the superposition of the three underlying sub-KDFs represented by gamma functions results in a distinct peak of the second mode. The position of the peak is equivalent to the position of one of the sub-KDFs containing the largest particles, while the remaining two sub-KDFs represent the first mode and particles in between. Overall, the modeling results are consistent with experimental findings regarding the marginal change in the number density of the peak of the log-normal mode. However, the peak position of this mode is only slightly shifted for varying strain rates and fuel mass fractions in computations.

A more detailed comparison of PSD evolution is presented in Fig. 10, where PSD profiles at different HABs are shown for the flame at $Y_{F,f} = 0.30$ and $K = 60\,s^{-1}$. The computed PSD profiles show strong variations in PSD shape along the HAB, including a transition from unimodal to a bimodal distribution. However, measured PSD profiles hardly show this transition, and PSDs predominantly exhibit the log-normal distribution. As it occurs in SF-type flame, consistent soot inception occurs at higher HABs (oxidizer side of stagnation plane), giving unimodal PSD shape (HAB = 6.0 mm) in simulations. At the spatial position of HAB = 6.5 mm, which marks the start of the soot formation process, differences between the PSD shape predictions by the S-EQMOM and DSM models are prominent. The S-EQMOM model shows a slight contribution of surface growth, indicating that particles have already undergone some level of growth by this point. In contrast, the DSM model does not show significant surface growth at the start of the soot formation process (as can be seen also Figs. 7 and 8). This slight disparity in spatial positions of soot growth rate profiles essentially leads to a different shape of the particle size distribution (PSD) by both models at this position. Soot particles grow by surface growth and coagulation while being convicted towards the stagnation plane. In such conditions, the PSD becomes bimodal, with an increase in the median diameter of the log-normal mode.

Soot inception predominantly occurs for both models at HABs greater than 5.5 mm, with the peak of inception at approximately HAB = 6 mm and HAB = 6.25 mm for the respective models. However, at HAB = 5.5 mm, coagulation dominates the soot evolution processes. In Fig. 10 it is evident that smaller particles of the first mode, which are present at HAB = 6 mm in both models, undergo rapid growth and coagulation, transitioning towards the second mode. Due to slight variations in the spatial rate profiles of sooting subprocesses between the models, the coagulation process is more advanced in the S-EQMOM model at HAB = 5.5 mm, resulting in fewer inception particles despite higher inception rates in Figs. 8 and 7. The evolution of the growth processes seems to overweigh the inception rate at this position in the flame. This PSD evolution is qualitatively well captured by both DSM and S-EQMOM models. However, the soot formation is found to start at higher HABs in experiments, as evident from f_v profiles (see Fig. 5). Therefore discrepancy between numerical and measured profiles of PSD suggests that the soot inception locations are predicted at lower HABs in simulations as compared to measurements.

7. Concluding remarks

A systematic investigation of soot formation and particle size distributions in laminar ethylene counterflow flames is conducted by combining experimental and numerical methodology. The focus is given to the analysis of the influence of strain rate and fuel dilution on sooting characteristics. Such investigation is reported for the first time to the best of the authors' knowledge.

The modeling strategy consists of a recently developed reaction mechanism considering the description of PAHs up to A4 and two detailed soot modeling approaches DSM and S-EQMOM. The modeling results are compared against dedicated experiments with optical diagnostics measuring the soot volume fraction profiles and the PSD for a wide range of operation conditions. First, the kinetic scheme EST3 is validated for the prediction of gas-phase species including PAHs and temperature showing excellent agreement. The soot modeling results also closely reproduce their experimental counterparts regarding the strain rate and dilution effects on the soot volume fraction profiles. Additionally, the results suggest that strain rate variations mainly influence the residence time while only slightly affecting the rates of the underlying soot production processes. Furthermore, a reduction in the ethylene content of the fuel strongly reduces the soot production rates and, thus, the overall soot volume fraction. Modeled PAH-based sub-processes, namely inception, and condensation, exhibit higher sensitivity to the strain and fuel variations than the HACA process. The experimental results show a high sensitivity of soot formation to the ethylene content compared to numerical results. Overall, the simulation results are in close agreement with the experimental data revealing certain over-predictions acceptable for the soot models. Still, the predictivity of the models is considered good in the context of soot investigations for this wide range of flame conditions.

Both models show similar quantitative trends under strain rate and fuel composition variation, suggesting a high generality of the findings and being independent of the applied soot modeling strategy. Differences between DSM and S-EQMOM are limited to minor deviations of the overall quantity in the rate profiles of different sub-processes

or slight shifts in their peak positions. One of the key highlights of this study is the joint experimental and numerical investigation of the soot PSDs for varying strain rates and fuel compositions, where a close agreement is observed between modeling and measurement for the response of soot PSD to these two changes. Nevertheless, the numerical PSD profiles exhibit reduced sensitivities to these variations as compared to the measurements.

Additionally, the present study demonstrates the promising capabilities of the kinetic scheme EST3 in combination with detailed soot models in capturing experimentally observed responses of soot formation and PSD evolution in laminar flames. While this study focuses on the well-understood ethylene fuel, the applied kinetic mechanism allows an extension of these investigations to more complex fuels such as kerosene surrogates.

Declaration of competing interest

The authors declare that they have no known competing financial interests or personal relationships that could have appeared to influence the work reported in this paper.

Acknowledgments

The research leading to these results has received funding from the European Union's Horizon 2020 Programme under the ESTiMatE project, grant agreement No. 821418.

References

[1] C. Voigt, J. Kleine, D. Sauer, R.H. Moore, T. Bräuer, P. Le Clercq, S. Kaufmann, M. Scheibe, T. Jurkat-Witschas, M. Aigner, et al., Cleaner burning aviation fuels can reduce contrail cloudiness, Commun. Earth Environ. 2 (1) (2021) 114.
[2] European Commission and Directorate-General for Mobility and Transport and Directorate-General for Research and Innovation, Flightpath 2050: Europe's Vision for Aviation: Maintaining Global Leadership and Serving Society's Needs, Publications Office of the European Union, Luxembourg, Luxembourg, 2011.
[3] M. Sirignano, J. Kent, A. D'Anna, Modeling formation and oxidation of soot in nonpremixed flames, Energy Fuels 27 (4) (2013) 2303–2315.
[4] M. Sirignano, J. Kent, A. D'Anna, Further experimental and modelling evidences of soot fragmentation in flames, Proc. Combust. Inst. 35 (2) (2015) 1779–1786.
[5] A. Cuoci, A. Frassoldati, T. Faravelli, E. Ranzi, Soot formation in unsteady counterflow diffusion flames, Proc. Combust. Inst. 32 I (1) (2009) 1335–1342.
[6] P. Rodrigues, B. Franzelli, R. Vicquelin, O. Gicquel, N. Darabiha, Unsteady dynamics of PAH and soot particles in laminar counterflow diffusion flames, Proc. Combust. Inst. 36 (1) (2017) 927–934.
[7] W. Pejpichestakul, A. Frassoldati, A. Parente, T. Faravelli, Soot modeling of ethylene counterflow diffusion flames, Combust. Sci. Technol. (2018).
[8] H. Wang, D. Du, C. Sung, C. Law, Experiments and numerical simulation on soot formation in opposed-jet ethylene diffusion flames, Symp. (Int.) Combust. 26 (2) (1996) 2359–2368.
[9] H. Böhm, K. Kohse-Höinghaus, F. Lacas, C. Rolon, N. Darabiha, S. Candel, On PAH formation in strained counterflow diffusion flames, Combust. Flame 124 (1–2) (2001) 127–136.
[10] M. Yamamoto, S. Duan, S. Senkan, The effect of strain rate on polycyclic aromatic hydrocarbon (PAH) formation in acetylene diffusion flames, Combust. Flame 151 (3) (2007) 532–541.
[11] Y. Wang, S. Chung, Strain rate effect on sooting characteristics in laminar counterflow diffusion flames, Combust. Flame 165 (2016) 433–444.
[12] S. Kruse, A. Wick, P. Medwell, A. Attili, J. Beeckmann, H. Pitsch, Experimental and numerical study of soot formation in counterflow diffusion flames of gasoline surrogate components, Combust. Flame 210 (2019) 159–171.
[13] E. Quadarella, J. Guo, H.G. Im, A consistent soot nucleation model for improved prediction of strain rate sensitivity in ethylene/air counterflow flames, Aerosol Sci. Technol. 56 (7) (2022) 636–654.
[14] P.H. Joo, Y. Wang, A. Raj, S.H. Chung, Sooting limit in counterflow diffusion flames of ethylene/propane fuels and implication to threshold soot index, Proc. Combust. Inst. 34 (1) (2013) 1803–1809.
[15] F. Carbone, F. Cattaneo, A. Gomez, Structure of incipiently sooting partially premixed ethylene counterflow flames, Combust. Flame 162 (11) (2015) 4138–4148.
[16] K. Gleason, F. Carbone, A. Gomez, Effect of temperature on soot inception in highly controlled counterflow ethylene diffusion flames, Combust. Flame 192 (2018) 283–294.
[17] Y. Wang, S.H. Chung, Soot formation in laminar counterflow flames, Prog. Energy Combust. Sci. 74 (2019) 152–238.
[18] F.P. Hagen, P. Vlavakis, H. Bockhorn, R. Suntz, D. Trimis, From molecular to sub-μm scale: The interplay of precursor concentrations, primary particle size, and carbon nanostructure during soot formation in counter-flow diffusion flames, Combust. Flame (2023) 112729.
[19] C. Hoerlle, F. Pereira, Effects of CO_2 addition on soot formation of ethylene non-premixed flames under oxygen enriched atmospheres, Combust. Flame 203 (2019) 407–423.
[20] S. Salenbauch, C. Hasse, M. Vanni, D.L. Marchisio, A numerically robust method of moments with number density function reconstruction and its application to soot formation, growth and oxidation, J. Aerosol Sci. 128 (2019) 34–49.
[21] A. Ramirez Hernandez, T. Kathrotia, T. Methling, M. Braun-Unkhoff, U. Riedel, Reaction model development of selected aromatics as relevant molecules of a kerosene surrogate—The importance of m-xylene within the combustion of 1,3,5-trimethylbenzene, J. Eng. Gas Turbines Power 144 (2) (2022) 021002.
[22] Y. Wang, A. Raj, S.H. Chung, A PAH growth mechanism and synergistic effect on PAH formation in counterflow diffusion flames, Combust. Flame 160 (9) (2013) 1667–1676.
[23] F.P. Hagen, P. Vlavakis, M. Seitz, T. Klövekorn, H. Bockhorn, R. Suntz, D. Trimis, Soot nanoparticle sizing in counterflow flames using in-situ particle sampling and differential mobility analysis verified with two-colour time-resolved laser-induced incandescence, Proc. Combust. Inst. 39 (2023) 1119–1128.
[24] A.M. Valencia-López, F. Bustamante, A. Loukou, B. Stelzner, D. Trimis, M. Frenklach, N.A. Slavinskaya, Effect of benzene doping on soot precursors formation in non-premixed flames of producer gas (PG), Combust. Flame 207 (2019) 265–280.
[25] R. Khare, P. Vlavakis, T. Von Langenthal, A. Loukou, M. Khosravi, U. Kramer, D. Trimis, Experimental investigation of the effect of hydrogen addition on the sooting limit and structure of methane/air laminar counterflow diffusion flames, Fuel 324 (2022) 124506.
[26] C.R. Shaddix, Correcting thermocouple measurements for radiation loss: a critical review, 1999.
[27] M. Sentko, S. Schulz, C. Weis, B. Stelzner, C. Anderlohr, M. Vicari, D. Trimis, Experimental investigation of synthesis gas production in fuel-rich oxy-fuel methane flames, Fuel 317 (2022) 123452.
[28] Y. Karakaya, J. Sellmann, I. Wlokas, T. Kasper, Influence of the sampling probe on flame temperature, species, residence times and on the interpretation of ion signals of methane/oxygen flames in molecular beam mass spectrometry measurements, Combust. Flame 229 (2021) 111388.
[29] H. Shariatmadar, P.G. Aleiferis, R. Lindstedt, Particle size distributions in turbulent premixed ethylene flames crossing the soot inception limit, Combust. Flame 243 (2022) 111978.
[30] F.P. Hagen, A. Rinkenburger, J. Günther, H. Bockhorn, R. Niessner, R. Suntz, A. Loukou, D. Trimis, C. Haisch, Spark discharge-generated soot: Varying nanostructure and reactivity against oxidation with molecular oxygen by synthesis conditions, J. Aerosol Sci. 143 (2020) 105530.
[31] I. Frenzel, H. Krause, D. Trimis, Study on the influence of ethanol and butanol addition on soot formation in iso-octane flames, Energy Procedia 120 (2017) 721–728.
[32] A. Ramirez Hernandez, T. Kathrotia, T. Methling, M. Braun-Unkhoff, U. Riedel, An upgraded chemical kinetic mechanism for iso-octane oxidation: Prediction of polyaromatics formation in laminar counterflow diffusion flames, J. Eng. Gas Turbines Power 145 (6) (2023) 061006.
[33] T. Kathrotia, P. Oßwald, C. Naumann, S. Richter, M. Köhler, Combustion kinetics of alternative jet fuels, Part-II: Reaction model for fuel surrogate, Fuel 302 (2021) 120736.
[34] T. Kathrotia, T. Methling, https://www.dlr.de/vt/mechanisms, 2022.
[35] D.G. Goodwin, H.K. Moffat, R.L. Speth, Cantera: An object-oriented software toolkit for chemical kinetics, thermodynamics, and transport processes, 2022.
[36] S. Friendlander, Smoke, Dust and Haze: Fundamentals of Aerosol Dynamics, Oxford University Press, New York, USA, 2000.
[37] M. Frenklach, H. Wang, Detailed modeling of soot particle nucleation and growth, Symp. (Int.) Combust. 23 (1) (1991) 1559–1566.
[38] J. Appel, H. Bockhorn, M. Frenklach, Kinetic modeling of soot formation with detailed chemistry and physics: laminar premixed flames of C2 hydrocarbons, Combust. Flame 121 (1–2) (2000) 122–136.
[39] S. Kumar, D. Ramkrishna, On the solution of population balance equations by discretization–I. a fixed pivot technique, Chem. Eng. Sci. 51 (8) (1996) 1311–1332.
[40] A. Kalbhor, J. van Oijen, Effects of hydrogen enrichment and water vapour dilution on soot formation in laminar ethylene counterflow flames, Int. J. Hydrogen Energy 45 (43) (2020) 23653–23673.
[41] A. Kalbhor, Model Development and Numerical Investigation of Soot Formation in Combustion (Ph.D. thesis), Eindhoven University of Technology, the Netherlands, 2023.
[42] C. Yuan, F. Laurent, R.O. Fox, An extended quadrature method of moments for population balance equations, J. Aerosol Sci. 51 (2012) 1–23.
[43] S. Salenbauch, Modeling of Soot Formation and Oxidation in Reacting Flows (Ph.D. thesis), Technical University of Darmstadt, 2018.

[44] F. Ferraro, S. Gierth, S. Salenbauch, W. Han, C. Hasse, Soot particle size distribution reconstruction in a turbulent sooting flame with the split-based extended method of moments, Phys. Fluids 075121 (2022).
[45] Y. Wang, W. Han, T. Zirwes, A. Attili, L. Cai, H. Bockhorn, L. Yang, Z. Chen, A systematic analysis of chemical mechanisms for ethylene oxidation and PAH formation, Combust. Flame 253 (2023) 112784.
[46] B. Somers, The Simulation of Flat Flames with Detailed and Reduced Chemical Models (Ph.D. thesis), Eindhoven University of Technology, 1994.
[47] CHEM1D: One-Dimensional Laminar Flame Code, Eindhoven University of Technology, 2022.
[48] A. Zschutschke, D. Messig, A. Scholtissek, C. Hasse, Universal laminar flame solver (ULF), 2017.
[49] L. Xu, F. Yan, M. Zhou, Y. Wang, S.H. Chung, Experimental and soot modeling studies of ethylene counterflow diffusion flames: Non-monotonic influence of the oxidizer composition on soot formation, Combust. Flame 197 (2018) 304–318.
[50] K.C. Kalvakala, V.R. Katta, S.K. Aggarwal, Effects of oxygen-enrichment and fuel unsaturation on soot and NO emissions in ethylene, propane, and propene flames, Combust. Flame 187 (2018) 217–229.
[51] J. Singh, R.I. Patterson, M. Kraft, H. Wang, Numerical simulation and sensitivity analysis of detailed soot particle size distribution in laminar premixed ethylene flames, Combust. Flame 145 (1–2) (2006) 117–127.
[52] A.D. Abid, J. Camacho, D.A. Sheen, H. Wang, Quantitative measurement of soot particle size distribution in premixed flames–the burner-stabilized stagnation flame approach, Combust. Flame 156 (10) (2009) 1862–1870.

P5 Fuel 286 (2021), 119353

F. Ferraro, C. Russo, **R. Schmitz**, C. Hasse, and M. Sirignano, "Experimental and numerical study on the effect of oxymethylene ether-3 (OME_3) on soot particle formation," Fuel, vol. 286, p. 119353, Feb. 2021, doi: 10.1016/j.fuel.2020.119353.

As one of the authors of this Elsevier article, I retain the right to include this article in this manuscript [128]. The original source is available under the digital object identifier above.

Author contributions

Tab. P.5: Author contributions to publication [130] following CRediT [127]

Federica Ferraro	Conceptualization of the numerical setup and investigations (equal) Interpretation and discussion of the experimental and numerical results (lead) Data analysis and visualization (equal) Writing – Original draft Main and corresponding author
Carmela Russo	Conceptualization of the design of experiment (equal) Conduction of the experimental investigations (equal) Data analysis and visualization (support) Interpretation and discussion of the experimental and numerical results (equal)
Robert Martin Schmitz	Conceptualization of the numerical setup and investigations (equal) Conduction of the detailed numerical simulations Validation of numerical setup and software Data analysis of numerical results Interpretation and discussion of the experimental and numerical results (equal)
Christian Hasse	Conceptualization of the numerical setup and investigations (equal) Supervision (lead) Funding acquisition
Mariano Sirignano	Conceptualization of the design of experiment (equal) Conduction of the experimental investigations (equal) Data analysis and visualization (equal) Interpretation and discussion of the experimental and numerical results (equal) Supervision (support)
All co-authors	Writing – Review & Editing

Use of publication contents in finalized and ongoing dissertations

This publication is part of the ongoing dissertation of Robert Martin Schmitz at the Institute for Simulation of reactive Thermo-Fluid Systems at the Technical University of Darmstadt, Germany

Fuel 286 (2021) 119353

Contents lists available at ScienceDirect

Fuel

journal homepage: www.elsevier.com/locate/fuel

Full Length Article

Experimental and numerical study on the effect of oxymethylene ether-3 (OME_3) on soot particle formation

Federica Ferraro [a,*], Carmela Russo [b], Robert Schmitz [a], Christian Hasse [a], Mariano Sirignano [c]

[a] Institute for Simulation of Reactive Thermo-Fluid Systems (STFS), Technische Universität Darmstadt, Otto-Berndt-Straße 2, Darmstadt 64287, Germany
[b] Istituto di Ricerche sulla Combustione, Consiglio Nazionale delle Ricerche, P.le Tecchio 80, 80125 Napoli, Italy
[c] Dipartimento di Ingegneria Chimica, dei Materiali e della Produzione Industriale – Università degli Studi di Napoli Federico II, P. le Tecchio 80, 80125 Napoli, Italy

ARTICLE INFO

Keywords:
Oxymethylene ether-3 (OME_3)
Polyoxymethylene dimethyl ether-3 ($PODE_3$)
Soot
Alternative fuels
Quadrature Method of Moments (QMOM)

ABSTRACT

The reduction and control of particulate matter generated by fossil fuel combustion are among the main issues for actual and future combustion devices due to the increasingly stringent emission regulations. Recently, various fuels have been investigated as a potential substitute or additive for diesel and gasoline. This work focuses on how oxymethylene ether-3 (OME_3), the smallest promising OME compound, affects carbon particulate formation when blended with ethylene in burner-stabilized premixed flames at different equivalence ratios. Particle size distribution (PSD) and Laser-Induced Fluorescence (LIF) and Incandescence (LII) along with numerical (Conditional Quadrature Method of Moments – CQMOM, based on D'Anna physico-chemical soot model) investigations were conducted to study particle formation and growth in pure ethylene and ethylene/OME_3 flames. The soot volume fraction and PSD indicate a reduction in the total number and the size of the soot particles at all equivalence ratios, while the number of small nanoparticles remains almost unchanged. The CQMOM model is able to predict similar trends for the soot volume fraction and, using the entropy maximization concept, the general shape of the PSD for both pure ethylene and OME_3-blended flames, compared to the experimental measurements.

Further, carbon particulate matter was thermophoretically sampled in the highest equivalence ratio conditions and spectroscopically analyzed. The soot structure was investigated using UV–Visible and Raman spectroscopy, finding a slightly higher aromaticity for the pure ethylene soot. FTIR analysis showed that carbon particulate matter produced from an OME_3-doped flame contained larger amounts of oxygen, mainly in the form of C═O.

1. Introduction

Soot is a particulate pollutant generated by the incomplete combustion of all hydrocarbons, including oxygenated ones. Due to its carcinogenic effects on human health and its detrimental impact on polar ice melting and climate change, the soot emission limits for combustion devices have become more stringent. Both the soot mass concentration and particle size distribution (PSD) need to be controlled and accurately predicted to design the next generation of combustion devices.

While bigger particles can be filtered with exhaust gas aftertreatment systems, small nanoparticles are more difficult to trap [1] and, once released into the atmosphere, can penetrate deeper into the human respiratory system, causing severe damage [2,3].

In order to reduce the carbon footprint, as well as the particulate emissions of combustion systems, the use of alternative synthetic fuels has been widely explored [4,5]. Oxygenated fuels including molecules that can be mixed with diesel (dimethyl ether (DME), biodiesel, etc.) and gasoline (bioethanol, biobutanol, etc.) have been developed in recent years. The general belief is that due to their intrinsic structure with high levels of embedded oxygen, the decomposition/oxidation of oxygenated fuel molecules is faster and more efficient [5] and lower amounts of particulate pollutants are emitted [6,7]. Despite these advances, recent studies have shown that these fuels indeed have great potential in reducing the total amount of particulate produced and hence emitted; however, particles are produced which are smaller in size [8] and, in some combustion conditions, higher in concentration [4]. Additionally, recent findings have shown that the use of oxygenated fuels can lead to the production of oxy-PAHs (polycyclic aromatic hydrocarbons) [9] and of particles with different chemical features, namely a larger presence of

* Corresponding author.
E-mail address: ferraro@stfs.tu-darmstadt.de (F. Ferraro).

https://doi.org/10.1016/j.fuel.2020.119353
Received 28 May 2020; Received in revised form 23 July 2020; Accepted 26 September 2020
Available online 1 November 2020

oxygen incorporated into particles [6,7,10]. This latter aspect could be responsible for the higher reactivity to oxidation [6,8,11–16] exhibited by the particulate which is formed, resulting in easier abatement in the after-treatment systems, but also in a higher propensity to interact with biological systems, yielding potentially higher toxicity [3]. These controversial aspects have to lead to research into new alternative fuel candidates in order to prevent possible negative outcomes from their use on a large scale.

Among several alternative fuel candidates, oxymethylene ethers (OME_n), $CH_3O(CH_2O)_nCH_3$, also known as polyoxymethylene dimethyl ethers (PODEs), are promising for realizing carbon–neutral combustion, when used as additives or substitutes for diesel engines. OMEs belong to the class of e-fuels, i.e., fuels that can be produced by recycling CO_2 via electrolysis using renewable energies, contributing to the overall greenhouse gas balance [17]. The high oxygen content and the lack of C—C bonds of OMEs generate fewer soot precursors such as C_2H_2, C_2H_4 and C_3H_3, indicating that there could be a potential reduction in carbon particulates [18]. OMEs with $n > 1$ have a high propensity to ignite, with a cetane number exceeding 60 [18]. Additionally, OMEs are non-toxic and miscible in diesel fuel. OMEs have shown positive effects in terms of reducing CO, unburned hydrocarbons and soot particle emissions when used as an additive to diesel in engine experiments [19–25]. A higher rate of exhaust gas recirculation (EGR) can be applied to reduce NO_x emissions [23,26]. Investigations on OME_1 as an alternative fuel indicate that soot is suppressed entirely [27]. However, since severe modifications are required for the engine and fuel supply system, blending OMEs into diesel fuels is a more feasible strategy.

Previous studies have identified OME_3 as the smallest-sized OME_n compound qualified for practical applications [18]. It has a high cetane number equal to 78, a low melting point at −41 °C and a high boiling point at 156 °C [24]. Examining the physico-chemical properties of the other OME_n compounds [18,24] it can be determined that: OME_1 has a low cetane number (29) and low boiling point (42 °C), therefore it is highly volatile and can vaporize during storage; OME_2 has a suitable cetane number (63), but a too low flash point to satisfy safety criteria [28]; OME_4 has a cetane number of 90, a melting point of −7 °C and a boiling point of 202 °C. Additionally, OMEs with $n > 5$ have a too high melting point. In summary, optimal compounds for blending with traditional fuels have $n = 3-4$ or $n = 3-5$ [18]. When OME_3 is compared with OME_4 and OME_5, OME_3 has a better low-temperature fluidity and volatility; therefore, it has been investigated in this study. In future, attention will be devoted to larger OME compounds and their blends.

Recently, reduced and detailed kinetic mechanisms have been developed for $OME_{1\text{-}3}$ [18,29,30] and for $OME_{2\text{-}4}$ [17], validated against experimental data on the ignition delay time [17,18] and laminar flame speed [29]. The sooting propensity of OME/diesel blends in diffusion flames has been studied in [31] and a reduction in soot was found when OME compounds are added.

Following previous studies on other alternative fuels [6,7,10,32–36], the primary goal of this work is to characterize the sooting properties of OME_3 used as an additive in ethylene/air flames at different equivalence ratios [37]. In order to evaluate the effect of OME_3 and to identify some specific patterns related to the fuel structure, both experimental and numerical investigations are performed. To the best of our knowledge, there are no comprehensive studies on sooting behavior in laminar flames when OME_3 is used for blending other fuels. Experimental investigations include quantitative measurements of particulate both in situ (laser-based technique) and ex situ (particle size distribution measurements), and the characterization of particulate (UV–Visible (UV–Vis), Raman, FTIR analysis) in terms of its composition and nanostructure. Simulations are performed with the detailed physico-chemical soot model proposed by D'Anna et al. [38,39] integrated into a Conditional Quadrature-based Method of Moments (CQMOM) approach [40,41]. Different types of species such as large PAHs, clusters and agglomerates are accounted for in the soot model, as well as dehydrogenation and oxidation-induced fragmentation processes. $OME_{1\text{-}3}$ kinetics from Sun et al. [29] has been included in the gas-phase kinetic mechanism to account for the fuel mixture oxidation. Classical CQMOM methods are not able to approximate the PSD directly, and the Extended Quadrature Method of Moments [42–44] has recently been introduced to cope with this problem. Below [41], an alternative approach based on the entropy maximization concept is employed here, which allows the PSD to be reconstructed, given a suitably selected set of transported moments.

2. Experimental setup

Premixed ethylene/air flames at atmospheric pressure and with equivalence ratios, ϕ, equal to 2.01, 2.16, 2.31 and 2.46 are stabilized on a capillary burner (inner diameter of 5.8 cm) by means of a stainless steel plate located 30 mm above the burner surface. These flames are the reference cases for studying the effect of OME_3 blending on particle formation and growth. OME_3 was fed in by means of a syringe pump and pre-vaporized by the preheated ethylene/oxygen/nitrogen stream (150 °C). OME_3 was added by replacing some of the ethylene (20% of the total carbon) fed to the reference ethylene/air flames. The equivalence ratio, the cold gas velocity and the total carbon flow rate were kept constant while OME_3 was added. In order to achieve this, the nitrogen and oxygen streams were adapted accordingly. The combustion conditions investigated in this work are reported in Table 1. The same approach and experimental setup have been used for studying other alternative fuels such as butanols [10], furans [33], ethanol [34], and dimethyl ether [36].

Flame temperatures were not measured for OME_3/ethylene flames, whereas temperature profiles were available for pure ethylene flames [10]. However, by keeping the combustion parameters constant as described above, the effect of OME_3 on the flame temperature was considered to be negligible, similarly to the case of other alternative fuels [33]. The temperature profiles for pristine flames were used as an input for the modeling. In these conditions, the chemical effect of OME_3 on particle formation is isolated from the thermal effect.

The experimental setup for optical and particle size distribution, as well as the method of collecting particulate on a glass plate, are the same adopted in previous works (see [10,33,35]). Below, a brief description is given for completeness.

Laser-Induced Emission (LIE) measurements in the 200–550 nm range were used to detect particles in the flame, using the fourth harmonic of a Nd:YAG laser at 266 nm as the excitation source [32,35–37]. The emitted spectra were collected with an ICCD camera with a gate of 100 ns, allowing to distinguish between the broad Laser-Induced

Table 1
Flame conditions. Inflow mixture composition is given in mole fraction. Inlet Gas velocity @STP = 10 cm/s.

ϕ	% OME_3	0	20
2.01	C_2H_4	0.1234	0.0987
	O_2	0.1841	0.1767
	N_2	0.6925	0.7147
	OME_3	0	0.0099
2.16	C_2H_4	0.1313	0.1051
	O_2	0.1824	0.1751
	N_2	0.6862	0.7093
	OME_3	0	0.0105
2.31	C_2H_4	0.1392	0.1114
	O_2	0.1808	0.1735
	N_2	0.68	0.704
	OME_3	0	0.0111
2.46	C_2H_4	0.1469	0.1175
	O_2	0.1792	0.172
	N_2	0.6739	0.6987
	OME_3	0	0.0118

Fluorescence (LIF) signal, ranging between 300 and 450 nm, and the Laser-Induced Incandescence (LII) following a blackbody curve and evaluated at 550 nm.

In order to retrieve information on the PSD, particle sampling from the flames was performed with a horizontal probe [45–50]. The horizontal probe adopted here has an inner diameter of 8 mm, a wall thickness of 0.5 mm, and a pinhole diameter of 0.8 mm. This very large pinhole was set up here with a two-stage dilution system: the carrier gas was set to 4 Nl/min (at 273 K) for the first dilution and to 65 Nl/min in the second dilution stage [32,37,45]. An overall dilution of 500 was achieved.

Particles sampled from the flame were sent to a nano-Differential Mobility Analyzer (DMA) (TapCon 3/150 DMA system with a nominal size range of 2–100 nm, equipped with a Faraday Cup Electrometer detector). In order to charge the particles to Fuchs' steady-state charge distribution [51], a Soft X-Ray Advanced Aerosol Neutralizer (TSI model 3088) was used. The PSDs were obtained by averaging over 3 scans and resulting uncertainty is reported as error bars. The PSDs obtained by DMA were corrected for losses in the pinhole and the probe, following the procedure reported in the literature [52–54]. DMA separates particles based on their mobility diameter, so the particle diameter could be retrieved from the correlation proposed by Singh et al. [55]. Nano-DMA errors originate in the fluctuation of the suction pressure, the partial clogging of the orifice due to soot deposition at high equivalence ratios, wall losses and the coagulation of small particles onto large ones. Hence, the largest uncertainties concern the smallest particles.

A 75 × 25 × 1 mm glass plate was horizontally inserted into the flame for 2 s to collect material from the flame at the highest equivalence ratio. The operation was repeated several times with a cooling cycle at room temperature of 10 s after each insertion. The procedure has been tested and validated before [7,56]. Spectroscopic techniques were used to characterize the sampled material, similarly to what has been done for particles collected in flames fueled with other oxygenated fuels [33] and benzene [56].

Raman spectra were measured directly on the carbon samples deposited on a glass plate using a Horiba XploRA Raman microscope system (Horiba Jobin Yvon, Japan) equipped with a frequency-doubled Nd:YAG solid-state laser (λ = 532 nm) [33]. Raman spectra analysis provides information on the features of the carbon network. FTIR and UV–Vis spectroscopy were performed on the samples removed from the glass plate. FTIR spectra in the 3400–600 cm^{-1} range were acquired in the transmittance mode using a Nicolet iS10 spectrophotometer. For FTIR analysis, the sample needs to be prepared; in particular, carbon particulate matter samples were mixed and ground in KBr pellets (0.2–0.3 wt%) [57]. FTIR gives information on the presence of oxygen within the carbon network. For the UV–Vis analysis, carbon particulate matter samples were suspended in N-methyl-2-pyrrolidone (NMP, with a concentration of 10 mg/L) and analyzed in a 1-cm path length quartz cuvette using an Agilent UV–Vis 8453 spectrophotometer. The UV–Vis spectra were also measured on the soot fraction < 20 nm obtained by filtration on an Anotop filter (Whatman) of a 100 mg/L total particulate suspension. UV–Vis analysis provides information on the mass absorption coefficients for the particles sampled, indicating the level of aromaticity.

Each sampling point was repeated at least three times. Each sample for each experimental condition was preliminarily analyzed using Raman spectroscopy to ensure the sampling reproducibility. After this check, the samples were added together for further spectroscopic analysis. The experimental error for Raman and UV–Vis spectroscopy measurements was evaluated as being less than 5%, whereas for FTIR spectroscopy the error was less than 10%.

3. Numerical modeling

3.1. Gas phase kinetic mechanism and soot model

A detailed kinetic mechanism is used in this work, which includes the kinetic mechanism developed by D'Anna and coworkers [33,38,39,58] and the $OME_{1\text{-}3}$ kinetics taken from Sun et al. [29]. The entire mechanism consists of 141 species and 674 reactions, of which 41 species and 213 reactions are added to include the $OME_{1\text{-}3}$ oxidation kinetics [29].

The physico-chemical soot formation model employed in this work [38] has been combined with the CQMOM approach to track the particulate evolution in [40] and successfully applied for simulating lightly and highly sooting flames in [40,41]. The present model distinguishes between different particle structures based on their state of aggregation, i.e. high-molecular-mass aromatic molecules (*molecules or large PAHs*), clusters of molecules (*clusters*) and agglomerates of particles (*aggregates*) [38]. This allows not only the mass of the formed particles to be followed, but also their hydrogen content and internal structure. Oxidation-induced fragmentation is also accounted for. Oxygen is considered the only species which can avoid reaction on the surface and diffuse towards the points of contact of the primary particles, causing internal oxidation and subsequent particle fragmentation. PAH formation is modeled by the H-Abstraction-C_2H_2-Addition (HACA) route and the resonantly stabilized free radical (RSFR) mechanism [38], while the molecular growth is described from benzene up to pyrene. All the PAH compounds with a molecular weight larger than pyrene are not treated as individual species but considered as lumped species (*large PAHs*), whose evolution is described by the CQMOM. If the Van der Waals forces are strong enough to hold together these large molecules, *clusters* are formed. *Clusters* can grow via chemical pathways and can interact through coagulation. When larger clusters are formed, coagulation becomes an aggregation process, forming chain-like soot particles (*aggregates*). Their reactions are described based on similarity with gas-phase kinetics following Arrhenius-rate laws.

3.2. CQMOM model

Large hydrocarbons and particulates which are not directly solved in the gas-phase kinetics are described by the evolution of the population balance equation (PBE) for the number density function (NDF) $f\left(\underline{\xi};\underline{x},t\right)$. Here, $\underline{x}$ is the space vector, t is the time, and $\underline{\xi}$ is the internal coordinate vector defined as $\underline{\xi} = \left[\xi_{nc},\xi_{H/C},\xi_{stat},\xi_{typ}\right]^T$, where ξ_{nc} is the number of carbon atoms, with $\xi_{nc} \in [0,\infty)$, $\xi_{H/C}$ is the H/C ratio with $\xi_{H/C} \in [0,1]$, ξ_{stat} represents the state of the particular entity with $\xi_{stat} \in A, A = \{stable, radical\}$, and ξ_{typ} is the type of the entity with $\xi_{typ} \in B, B = \{largePAHs, clusters, agglomerates\}$. Note that the four coordinates are independent of one other, and the two coordinates ξ_{stat} and ξ_{typ} are discrete in nature. Using the concept of the conditional density function allows the quadrivariate NDF to be written as

$$f\left(\underline{\xi}\right) = f_{H/C}\left(\xi_{H/C}|\xi_{nc},\xi_{stat},\xi_{typ}\right)\cdot f_{nc}\left(\xi_{nc}|\xi_{stat},\xi_{typ}\right)\cdot n\left(\xi_{stat},\xi_{typ}\right), \quad (1)$$

where $\underline{x}$ and t dependencies are dropped for convenience. Here, $f_{H/C}$ represents the distribution of $\xi_{H/C}$ conditioned on a certain state $(\xi_{nc}, \xi_{stat}, \xi_{typ})$ and f_{nc} represents the distribution of ξ_{nc} conditioned on a state (ξ_{stat},ξ_{typ}). The joint bi-variate distribution $n\left(\xi_{stat},\xi_{typ}\right)$ can assume only six different values, one for each possible combination (u,v) of their discrete domain parameters $\xi_{stat} = \xi_{stat,u}$, $\xi_{typ} = \xi_{typ,v}$. Therefore, evaluating $n\left(\xi_{stat},\xi_{typ}\right)$ at the six discrete points (u,v) allows the quadrivariate $f\left(\underline{\xi}\right)$ to be reformulated as a set of six bivariate NDFs $\Pi_{u,v}$

$$\Pi_{u,v}\left(\xi_{nc},\xi_{H/C}\right) = f_{H/C}^{u,v}\left(\xi_{H/C}\middle|\xi_{nc}\right)\cdot f_{nc}^{u,v}\left(\xi_{nc}\right)\cdot n_{u,v}, \quad (2)$$

where $f_{H/C}^{u,v}\left(\xi_{H/C}|\xi_{nc}\right)$ is a conditional NDF, $f_{nc}^{u,v}(\xi_{nc})$ is a marginal NDF depending only on ξ_{nc} and $n_{u,v}$ is the number density for each combination of (u,v). This is numerically convenient for the moment-based CQMOM approach used in this work. However, the six bivariate distributions $\Pi_{u,v}$ are not independent of each other, but strongly coupled by

different source terms, e.g. the condensation of large PAHs on agglomerates, which modifies both NDFs. A complete description of the coupling approach is described in [40]. Similarly to [41], transport equations for the fractional moments $m_{u,v}^{\frac{k_1}{3},k_2}$ of the six bivariate NDFs in Eq. (2) are solved

$$m_{u,v}^{\frac{k_1}{3},k_2} = \int_0^\infty \int_0^1 \xi_{nc}^{\frac{k_1}{3}} \xi_{H/C}^{k_2} \Pi_{u,v}(\xi_{nc}, \xi_{H/C}) \mathrm{d}\xi_{H/C} \mathrm{d}\xi_{nc}. \quad (3)$$

In the present study, fractional moments with $z = 3$ are used for the property ξ_{nc}.

The moment inversion procedure for fractional moments in the CQMOM context has been extended in [41] and is used here. When the moment inversion is completed, the $N_{\xi_{nc}}$ quadrature nodes $\xi_{nc,i}^{1/3}$ and weights $w_{nc,i}$ for the coordinate ξ_{nc}, and the $N_{\xi_{H/C}}$ conditional nodes $\xi_{H/C,i,j}$ and weights $w_{H/C,i,j}$ for the coordinate $\xi_{H/C}$, for each combination (u,v), are employed to determine the unclosed moment source terms for all the physical and chemical processes described in [38] and treated here in a lumped formulation [40,41]. Two-way coupling between the soot phase and the gas phase is considered. The molecular diffusion of soot is neglected, as well as the thermophoresis, which is known to have negligible effects in premixed flames [59].

Following Salenbauch et al. [41], the entropy maximization (EM) concept is employed in post-processing to evaluate the PSD, without prescribing the distribution shape. It is noteworthy that solving for the fractional moments offers the advantage of being able to directly evaluate the PSD, applying the EM concept. Indeed, using the relation between the equivalent-volume sphere diameter d_p and the coordinate ξ_{nc}

$$d_p = \left(\frac{6W_c}{\pi\rho_s}\right)^{1/3} \xi_{nc}^{1/3} = L^{1/3} \xi_{nc}^{1/3}, \quad (4)$$

with W_c the mass of a single carbon atom and ρ_s the soot density, the transported fractional moments $m_{u,v}^{\frac{k_1}{3},0}$ can be directly transformed into diameter-based moments $\langle m_{u,v}^{k_1} \rangle$

$$\langle m_{u,v}^{k_1} \rangle = \int_0^\infty d_p^{k_1} f_{d_p}(d_p) \mathrm{d}d_p = L^{k_1/3} \int_0^\infty \xi_{nc}^{k_1/3} f_{nc}(\xi_{nc}) \mathrm{d}\xi_{nc} = L^{k_1/3} m_{u,v}^{\frac{k_1}{3},0}. \quad (5)$$

The diameter-based moments are then employed with the EM concept to evaluate the NDF $f_{d_p}(d_p)$ at each location in the domain. Further details can be found in [40,41].

4. Results and discussion

Burner-stabilized ethylene/air and ethylene/OME_3/air flames with different equivalence ratios ϕ (see Table 1) are investigated both experimentally and numerically. One-dimensional simulations have been performed imposing temperature profiles measured in the experiments for the pure ethylene flames at different equivalence ratios.

Thus, the same temperature profiles are used at each equivalence

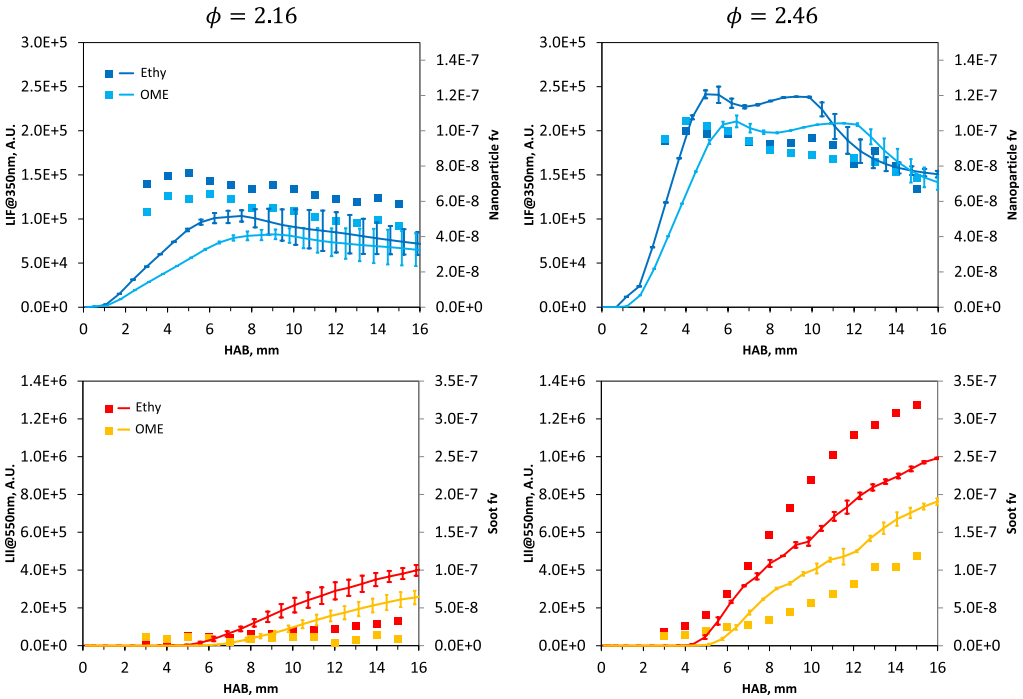

Fig. 1. Comparison of the soot volume fraction predicted by the model with the experimental measured LIF signal (top) and LII signal (bottom) for $\phi = 2.16$ (left) and 2.46 (right) flames: ethylene/air (blue line and symbols: LIF; red line and symbols: LII), ethylene/OME_3/air (cyan line and symbols: LIF; orange line and symbols: LII). A separation is carried out for the particles calculated by CQMOM based on the PSD reconstruction with EM: for LIF, $d_p < d_{p,split}$, for LII, $d_p > d_{p,split}$. Error bars indicate the sensitivity with respect to the value of $d_{p,split}$ in the range of 2 nm $\leq d_{p,split} \leq$ 7 nm. (For interpretation of the references to colour in this figure legend, the reader is referred to the web version of this article.)

ratio for flames of pure ethylene and with added OME_3. The CQMOM-based soot model is applied to solve the PBE for large PAHs, particle clusters and agglomerates. Two quadrature nodes for ξ_{nc} and one quadrature node for $\xi_{H/C}$ conditioned on each ξ_{nc} node for all of the six combinations (state, type) are used, leading to a total of 36 moment transport equations. A variable soot density ρ_s is considered between 1000 and 1800 kg/m^3 as an inverse function of the H/C ratio. It is worth underlining the fact that the simulations are performed without tuning or modifying the model parameters for the different equivalence ratios and fuel mixtures.

4.1. Soot evolution

In Fig. 1, the comparison between LIF and LII signals and the respective simulated volume fraction is only qualitative and reported for two equivalence ratios: 2.16 and 2.46. It is worth noting that the pure ethylene flame at an equivalence ratio of 2.16 is the first flame condition where LII has been detected above the noise level.

According to previous studies, LIF signals here are attributed to aromatic hydrocarbons in condensed-phase nanostructures that are not able to incandesce (see [2,37] and references therein). This attribution significantly affects the selection of adequate species from the modeling results for comparison with the LIF signal. In previous works, the LIF signal has been assumed to be directly related to the formation of condensed-phase nanostructures, i.e. particles with diameters of $d_p \leq$ 7 nm [41], while the detection of the LII signal indicates the presence of larger particles [10]. Following [41], the simulated PSD obtained with CQMOM and EM, as described in Section 3.2, is split in a post-processing step to account for small particles with diameters of $d_p < d_{p,split}$ and larger particles with $d_p > d_{p,split}$, for comparison with the LIF and LII signals, respectively. The value of the split diameter was varied within the relevant range of 2 nm $\leq d_{p,split} \leq$ 7 nm and the results are indicated by the error bars in Fig. 1. The CQMOM model is able to predict a substantially unchanged volume fraction of small particles (as from LIF) when OME_3 is added for both equivalence ratios shown in Fig. 1 (top).

Furthermore, the simulations are able to reproduce the trend of large particles having an increasing volume fraction (as from LII in Fig. 1) as the equivalence ratio increases, and their volume fraction decreasing when OME_3 is added. The simulations predict a delay in the onset of small particles, which suggests that OME_3 affects their formation process. Similarly to the large particle aggregates, the effect of OME_3 is linked to a delay in the onset and particle growth. More specifically, this is due to the lower abundance of particle gas-phase precursors, such as PAHs, and different concentrations of other important species such as C_2H_2, which is responsible for surface growth at high equivalence ratios. The simulations predict a lower reduction in large particles than that observed in experiments, which can be seen particularly clearly in the richest conditions investigated at $\phi = 2.46$.

The effects of OME_3 shown so far have been similarly observed in ethylene flames doped with other oxygenated compounds such as ethanol [35], dimethyl ether [36], butanols [10] and furans [33]. This suggests, as for the other fuels, that the particle reduction must mainly be attributed to the modification of gas-phase precursors when OME_3 is added. Hence it is possible that the gas-phase model adopted here, developed mostly in a low-pressure environment [29], needs to be updated to predict gas-phase compounds.

Fig. 2 shows the PSD measured at a height above the burner (HAB) of 15 mm for the four equivalence ratios investigated, with and without the

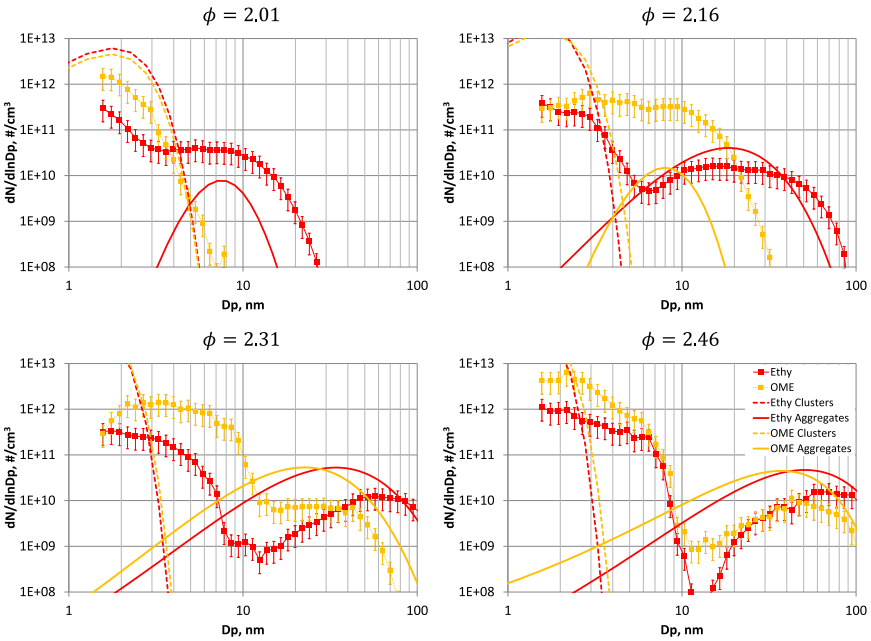

Fig. 2. Particle size distributions determined with EM on the CQMOM simulation results compared with the experimental measurements (SMPS) at HAB = 15 mm for flames with different equivalence ratios of 2.01, 2.16, 2.31 and 2.46: ethylene/air (red line and symbols), ethylene/OME_3/air (orange line and symbols). Dashed lines indicate the clusters and solid lines the aggregates. (For interpretation of the references to colour in this figure legend, the reader is referred to the web version of this article.)

addition of OME_3. The measurements are compared with the predicted PSD from the EM procedure applied to CQMOM flame solutions. For soot particle aggregates, the simulated PSDs are plotted versus the mobility diameter d_m, here equal to the collision diameter d_c as in [60], $d_m \equiv d_c = d_p n_p^{1/D_f}$, where n_p is the number of primary particles in an aggregate calculated on the base of the ratio between the mass of the aggregate and the mass of the primary particle. In this work, the fractal dimension D_f is assumed to be equal to 1.8 and the primary particle diameter d_p to be equal to 15 nm for all the investigated conditions to avoid altering the assessment of the model performance. It is worth underlining that the correlation has been used in order to provide a direct comparison between the simulation results and the data coming from the nano-DMA. Since calculating the mobility diameter from the mass can be difficult, here the aim of the comparison is to show the output of the model. The chosen parameters can be considered reasonable compared with the average values used in the literature [60].

In Fig. 2 it can be observed that for slightly sooting conditions with $\phi = 2.01$, adding OME_3 changes the shape of the PSD from bimodal to unimodal. A bimodal PSD remains evident, instead, for higher equivalence ratio conditions. An additional effect of the OME_3 blending is that a slightly higher number of small particles with $d_p < 5$ nm is formed, while the number of larger particles with $d_p > 20$ nm is drastically reduced at all equivalence ratios.

The modeled PSDs indicate that all the relevant effects of adding OME_3 described above are captured qualitatively. In particular, the model is able to reproduce the trend of increasing size and the total amount of aggregates at increasing equivalence ratios, and a substantially unchanged total number concentration of particles smaller than 10 nm. However, the number concentration of small particles is overpredicted at all equivalence ratios. It has been also reported above and in previous work [37,61] that the SMPS measurements may be affected by significant losses of small particles.

The reduction in the total number of particles produced and the minor or even enhancing effect of small particles is in line with the other oxygenated fuels studied in the same conditions [10,33–36]. The absence of C—C bonds as in DME leads to an even more significant, faster decomposition/oxidation and thus a reduction in gas-phase precursors including PAHs and C_2H_2. As for other investigated biofuels, the presence of oxygenated molecules in fuel streams does not alter the process leading to particle formation, which mostly affects the main gas phase pathways. However, the formation of a small/trace amount of particular compounds – such as oxy-PAHs or other oxygenated large molecules – which may not even play a role in determining the total number of particles or the PSD – can significantly alter the features of the particles produced (see Section 4.2).

4.1.1. Modeling tests

In order to further investigate the importance of the different kinetic pathways that lead to the gas-phase decomposition of OME_3 and its role in particle formation, a numerical experiment was performed. OME_3 was numerically fed into the flame, decomposed into smaller hydrocarbons, to simulate fast decomposition towards the final products. The richest condition ($\phi = 2.46$) was chosen for this study since the largest discrepancy with the experimental data in terms of soot reduction was found in this context (see Fig. 1). In particular, three possible cases were analyzed.

$$OME_3 \Rightarrow 4\ CH_2O + CH_4 \quad \text{(Case 1)}$$

$$16\ OME_3\ (+39\ O_2) \Rightarrow 80\ CO + 34\ H_2 + 62\ H_2O \quad \text{(Case 2)}$$

$$OME_3\ (+6\ O_2) \Rightarrow 5\ CO_2 + 6\ H_2O \quad \text{(Case 3)}$$

It is possible to see that Case 1 is pure decomposition whilst the others are decomposition plus partial oxidation (Case 2) or complete oxidation (Case 3). In all the decompositions, the cold gas velocity was kept the same by adjusting the nitrogen flow rate and, overall, the same number of moles of C, H, and O were fed into the system. In fact, when OME_3 was considered partially or fully oxidized, the oxygen in the fed stream was adjusted accordingly. For the sake of clarity, in Table 2 the molar fractions of the streams in the decomposed tests are reported together with the base case. The temperature profile was kept equal to the base case in order to evaluate only the chemical effects.

In Case 1, OME_3 was decomposed into 4 molecules of CH_2O and 1 molecule of CH_4; this is the simplest possible decomposition and simulates the fast breaking of the C—O bonds. In Case 2, OME_3 was broken and partially oxidized: all the carbon atoms coming from OME_3 were considered to be partially oxidized to CO, the hydrogen atoms coming from OME_3 were fed both as H_2 and H_2O. The amount of H_2 converted to H_2O was decided by leaving the remaining ethylene burning with $C_2H_4/O_2 = 0.82$ (i.e. ϕ for the ethylene equal to 2.46 – see Table 2). This decomposition simulates the capability of OME_3 to go towards partially oxidized products. Finally, in Case 3, OME_3 is considered to be fast enough to go towards the fully oxidized products and OME_3 is decomposed in CO_2 and H_2O. The selected pathways are used here to indicate whether considering a faster oxidation of the OME_3 results in a further reduction of particles formed with respect to the current mechanism.

In Fig. 3, modeling results for the base case and the three decomposition cases are reported in comparison with experimental data: the comparison with LIF is reported in the upper panel and the comparison with LII in the lower panel. It is possible to see that not all decomposition cases lead to an increase in particle reduction. In particular, when OME_3 is decomposed into smaller, highly reactive hydrocarbons (CH_2O and CH_4, the blue line in Fig. 3), the results do not significantly differ from the base case. This suggests that OME_3 decomposition – according to the kinetic scheme adopted here – is already fast enough to form small hydrocarbons. The lower increase may be associated with the higher propensity to form the radicals for molecular growth associated with CH_2O.

Looking at the second decomposition (the green line in Fig. 3), the reduction of both the nanoparticles and soot particles with respect to the base case is significant. In this case, the presence of stable species (CO and H_2) is chemically slowing down the molecular growth process (radicals are less abundant).

Finally, when OME_3 is decomposed and fully oxidized, and CO and H_2O are thus added to the system (the red line in Fig. 3), an increase in particle production is observed. The increase in particle formation has to be linked to the fact that the remaining ethylene and oxygen are burning in a much richer environment, even though it is diluted by CO_2 and H_2O. The increase in the equivalence ratio overwhelms the dilution effect and the chemical effect of CO_2 and H_2O that would lead to a reduction in the number of particles.

Overall, the numerical tests suggest that the kinetic scheme used in

Table 2
Flame conditions for the decomposition cases with equivalence ratio $\phi = 2.46$. Inflow mixture composition is given in mole fraction. Inlet gas velocity @STP = 10 cm/s.

	Base case OME_3	Case 1 $CH_2O + CH_4$	Case 2 $CO + H_2 + H_2O$	Case 3 $CO_2 + H_2O$
C_2H_4	0.1175	0.1175	0.1175	0.1175
O_2	0.172	0.172	0.1433	0.1015
N_2	0.6987	0.6517	0.6099	0.6517
OME_3	0.0118	–	–	–
CH_4	–	0.0118	–	–
CH_2O	–	0.047	–	–
CO	–	–	0.0588	–
H_2	–	–	0.025	–
CO_2	–	–	–	0.0588
H_2O	–	–	0.0455	0.0705
C, mmol/s	**2.97**	**2.97**	**2.97**	**2.97**
H, mmol/s	**6.18**	**6.18**	**6.18**	**6.18**
O, mmol/s	**3.96**	**3.96**	**3.96**	**3.96**

this work is probably underestimating the capability of OME_3 to go towards partially oxidized products. It is possible that in conditions with a medium-high temperature and oxygen-rich environment – such as in the preheating zone of the investigated flame – a faster/direct formation of partially oxidized products could be favored. Future analysis and comparison with experimental data on gas-phase products could help to shed light on this point.

4.2. Soot structure analysis

A detailed spectroscopic analysis of the thermophoretically collected samples was performed to verify how OME_3 affected particulate properties. The analysis was carried out on carbon particulate matter collected on a glass plate at 15 mm HAB and $\phi = 2.46$ in the pure ethylene and ethylene/OME_3 flames. UV–Vis spectroscopy was performed on NMP suspensions with a known concentration of carbon particulate matter removed from the glass plate. UV–Vis mass absorption coefficients in the 250–900 nm range are reported in Fig. 4. The spectrum of particles sampled in the ethylene/OME_3 flame in comparison with that measured for the ethylene flame presents slightly lower mass absorption coefficient values, indicative of a lower aromaticity. On the other hand, the UV–Vis spectrum values of the soot fraction < 20 nm filtered from the total ethylene/OME_3 particulate appear more intense with respect to those measured for the pure ethylene flame, as shown in Fig. 5. In view of the similarity in terms of the shape of the bulk absorption spectra reported in Fig. 4, the lower absorption intensity for the ethylene/OME_3 flame can be justified by the greater abundance of the less light-absorbing particles < 20 nm [62] in this flame, as also confirmed by PSD reported in Fig. 2.

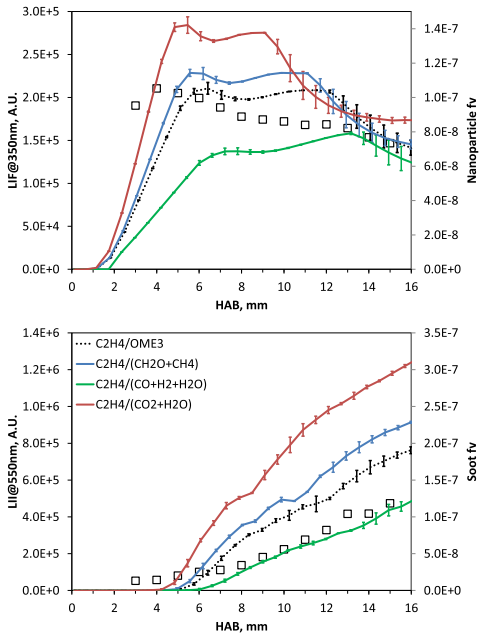

Fig. 3. Comparison of soot volume fractions predicted by the model with the experimentally measured LIF signal (top) and LII signal (bottom) for $\phi = 2.46$ flames of ethylene/OME_3/air (empty symbols). The differently colored continuous lines represent modeling results for the decomposition cases as reported in Table 2, with the dotted line representing modeling results for the base case. A separation is carried out for the particles calculated with CQMOM based on the PSD reconstruction with EM: for LIF, $d_p < d_{p,split}$, for LII, $d_p > d_{p,split}$. Error bars indicate the sensitivity to the value of $d_{p,split}$ in the range of 2 nm $\leq d_{p,split} \leq$ 7 nm. (For interpretation of the references to colour in this figure legend, the reader is referred to the web version of this article.)

The upper panel of Fig. 6 reports the first-order region of the Raman spectra of particles sampled in ethylene and ethylene/OME_3 flames. The spectra present the typical features of disordered/amorphous carbons: a G peak at 1600 cm^{-1} (vibration mode associated with the in-plane bond-stretching motion of pairs of C sp^2 bonds), and a D peak at 1350 cm^{-1} linked with the disorder present in the carbon network [63]. The spectra have been normalized at the G peak to allow an immediate comparison of the spectral features. The G peak position is seen to be higher for the particulate collected in the OME_3/ethylene. It should be remembered that, whatever the excitation energy, the G peak position has a fixed value of 1580 cm^{-1} in perfect and infinite graphite crystals [63], shifted upward to 1600 cm^{-1} for microcrystalline graphite due to the finite crystal size [63]. The G peak position in carbon materials can be shifted up from the 1600 cm^{-1} band limit of purely graphitic carbon by the presence of shorter sp^2 C—C bonds, featuring olefinic bonds and/or small aromatic layers ([64,65]). Thus, the higher G peak position of OME_3/ethylene soot (1606 cm^{-1}) in comparison to pure ethylene soot (1600 cm^{-1}) suggests a higher abundance of olefinic bonds (i.e. a lower abundance of sp^2 aromatic carbon) and/or smaller aromatic layers.

The ratio of the D to the G peak intensity, I(D)/I(G), is the main Raman parameter used for quantifying order/disorder, giving a quantitative measure of the size of the aromatic sp^2 phase organized in clusters. For highly disordered carbons, characterized by an aromatic cluster size smaller than 2 nm, the I(D)/I(G) ratio increases linearly with the crystal area following the equation proposed by Ferrari and Robertson [63].

As can be seen from the upper part of Fig. 6, the spectrum of the OME_3/ethylene soot is characterized by a slightly lower intensity of the I(D)/I(G) ratio. Along with the slightly high position of the G peak, this demonstrates that the average aromatic island size within the carbon network in the ethylene/OME_3 particles is smaller. This suggests that the addition of OME_3 slows soot aromatization and growth. These features can be associated with the generally smaller sizes of particles collected in ethylene/OME_3 flame with respect to pure ethylene flames. A shift of PSD towards small particles indicates a slowing of the growth process that can also be associated with a lower level of aromatization.

Finally, to verify the effect of OME_3 on the composition of carbon particles, FTIR spectroscopy was performed to identify the functional groups of soot particles [57]. The spectra were measured in the same conditions, i.e. the same carbon concentration within the KBr disk and disk thickness, to compare the results. More details on the sample

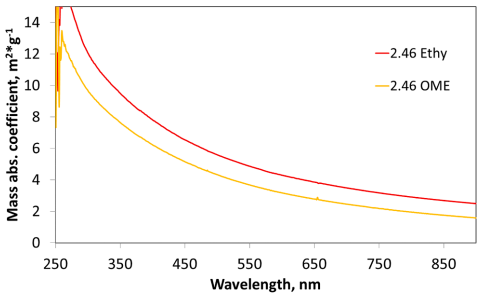

Fig. 4. UV–Vis mass absorption coefficient of particulate collected at 15 mm HAB in the ethylene/air flame (red line) and ethylene/OME_3/air flame (orange line) at $\phi = 2.46$. (For interpretation of the references to colour in this figure legend, the reader is referred to the web version of this article.)

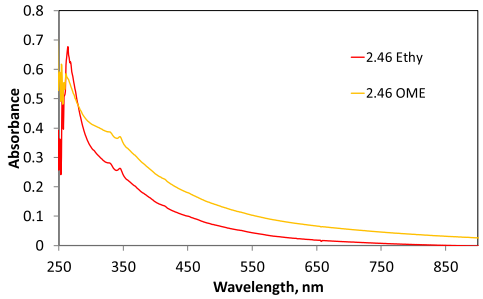

Fig. 5. UV–Vis absorption spectra of the filtered fraction (< 20 nm) of 100 ppm of total particulate collected at 15 mm HAB in the ethylene/air flame (red line) and ethylene/OME_3/air flame (orange line) at $\phi = 2.46$. (For interpretation of the references to colour in this figure legend, the reader is referred to the web version of this article.)

preparation for FTIR measurements are available elsewhere [57].

The spectra in the FTIR spectral region 4000–2500 cm^{-1} where OH stretching peaks (around 3500 cm^{-1}) and CH stretching peaks (3100–2800 cm^{-1}) occur do not exhibit any significant differences, and for this reason they are not reported. Thus, no significant differences in terms of hydrogen content were found, differently from our previous studies on flames doped with 2,5-dimethylfuran [7] and ethanol [6]. This confirms that the main features of the particles produced in pure ethylene and ethylene/OME_3 flames can be considered to be quite similar.

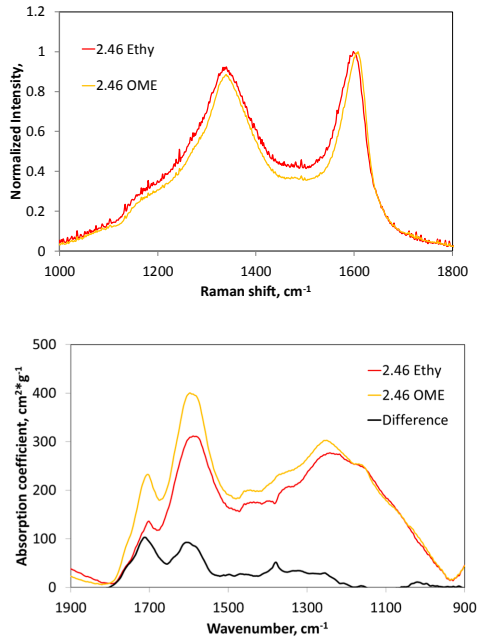

Fig. 6. Raman spectra (top) and infrared mass absorption coefficients (bottom) of soot particles sampled at 15 mm HAB and $\phi = 2.46$ in ethylene/air flames (red line) and ethylene/OME_3/air flames (orange line). The difference in the infrared mass absorption coefficient between ethylene/air flames and ethylene/OME_3/air flames is shown by the black line (bottom). (For interpretation of the references to colour in this figure legend, the reader is referred to the web version of this article.)

Infrared mass absorption coefficients of carbon samples collected in the ethylene and ethylene/OME_3 with $\phi = 2.46$ are reported in the lower panel of Fig. 6 in the range 1900–900 cm^{-1}. They are mostly sensitive to the carbon skeleton and oxygen (C═O and C—O—C) functionalities, and some differences between the spectra are noticeable. These differences in the FTIR signal intensity are better shown in Fig. 6, which also illustrates the spectrum obtained as the difference between the infrared mass absorption coefficients of carbon particulate of ethylene/OME_3 flames and that of the pure ethylene flame.

The higher intensity of the 1600 cm^{-1} peak, due to the C═C stretching mode of polyaromatic systems, is clearly visible for particles collected in the flame doped with OME_3. The irregularity/dissymmetry of the aromatic moiety caused by whichever kind of ring substitution usually causes a strengthening of the 1600 cm^{-1} peak. In particular, it was found that the increase in the dipole moment associated with ring vibrations in the presence of oxygen enhances the intensity of the C═C stretching peak [57,66]. In this regard, soot sampled from the ethylene/OME_3 flame also exhibits a higher intensity of the 1720 cm^{-1} absorption peak, due to the stretching of ketonic and/or esteric C═O groups [67].

Moreover, no significant differences were found in the 1300–1000 cm^{-1} range associated with other oxygen functionalities such as ether type structures (C—O—C), as previously reported for flames doped with butanols [10] and dimethylfuran [7].

Overall, the presence of oxygen functionalities within the carbon network is in line with previous findings for other oxygenated fuels. Comparing these results with those obtained for ethanol [6], butanols [10] and furans [33], the main role of the oxygenated fuels appears to rely on the gas phase pathways: on one hand, oxygen incorporated into the fuel structure improves the decomposition/oxidation pathways, reducing the total number of precursors and hence the total number of particles produced; on the other hand, the same oxygenated group in rich conditions can lead to the formation – in small amounts – of oxy-PAHs or other large oxygen-containing molecules that can finally be included into particles. Studies are ongoing regarding the exact nature of these PAHs. The distinctive feature of OME_3 seems to be the predominance of C═O over C—O—C and OH functionalities and it is probably due to the different molecular structure of the fuel studied here with respect to other biofuels that have been investigated. The presence of C—O bonds in the fuel structure and the absence of C—C bonds probably drive the process toward the preferential formation of C═O bonds. Hence, in the case of OME_3 it seems that oxygenated functionalities are not embedded inside the aromatic network of soot particles, but are just located at the edge of the aromatic systems in the form of C═O groups. It is not possible so far to conclude which pathways lead to the presence of oxygen that is incorporated into the particles. Numerical results and the present gas-phase scheme do not include the presence and/or an active role for oxy-PAH in particle formation. Their impact on the total number of particles or even on the PSD is generally considerable less significant than other combustion and kinetic parameters. However, further studies will have to examine this topic in greater depth, also considering the significant role that the presence of oxygen can have in terms of after-treatment systems and the impact on human health [3,4].

5. Conclusions

In this study, the effects of OME_3 addition on soot particle formation in burner-stabilized premixed ethylene flames have been investigated with experiments and numerical simulations based on the CQMOM approach. 20% of the total carbon was replaced with OME_3 for four equivalence ratios – 2.01, 2.16, 2.31 and 2.46 – while the cold gas velocity was kept constant. The experiments (LII and PSD) and numerical results indicate that there is a reduction in the total number and the size

of soot particles in the OME_3-blended flame. An almost negligible effect was observed on the small condensed-phase nanostructures tracked by the LIF signal. Comparisons with experimental data for pure ethylene and blended flames indicate that the model predictivity is fair both in terms of the soot volume fraction and PSD, without any tuning for different equivalent ratios and fuel mixtures. In very rich conditions, the soot reduction due to the addition of OME_3 is underpredicted. This behavior has been hypothesized to be linked with the decomposition/oxidation of OME_3 in the early stage of combustion and subsequent formation of partially oxidized by-products and radicals. The gas-phase kinetic scheme for OME_3 taken from the literature was originally developed for different combustion conditions. To investigate the influence of the gas-phase reaction pathways on particle formation, numerical tests have been performed using, instead of OME_3, its decomposed or oxidized products to identify possible chemical pathways that lead to a reduction in the particle growth. It has been observed that a faster formation of partially oxidized products in the gas-phase kinetics may favor a further soot reduction with respect to the actual scheme; however, further research is needed to investigate the gas-phase pathways.

Finally, the effects of OME_3 addition on the chemical features of the particles, i.e. aromaticity and composition, have been analyzed in the highest equivalence ratio conditions. UV–Visible and Raman spectroscopy analysis suggest that there is a slightly lower degree of aromatization in OME_3-doped flames, probably due to the higher concentration of particles smaller than 20 nm. A higher presence of C═O functionalities was found when analyzing the FTIR spectra of the particle samples, while no significant differences were observed in C—O—C, OH, and CH functionalities. This could be attributed to the presence in the OME_3 molecule of C—O—C bonds and the total absence of C—C bonds. The presence of C═O groups associated with this fuel structure could be relevant for future studies of similar alternative fuels.

CRediT authorship contribution statement

Federica Ferraro: Conceptualization, Writing - review & editing. **Carmela Russo:** Writing - review & editing. **Robert Schmitz:** Writing - review & editing. **Christian Hasse:** Conceptualization, Funding acquisition. **Mariano Sirignano:** Conceptualization, Writing - review & editing.

Declaration of Competing Interest

The authors declare that they have no known competing financial interests or personal relationships that could have appeared to influence the work reported in this paper.

Acknowledgments

The authors gratefully acknowledge the funding by the German Federal Ministry of Education and Research (BMBF) as part of the NAMOSYN Project (project number 03SF0566R0) and, additionally, by the Clean Sky 2 Joint Undertaking under the European Union's Horizon 2020 research and innovation programme under the ESTiMatE project, grant agreement No. 821418.

References

[1] Sirignano M, Conturso M, Magno A, Di Iorio S, Mancaruso E, Maria Vaglieco B, et al. Evidence of Sub-10 nm particles emitted from a small-size diesel engine. Exp Therm Fluid Sci 2018;95:60–4. https://doi.org/10.1016/j.expthermflusci.2018.01.031.

[2] D'Anna A. Combustion-formed nanoparticles. Proc Combust Inst 2009;32:593–613. https://doi.org/10.1016/j.proci.2008.09.005.

[3] De Falco G, Colarusso C, Terlizzi M, Popolo A, Pecoraro M, Commodo M, et al. Chronic obstructive pulmonary disease-derived circulating cells release IL-18 and IL-33 under ultrafine particulate matter exposure in a caspase-1/8-independent manner. Front Immunol 2017:8. https://doi.org/10.3389/fimmu.2017.01415.

[4] Kohse-Höinghaus K, Oßwald P, Cool TA, Kasper T, Hansen N, Qi F, et al. Biofuel combustion chemistry: from ethanol to biodiesel. Angew Chemie - Int Ed 2010;49:3572–97. https://doi.org/10.1002/anie.200905335.

[5] Battin-Leclerc F, Curran H, Faravelli T, Glaude PA. Specificities related to detailed kinetic models for the combustion of oxygenated fuels components. In: Battin-Leclerc FJM, Simmie E, editors. Blurock Clean. Combust. Dev. Detail. Chem. Kinet. Model. London: Springer London; 2013. p. 93–109. https://doi.org/10.1007/978-1-4471-5307-8_4.

[6] Sirignano M, Ciajolo A, D'Anna A, Russo C. Chemical features of particles generated in an ethylene/ethanol premixed flame. Energy Fuels 2017;31:2370–7. https://doi.org/10.1021/acs.energyfuels.6b02372.

[7] Russo C, D'Anna A, Ciajolo A, Sirignano M. Analysis of the chemical features of particles generated from ethylene and ethylene/2,5 dimethyl furan flames. Combust Flame 2016;167:268–73. https://doi.org/10.1016/j.combustflame.2016.02.003.

[8] Lapuerta M, Oliva F, Agudelo JR, Boehman AL. Effect of fuel on the soot nanostructure and consequences on loading and regeneration of diesel particulate filters. Combust Flame 2012;159:844–53. https://doi.org/10.1016/j.combustflame.2011.09.003.

[9] Guan C, Cheung CS, Li X, Huang Z. Effects of oxygenated fuels on the particle-phase compounds emitted from a diesel engine. Atmos Pollut Res 2017;8:209–20. https://doi.org/10.1016/j.apr.2016.08.005.

[10] Russo C, D'Anna A, Ciajolo A, Sirignano M. The effect of butanol isomers on the formation of carbon particulate matter in fuel-rich premixed ethylene flames. Combust Flame 2019;199:122–30. https://doi.org/10.1016/j.combustflame.2018.10.025.

[11] Ess MN, Bladt H, Mühlbauer W, Seher SI, Zöllner C, Lorenz S, et al. Reactivity and structure of soot generated at varying biofuel content and engine operating parameters. Combust Flame 2016;163:157–69. https://doi.org/10.1016/j.combustflame.2015.09.016.

[12] Lapuerta M, Armas O, Rodríguez-Fernández J. Effect of biodiesel fuels on diesel engine emissions. Prog Energy Combust Sci 2008;34:198–223. https://doi.org/10.1016/j.pecs.2007.07.001.

[13] Song J, Alam M, Boehman AL, Kim U. Examination of the oxidation behavior of biodiesel soot. Combust Flame 2006;146:589–604. https://doi.org/10.1016/j.combustflame.2006.06.010.

[14] Pinzi S, Rounce P, Herreros JM, Tsolakis A, Pilar DM. The effect of biodiesel fatty acid composition on combustion and diesel engine exhaust emissions. Fuel 2013;104:170–82. https://doi.org/10.1016/j.fuel.2012.08.056.

[15] Yehliu K, Vander Wal RL, Armas O, Boehman AL. Impact of fuel formulation on the nanostructure and reactivity of diesel soot. Combust Flame 2012;159:3597–606. https://doi.org/10.1016/j.combustflame.2012.07.004.

[16] Guo Y, Ristovski Z, Graham E, Stevanovic S, Verma P, Jafari M, et al. The correlation between diesel soot chemical structure and reactivity. Carbon N Y 2020;161:736–49. https://doi.org/10.1016/j.carbon.2020.01.061.

[17] Cai L, Jacobs S, Langer R, vom Lehn F, Heufer KA, Pitsch H. Auto-ignition of oxymethylene ethers (OMEn, n = 2–4) as promising synthetic e-fuels from renewable electricity: shock tube experiments and automatic mechanism generation. Fuel 2020;264:116711. https://doi.org/10.1016/j.fuel.2019.116711.

[18] He T, Wang Z, You X, Liu H, Wang Y, Li X, et al. A chemical kinetic mechanism for the low- and intermediate-temperature combustion of Polyoxymethylene Dimethyl Ether 3 (PODE3). Fuel 2018;212:223–35. https://doi.org/10.1016/j.fuel.2017.09.080.

[19] Sanfilippo D, Patrini R, Marchionna M. Use of an oxygenated product as a substitute of gas oil in diesel engines. US 7235113 B2, 2007.

[20] Omari A, Heuser B, Pischinger S. Potential of oxymethylenether-diesel blends for ultra-low emission engines. Fuel 2017;209:232–7. https://doi.org/10.1016/j.fuel.2017.07.107.

[21] Pélerin D, Gaukel K, Härtl M, Jacob E, Wachtmeister G. Potentials to simplify the engine system using the alternative diesel fuels oxymethylene ether OME1 and OME3−6 on a heavy-duty engine. Fuel 2020;259:116231. https://doi.org/10.1016/j.fuel.2019.116231.

[22] Pellegrini L, Marchionna M, Patrini R, Florio S. Emission performance of neat and blended polyoxymethylene dimethyl ethers in an old light-duty diesel car. SAE Tech Pap 2013:2. https://doi.org/10.4271/2013-01-1035.

[23] Lumpp B, Rothe D, Pastotter C, Lämmermann R, Jacob E. Oxymethylene ethers as diesel fuel. Mtz Worldw 2011;78:34–8.

[24] Liu H, Wang Z, Wang J, He X. Improvement of emission characteristics and thermal efficiency in diesel engines by fueling gasoline/diesel/PODEn blends. Energy 2016;97:105–12. https://doi.org/10.1016/j.energy.2015.12.110.

[25] Parravicini M, Barro C, Bouloucos K. Compensation for the differences in LHV of diesel-OME blends by using injector nozzles with different number of holes: emissions and combustion. Fuel 2020;259:116166. https://doi.org/10.1016/j.fuel.2019.116166.

[26] Popp T, Lechner R, Becker M, Hebauer M, O'Connell N, Brautsch M. Potentials of OME/diesel blends for stationary power production – improving emission characteristics of a diesel CHP unit. Appl Therm Eng 2019;153:483–92. https://doi.org/10.1016/j.applthermaleng.2019.03.015.

[27] Ogawa H, Nabi N, Minami M, Miyamoto N, Kim BS. Ultra low emissions and high performance diesel combustion with a combination of high EGR, three-way catalyst, and a highly oxygenated fuel, dimethoxy methane (DMM). SAE Tech Pap 2000. https://doi.org/10.4271/2000-01-1819.

[28] Zheng Y, Tang Q, Wang T, Liao Y, Wang J. Synthesis of a green fuel additive over cation resins. Chem Eng Technol 2013;36:1951–6. https://doi.org/10.1002/ceat.201300360.

[29] Sun W, Wang G, Li S, Zhang R, Yang B, Yang J, et al. Speciation and the laminar burning velocities of poly(oxymethylene) dimethyl ether 3 (POMDME3) flames: an experimental and modeling study. Proc Combust Inst 2017;36:1269–78. https://doi.org/10.1016/j.proci.2016.05.058.
[30] Ren S, Wang Z, Li B, Liu H, Wang J. Development of a reduced polyoxymethylene dimethyl ethers (PODEn) mechanism for engine applications. Fuel 2019;238:208–24. https://doi.org/10.1016/j.fuel.2018.10.111.
[31] Tan YR, Botero ML, Sheng Y, Dreyer JAH, Xu R, Yang W, et al. Sooting characteristics of polyoxymethylene dimethyl ether blends with diesel in a diffusion flame. Fuel 2018;224:499–506. https://doi.org/10.1016/j.fuel.2018.03.051.
[32] Conturso M, Sirignano M, D'Anna A. Effect of furanic biofuels on particles formation in premixed ethylene-air flames: an experimental study. Fuel 2016;175:137–45. https://doi.org/10.1016/j.fuel.2016.02.038.
[33] Conturso M, Sirignano M, D'Anna A. Effect of 2,5-dimethylfuran doping on particle size distributions measured in premixed ethylene/air flames. Proc Combust Inst 2017;36:985–92. https://doi.org/10.1016/j.proci.2016.06.048.
[34] Salamanca M, Sirignano M, Commodo M, Minutolo P, D'Anna A. The effect of ethanol on the particle size distributions in ethylene premixed flames. Exp Therm Fluid Sci 2012;43:71–5. https://doi.org/10.1016/j.expthermflusci.2012.04.006.
[35] Salamanca M, Sirignano M, D'Anna A. Particulate formation in premixed and counter-flow diffusion ethylene/ethanol flames. Energy Fuels 2012;26:6144–52. https://doi.org/10.1021/ef301081q.
[36] Sirignano M, Salamanca M, D'Anna A. The role of dimethyl ether as substituent to ethylene on particulate formation in premixed and counter-flow diffusion flames. Fuel 2014;126:256–62. https://doi.org/10.1016/j.fuel.2014.02.039.
[37] Sirignano M, Bartos D, Conturso M, Dunn M, D'Anna A, Masri AR. Detection of nanostructures and soot in laminar premixed flames. Combust Flame 2017;176:299–308. https://doi.org/10.1016/j.combustflame.2016.10.009.
[38] D'Anna A, Sirignano M, Kent J. A model of particle nucleation in premixed ethylene flames. Combust Flame 2010;157:2106–15. https://doi.org/10.1016/j.combustflame.2010.04.019.
[39] Sirignano M, Kent J, D'Anna A. Detailed modeling of size distribution functions and hydrogen content in combustion-formed particles. Combust Flame 2010;157:1211–9. https://doi.org/10.1016/j.combustflame.2009.11.014.
[40] Salenbauch S, Sirignano M, Marchisio DL, Pollack M, Anna AD, Hasse C. Detailed particle nucleation modeling in a sooting ethylene flame using a Conditional Quadrature Method of Moments (CQMOM). Proc Combust Inst 2016;36:1–9. https://doi.org/10.1016/j.proci.2016.08.003.
[41] Salenbauch S, Sirignano M, Pollack M, D'Anna A, Hasse C. Detailed modeling of soot particle formation and comparison to optical diagnostics and size distribution measurements in premixed flames using a method of moments. Fuel 2018;222:287–93. https://doi.org/10.1016/j.fuel.2018.02.148.
[42] Yuan C, Kong B, Passalacqua A, Fox RO. An extended quadrature-based mass-velocity moment model for polydisperse bubbly flows. Can J Chem Eng 2014;92:2053–66. https://doi.org/10.1002/cjce.22006.
[43] Salenbauch S, Hasse C, Vanni M, Marchisio DL. A numerically robust method of moments with number density function reconstruction and its application to soot formation, growth and oxidation. J Aerosol Sci 2019;128:34–49. https://doi.org/10.1016/j.jaerosci.2018.11.009.
[44] Wick A, Nguyen T, Laurent F, Fox RO, Pitsch H. Modeling soot oxidation with the extended quadrature method of moments. Proc Combust Inst 2017;36:789–97. https://doi.org/10.1016/j.proci.2016.08.004.
[45] Sirignano M, D'Anna A, D'Anna A. Coagulation of combustion generated nanoparticles in low and intermediate temperature regimes: an experimental study. Proc Combust Inst 2013;34:1877–84. https://doi.org/10.1016/j.proci.2012.06.119.
[46] Zhao B, Yang Z, Johnston MV, Wang H, Anthony S, Balthasar M, et al. Measurement and numerical simulation of soot particle size distribution functions in a laminar premixed ethylene-oxygen-argon flame. Combust Flame 2003;133:173–88. https://doi.org/10.1016/S0010-2180(02)00574-6.
[47] Maricq MM. A comparison of soot size and charge distributions from ethane, ethylene, acetylene, and benzene / ethylene premixed flames 2006;144:730–43. DOI:10.1016/j.combustflame.2005.09.007.
[48] Zhao B, Yang Z, Li Z, Johnston MV, Wang H. Particle size distribution function of incipient soot in laminar premixed ethylene flames: effect of flame temperature. Proc Combust Inst 2005;30:1441–8. https://doi.org/10.1016/j.proci.2004.08.104.
[49] Thierley M, Grotheer H-H, Aigner M, Yang Z, Abid A, Zhao B, et al. On existence of nanoparticles below the sooting threshold. Proc Combust Inst 2007;31:639–47. https://doi.org/10.1016/j.proci.2006.08.035.
[50] Sgro LA, De Filippo A, Lanzuolo G, D'Alessio A. Characterization of nanoparticles of organic carbon (NOC) produced in rich premixed flames by differential mobility analysis. Proc Combust Inst 2007;31(I):631–8. https://doi.org/10.1016/j.proci.2006.08.026.
[51] Reischl GP, Mäkelä JM, Karch R, Necid J. Bipolar charging of ultrafine particles in the size range below 10 nm. J Aerosol Sci 1996;27:931–49. https://doi.org/10.1016/0021-8502(96)00026-2.
[52] Hinds WC. Properties, behavior, and measurement of airborne particles. J Aerosol Sci 1999. https://doi.org/10.1016/0021-8502(83)90049-6.
[53] Sgro LA, D'Anna A, Minutolo P. Charge distribution of incipient flame-generated particles. Aerosol Sci Technol 2010;44:651–62. https://doi.org/10.1080/02786826.2010.483701.
[54] Minutolo P, D'Anna A, D'Alessio A. On detection of nanoparticles below the sooting threshold. Combust Flame 2008;152:287–92. https://doi.org/10.1016/j.combustflame.2007.09.007.
[55] Singh J, Patterson RIA, Kraft M, Wang H. Numerical simulation and sensitivity analysis of detailed soot particle size distribution in laminar premixed ethylene flames 2006;145:117–27. DOI:10.1016/j.combustflame.2005.11.003.
[56] Sirignano M, Russo C, Ciajolo A. One-step synthesis of carbon nanoparticles and yellow to blue fluorescent nanocarbons in flame reactors. Carbon N Y 2020;156:370–7. https://doi.org/10.1016/j.carbon.2019.09.068.
[57] Russo C, Stanzione F, Tregrossi A, Ciajolo A. Infrared spectroscopy of some carbon-based materials relevant in combustion: qualitative and quantitative analysis of hydrogen. Carbon N Y 2014;74:127–38. https://doi.org/10.1016/j.carbon.2014.03.014.
[58] Sirignano M, Kent J, D'Anna A. Modeling formation and oxidation of soot in nonpremixed flames. Energy Fuels 2013;27:2303–15. https://doi.org/10.1021/ef400057r.
[59] Appel J, Bockhorn H, Wulkow M. A detailed numerical study of the evolution of soot particle size distributions in laminar premixed flames. Chemosphere 2001;42:635–45.
[60] Kruis FE, Kusters KA, Pratsinis SE, Scarlett B. A simple model for the evolution of the characteristics of aggregate particles undergoing coagulation and sintering. Aerosol Sci Technol 1993;19:514–26. https://doi.org/10.1080/02786829308959656.
[61] Sirignano M, Ciajolo A, D'Anna A, Russo C. Particle formation in premixed ethylene-benzene flames: an experimental and modeling study. Combust Flame 2019;200:23–31. https://doi.org/10.1016/j.combustflame.2018.11.006.
[62] Russo C, Apicella B, Lighty JS, Ciajolo A, Tregrossi A. Optical properties of organic carbon and soot produced in an inverse diffusion flame. Carbon N Y 2017;124:372–9. https://doi.org/10.1016/j.carbon.2017.08.073.
[63] Ferrari AC, Robertson J. Interpretation of Raman spectra of disordered and amorphous carbon. Phys Rev B 2000;61:14095–107. https://doi.org/10.1103/PhysRevB.61.14095.
[64] Russo C, Ciajolo A. Effect of the flame environment on soot nanostructure inferred by Raman spectroscopy at different excitation wavelengths. Combust Flame 2015;162:2431–41. https://doi.org/10.1016/j.combustflame.2015.02.011.
[65] Russo C, Ciajolo A, D'Anna A, Sirignano M. Modelling analysis of PAH and soot measured in a premixed toluene-doped methane flame. Fuel 2018;234:1026–32. https://doi.org/10.1016/j.fuel.2018.07.112.
[66] Fuente E, Menéndez JA, Díez MA, Suárez D, Montes-Morán MA. Infrared spectroscopy of carbon materials: a quantum chemical study of model compounds. J Phys Chem B 2003;107:6350–9. https://doi.org/10.1021/jp027482g.
[67] Akhter MS, Chughtai AR, Smith DM. The structure of hexane soot I: spectroscopic studies. Appl Spectrosc 1985;39:143–53.